Università degli studi di Padova

FACOLTÀ DI INGEGNERIA
Corso di Laurea in Elettronica

TESI DI LAUREA

Study of the reliability of power LEDs for color mixing applications

Relatore:
Ch.mo Prof. Enrico Zanoni

Laureando:
Marioli Michael Simone
Matricola 1014285

Correlatore:
Ing. Matteo Meneghini

ANNO ACCADEMICO 2012-2013

Alla mia famiglia

Contents

Abstract

The aim of this thesis is the reliability analysis of high-power monochromatic and white LEDs provided by six different manufacturers. Operating temperature and forward current are the main causes of the optical and electrical degradation in high power LEDs. In order to evaluate the characteristics of these devices in terms of lifetime and optical power maintenance combined thermal and current stress tests have been carried out, verifying the changes of the optical and electrical characteristics of the devices during the stress. The results of this work have revealed several types of degradation of tested devices from both electrical and optical point of view.

Introduction

Solid State lighting (SSL) based on LEDs is an emerging technology with potential to greatly exceed the efficiency of traditional lamp-based lighting systems. Whereas energy efficiency is the primary motivation behind SSL, LEDs are also anticipated to bring entirely new functionalities to lighting systems, greatly enhancing the ways in which we use light. LEDs have already replaced traditional lamps in a number of lighting systems, including traffic lights, signs, and displays. Many of these applications require monochromatic light and the narrowband emission properties of LEDs present a clear advantage over filtered-lamp approaches. However, the recent development of more efficient and reliable LED light sources, pushed, in recent years, their gradual integration into the general lighting market, leading to the gradual replacement of traditional light sources with solid-state solutions.

In most of the LED lighting systems the generation of white light is made by *Phosphor conversion*: this method involves coating LEDs of one color (mostly blue LEDs made of InGaN) with phosphors of different colors to form white light. The light generated by the LED excites the phosphors, which emit at longer wavelengths where LED performance is deficient. The union of the two spectra is perceived by the human eye as white light. The phosphor conversion approach is most commonly based on a blue LED combined with a yellow phosphor (usually cerium-doped yttrium aluminum garnet or YAG:Ce).

Depending on the properties of the phosphor layer utilised, different types of white lights can be realised: from colder ones to those warmer.

Moreover, the maturity reached by the Gallium Nitride technology, has also led to an excellent robustness and efficiency of this type of white LEDs. A big limit of this technology is constituted by the performance in color rendering, which hardly reaches levels of incandescent lamps.

The standars method of characterizing the quality of light is to use the *color-rendering index (CRI),* which specifies how well a light source can illuminate, o render, the true color of an object. In the case of incandescent lamps (and for all so-called "continuos spectrum radiators") this index is 100; in the phosphor-converted white LEDs, the CRI hardly reaches values above 95, since the white light is obtained by the union of only two chromatic components (see Figure 1).

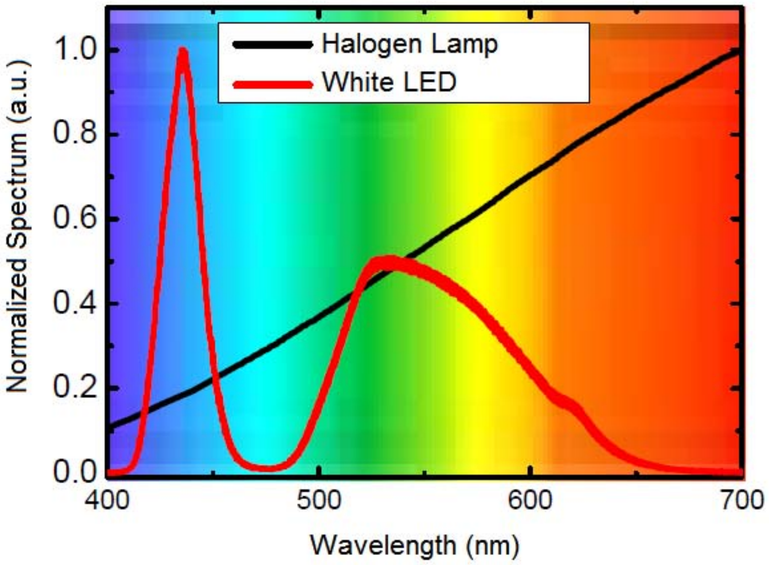

Figure 1: Comparison between the emission spectrum of an incandescent lamp and a phosphor-converted white LED.

To overcome this problem it is required the use of light sources based on *color mixing*, that uses LEDs of various colors with the white LEDs to improve the color characteristics of the generated white light. As a matter of fact the use of blue, green and red LEDs in white light source can greatly extend the spectral range of the generated light, resulting in improved color rendering.

In the lighting market are already present LED light sources based on color mixing which boast a CRI of about 98. At the expense of increased circuit complexity, this technique not only allows to obtain excellent chromatic performance but also to realize light sources that vary their colorimetric characteristics (e.g. CCT) depending on the needs.

However, from the reliability point of view, the use of different color LEDs could prove problematic, because the various materials with which they are produced may give rise to very different degradation kinetics during their life time. If in the case of the InGaN/GaN based LEDs (white and blue) have been recently conducted many studies of reliability, it is not as well known the robustness of Monochromatic LEDs (green, red, yellow, amber, etc.) in high-power operating conditions (high operating temperatures, high values of current injection). In particular, it is interesting to understand how the degradation kinetics changes in the various types of LED subjected to the same operating conditions, in order to provide important guidelines for the design of color-mixing based light sources with high reliability.

The aim of this work is to investigate the reliability characteristics of the RGB and white LEDs manufactured by three of the major players in the SSL market: Cree, Osram Opto Semiconductors and Philips Lumileds. In order to understand the role of temperature and operative current in degradation mechanisms of SSL devices, DC current stress have been carried out on different conditions of temperature. These commercial LEDs are: Cree XP-E, Osram OSLON SSL and SX, and Luxeon REBEL. In order to realise if the degradation mechanisms are caused only by temperature or by the combination of temperature and current injection, pure thermal stress have been carried out on the devices. During the stress the devices were measured as well and the degradation kinetics were deeply analyzed, in order to qualify and quantify the mechanisms that brought to certain changing in the electrical, thermal and optical behaviour of the investigated devices. As the principal degrading causes are thermally-activated, a special investigation has been conducted about the thermal characterization of the studied devices. At a later time we have also analyzed the reliability of white LEDs of other manufacturers in order to to have an overview of the devices on the market. They are: Samsung LH351A-3535 , LG 3535, Seoul semiconductor Z5M and Seoul semiconductor Z5P

The experimental results will be discussed in the last chapters, while we previously need to consider some basilar characteristics concerning the world of the SSL, especially its principal rules and phenomenology. This thesis report is thus structured in seven chapters:

- **Chapter 1** discusses some issues related to solid-state lighting, such as the human vison, photometry, colorimetry and the technologies developed to obtain white light.

- **Chapter 2** presents theory of light-emitting diodes. In this chapter recombination mechanisms, LED structures and LEDs optical properties are examined.

- **Chapter 3** presents the commercial devices used for this by listing their characteristics provided by manufacturers.
- **Chapter 4** will include the description of the setup used in the lab, the instrumentation and the methodology applied on the measurements of the electrical, thermal and luminous behaviour of the devices.
- **Chapter 5** describes the stress conditiosn chosen, the LEDs setup onto the MCPCB and the whole structure of the device that has been measured including the applied heatsink and the thermal interfaces, and reports the thermal characterization results.
- **Chapter 6** will be focused on a critical analysis of the principal degrading dynamics of LEDs and the exposition of practical results concerning the achieved stress level in the final part of the thesis work.
- **Conclusions** and comments to the experimental details will be reported in the last chapter.

CHAPTER 1

Human vision, Photometry, and Colorimetry

In this chapter we will offer a review of vision, photometry and colorimetry in terms of the basic topics that are most relevant for solid state lighting. We will also present the principal features of a light source and introducce important concepts such as temperature color, color-mixing, color-rendering index and color quality scale. In order to evaluate the potentialities of the SSL technology, we will compare its features with the ones of the traditional light sources.

1.1 Human Vision

Lighting technology relies on the property of human vision. Vision is a complex multistage process which yields meaning as to the changing pattern of ambient luminance and chromaticity. The properties of vision determine the quantity and quality requirements for lighting.

The primary process of vision occurs in the eye, where the image is projected onto the retina. Figure 1.1 (a) shows a schematic illustration of the human eye.

The retina includes rod and cone light receptors. Cone cells are responsible for the color perception of the eye and define the lightadapted vision, that is, the *photopic vision.* The cones exhibit high resolution in the central part of the retina, the *foveal region* (fovea centralis), which is the region of greatest visual acuity. There are three

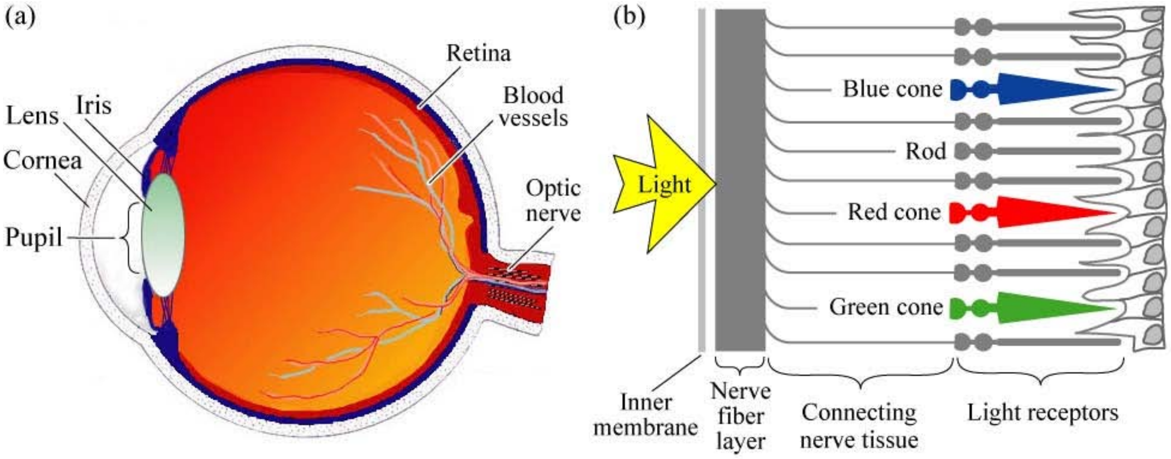

Figure 1.1: (a) Cross section of a human eye. (b) Schematic view of the retina including rod and cone light receptors.

types of cone cells. The first responds the most to light of long wavelengths, peaking at a reddish colour; this type is sometimes designated L for long. The second type responds the most to light of medium-wavelength, peaking at a green colour, and is abbreviated M for medium. The third type responds the most to short-wavelength light, of a bluish colour, and is designated S for short. The three types have peak wavelengths near 564–580 nm, 534–545 nm, and 420–440 nm, respectively. The different responsivity of these three types of cones, illustrated in Figure 1.2, generates different response signals to light that are later elaborated by the brain, permitting the perception of colors.

The second type of cells, the rods, are more abundant and more sensitive to light than cone cells. In addition, they are sensitive over the entire visible range and play an important role in night vision. They define the *scotopic vision*, which is the human vision at low luminance. They have lower resolution ability than the foveal cones. Rods are located outside the foveal region, and therefore, are responsible for the *peripheral vision*. The response of the rods at high-ambient-light levels is saturated and the vision is determined entirely by the cone cells.

Due to the different photoreceptors involved, the spectral sensitivities of scotopic vision and overall photopic vision differ. The spectrum of scotopic sensitivity, which is determined by the photoresponse of rods and the transmittance of pre-retinal media, peaks in the blue-green region at a wavelength of 505 nm in air. The photopic spectrum is red-shifted with respect to the scotopic spectrum. The peak of the photopic sensitivity resides in the yellow-green region at a wavelength of 555 nm in air. Most human activities involve photopic vision, which is the most important from the point of view of lighting technology. Therefore, much effort has been expended to calibrate

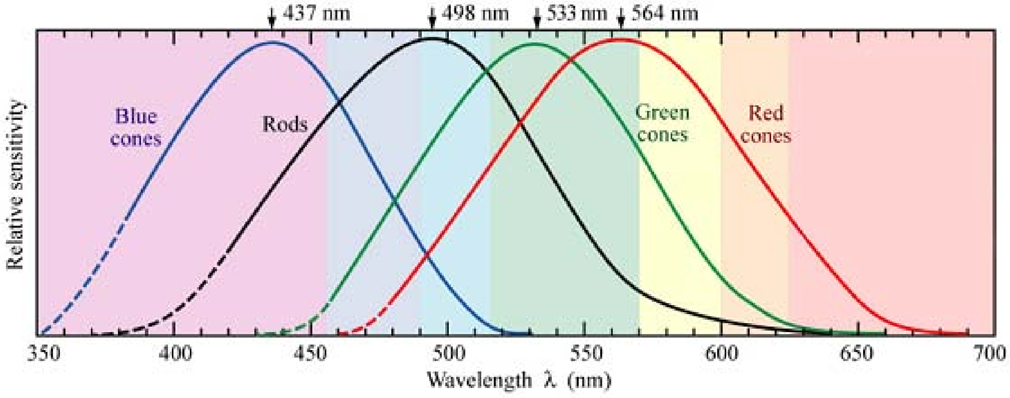

Figure 1.2: Normalized spectral sensitivity of retinal rod and cone cells of the human eye.

and digitize the spectral response and color resolution of photopic vision. In 1924, the International Commission on Illumination (CIE) introduced the *relative luminous efficiency function* or *eye sensitivity function*, *V(λ)*, for photopic vision. This function is referred to as the *CIE 1931 V(λ) function*. It is the current photometric standard in the United States. A modified V(λ) function was introduced by Judd and Vos in 1978 and this modified function is here referred to as the *CIE 1978 V(λ) function*. The modification was motivated by the underestimation of the human eye sensitivity in the blue and violet spectral region by the CIE 1931 V(λ) function. The modified function V(λ) has higher values in the spectral region below 460 nm. The CIE has endorsed the CIE 1978 V(λ) function by stating "the spectral luminous efficiency function for a point source may be adequately represented by the Judd modified V(λ) function" (CIE, 1988) and "the Judd modified V(λ) function would be the preferred function in those conditions where luminance measurements of short wavelengths consistent with color normal observers is desired" (CIE, 1990).

For wavelengths ranging from 390 to 720 nm, the eye sensitivity function V(λ) is greater than 10^{-3}. Although the human eye is sensitive to light with wavelengths $<$ 390 nm and $>$ 720 nm, the sensitivity at these wavelengths is extremely low. Therefore, the wavelength range 390 nm $\leq \lambda \leq$ 720 nm can be considered the *visible wavelength range*. The relationship between color and wavelength within the visible wavelength range is given in Table 1.1. This relationship is valid for monochromatic or near-monochromatic light sources such as LEDs. Note that color is, to some extent, a subjective quantity. Also note that the transition between different colors is continuous.

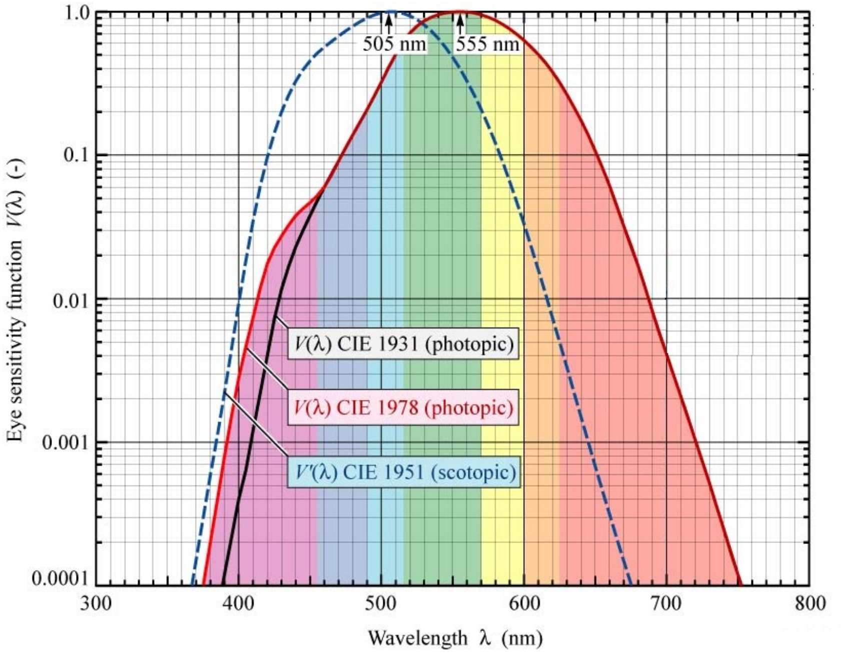

Figure 1.3: Comparison of CIE 1931 and CIE 1978 eye sensitivity function $V(\lambda)$ for the photopic vision regime. Also shown is the eye sensitivity function for the scotopic vision regime, $V'(\lambda)$, that applies to low ambient light levels.

Color	Wavelength
Ultraviolet	$<$ 390 nm
Violet	390–455 nm
Blue	455–490 nm
Cyan	490–515 nm
Green	515–570 nm

Color	Wavelength
Yellow	570–600 nm
Amber	590–600 nm
Orange	600–625 nm
Red	625–720 nm
Infrared	$>$ 720 nm

Table 1.1: Colors and associated typical LED peak wavelength ranges

1.2 Photometry

The physical properties of electromagnetic radiation are characterized by *radiometric units*. Using radiometric units, we can characterize light in terms of physical quantities; for example, the number of photons, photon energy, and optical power (in the lighting community frequently called the radiant flux). Radiometry, however, doesn't take any account of the interaction of light with the human eye, so that it is not useful in measuring light perception by a human being. This limitation of radiometry is overcome by *photometry* which is defined as the science of measurement of visible light in terms of its perceived brightness to human vision. A summary of the most important photometric quantities and units with their radiometric counterparts are given in Table

	Radiometric Quantities	**Units**	**Photometric Quantities**	**Units**
Energy	Radiant energy Q	J (joule)	Luminous energy Q_l	lm·s
Energy density	Radiant energy density $w = \frac{dQ}{dV}$	$\frac{J}{m^3}$	Luminous density $w = \frac{dQ}{dV}$	$\frac{J}{m^3}$
Power	Radiant flux or radiant power $\Phi(or\ P) = \frac{dQ}{dt}$	W or J/s	Luminous flux $\Phi_\lambda = \frac{dQ_\lambda}{dt}$	lm=cd·sr
Power per area	Radiant exitance $M = \frac{d\Phi}{da}$ (for emitter) or Irradiance $E = \frac{d\Phi}{da}$ (for receiver)	$\frac{W}{m^2}$	Luminous exitance $M_\lambda = \frac{d\Phi_\lambda}{da}$ (light emitter) or Irradiance $E_\lambda = \frac{d\Phi_\lambda}{da}$ (light receiver)	Lux or $\frac{lm}{m^2}$
Power per area per solid angle	Radiance $L = \frac{d\Phi}{d\Omega dacos\alpha} = \frac{dI}{dacos\alpha}$	$\frac{W}{srm^2}$	Luminance $L_\lambda = \frac{dI_\lambda}{dacos\alpha}$	$\frac{cd}{m^2} = \frac{lm}{m^2 sr}$
Intensity	Radiant intensity $I = \frac{d\Phi}{d\Omega}$	$\frac{W}{sr}$	Luminous intensity $I_\lambda = \frac{d\Phi_\lambda}{d\Omega}$	Candela or $\frac{lm}{sr}$

Table 1.2: Radiometric and Photometric Quantities and Units

1.2. Radiometric quantities appear in the literature either without subscripts or with the subscript e (electromagnetic). Photometric quantities usually are labeled with a subscript λ or v (visible) to indicate that only the visible spectrum is being considered.

The luminous intensity represents the light intensity of an optical source as perceived by the human eye and is measured in units of candela (cd). The candela is one of the seven basic units of the SI system. A monochromatic light source emitting an optical power of 1/683 W at 555 nm into the solid angle of 1 sr has a luminous intensity of 1 cd.

The *luminous flux*, Φ_λ (also called luminous power or luminosity), is the light power of a source as perceived by the human eye. The unit of luminous flux is the lumen (lm). It is defined as follows: *a monochromatic light source emitting an optical power of (1/683) watt at 555 nm has a luminous flux of 1 lumen (lm).* The lumen is an SI unit.

A comparison of the definitions for the candela and lumen reveals that 1 candela equals 1 lumen per steradian or cd = lm/sr. Thus, an isotropically emitting light source with luminous intensity of 1 cd has a luminous flux of 4π lm = 12.57 lm.

The *illuminance* is the luminous flux incident per unit area. The illuminance measured in lux (lux = lm/m2). It is an SI unit used when characterizing illumination conditions. Table 1.3 gives typical values of the illuminance in different environments.

The luminance of a surface source (i.e. a source with a non-zero light-emitting surface area such as a display or an LED) is the ratio of the luminous intensity emitted in a certain direction (measured in cd) divided by the projected surface area in that

Illumination condition	Illuminance
Full moon	1 lux
Street lighting	10 lux
Home lighting	30 to 300 lux
Office desk lighting	100 to 1000 lux
Surgery lighting	10000 lux
Direct sunlight	100000 lux

Table 1.3: Typical illuminance in different environments.

direction (measured in m^2). The luminance is measured in units of cd/m^2. In most cases, the direction of interest is normal to the chip surface. In this case, the luminance is the luminous intensity emitted along the chip-normal direction divided by the chip area. For LEDs, it is desirable to maximize luminous intensity and luminous flux while keeping the LED chip area minimal. Thus the luminance is a measure of how efficiently the valuable semiconductor wafer area is used to attain, at a given injection current, a certain luminous intensity.

The conversion between radiometric and photometric units is provided by the eye sensitivity function, V(λ). The eye has its peak sensitivity in the green at 555 nm, where the eye sensitivity function has a value of unity, that is, V(555 nm) = 1. For wavelengths smaller than 390 nm and larger than 720 nm, the eye sensitivity function falls off below 10^{-3}. The conversion from watts to lumens at any other wavelength involves the product of the radiant power and the V(λ) value at the wavelength of interest. The spectral density of the radiant flux, $\Phi(\lambda) = \frac{d\Phi}{dl}$, is the light power emitted per unit wavelength and measured in watts per nanometer, and is also called spectral power distribution. The luminous flux, Φ_λ, is related to the spectral density of the radiant flux $\Phi(\lambda)$ through the luminous efficiency function V(λ) measured in lumen:

$$\Phi_\lambda = 683 \left[\frac{lm}{W}\right] \int_\lambda V(\lambda)\Phi(\lambda)d\lambda. \tag{1.1}$$

This equation suggests that radiant flux of 1 W at a wavelength of 555 nm produces a luminous flux of 683 lm. This equation could also be used for other quantity pairs. For instance, luminous intensity (cd) and spectral radiant intensity (W/sr·nm), illuminance (lux) and spectral irradiance (W/m^2·nm), or luminance (cd/m^2) and spectral radiance (W/m^2·sr·nm). Equation 1.1 represents a weighting, wavelength by wavelength, of the radiant spectral term by the visual response at that wavelength. The wavelength limits can be set to restrict the integration only to those wavelengths where the product of the spectral term $\Phi(\lambda)$ and $V(\lambda)$ is nonzero. Practically, this means that the integration is over the entire visible spectrum, because out of the visible range, $V(\lambda) \cong 0$ and the integral tends to zero. As the V(λ) function is defined by a table of empirical values, the integration is usually done numerically. The optical power emitted by a light source is then given by:

$$\Phi = \int_{\lambda} \Phi(\lambda) d\lambda. \tag{1.2}$$

The luminous efficacy of optical radiation (also called the luminosity function), measured in units of lumens per watt of optical power, is the conversion efficiency from optical power to luminous flux. The luminous efficacy is defined as

$$Luminous\, efficacy = \frac{\Phi_{\lambda}}{P} = \left[683 \left[\frac{lm}{W} \right] \int_{\lambda} V(\lambda) P(\lambda) d\lambda \right] / \left[P = \int_{\lambda} P(\lambda) d\lambda \right]. \tag{1.3}$$

For strictly monochromatic light sources ($\Delta\lambda \rightarrow 0$), the luminous efficacy is equal to the eye sensitivity function V(λ) multiplied by 683 lm/W. However, for multicolor light sources and especially for white light sources, the luminous efficacy needs to be calculated by integration over all wavelengths.

As will be explained later, one of the most important parameters of an optical source such as an LED is its luminous efficiency, which is defined as:

$$Luminous\, efficiency = \Phi_{\lambda}/(IV) \tag{1.4}$$

i.e. it expresses the ratio of the luminous flux to the electrical power consumption of the device. It is a measure of the ability of converting the absorbed power into luminous flux, and is measured in units of lm/W. Note that in the lighting community, luminous efficiency is often referred to as *luminous efficacy of the source.*

1.3 Colorimetry

Colorimetry deals with measurement of color. The sensation of color is much more complex than sensation of the brightness. A numerical description of colors relies on a very simplied model of human vision and therefore might disagree with certain subjective observations. Nevertheless, the basic concepts of colorimetry, such as tristimulus values, chromaticity coordinates, color temperature, and color rendering, are well formulated at present. These concepts are of crucial importance in describing light sources for lighting applications.

1.3.1 Color-matching functions and chromaticity diagram

As stated in section 1.1 the perception of color is the result of the different amount of excitation of the the red, green and blue cone cells of the retina. The CIE has introduced the color-matching theory in 1931 in order to provide a method of understanding how a combination of these three stimuli results in the perception of a determined color. For this reason, the CIE has developed a set of three *color matching functions* (CMFs) $\bar{x}(\lambda)$, $\bar{y}(\lambda)$, and $\bar{z}(\lambda)$, represented in Figure 1.4. These functions approximate the relative sensitivity curves of the three types of cones; $\bar{y}(\lambda)$ also corresponds to the eye sensitivity function V(λ). The three color matching functions are used to calculate the tristimulus values X, Y and Z that account for the relative stimulation of each type of cone:

$$X = \int_{\lambda} \bar{x}(\lambda) P(\lambda) d\lambda; \tag{1.5}$$

$$Y = \int_{\lambda} \bar{y}(\lambda) P(\lambda) d\lambda; \tag{1.6}$$

$$Z = \int_{\lambda} \bar{z}(\lambda) P(\lambda) d\lambda. \tag{1.7}$$

Notice that the CMFs have no measurement unit, so the unit of the tristimulus values is "watt". These indexes are used to produce a very important diagram, the *CIE chromaticity diagram.*

As a matter of fact a normalization of the X, Y and Z values is possible in order to represent in a two-dimensional diagram the colors perceived by the human eye. The chromaticity coordinates **x** and **y** are are obtained by the following:

$$x = \frac{X}{X+Y+Z}, \tag{1.8}$$

$$y = \frac{Y}{X+Y+Z}. \tag{1.9}$$

Thus, the value of a chromaticity coordinate is the stimulation of each primary light (or of each type of retinal cone) divided by the entire stimulation (X + Y + Z). The value of the z chromaticity coordinate is calculated analogously, that is

$$z = \frac{Z}{X+Y+Z} = 1 - x - y. \tag{1.10}$$

Note that the z chromaticity value can be obtained from x and y, so that there is no new

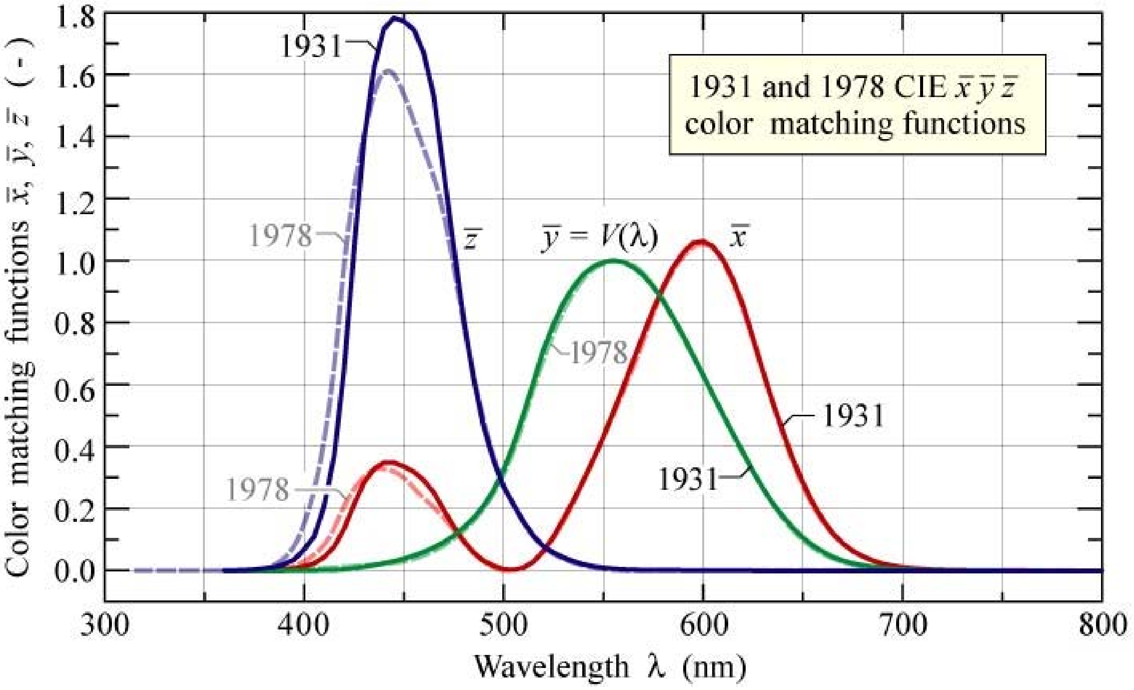

Figure 1.4: CIE 1931 and CIE 1978 $\bar{x}(\lambda)$,$\bar{y}(\lambda)$, and $\bar{z}(\lambda)$ color matching functions (CMFs). The $\bar{y}(\lambda)$ CMF is identical to the eye sensitivity function V (). Note that the CIE 1931 CMF is the currently valid official standard. (From .)

information provided by the z chromaticity coordinate. Therefore, the z coordinate is redundant and, for this reason, does not need to be used.

The chromaticity diagram is shown in Figure 1.5. Reddish and greenish colors are found for large values of x and y, respectively. Bluish colors are found for large values of z, which is, according to eq.1.10, for low values of x and y, or near the origin of the chromaticity diagram.

An assignment of common colors in the chromaticity diagram is given in Fig. 17.5. The figure also shows the equal-energy point located in the center of the chromaticity diagram at (x, y, z) = (1/3, 1/3, 1/3). The optical spectrum corresponding to the equal-energy point has a constant spectral distribution, i.e. the optical energy per wavelength interval dλ is constant across the visible spectrum. Such a spectrum also results in equal tristimulus values, i.e. X = Y = Z.Monochromatic or pure colors are found on the perimeter of the chromaticity diagram. White light is found in the center of the chromaticity diagram. All colors can be characterized in terms of their location in the chromaticity diagram.

As stated above monochromatic light sources ($\Delta\lambda \rightarrow 0$) are located on the perimeter of the chromaticity diagram. Light emission from LEDs is monochromatic (single color)

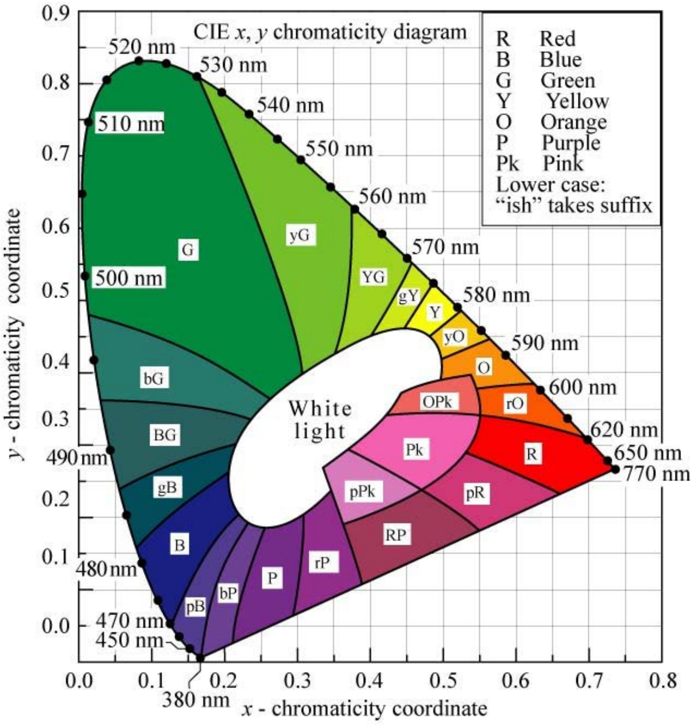

Figure 1.5: 1931 CIE chromaticity diagram with areas attributed to different colors

to the eye but LEDs are not monochromatic in the strict physical sense since LEDs have a spectral linewidth of about 1.8 kT. Owing to the finite spectral linewidth of LEDs, they are not located on the very perimeter of the chromaticity diagram but are located close to the perimeter. When a source emits light distributed over a range of wavelengths, then the chromaticity location moves towards the center of the diagram. The location of different LEDs on the chromaticity diagram is shown in Figure 1.7

1.4 White light

White light is a unique color. There are a very large number of optical spectra that can be used to generate white light. Among these spectra, the planckian black-body radiation spectrum forms a unique and very useful standard because it allows to describe the spectrum with only one parameter, namely the *color temperature*, which is equal to the temperature of the body. Furthermore, natural daylight closely resembles the planckian spectrum.

At low black-body temperatures, e.g. 2000 K, the radiation occurs mostly in the infrared. As the temperature increases, the maximum of the radiation moves into the visible wavelength range.

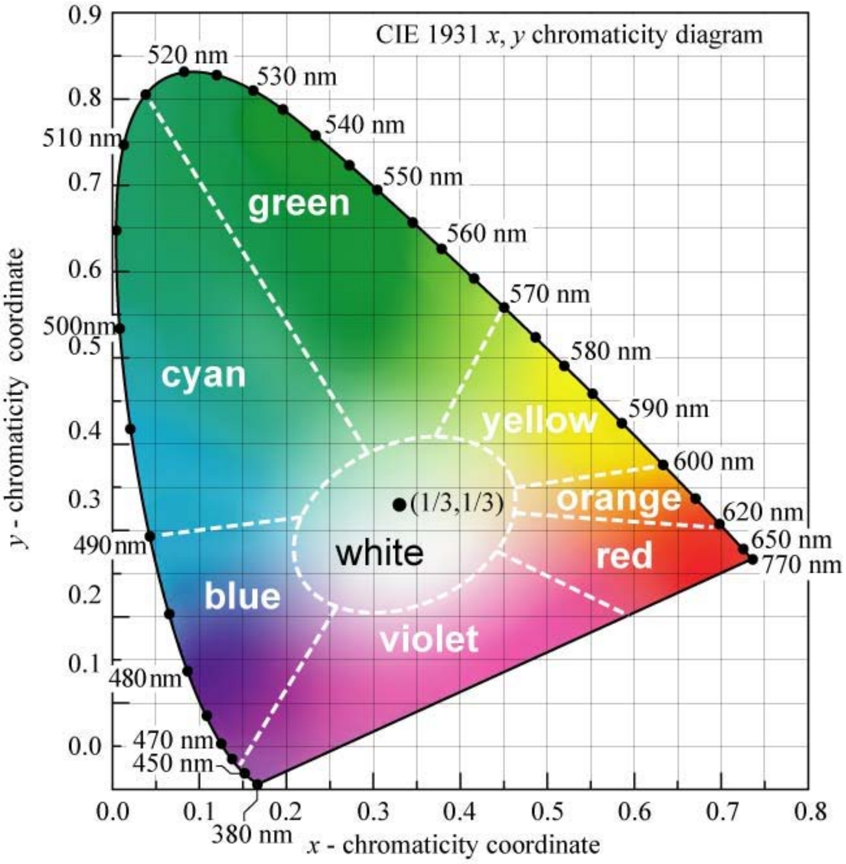

Figure 1.6: CIE 1931 (x, y) chromaticity diagram. Monochromatic colors are located on the perimeter. Color saturation decreases towards the center of the diagram. White light is located in the center. Also shown are the regions of distinct colors. The equal-energy point is located at the center and has the coordinates (x, y) = (1/3, 1/3).

The location of the black-body radiation in the chromaticity diagram (called planckian locus) is shown in figure 1.8. As the temperature of the black body increases, the chromaticity location moves from the red wavelength range towards the center of the diagram.

The color temperature (CT) of a white light source, given in units of Kelvin, is the temperature of a planckian black-body radiator that has the same chromaticity location as the white light source considered. If the color of a white light source does not fall on the planckian locus, the *correlated color temperature* (CCT), also given in units of Kelvin, is used. The correlated color temperature of a white light source is defined as the temperature of a planckian black-body radiator, whose color is closest to the color of the white light source. Low CCT (less than 3000 K) is characteristic of warm white light, while high CCT (higher than 5000 K) represents cool, blueish white light.

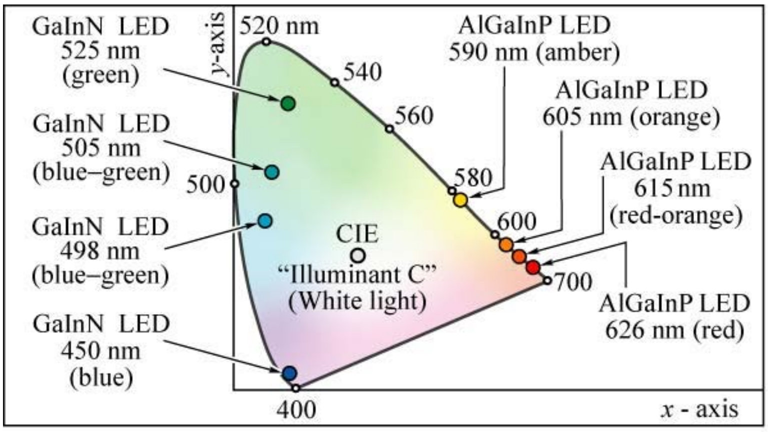

Figure 1.7: Location of LED light emission on the chromaticity diagram.

On the (x, y) chromaticity diagram, the correlated color temperature cannot be determined by using the shortest distance to the planckian locus due to the non-uniformity of the (x, y) chromaticity diagram. The lines of constant correlated color temperature in the (x, y) chromaticity diagram are shown in Figure 1.9.

1.5 Additive color mixing

The *combination* or *additive mixing* of two or more light sources is employed in a number of applications. In LED displays, three different types of LEDs, usually emitting in the red, green, and blue, are used. The three colors are mixed so that the observer can experience a wide range of colors. Another useful application of color mixing is the generation of white light by two, three, or more complementary colors. A schematic of additive color mixing and a corresponding experiment are shown in Figure 1.11.

Consider three sources with spectral power density $P_1(\lambda)$, $P_2(\lambda)$, and $P_3(\lambda)$ with peak wavelengths λ_1, λ_2, λ_3. We assume that each emission band is much narrower than any of the three color matching function. We further assume that the three light sources have the chromaticity coordinates (x_1, y_1), (x_2, y_2), and (x_3, y_3). Exploiting the fact that the spectral linewidth of the three sources is much narrower than the color matching functions, we can rewrite Eqs. 1.5, 1.6, 1.7 as

$$X = \int_\lambda \bar{x}(\lambda)P_1(\lambda)d\lambda + \int_\lambda \bar{x}(\lambda)P_2(\lambda)d\lambda + \int_\lambda \bar{x}(\lambda)P_3(\lambda)d\lambda \approx \bar{x}(\lambda_1)P_1 + \bar{x}(\lambda_2)P_2 + \bar{x}(\lambda_2)P_2 \tag{1.11}$$

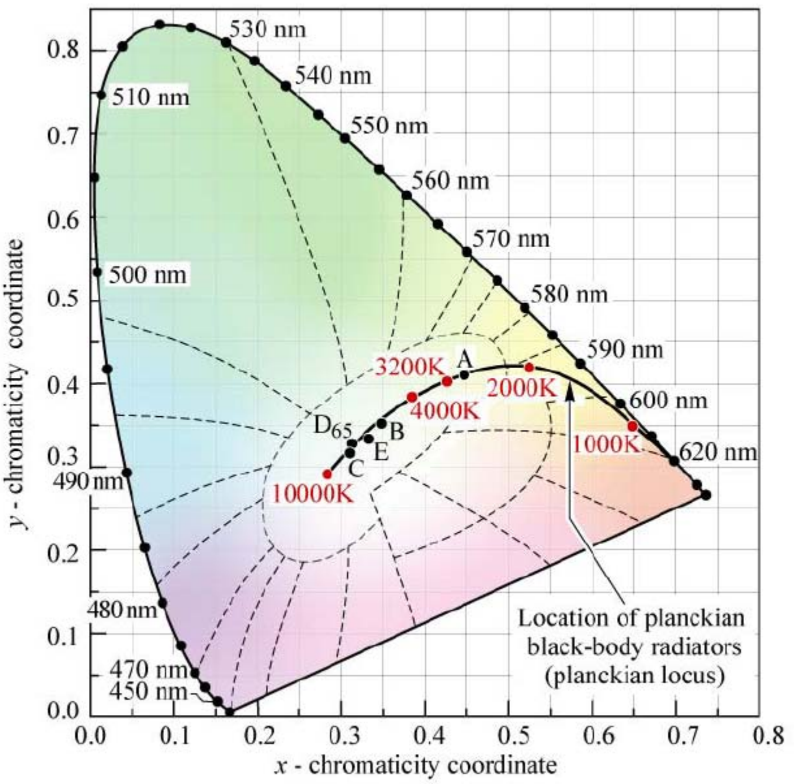

Figure 1.8: Chromaticity diagram showing planckian locus, the standardized white Illuminants A, B, C, D65, and E, and their color temperature.

$$Y = \int_\lambda \bar{y}(\lambda)P_1(\lambda)d\lambda + \int_\lambda \bar{y}(\lambda)P_2(\lambda)d\lambda + \int_\lambda \bar{y}(\lambda)P_3(\lambda)d\lambda \approx \bar{y}(\lambda_1)P_1 + \bar{y}(\lambda_2)P_2 + \bar{y}(\lambda_3)P_3; \tag{1.12}$$

$$Z = \int_\lambda \bar{z}(\lambda)P_1(\lambda)d\lambda + \int_\lambda \bar{z}(\lambda)P_2(\lambda)d\lambda + \int_\lambda \bar{z}(\lambda)P_3(\lambda)d\lambda \approx \bar{z}(\lambda_1)P_1 + \bar{z}(\lambda_2)P_2 + \bar{z}(\lambda_3)P_3 \tag{1.13}$$

where P_1, P_2, and P_3, are the optical powers emitted by the three sources. Using the abbreviations

$$L_1 = \bar{x}(\lambda_1)P_1 + \bar{y}(\lambda_1)P_1 + \bar{z}(\lambda_1)P_1 \tag{1.14}$$

$$L_2 = \bar{x}(\lambda_2)P_2 + \bar{y}(\lambda_2)P_2 + \bar{z}(\lambda_2)P_2 \tag{1.15}$$

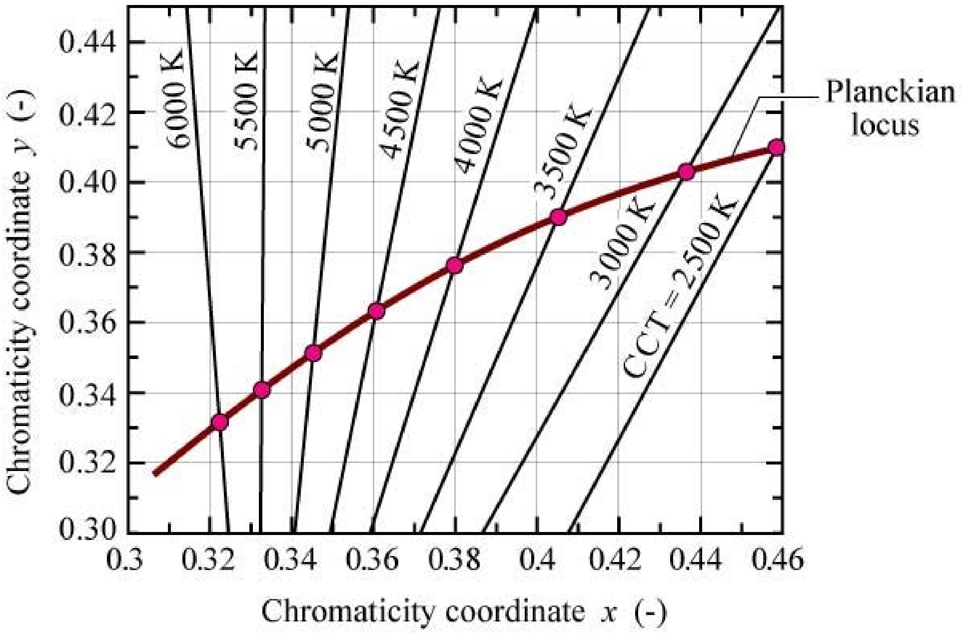

Figure 1.9: Lines of constant correlated color temperature in the (x, y) chromaticity diagram.

$$L_3 = \bar{x}(\lambda_3)P_3 + \bar{y}(\lambda_3)P_3 + \bar{z}(\lambda_3)P_3 \tag{1.16}$$

the chromaticity coordinates of the mixed light can be calculated from the tristimulus values to yield

$$x = \frac{x_1L_1 + x_2L_2 + x_3L_3}{L_1 + L_2 + L_3} \tag{1.17}$$

$$y = \frac{y_1L_1 + y_2L_2 + y_3L_3}{L_1 + L_2 + L_3}. \tag{1.18}$$

Thus, the chromaticity coordinate of the multi-component light is a *linear combination of the individual chromaticity coordinates* weighted by the L_i factors.

The principle of color mixing in the chromaticity diagram is shown in Figure 1.11. The figure shows the mixing of two colors with chromaticity coordinates (x1, y1) and (x2, y2). For the case of two colors, L3 = P3 = 0. The mixed color will be located on the straight line connecting the chromaticity coordinates of the two light sources. Thus any color (including white) located between the two chromaticity points can be created by mixing the two colors.

Figure 1.11 also shows the mixing of three colors, located in the red, green, and blue regions of the chromaticity diagram. The three chromaticity points, connected

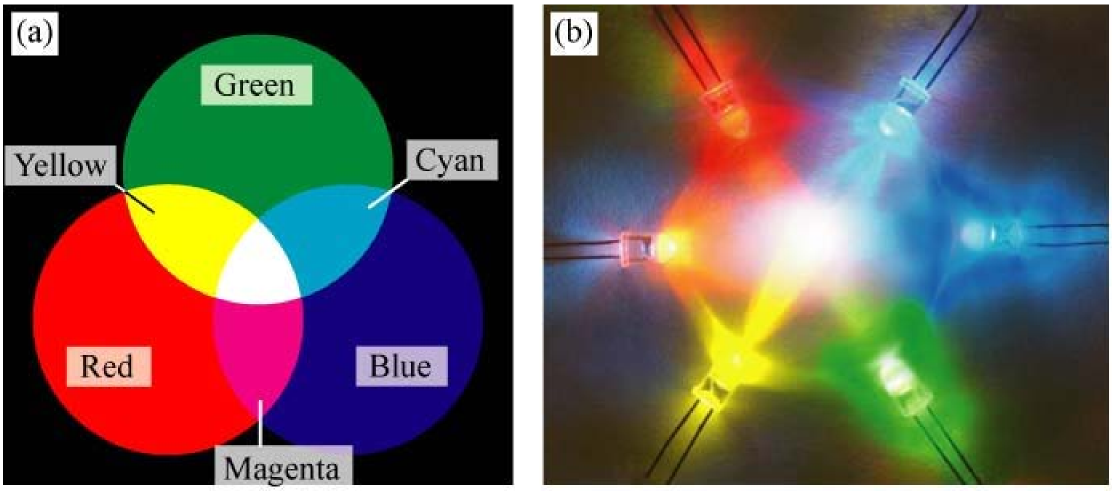

Figure 1.10: (a) Schematic of additive color mixing of three primary colors. (b) Additive color mixing using LEDs.

by a dashed line, are typical points for red, green, and blue LEDs. The area located within the dashed line, called the color gamut, represents all colors that can be created by mixing the three primary colors red, green, and blue. The ability to create a great variety of colors is an important quality for displays. It is desirable that the color gamut provided by the three light sources is as large as possible to create displays able to show brilliant, saturated colors.

This discussion on color mixing allows one to understand the location of different LEDs in the chromaticity diagram. The perimeter of the chromaticity diagram in the red spectral region is approximately a straight line, so that red LEDs, despite their thermal broadening, are located directly on the perimeter of the chromaticity diagram. In contrast, the perimeter is strongly curved in the green region, so that green LEDs, due to their spectral broadening, are displaced from the perimeter towards the center of the chromaticity diagram.

1.6 Color rendering index

Another important characteristic of a white light source is its ability to show (i.e. render) the true colors of physical objects that are being illuminated by the source. The ability to render the colors of an object is measured in terms of the *color-rendering index* or *CRI* . It is a quantitative measure of the ability of a light source to reproduce the colors of various objects faithfully in comparison with an ideal or natural light source. The color-rendering characteristics of a white light source are relevant for light

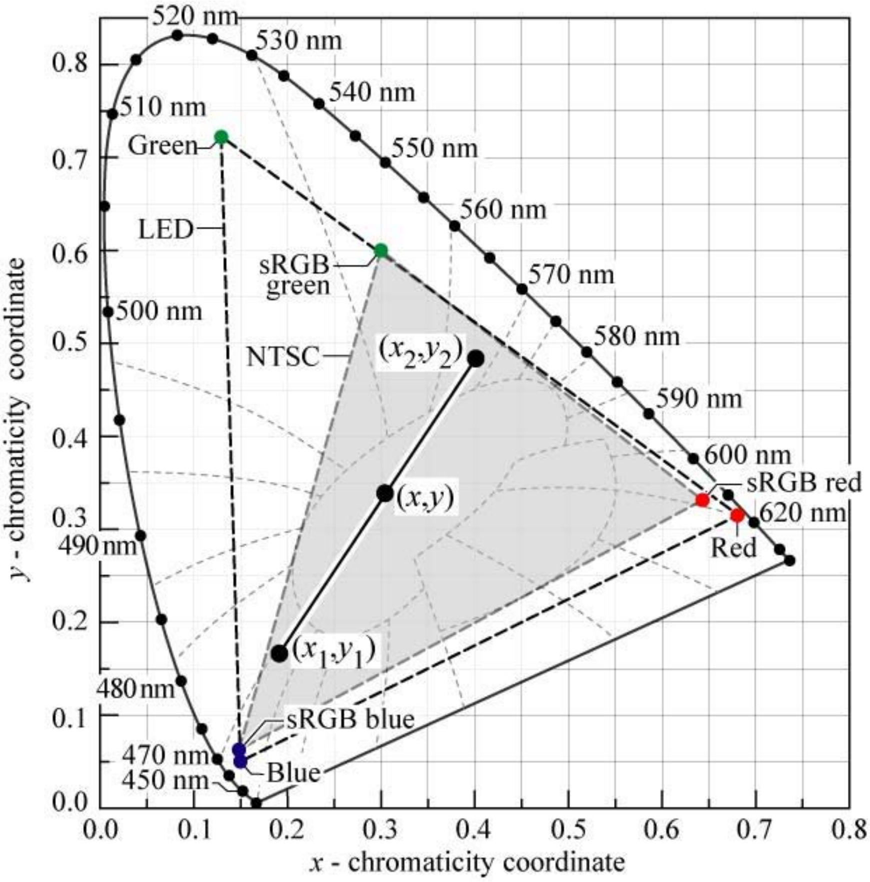

Figure 1.11: Principle of color mixing illustrated with two light sources with chromaticity coordinates (x_1, y_1) and (x_2, y_2). The resulting color has the coordinates (x, y). It is also shown the triangular area of the chromaticity diagram (color gamut) accessible by additive mixing of a red, green, and blue LED.

sources used for illumination purposes.

Figure 1.12 shows an example of a physical object under illumination with a high-CRI source and with a low-CRI source. Colors appear richer and more vivid under illumination with a high-CRI source.

This index can be measured by illuminating a standard set of color samples with a reference black body radiation, whose temperature is the same of the light source of interest, and then comparing the results with the ones obtained illuminating the same color samples with the light source. Each couple of measurements in the same color sample returns a couple of coordinates (C,D), the average of the Euclidian distance between them, $\Delta\overline{CD}$, substituted in the formula:

$$CRI = 100 - 4.6\Delta\overline{CD} \tag{1.19}$$

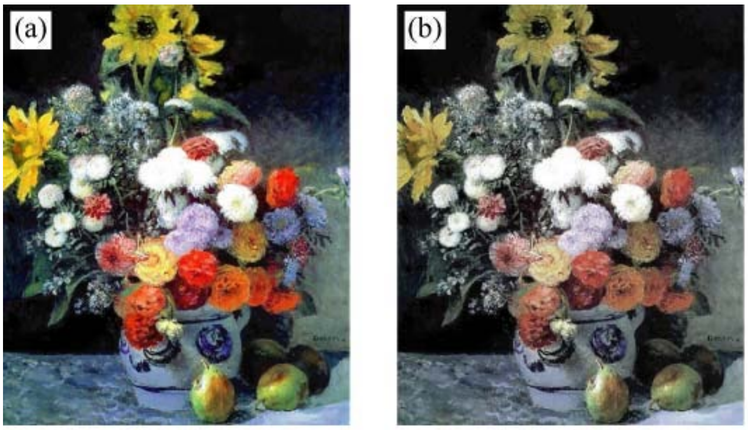

Figure 1.12: Comparison between an object illuminated with (a) high-CRI source and (b) low-CRI source

givess the CRI. This proceeding is commonly repeated for just eight standard color samples (general CRI) and the results are always less than 100: indeed if the light source is perfectly matched by the black body radiation, the distance would be zero and the CRI would be the maximum possible.

For more details about the procedure to calculate the CRI factor of a light source see [1].

Using CRI as an index of light quality means that any deviation from how an object appears when illuminated by a black body is considered bad: in other words, the perfect way to illuminate an object is using a black body radiation, exactly as it happens for the sunlight, or the incandescent light, indipendently from its color temperature. If we want to evaluate another light source, and consider its spectrum, as much the spectrum is far from the one of a black body, as much that source will be bad.

In typical applications, a CRI higher than 80 is required in order to render colors adequately. When high color rendering needs to be achieved, as in the case of artworks illumination, light sources with a CRI higher than 90 are employed.

1.6.1 Shortcomings and Problems of CIE CRI

The CIE method of measuring and specifying color rendering properties of light sources (CIE CRI) has many deficiencies and limitations. These deficiencies and limitation are explained below [2].

CIE test sample method requires a reference illuminant and selection of reference illuminant has profound influence in the calculation result. The only criterion to select reference illuminant is the CCT of test source. Reference illuminant is selected from the pool of black-body radiators if CCT of test source is below 5000K, and from the phases of daylight if CCT of test source is above 5000K. This means there can be infinite numbers of reference illuminant which lead to confusion. Matching the CCT of the reference light source to that of test light source is another problem. CIE CRI specifies that the CCT of the reference light source be matched to that of the test source, which assumes complete chromatic adaptaion to any light source CCT. However, this assumption fails at extreme CCT. For example, a 2000K (very reddish) blackbody source and a daylight spectrum of 20000K (very bluish) both achieves CIE CRI of 100 but the colors of objects illuminated by these sources will appear noticeably distorted.

The maximum value of the index is assigned to the reference illuminant which means no light source can render color better than reference source. It limits the innovation of new light sources and motivates lamp manufactures to produce lamps that render object similarly to how they are rendered under daylight or blackbody radiation.

The CIE CRI uses the CIE U*V*W* color space for all calculation. The CIE U*V*W* color space is visually non-uniform, inadequate, and outdated. CIE recommends CIELAB and CIELUV color space for calculating object color differences . The von Kries chromatic adaption transform used in CIE CRI is also considered obsolete, inadequate, and is not applicable for large chromatic difference condition. There are some new chromatic transform like CMCCAT2000, CIECAT02 which perform better than von Kries chromatic adaption transform and provide results more consistent with the human vision

The eight test color samples used in the calculation of CIE CRI have medium lightness and medium saturation. None of them are highly saturated and are available anymore in their original form. These color samples are less relevant to environment rich in saturated colors and can be problematic especially for RGB white LEDs with strong peaks and pronounced valleys in their spectra. It is possible for a light source to render well on non-saturated sample while render poorly on saturated one.

For some lamps like low-pressure sodium CIE CRI is negative which is difficult to interpret. The eight special color rendering indices are combined by a simple averaging to obtain general color rendering index. This makes possible for a lamp to score high CIE CRI even when it renders one or two colors very poorly. LEDs are at an increased risk of being affected by this problem, as their peaked spectra are more vulnerable to poor rendering in only certain areas of color space.

Finally, the very definition of color rendering is flawed for many applications. Color rendering is a measure of only the fidelity of object colors under the illuminant of interest and any deviations of object color appearance from under a blackbody source is considered bad. Due to this constraint, all shifts in perceived object hue and saturation result in equal decrements in CRI score. In practical application, however, increases in chromatic saturation, observed when certain sources illuminate certain surfaces, is considered desirable. Increases in saturation yield better visual clarity and enhance perceived brightness. It is proposed that the absolute focus on color fidelity of the CRI is flawed and a more general metric of color quality must be considered.

1.6.2 Color Quality Scale (CQS)

In recognition of these problems NIST (the National Institute of Standards and Technology) has been working on a new means for measuring and reporting color rendition called the *Color Quality Scale (CQS)*. Unlike the CIE CRI, which only considers color rendering or color fidelity CQS integrates several dimensions of color quality including color rendering, chromatic discrimination and observer preferences.

The CQS, like the CRI, is a test sample method. That is, color differences are calculated for a standard set of colored samples when illuminated by the test source and a reference illuminant. As mentioned above the CRI samples are all relatively unsaturated colors and this can hide problems a source may have rendering more saturated tones. NIST has established through extensive computational testing that, although light sources can perform poorly with saturated samples even when performing well with unsaturated ones, the inverse is never true. That is, there is no light source spectrum that would render saturated colors well, and render unsaturated colors poorly. This important result shows that nothing is lost and everything is gained by only using saturated colors as our new sample set. Therefore, CQS uses fifteen saturated colors chosen to be evenly spaced across the entire visible spectrum (Figure 1.13).

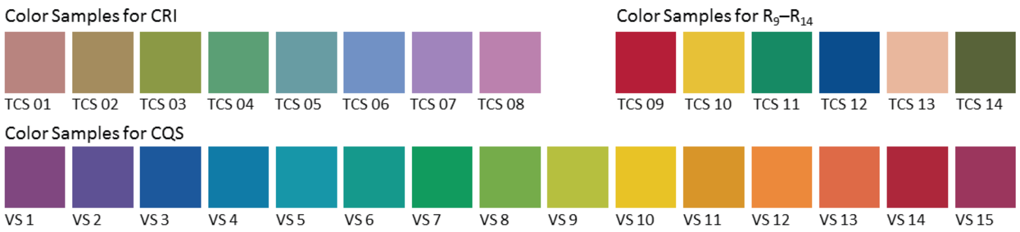

Figure 1.13: Approximation of color samples used for the calculation of CRI, R9–R14, and CQS. Beacuse appearance will vary based on the illumination condition, display settings, printing properties, and/or viewing conditions, these are only examples.

In the CIE CRI, the CCT of the reference source is matched to that of the test source which assumes complete chromatic adaptation to any light source CCT . Because of this, the CIE CRI score can be perfect ($CRI = 100$) for reference illuminants of any CCT. However, actual color rendering is degraded at extreme CCTs. The CQS addresses this problem using CCT factor which penalizes source with extreme CCTs.

The uniform object color space (CIE 1964 U*V*W*) used in the calculation of CIE CRI is outdated, and is very non-uniform. In the CQS, the U*V*W* color space has been replaced by CIELAB, which is currently recommended by CIE and is widely used in many applications [41]. The Von Kries chromatic adaptation transform used in CIE CRI is considered to be incomplete and outdated. CQS uses CMCCAT2000 which is more updated and accurate chromatic transform and has shown to provide results more consistent with the human vision.

Another important factor considered in the calculation of CQS is the saturation factor. CIE CRI being a purely fidelity metric penalizes all shifts in perceived object hue and saturation. However, increase in chroma as long as they are not excessive, yields better visual clarity and enhance perceived brightness which is generally preferred. In the CQS, with the implementation of the saturation factor a test source that increases the object chroma is not penalized, but is also not rewarded. In this way with the introduction of saturation factor, CQS takes the color preference and color discrimination into account.

In the calculation of the CIE CRI, the eight special color rendering indices are combined by a simple averaging to obtain the general color rendering index. This makes it possible for a lamp to score quite well even when it renders one or two colors very poorly. This situation is even more likely with SPDs having narrowband peaks [41]. RGB LEDs are at increased risk of being affected by this problem because their unique spectra are more vulnerable to poor rendering in only certain areas of color space [33]. To ensure the influence of poor rendering of even a few samples on the results, the rootmean- square of color shifts of each individual sample is used in CQS rather than arithmetic mean.

For more details about the procedure to calculate the CQS factor of a light source see [2].

1.7 Efficacy of a lighting system

In section 1.2we have already introduced the concept of luminous efficacy of a light source, which is a measure of the ability of the device in transforming electrical power into luminous flux. However, it is not the only parameter to be considered when evaluating the efficacy of an entire lighting system e.g., a lamp. In fact, we should distinguish between the *system efficacy*, that takes on account both the efficiency of the electronic ballast (or of the LED driver), the device itself and even the fixture efficiency, and the *device efficacy*, that evaluates just the efficacy of the light source. Figure 1.14 illustrates the range of values of these three parameters for different types of lighting systems employing commonly available light sources [3].

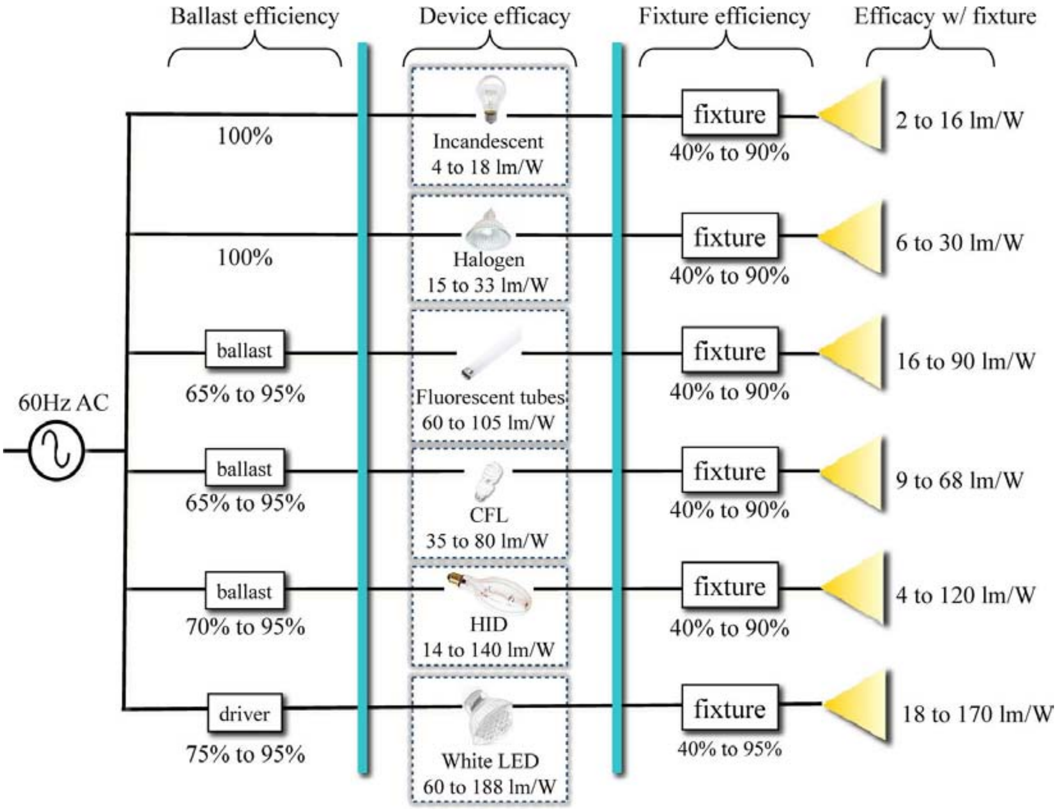

Figure 1.14: Efficacy of lighting devices and fixtures. The 188 lm/W for the LED device efficacy corresponds to the target for white LEDs for 2015. [?]

The leftmost column reports the typical ranges of ballast efficiency. Apart from incandescent and halogen bulbs that work directly connected to the mains supply, lighting devices need to be powered by a ballast, i.e. an electrical circuit that adjusts the current waveform as needed. In the case of LEDs, the converter is called driver.

Lighting systems normally have a fixture applied to the lamp, in order to diffuse light. At the same time, the fixture reduces the extraction efficiency of light; its efficiency can vary greatly, as shown by the values in the rightmost column of Figure 1.14. In the case of LED lamps, being this a brand new technology, fixture designers have the freedom to develop new fixtures with much lower losses

The central column shows common lighting devices along with their range of luminous efficacy.

For the incandescent lamps the device efficiency is limited by the tungsten filament efficacy, and the lumen depreciation ranges from 10% to 15 of the initial output over the course of the 1000 h lifetime. This mainly results from depletion of the tungsten filament over time and the accumulation of evaporated tungsten particles on the interior surface of the bulb. This process can be limited using certain noble gases inside the bulb, but it is evidently an intrinsic limit of the lamp.

Fluorescent lamps usually experience less than a 20 depreciation over their 10000 hour lifetime. However, depreciation is generally less than 10% for the case of high-quality fluorescent tubes using rare earth phosphors. The lumen depreciation in fluorescent lamps arises from photochemical degradation of the phosphor coating and the glass tube, as well as the accumulation of light-absorbing deposits within the lamp.

In the case of LEDs the efficacy is generally lowered because of a poor removal of the heat generated at the junction, leading to an increase of the lamp temperature, which results in a lower light output. This depends principally by the chip design, that can be improved in order to better promote the flux of heat outside the junction and towards the thermal pad, to induce the flux of electrons inside it and, the principal one, the flux of photons towards the collector dome. Because of the use of phosphors in white LEDs, the down-conversion of light is another term that influences the complexive device efficacy.

As concerns the SSL based on LED technology, it has undergone dramatic improvements since it has been developed in 1996. Today the efficacy of a cool white LED is around 80 lm/W . By 2015, the DOE (U.S. Department of Energy) is projecting cool white LEDs to be at 174 lm/W. These advancements will come from improvements in internal quantum efficiency (the ratio of injected electrons to emitted photons in the active region), extraction efficiency (the efficiency of extracting generated photons from the active regions out of the packaged part), phosphor advancements, and improvements in scattering efficiency (the efficiency of extracting photons from the phosphor versus all the photons coming from the chip). In addition to improvements in efficiency, improvements in packaging are increasing the lifetime of LEDs to 30 000–50 000 h.

In this scenario, the LED technology efficiency would overcome the one of all the best existent commercial light sources and, if equal improvements would follow in the thermal stabilization as well as in color and ageing control, this technology would soon substitute the traditional lamps.

1.8 A brief comparison of lighting technologies

In Table 1.4 is reported a comparison of the key characteristics of the already mentioned lighting technologies. The first thing to notice is that while for the traditional lighting sources the technology is stable and no more significant improvement is possible, for the LED one these data are only indicative and temporary, because they are fastly evolving. This table has been adapted from [3], dated 2009: as we will see in the next chapters, the LEDs measured in this thesis work are fine better than those mentioned here.

Lamp Type	Power (W)	Efficacy (lm/W)	Lifetime (x1000 h)	CCT (K)	CRI
Incandescent	3-150	4-18	1	2400-3100	98-100
Halogen	-	15-33	2-6	3000-3100	98-100
Fluorescent	4-120	35-80	5-20	3000-6500	75-90
SSL LEDs	1-20	160 (lab), 20-55	20-40	5000-6000	70-80

Table 1.4: Main characteristics of lamps, adapted from [3].

CHAPTER 2

Light Emitting Diodes

This chapter provides the basic concepts necessary to understand how Light Emitting Diodes (LEDs) work. For this reason after a brief note on semiconductors, radiative recombination, which is the mechanism responsible for emission of light, is explained and confronted with other non-radiative recombination mechanisms. The electrical properties of LEDs are then derived, revealing the importance of the use of heterostructures and Quantum Wells (QWs) in LED design. Also the optical properties of LEDs such as their efficiency and spectral emission are examined, along with the reason for the use of downconverting phosphors to obtain white light employing monochromatic LEDs.

2.1 Operating principle

The basic mechanism by which LEDs produce light can be summarized, however, by a simple conceptual description. The familiar light bulb relies upon temperature to emit visible light (and significantly more invisible radiation in the form of heat) through a process known as incandescence. In contrast, the light emitting diode employs a form of *electroluminescence*, which results from the electronic excitation of a semiconductor material. The basic LED consists of a junction between two different semiconductor materials, in which an applied voltage produces a current flow, accompanied by the emission of light when charge carriers injected across the junction are recombined.

The fundamental element of the LED is a semiconductor chip (similar to an integrated circuit), which is mounted in a reflector cup supported by a lead frame connected to two electrical wires, and then embedded in a solid epoxy lens (see Figure 1.1). One of the two semiconductor regions that comprise the junction in the chip is dominated by negative charges (n-type region), and the other is dominated by positive charges (p-type region). When a sufficient voltage is applied to the electrical leads, current flows and electrons move across the junction from the n region into the p region where the negatively charged electrons combine with positive charges. Each combination of charges is associated with an energy level reduction that may release a quantum of electromagnetic energy in the form of a light photon. The frequency, and perceived color, of emitted photons is characteristic of the semiconductor material, and consequently, different colors are achieved by making changes in the semiconductor composition of the chip.

2.2 Semiconductors

Semiconductors are materials that have electrical conductivity intermediate to that of metals and insulators. Their energy band structure is characterized by the presence of a forbidden interval, which means that electrons can never assume an energy comprised in that interval. This energy gap is called *bandgap*, and the energy levels below it form what is called the *valence band*, while the levels at higher energies form the *conduction band*.

While for a conductive material the conduction and valence bands are not energically separated, thus the transition of electrons between them thanks to their thermal energy is always possible because there is no energy gap, in a semiconductor a transition is more difficult to achieve, because the two bands are well distinguished, as shown in Figure 2.1. In order to obtain, for example, an electron promotion from the valence to the conduction band, an amount of energy equal to the energy gap E_G that it has to overcome has to be externally supplied. On the other hand a decay of one electron from the conduction to the valence band, and the subsequent recombination with a hole can give origin to a radiation process, that is accompained by a release of a photon with a frequency $v = Eg/h$[1].

The distribution of electrons in a semiconductor can be described with the Fermi-Dirac function $f(E)$, which gives the probability of finding an electron with energy E, and is given by

---

[1] The formula $Eg = hv$ contains the radiation frequency and the Planck constant $h = 6.63 \cdot 10^{-34} Js$

$$f(E) = \frac{1}{1 + exp(\frac{E-E_F}{k_B T})} \tag{2.1}$$

where k_B is the Boltzmann constant, T is the temperature in kelvins, and E_F is a parameter called the *Fermi level* which is a hypothetical level of potential energy for an electron inside a crystalline solid. The Fermi level is related to an energy state with 50% chance of being occupied by an electron for the given temperature of the solid. The electron concentration n and hole concentration p in a semiconductor, under equilibrium conditions, are related by the mass action law:

$$np = n_i^2, \tag{2.2}$$

where ${n_i}^2$ is the *intrinsic carrier concentration.*

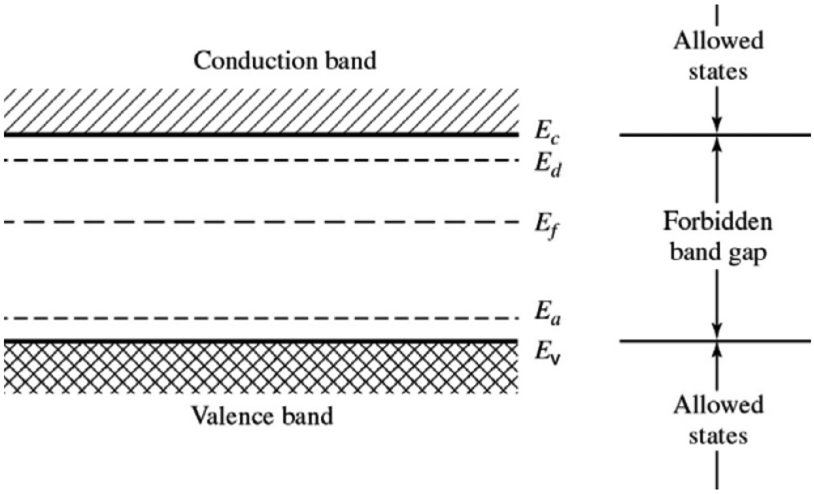

Figure 2.1: The conduction and valence band scheme, in a semiconductor.

In nature, an intrinsic semiconductor is not very useful, because at steady state the promotion and decay processes are balanced, and it is not able neither to produce nor to absorb additive photons. If we want to increase, for example, the number of radiative decays, it has to be doped, introducing into the lattice some impurities, i.e. atoms that can raise the number of electrons or lower it. The materials chosen as suitable dopants depend on the atomic properties of both the dopant and the material to be doped. In general, dopants that produce the desired controlled changes are classified as either electron *acceptors* or *donors.* Semiconductors doped with donor impurities are called n-type, while those doped with acceptor impurities are known as p-type. The n

---

[2] n_i can be calculated by $n_i^2 = BT^3 exp\left\{-\frac{E_g}{kT}\right\}$.

and p type designations indicate which charge carrier acts as the material's majority carrier. The opposite carrier is called the minority carrier, which exists due to thermal excitation at a much lower concentration compared to the majority carrier.

The Fermi level is strictly dependant to the doping of the semiconductor, indeed the larger the p-doping (or the n-doping), the nearer is the Fermi level to the VB (or the CB), and this increases the probability to find acceptors (or donors) in there. In other terms, if the semiconductor is intrinsic, we can approximate $n \simeq p$ and the intrinsic Fermi level $E_f = E_i$ is right in the middle of the bandgap, $|E_c - E_i| \simeq |E_i - E_v|$. If the semiconductor is p-doped, then $|E_c - E_f| \ggg |E_f - E_v|$, otherwise, in a n-doped one,$|E_c - E_f| \lll |E_f - E_v|$.

2.2.1 Direct and indirect bandgap semiconductors

The energy band structure of semiconductor materials varies with the atomic structure. For this reason, an accurate representation is usually given in a diagram showing the relation between energy and electron momentum or, equivalently, lattice orientation k of the material. Analyzing these dispersion relation diagrams we can divide semiconductors into two categories, depending on where the minimum of the conduction band and the maximum of the valence band happen to be inside the crystal structure. When these two energy levels have the same momentum, we talk about *direct bandgap* semiconductors. For such materials, the recombination process usually takes place when an electron from the conduction band edge loses part of its energy and ends up into the valence band without any change in its momentum, as shown in figure 1.1. The electron loses an amount of energy equal to the difference between the two bands' edges, i.e. the energy gap E_G. This energy is emitted in the form of a photon with energy $E_{ph} = E_G$.

In other materials the minimum of the conduction band has a different k value with respect to that of valence band's maximum, and so we speak of *indirect bandgap* semiconductors. In this case the recombination process involves the interaction of the electron with a phonon, which represents quantized vibrational energy of the lattice. The electron therefore moves to the valence band changing its momentum and emitting a photon whose energy is equal to the difference between the energy gap and the phonon's energy, i.e. $E_{ph} = E_G - Ephonon$. Because of the improbability of this spontaneous contribution of phonons to the lattice, this transition hardly happens thus this kind of semiconductors are not used as light emitters.

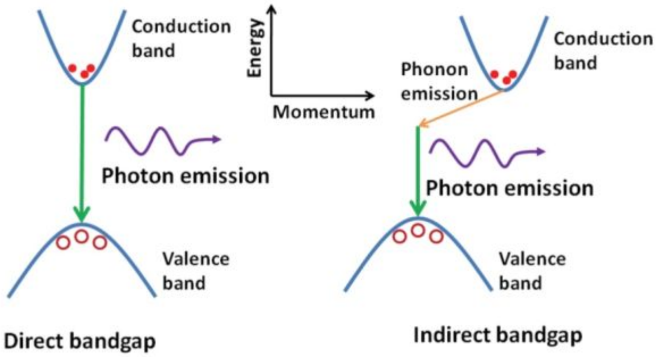

Figure 2.2: Energy vs. momentum diagrams of direct (left) and indirect (right) bandgap semiconductors.

2.3 Recombination

The light emission precess inside an LED is based on the radiative electron-hole recombination. In every semiconductor two antagonist phenomena take place: *generation* and *recombination* of *electron and hole pairs* (EHP). Carrier generation is a process where electron-hole pairs are created by exciting an electron from the valence band of the semiconductor to the conduction band, thereby creating a hole in the valence band. Recombination is the reverse process where electrons and holes from the conduction respectively valence band recombine and are annihilated.

During a recombination a certain amount of energy, the differential energy of the electron before and after the recombination, is transformed into a different form of energy. The energy resulting from the recombination can be of different forms: heat (phonon), light (photon) and kinetic (in the case of auger recombination). Therefore the recombination mechanisms in semiconductors are classified with different names, *radiative*, *non-radiative* and *Auger* recombination. In a radiative event, one photon with energy equal to the bandgap energy of the semiconductor is emitted, while during non-radiative recombination, the electron energy is converted to vibrational energy of lattice atoms, emitting a phonon, the energy is thus converted in heat. In semiconductor generally two different types of non-radiative recombination take place: i) Deep level defect recombinations and ii) surface level recombinations.

2.3.1 Radiative recombination

As stated before, for a semiconductor at thermal equilibrium, the concentration of holes and electrons is related by the mass action law of Eq.2.2. Also, when at thermal equilibrium, the ehp generation and recombination rates are equal.

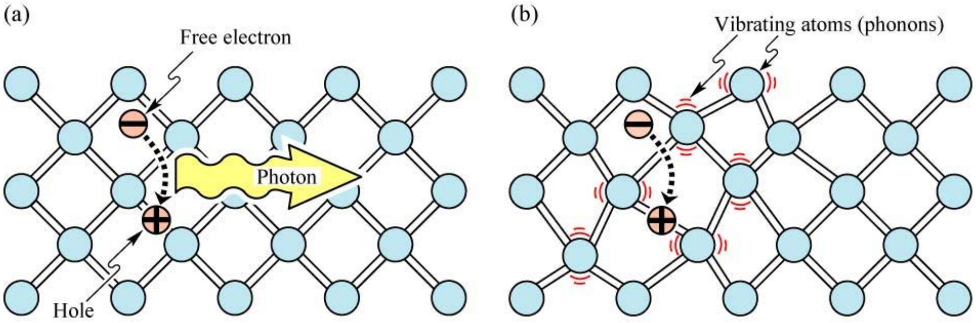

Figure 2.3: (a)Radiative recombination of an electron-hole pair accompained by the emission of a photon with energy $hv \simeq Eg$. (b) In non-radiative recombination events, the energy released during the electron-hole recombination is converted to phonon.

Excess carriers in semiconductors can be generated by either absorption of light or by an injection current. The total carrier concentration is then given by the sum of equilibrium and excess carrier concentrations, i.e.

$$n = n_0 + \Delta n; \; and\, p = p_0 + \Delta p \tag{2.3}$$

where Δn and Δp are the excess electron and hole concentrations, respectively.

The bigger is the number of excess carriers, the higher is the probability that an electron recombines with a hole. The recombination rate R will therefore be proportional to the hole concentration in the valence band, $R \propto p$, and also to the electron concentration in the conduction band. Thus the recombination rate is proportional to the product of electron and hole concentrations, that is, $R \propto np$. This proportionality is expressed by the bimolecular rate equation :

$$R = -\frac{dn}{dt} = \frac{dp}{dt} = Bnp, \tag{2.4}$$

where B is the *bimulecolar recombination coefficient*, which depends from the semiconductor. It has typical values of 10^{-11}- 10^{-9} $^{cm^3}/_{s}$ for direct-gap III-V semiconductors.

2.3.1.1 Radiative recombination for low-level excitation

We are now intersted in determining the recombination dynamics as a function of time. Consider a semiconductor subjected to photoexcitation. The equilibrium and excess electron and hole concentrations are n_0, p_0, Δn, and Δp, respectively. Since electrons and holes are generated and annihilated (by recombination) in pairs, the steady-state electron and hole excess concentrations are equal,

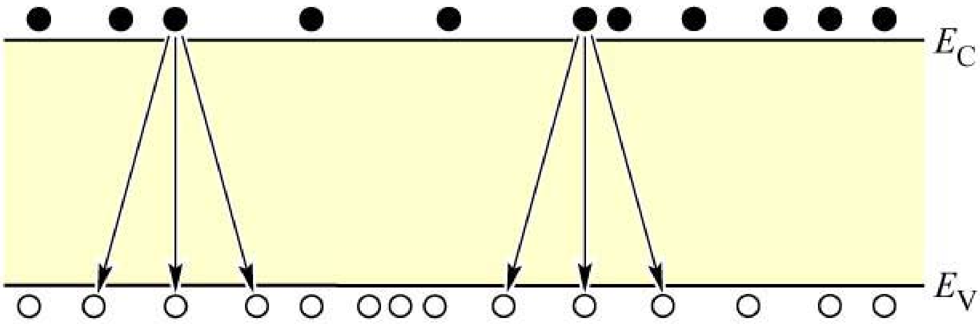

Figure 2.4: Illustration of electron-hole recombination. The number of recombination events per unit time per unit volume is proportional to the product of electron and hole concentrations.

$$\Delta n(t) = \Delta p(t). \tag{2.5}$$

Using the bimolecular rate equation, the recombination rate is given by

$$R = B[n_0 + \Delta n(t)][p_o + \Delta p(t)]. \tag{2.6}$$

For the case of low-level excitation, the photogenerated carrier concentration is much smaller than the majority carrier concentration, i.e. $\Delta n << (n_0 + p_0)$, using Δn(t)=Δp(t), we obtain from Eq. 2.6

$$\begin{aligned} R &= B[n_0p_0 + n_0\Delta n(t) + p_0\Delta n(t) + \Delta n(t)\Delta n(t)] \\ &= B[n_0p_0 + n_0\Delta n(t) + p_0\Delta n(t)] \\ &= Bn_i^2 + B(n_0 + p_0)\Delta n(t) \\ &= R_0 + R_{excess}. \end{aligned} \tag{2.7}$$

The first summand on the right-hand side of the equation can be identified as the equilibrium recombination rate and the second term as the excess recombination rate.

The time-dependent carrier concentration can be calculated from the rate equation:

$$\frac{dn(t)}{dt} = G\text{-}R = (G_0 + G_{excess}) - (R_0 + R_{excess}), \tag{2.8}$$

where G_0 and R_0 are the equilibrium generation and recombination rates, respectively.

Suppose that excess carriers are generated by photogeneration illuminating the semiconductor, and that light is turned o at time $t = 0$, so that $G_{excess} = 0$ for$t > 0$. Being $G_0 = R_0$, for t > 0 Equation 2.8 yields:

$$\frac{d}{dt}\Delta n(t) = -B(n_0 + p_0)\Delta n(t). \tag{2.9}$$

Solving this differential equation by separation of variables, we obtain:

$$\Delta n(t) = \Delta n_0 e^{-B(n_0+p_0)t}, \tag{2.10}$$

where $\Delta n_0 = \Delta n(t = 0)$.

Rewriting the result as

$$\Delta n(t) = \Delta n_0 e^{-t/\tau} \tag{2.11}$$

we can identify the carrier lifetime, that is the time constant of the excess carriers exponential decay, as

$$\tau = [B(n_0 + p_0)]^{-1} \tag{2.12}$$

For semiconductors with a specific doping type, Eq. (2.11) reduces to

$$\tau_n = \frac{1}{Bp_0} = \frac{1}{BN_A} \quad \text{for p-type semiconductor} \tag{2.13}$$

and

$$\tau_p = \frac{1}{Bn_0} = \frac{1}{BN_D} \quad \text{for n-type semiconductor} \tag{2.14}$$

where τ_n and τ_p are the electron and hole lifetimes, while N_D and N_A are the donor and the acceptor concentration impurities, respectively. Using this result, the rate equation, Eq. 2.9, can be simplified for semiconductors of a specic conductivity type. One obtains the *monomolecular rate equations*:

$$\frac{d}{dt}\Delta n(t) = -\frac{\Delta n(t)}{\tau_n} \quad \text{for p-type semiconductor} \tag{2.15}$$

and

$$\frac{d}{dt}\Delta p(t) = -\frac{\Delta p(t)}{\tau_p} \quad \text{for n-type semiconductor} \tag{2.16}$$

Figure 2.5 shows the majority and minority carrier concentration in a p-type semiconductor as a function of time (similar considerations apply if an n-type semiconductor were chosen). Note that Figure 2.5 shows the case of low-level excitation in which the photogenerated carrier concentration is much smaller than the majority carrier concentration. However, the photogenerated carrier concentration is much larger than the minority carrier concentration. Once photoexcitation is terminated, the minority carrier concentration decays exponentially with a characteristic time constant denoted as the *minority carrier lifetime* τ. It is the mean time between generation and recombination of a minority carrier.

Note that the majority carrier concentration also decays with the same time constant τ. However, only a very small fraction of the majority carriers disappear by recombination, as illustrated in Figure 2.5. Thus, for low-level excitation, the average time it takes for a majority carrier to recombine is much longer than the minority carrier lifetime. For many practical purposes, the majority carrier lifetime can be assumed to be infinitely long.

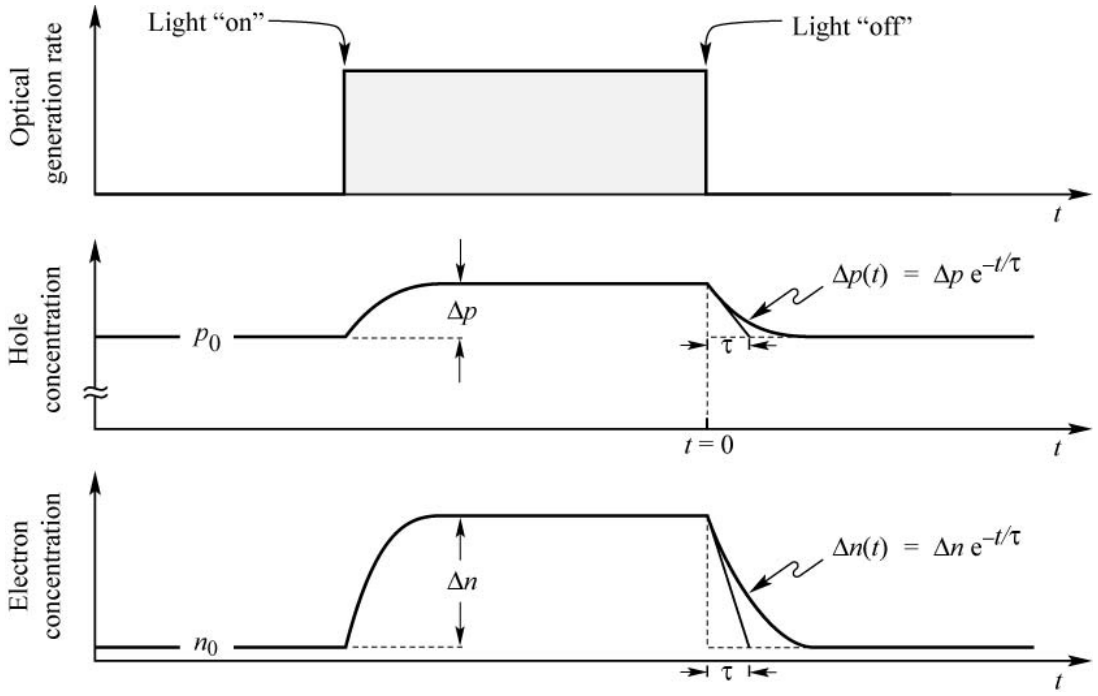

Figure 2.5: Carrier concentration as a function of time before, during and after an optical excitation pulse. The semiconductor is assumed to be p-type and thus it is $p_0 >> n_0$. Electrons and holes are generated in pairs, thus $\Delta p = \Delta n$. Under low-level excitation as shown here, it is$\Delta n << p_0$.

2.3.1.2 Radiative recombination for high-level excitation

We speak of high-level excitation when the photogenerated carrier concentration is larger than the equilibrium carrier concentration, i.e. $\Delta n >> (n_0 + p_0)$. The bimolecular rate equation (Eq. 2.4) is then given by

$$\frac{d\Delta n(t)}{dt} = -B\Delta n(t)^2. \tag{2.17}$$

Solving this differential equation by the separation-of-variables method and using the initial condition $\Delta n(0) = \Delta n_0$ yields the solution

$$\Delta n(t) = \frac{1}{Bt + \Delta n_0^{-1}} \tag{2.18}$$

This solution represents, in contrast to the low-density approximation, a non-exponential carrier decay. It is however possible to calculate an equivalent time constant given by the slope of the decay, i.e. $\tau(t) = \frac{\Delta n(t)}{\frac{d\Delta n(t)}{dt}}$, obtaining

$$\tau(t) = t + \frac{1}{B\Delta n_0}. \tag{2.19}$$

Thus, for non-exponential decays, the "time constant" depends on time. Equation 2.19 shows that the minority carrier lifetime increases with time. For sufficiently long times, low-level excitation conditions will be reached and τ will approach the low-level value.

2.3.2 Luminescence decay

The carrier decay in semiconductors can be measured by the decay of the luminescence after a short optical excitation pulse. The luminescence intensity is proportional to the recombination rate.

Figure 2.3 illustrates schematically the decay of the luminescence after optical excitation by a short pulse. For the case of low excitation density, the decay is exponential with a time constant . For the case of high excitation, the decay is non-exponential. All non-exponential decay functions can be expressed by an exponential function with a time-dependent time constant ($e^{-t/\tau(t)}$). The time constant increases with time. This type of decay function is frequently called a *stretched exponential function.*

The recombination dynamics of carriers in LEDs is one of the factors that limits the time it takes to switch an LED on and off. The modulation speed of LEDs used for communication applications can be limited by the minority carrier lifetime. The carrier lifetime can be reduced by either a high doping of the active region or a high concentration of injected carriers in the active region. Heterostructures that confine free carriers to the small well region are frequently employed to obtain high carrier concentrations and thus short carrier lifetimes.

2.3.3 Non-radiative recombination

There are several physical mechanisms that can generate non-radiative recombination, most of them are caused by defects in the crystal structure. These defects include

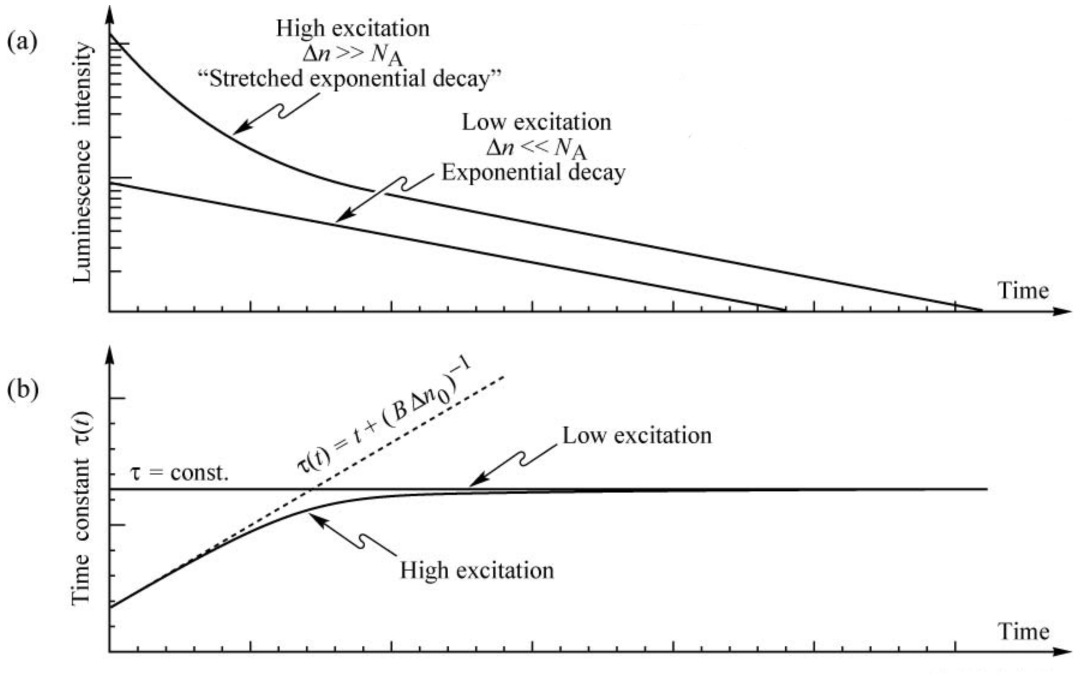

Figure 2.6: (a)Luminescence decay for low and high excitation densities. (b) Time constants for low and high excitation densities

unwanted foreign atoms, native defects and dislocations. In compound semiconductors, native defects include interstitials, vacancies, and antisite defects. All such defects have energy level structures that are different from substitutional semiconductors atoms and it is quite common for such defects to form one or more energy levels within the forbidden gap of the semiconductor. Other mechanisms are due to the concentration of carriers such as Auger recombination.

Deep state recombination Energy levels within the gap of the semiconductor are efficient recombination centers, in particular, if the energy level is close to the middle of the gap. These levels are called *luminescence killer* because they increase the probability of non-radiative recombination. The recombination of free carriers via deep levels was first analyzed by Shockley, Read, and Hall. According to SRH theory, the non-radiative recombination rate through a deep level with trap energy E_T and concentration N_T is given by

$$R_{SHR} = \frac{p_0\Delta n + n_0\Delta p + \Delta n\Delta p}{(N_T v_p\sigma_p)^{-1}(n_0 + n_1 + \Delta n) + (N_T v_n\sigma_n)^{-1}(p_0 + p_1 + \Delta_p)} \tag{2.20}$$

where $\Delta n = \Delta p$ are the variation in electron and hole density relative to steady state; v_n and v_p are the electron and hole thermal velocities, and σ_n and σ_p are the capture cross sections of the traps. The quantities n_1 and p_1 are the electron and hole concentrations if the Fermi energy is located at the trap levels:

$$n_1 = n_i exp\left(\frac{E_T\text{-}E_{Fi}}{kT}\right) \quad \text{and} \quad p_1 = n_i exp\left(\frac{E_{Fi}\text{-}E_T}{kT}\right) \tag{2.21}$$

where E_{Fi} is the Fermi level in the intrinsic semiconductor, which is typically close to the middle of the gap.

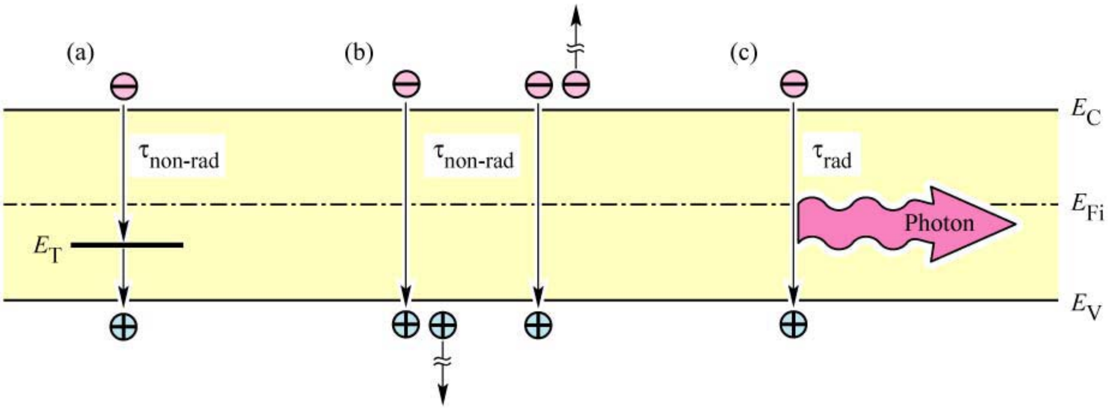

Figure 2.7: Illustration on a band diagram of (a) Schockley-Hall-Read and (b) Auger non-radiative recombination and (c) radiative recombination.

The non-radiative lifetime of excess electrons can be calculated considering that $R_{SHR} = {}^{\Delta n}/_{\tau}$, and is expressed as

$$\frac{1}{\tau} = \frac{p_0 + n_0 + \Delta n}{(N_T v_p \sigma_p)^{-1}(n_0 + n_1 + \Delta n) + (N_T v_n \sigma_n)^{-1}(p_0 + p_1 + \Delta_p)}. \tag{2.22}$$

In the case that analyzed semiconductor is p-type, the holes are the majority, i.e. $p_0 \gg n_0$ and $p_0 \gg p_1$. If deviation from equilibrium is minimum, i.e. $\Delta n \ll p0$. then the minority carrier lifetime can be approximated as

$$\frac{1}{\tau} = \frac{1}{\tau_{n_0}} = N_T v_n \sigma_n, \tag{2.23}$$

and the corresponding recombination rate, in the case of low injection conditions,

$$R_n = \frac{n\text{-}n_0}{\tau_{n_0}}. \tag{2.24}$$

In the case of n-type material, the holes lifetime and recombination rate are obtained in analogous way:

$$\frac{1}{\tau} = \frac{1}{\tau_{p_0}} = N_T v_p \sigma_p, \tag{2.25}$$

$$R_p = \frac{p\text{-}p_0}{\tau_{p_0}}. \tag{2.26}$$

As can be noticed from previous equations, SRH recombination rate is limited by the rate of capture of minority carriers. This result suggests itself since the capture of majority carriers is a much more likely event than the capture of minority carriers.

Equation 2.22 can then be written as

$$\frac{1}{\tau} = \frac{p_0 + n_0 + \Delta n}{\tau_{p_0}(n_0 + n_1 + \Delta n) + \tau_{n_0}(p_0 + p_1 + \Delta_p)}. \tag{2.27}$$

Assuming that the trap captures electrons and holes at the same rate: $v_p\sigma_p = v_n\sigma_n$ and $\tau_{n_0} = \tau_{p_0}$ we obtain:

$$\tau = \tau_{n_0}\left(1 + \frac{p_1 + n_1}{n_0 + p_0}\right) = \tau_{n_0}\left[1 + \frac{2n_i cosh\left(\frac{E_T - E_{Fi}}{kT}\right)}{n_0 + p_0}\right]. \tag{2.28}$$

The cosh function has a minimum when the argument of the function is zero. Thus the non-radiative lifetime is minimized if E_T–E_{Fi} is zero; i.e. when the trap level is at or close to the midgap energy. This result demonstrates that deep levels are effective recombination centers if they are near the middle of the gap. Taking a close look to equation 2.28 it is possible to realize that SRH recombination is temperature dependent. As T increases the nonradiative recombination lifetime decreases. As a result, the radiative band-to-band recombination efficiency decreases at high temperatures. The highest band-to-band radiative efficiencies of direct-gap semiconductors can be obtained at cryogenic temperatures.

However, some devices are based on radiative recombination through a deep state. A wellknown example of radiative recombination mediated by a deep level is N-doped GaP. It follows from the Shockley–Read model that the deep-level recombination rate increases with increasing temperature. In indirect-gap semiconductors such as GaP, radiative transitions are mediated by phonons. That is, radiative recombination must be accompanied by absorption or emission of a phonon. Since phonons are more abundant at high temperatures, radiative recombination (mediated by the absorption of a phonon) can increase with temperature.

In the vicinity of a deep level, the luminescence intensity decreases. A single point defect will be difficult to observe due to its relatively small effect. Frequently, however, defects group into clusters of defects or extended defects. Such extended defects are, for example, threading dislocations and mist dislocations occurring when epitaxial semiconductors are grown on mismatched substrates, i.e. substrates with a different lattice constant from that of the epitaxial layer.

Auger recombination involves an electron-hole pair and a third element which can be either an electron or a hole. The energy lost in the ricombination process is gained by this third particle which is excited high in the conduction band if it's an electron, or it will be deeply excited in tha valence band if it's a hole, as shown in figure 1.5 (b). The electron (or the hole) will then lose part of its energy in the form of phonons until it gets close to the band edge. The recombination rates of these two processes are given by:

$$R_{Auger} = C_n n^2 p \tag{2.29}$$

and

$$R_{Auger} = C_p n p^2 \tag{2.30}$$

where C_n and C_p are the Auger coefficients.

Auger recombination is proportional to the square of the carrier concentration (either p^2 or n^2) since two carriers of the same type (either two holes or two electrons) are required for the recombination process. The first process (see equation 2.29) is more likely to happen in p-type semiconductors due to the abundance of holes. The second process (see equation 2.30) is more likely in n-type semiconductors due to the abundance of electrons. During Auger recombination, energy and momentum must be conserved. Owing to the differences in conduction and valence band structure in semiconductors, the two Auger coefficients C_p and C_n are generally different.

In the high-excitation limit in which the non-equilibrium carriers have a higher concentration than equilibrium carriers, the Auger rate equations reduce to:

$$R_{Auger} = (C_n + C_p) n^3 = C n^3 \tag{2.31}$$

where C is the Auger coefficient. Typical values for the Auger coefficient are$10^{-28} - 10^{-29} cm^6/s$ for III -V semiconductors.

Auger recombination reduces the luminescence efficiency in semiconductors only at very high excitation intensity or at very high carrier injection currents. This is due to the cubic carrier concentration dependence. At lower carrier concentrations, the Auger recombination rate is very small and can be neglected for practical purposes.

Non-radiative recombination at surfaces Surfaces are a strong perturbation of the periodicity of a crystal lattice. Recall that the band diagram model is based on the strict periodicity of a lattice. Since this periodicity ends at a surface, the band diagram will need to be modified at a semiconductor surface. This modification includes the addition of electronic states within the forbidden gap of the semiconductor.

From a chemical point of view, atoms at the surface cannot have the same bonding structure as bulk atoms due to the lack of neighboring atoms. Thus some of the valence orbitals do not form a chemical bond and result partially filled. These dangling bonds are electronic states that can be located in the forbidden gap of the semiconductor where they act as recombination centers. The behaviour of these dangling bonds can be quite disparate: depending on the charge state of these valence orbitals, the states can be acceptor-like or donor-like states; the dangling bonds can rearrange themselves and form bonds between neighboring atoms in the same surface plane and this can lead to a locally new atomic structure with state energies different from bulk atomic states.

An evaluation of the effect of surface recombination on the carrier distribution can be done considering the continuity equation in the case of a p-doped semiconductor under illumination condition, thus considering a constant carrier generation G:

$$\frac{d\Delta n}{dt} = G - R + \frac{1}{q}\frac{dJ_n}{dx}, \tag{2.32}$$

that takes on account the diusion current of electron towards the surface Jn, given by

$$J_n = qD_n\frac{d\Delta n(x,t)}{dx}; \tag{2.33}$$

considering the latter, eq.2.32 becomes

$$\frac{d\Delta n(x,t)}{dt} = G - \frac{\Delta n(x,t)}{\tau_n} + D_n\frac{d^2\Delta n(x,t)}{dx^2}. \tag{2.34}$$

The boundary condition at the surfaceis given by

$$qD_n\frac{d\Delta n(0,)}{dt} = qS\Delta n(0,t) \tag{2.35}$$

here S is the surface recombination velocity, and depends from the considered semiconductor. This condition states that minority carriers diffusing to the surface will recombine at the surface.

Considering eq. 2.35, the steady-state solution to the differential equation 2.34 is given by

$$n(x) = n_0 + \Delta n(x) = n_0 + \Delta n_\infty \left[1 - \frac{\tau_n S e^{-x/L_n}}{L_n + \tau_n S}\right] \tag{2.36}$$

where Δn_∞ is the steady state carrier density ($\Delta n_\infty = G\tau_n$) and L_n is the carrier recombination length.

The carrier concentration near a semiconductor surface is shown in Figure 2.8 for different surface recombination velocities.

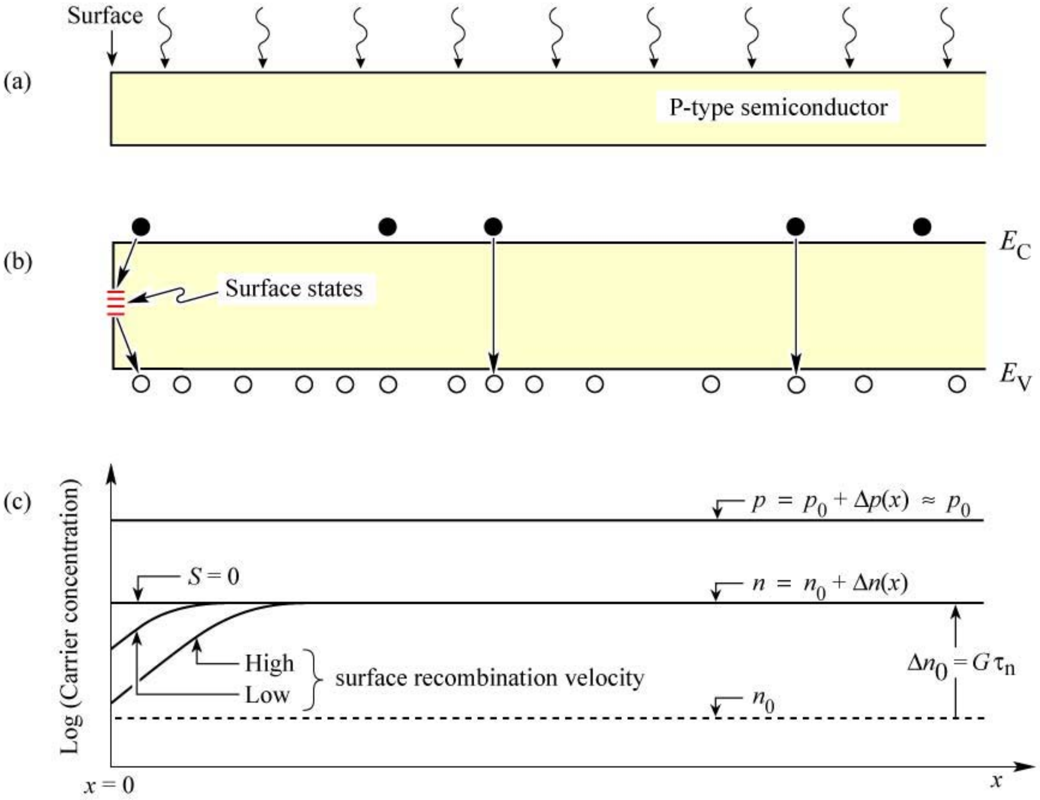

Figure 2.8: (a) Illuminated p-type semiconductor, (b) band diagram, and (c) minority and majority carrier concentration near the surface assuming uniform carrier generation due to illumination. The excess carrier concentrations are Δ_n and Δ_p .

Surface recombination leads to a reduced luminescence efficiency and also to heating of the surface due to non-radiative recombination at the surface. Both effects are unwanted in electroluminescent devices.

Surface recombination can occur only when both types of carriers are present. It is important in the design of LEDs that the carrier-injected active region, in which naturally both types of carriers are present, be far removed from any surface. This can be achieved, for example, by carrier injection under a contact that is much smaller than the semiconductor die. Furthermore, the contact must be sufficiently far away from the side surfaces of the die. If the current flow is confined to the region below the contact, carriers will not “see” any semiconductor surfaces.

Several passivation techniques have been developed to reduce the surface recombination in semiconductors, including treatments with sulfur, and other chemicals.

2.4 Internal quantum efficiency

In prevoius section we have described how radiative and non-radiative processes contribute to carriers recombination. These processes are in competition: in particular, even if they have a detrimental effect on the characteristics of the optoelectronic devices, non-radiative processes can not be completely avoided. Therefore, it can be useful to define a parameter that expresses how the radiative and non-radiative processes are balanced. This parameter is the internal quantum efficiency and is defined as

$$\eta_{int} = \frac{\tau_r^{-1}}{\tau_r^{-1} + \tau_{nr}^{-1}} \tag{2.37}$$

where τ_r is the carriers lifetime associated to radiative recombination processes and τ_{nr} is the carriers lifetime associated to non-radiative recombination processes. This parameter is an expression of the ratio between the number of photons generated and the number of carriers that undergo recombination.

2.5 Electrical properties of LEDs

The basic element of an LED is a semiconductor electroluminescent structure, that comprises, at least, a region of radiative recombination and regions of different conductivity type (p and n) that supply the recombining carriers. In the simpliest design, the structure relies on a junction between a p-type semiconductor and a n-type semiconductor of the same kind (*p-n homojunction)* with one or both conductivity regions employed as the radiative-recombination region or regions. Although this LED design is somewhat obsolete and note used in modern high-brigthness LEDs, it is consider here to illustrate the basic principles of the carrier injection in an electroluminescent device.

2.5.1 Diode current-voltage characteristic

As explained above, a LED device is essentially a diode, thus it has its same electric characterictics.

For the description of the current-voltage (I-V) characteristics of the diodes, we can consider an abrupt p-n junction (Figure 2.9) with a donor concentration of N_D and an acceptor concentration of N_A. All dopants are assumed to be fully ionized so that the free electron concentration is given by $n = N_D$ and the free hole concentration is given by $p = N_A$. It is further assumed that no compensation of the dopants occurs by unintentional impurities and defects.

In the absence of any applied bias, there is no net current in the system and the Fermi level is uniform throughout the structure. In figure 2.10(a) we show a schematic of the band diagram of a p-n junction.

Majority carriers near the interface on both sides diffuse across the junction (holes from p side and electrons from n side), as a result of the difference in electron and hole densities across the junction. Most of the electrons which diffuse to the p-side recombine with holes, and most of the holes which diffuse to the n-side recombine with electrons. As a result, a region is formed near the junction that has been depleted of mobile carriers. This region is known as the *depletion region.* In this situation, the only charge present in the depletion layer is due to the fixed donors and acceptor: this charge generates an electric field, and a built-in potential drop, that acts as a barrier for the diffusion of the carriers. When equilibrium is reached, the magnitude of the field is such that the tendency of electrons to diffuse from n-type region into the p-type region is exactly balanced by tendency of electrons to drift in the opposite direction under the influence of the built-in field.

The potential drop across the junction, that is called the *diffusion voltage* (V_D)*,* is given by

$$V_D = \frac{kT}{q} \ln \frac{N_A N_D}{n_i^2} \tag{2.38}$$

where n_i is the intrinsic carrier concentration of the semiconductor, and q is the charge of the electron.

The width of the depletion region can be calculated starting from the Poisson equation, and is found to be equal to

$$W_D = \sqrt{\frac{2\varepsilon}{e} (V_D - V) \left(\frac{1}{N_A} + \frac{1}{N_D} \right)} \tag{2.39}$$

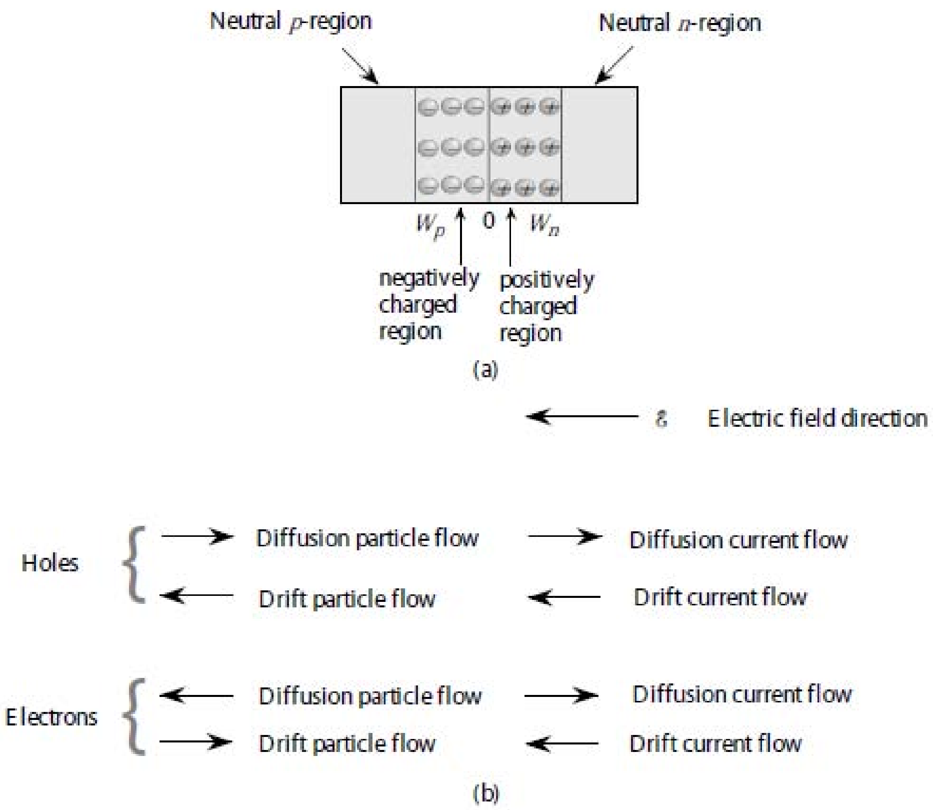

Figure 2.9: (a) Region of a p-n junction without bias, showing the neutral and depletion areas. (b) A schematic showing various current and particle flow components in the p-n diode at equilibrium.

where $\varepsilon = \varepsilon_r \varepsilon_0$ is the dielectric permittivity of the semiconductor and V is the diode bias voltage.

Upon application of the bias voltage to the p-n junction, the voltage is going to drop across the depletion region. This region is highly resistive due to the fact that it is depleted of free carriers. An external bias therefore decreases or increases the p-n junction barrier for forward or reverse bias, respectively. Under forward-bias conditions, electrons and holes are injected into the region with opposite conductivity type and current flow increases. The carriers diffuse into the regions of opposite conductivity type where they will eventually recombine, thereby emitting a photon.

The current-voltage equation of a p-n junction, usually referred to as *Schockley equation*, is

$$I = qA \left(\sqrt{\frac{D_p}{\tau_p}} \frac{n_i^2}{N_D} + \sqrt{\frac{D_n}{\tau_n}} \frac{n_i^2}{N_A} \right) \left(exp \left(\frac{qV}{kT} \right) - 1 \right) \tag{2.40}$$

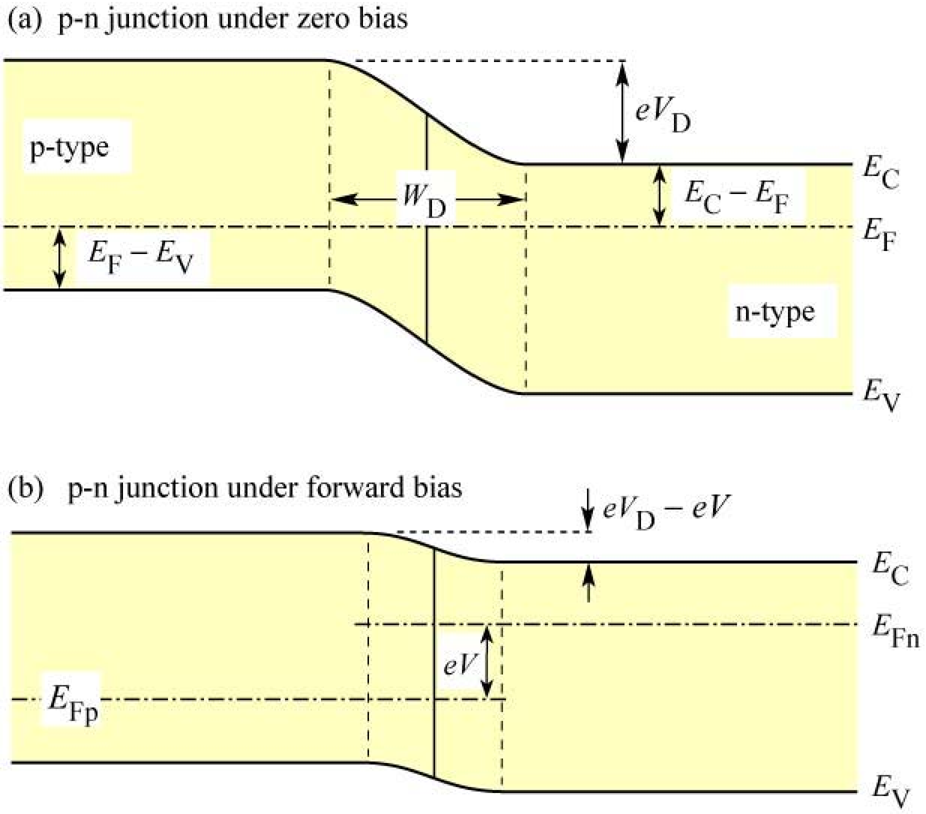

Figure 2.10: p-n junction under (a) zero bias and (b) forward bias. Under forward bias conditions, minority carriers diuse into the neutral re- gions where they recombine.

where A is the area of the devices, D_n and D_p are the diffusion coefficients and τ_n and τ_p the minority carriers liferimes for electrons and holes respectively. Under reverse-bias conditions, the diode current saturates and the saturation current is given by the factor preceding the exponential function in the Shockley equation. The diode I–V characteristic can be written as

$$I = I_S\left(exp\left(\frac{qV}{kT}\right) - 1\right) \quad \text{with} \quad I_S = qA\left(\sqrt{\frac{D_p}{\tau_p}}\frac{n_i^2}{N_D} + \sqrt{\frac{D_n}{\tau_n}}\frac{n_i^2}{N_A}\right). \tag{2.41}$$

Under typical forward bias conditions, the diode voltage is $V \gg \frac{kT}{e}$ and therefore the relation between current and voltage becomes exponential. Using Equation 2.38, Equation 2.40 can be re-written as

$$I = qA\left(\sqrt{\frac{D_p}{\tau_p}}N_A + \sqrt{\frac{D_n}{\tau_n}}N_D\right) exp\left[\frac{q\left(V - V_D\right)}{kT}\right]. \tag{2.42}$$

The exponent of the exponential function in this equation illustrates that the current strongly increases as the diode voltage approaches the diffusion voltage, i.e. $V \approx V_D$. The voltage at which the current strongly increases is called the threshold voltage and this voltage is given by $V_{th} \approx V_D$.

The band diagram shown in Figure 2.10, also illustrates the separation of the Fermi level from the conduction and valence band edge. The difference in energy between the Fermi level and the band edges can be inferred from Boltzmann statistics and is given by

$$E_C - E_F = -kTln\frac{n}{N_C} \qquad \text{for the n-type side} \tag{2.43}$$

and

$$E_F - E_V = -kTln\frac{n}{N_V} \qquad \text{for the p-type side.} \tag{2.44}$$

The band diagram shown in Fig. 4.1 illustrates that the following sum of energies is zero:

$$eV_D - E_g + (E_F - E_V) + (E_C - E_F) = 0. \tag{2.45}$$

In highly doped semiconductors, the separation between the band edges and the Fermi level is small compared with the band-gap energy, i.e. $(E_C - E_F) \ll E_g$ on the n-type side and $(E_F - E_V) \ll E_g$ on the p-type side. Furthermore, these quantities depend only weakly (logarithmic dependence) on the doping concentration. Thus, the third and fourth summand of the last equation can be neglected and the diffusion voltage can be approximated by the band-gap energy divided by the elementary charge

$$V_{th} \approx V_D \approx {}^{E_g}/_{q}. \tag{2.46}$$

Several diode I–V characteristics of semiconductors made from different materials are shown in Figure 2.11 along with the bandgap energy of these materials. The experimental threshold voltages shown in the figure, and the comparison with the bandgap energy of these materials, indicates that the energy gap and the threshold voltage indeed agree reasonably well.

2.5.2 Deviations from the ideal I–V characteristic

The Shockley equation gives the expected theoretical IV characteristic of a p-n junction. To describe experimentally measured characteristics, the following equation is used:

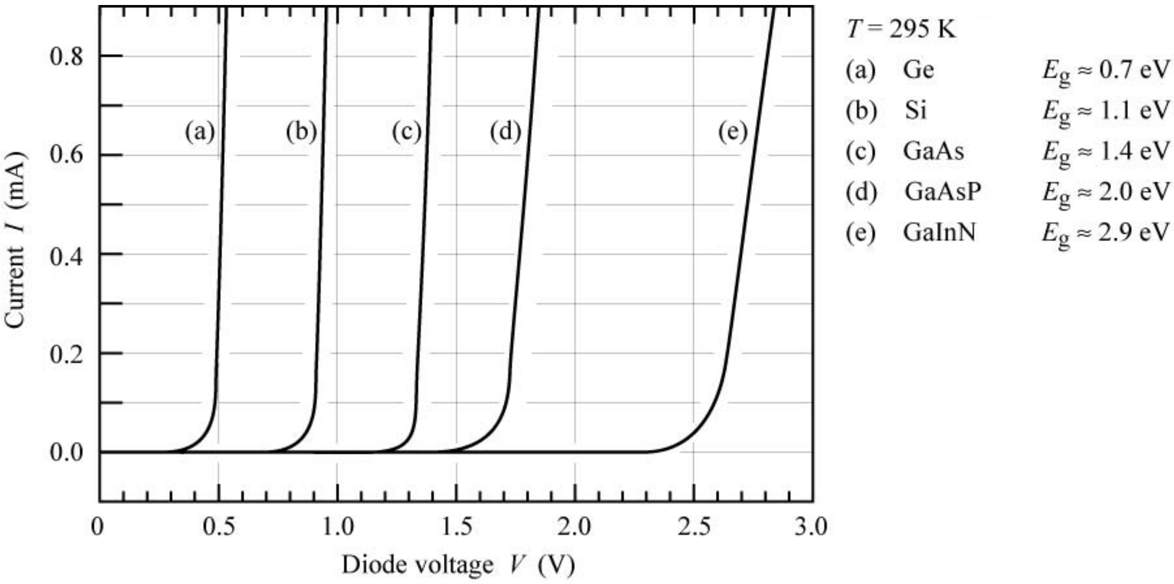

Figure 2.11: I-V characteristic of p-n junctions made from different semiconductors.

$$I = I_S exp\left(\frac{qV}{n_{ideal}kT}\right) \tag{2.47}$$

where n_{ideal} is the *ideality factor* of the diode. For a perfect diode, the ideality factor has a value of unity ($n_{ideal} = 1$). For real diodes, the ideality factor assumes values of typically $n_{ideal} = 1.1 - 1.5$. However, values as high as $n_{ideal} = 2$ n_ideal=2 have been found for III–V arsenide and phosphide diodes. Values as high as $n_{ideal} = 7$ have been found for GaN/GaInN diodes.

Frequently a diode has unwanted or parasitic resistances. A parasitic series resistance can be caused by excessive contact resistance or by the resistance of the neutral regions. The effect of this resistive component is to decrease diodes current in the high current region. On the other hand, a parallel resistance can be caused by damaged regions or surface leakage, that generate conduction paths in parallel to the diodes. The effect of this resistance (shunt resistor) is to significantly contribute to carrier flow when the diode is not conducting, i.e. for reverse and low forward applied voltage. A description of the effects of these parasitic resistance is given in Figure 2.12. In the inset of the same figure an equivalent model for the diode with the two parasitic resistors is described. The I-V characteristic, modified taking into account the effects of the two parasitic resistive components has the following form

$$I - \frac{(V - IR_s)}{R_p} = I_S exp\left[\frac{q(V - IR_S)}{n_{ideal}kT}\right]. \tag{2.48}$$

For Rp $\to \infty$ and Rs $\to 0$, this equation reduces to the Shockley equation.

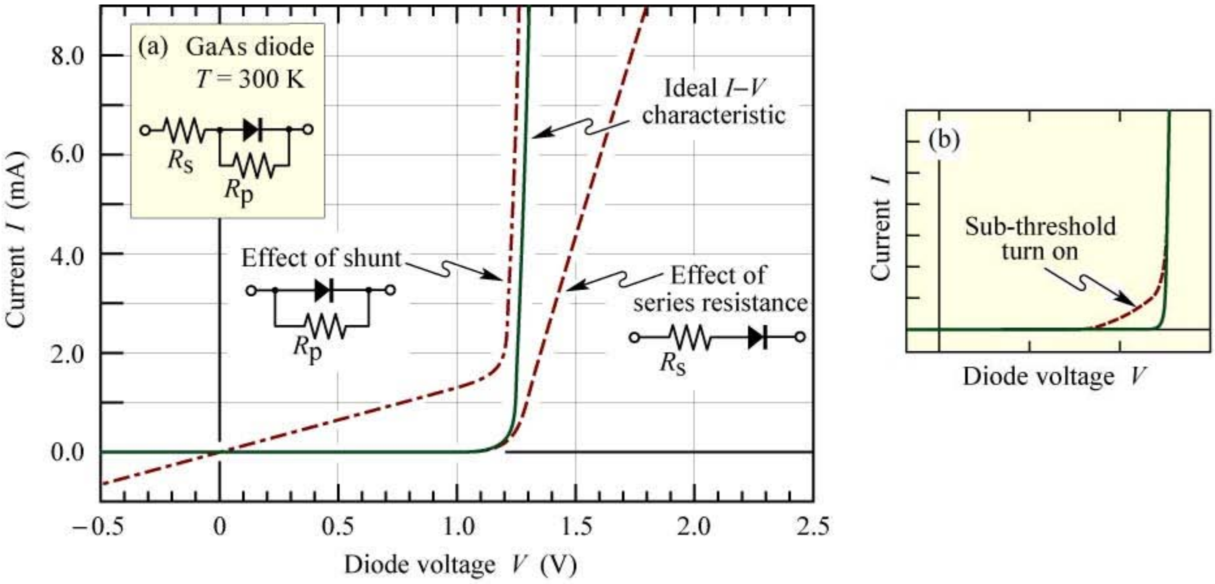

Figure 2.12: Effect of parasitic resistances on the characteristics of a diode.

Occasionally, the diode turn-on is distributed over a range of voltages rather than occurring abruptly at the threshold voltage. Both types of turn-on are shown in Fig. 2.12(b). The non-abrupt turn-on is referred to as *sub-threshold turn-on* or *premature turn-on*. The sub-threshold current can be caused by carrier transport through surface states or deep levels in the bulk of the semiconductor.

Detailed inspection of the diode I–V characteristic on a linear as well as logarithmic scale allows for the diagnosis of potential problems such as shunts, series resistances, premature turn-on, and parasitic diodes. Here we report a list of some parasitic effects that can occur in diodes showing the effect on the I-V characteristic.

Depletion region generation and recombination: The Shockley diode equation does not account for carrier generation and recombination events in the depletion region. However, in practical diodes, there are trap levels in the depletion region, which make such events likely. Carrier generation and recombination causes an excess current for both forward and reverse bias. In the forward-bias regime, the excess current is due to the recombination of minority carriers in the depletion region. This recombination current dominates only at low voltages and gives an ideality factor of 2.0. At higher voltages, the diffusion current dominates resulting in an ideality factor of 1.0. In the reverse-bias regime, the excess current is due to the generation of carriers in the depletion region. Under the influence of the electric field in the depletion region, generated carriers drift to the neutral regions. This generation current keeps increasing with reverse voltage due to the increasing depletion-layer width.

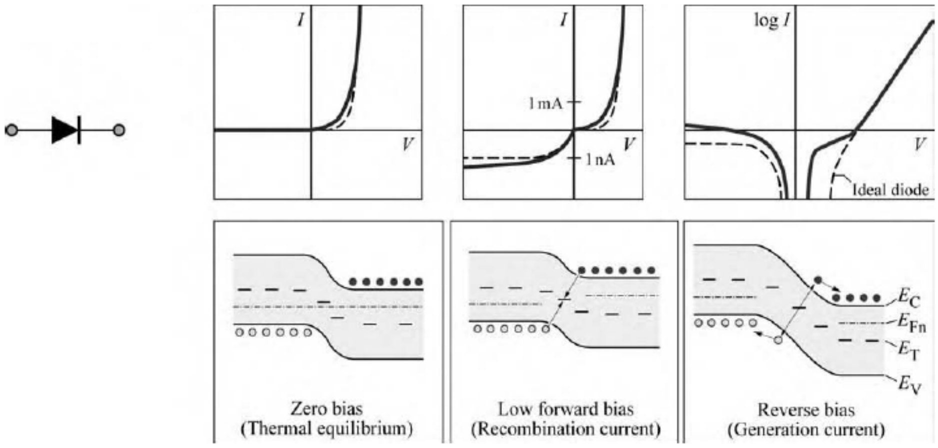

Figure 2.13

Photocurrent: In a practical measurement within a lighted room, a diode located in a transparent package generates a photocurrent. Therefore measurements need to be carried out in the dark. Switching off room lights or covering the setup with a dark cloth helps in reducing the photocurrent.

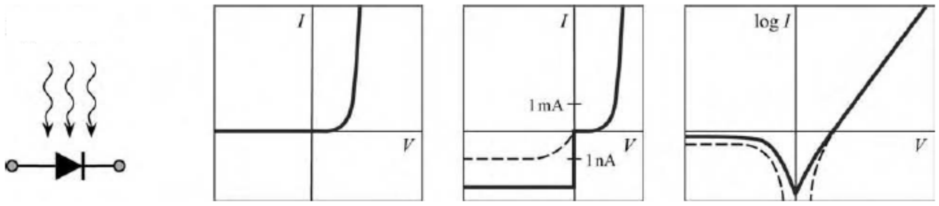

Figure 2.14

Diode with series resistance: A diode with a series resistance shows a deviation from the exponential behavior at high forward currents. According to Kirchhoff's voltage law, the voltages across the diode and the resistor add up. Note that a simple resistor has a linear and a logarithmic shape of the I-V characteristic when plotted on a linear and semi-logarithmic scale, respectively.

Diode with parallel resistance (shunt): According to Kirchhoff's current law, the currents through diode and resistor add up. Note that the forward "hump" seen on the semilogarithmic plot has about the same level as the reverse saturation current. This is a characteristic by which a shunt can be identified.

Parasitic diode with lower barrier height and smaller area than main diode: Such diodes display premature turn-on caused by leakage through either surface

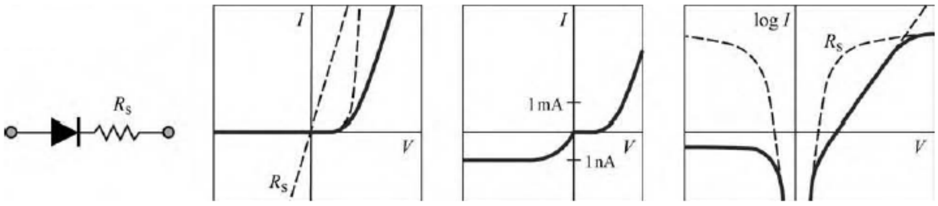

Figure 2.15

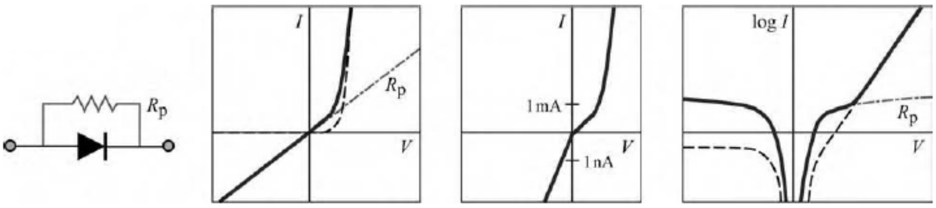

Figure 2.16

states at the perimeter of the diode chip or defective regions within the p-n junction plane that have a lower barrier height than the main p-n junction. Note that the forward "hump" on the semi-logarithmic plot has much higher level than the reverse saturation current, which is not the case for diodes with a shunt.

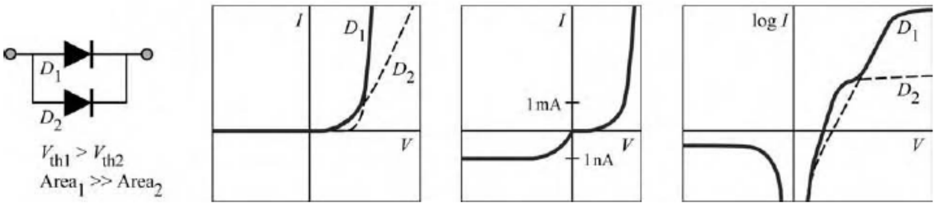

Figure 2.17:

2.5.3 LED voltage

The energy of an injected electron is converted into optical energy upon electron–hole recombination. Thus, conservation of energy requires that the drive voltage or forward voltage of a light-emitting device is equal to (or larger than) the bandgap energy divided by the elementary charge. The diode voltage is thus given by

$$V = \frac{h\nu}{q} = \frac{E_g}{q}. \tag{2.49}$$

There are several mechanisms causing the drive voltage to be slightly different from this value and these mechanisms will be discussed below.

Firstly, if the diode has a significant series resistance, an additional voltage drop occurs. The additional resistance can be caused by (i) contact resistance, (ii) resistances caused by abrupt heterostructures, and (iii) bulk resistance occurring particularly in materials with low carrier concentrations or low carrier mobilities. A voltage drop of magnitude I Rs occurs at the series resistance thereby increasing the drive voltage.

Secondly, carrier energy may be lost upon injection into a quantum well structure or double heterostructure. An example of non-adiabatic injection is shown in figure , which shows a thin quantum well under forward-bias conditions. The figure illustrates that upon injection into the quantum well, the electron loses energy $\Delta E_C – E_0$, where ΔE_C is the band discontinuity and E_0 is the energy of the lowest quantized state in the conduction-band quantum well. Similarly, the energy lost by holes is given by $\Delta E_V – E_0$, where ΔE_V is the band discontinuity and E_0 is the energy of the lowest state in the valence-band quantum well. Upon injection of carriers into the well, the carrier energy is dissipated by phonon emission, i.e. by conversion of the carrier energy to heat. The energy loss due to non-adiabatic injection of carriers is relevant in semiconductors with large band discontinuities, for example GaN and other group-III nitride materials.

Thus, the total voltage drop across a forward-biased LED is given by

$$V = \frac{E_g}{q} + IR_s + \frac{\Delta E_C – E_0}{q} + \frac{\Delta E_V – E_0}{q}. \tag{2.50}$$

where the first summand on the right-hand side of the equation is the theoretical voltage minimum, the second summand is due to the series resistance in the device, and the third and fourth summands are due to non-adiabatic injection of carriers into the active region.

One finds experimentally that the diode voltage can be slightly lower than the minimum value predicted by equation 2.50, i.e. can be slightly lower than $E_g/q \approx hv/q$. Both electrons and holes carry, on average, the thermal energy kT. In a forward-biased p-n junction, high-energy carriers are more likely than low-energy carriers to diffuse over to the side of opposite conductivity type where they recombine. At room temperature, 4kT/q amounts to a voltage of about 100 mV. In low-resistance devices, the diode voltage can be 100–200 mV lower than hv/q.

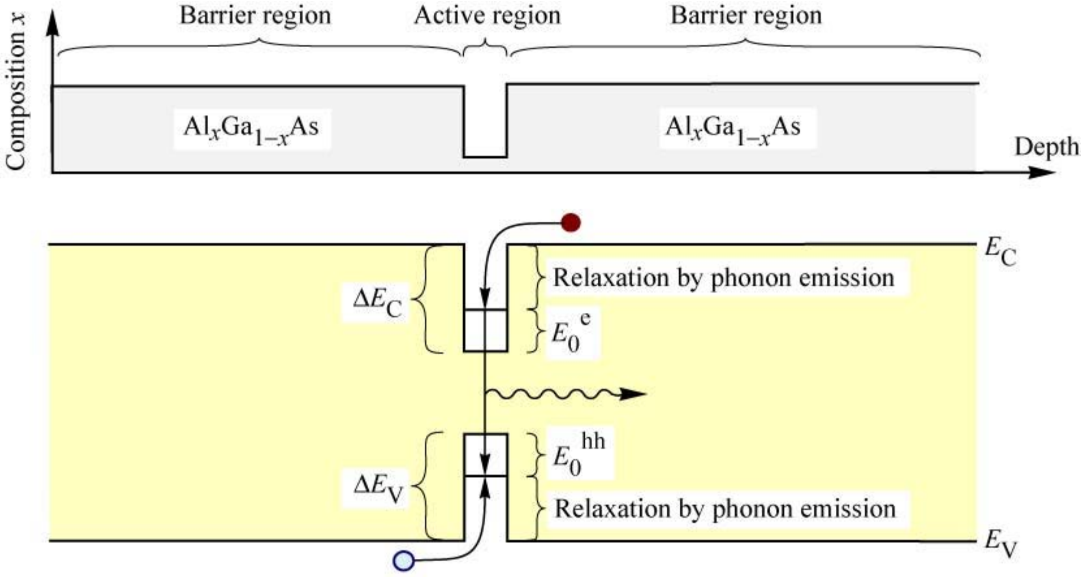

Figure 2.18

2.6 LED structures

The first visible-wavelength LED was fabricated in 1962 from "bulk" GaAsP (Holonyak and Bavacqua, 1962). Since that time, advance in the physical understanding of performance limitations, together with tremendous advances in alloy crystal growth and device fabrication technology, have led to fantastic improvements il LED efficiency. The basic structure (a p-n function diode) has remained constant.

2.6.1 Homojunction LEDs

The basic structure of a LED is the p-n homojunction. As stated in the previous sections, a p-n homojunction is the structure obtained by joining two parts of the same material, one doped n and one doped p.

In a forward-biased homojunction, electrons will be injected from the n-type layer into the p-type layer where they are minority carriers. This minority carrier injection process will be followed by recombinationof the electron with a (majority) hole. Similarly, holes may be injected from the p-type layer into the n-type layer, where they recombine with majority electrons. A third mechanism for current flow is injection of electrons and holes into the space-charge region where they may recombine. In each case, the elctron-hole recombination may occur either radiatively or nonradiatively, depending on the band structure, doping and defect concentrations.

Many importants elements of a practical LED are not shown in the simplified onedimensional band diagrams of figure 2.19. Low-resistance ohmic contacts must be made to both the n- and p-type layers to create a device with a low operating voltage of $V \sim E_G = hv$. The n-type and p-type doping levels throughout the LED must also be optimized. For example high doping is desiderable for low series resistance and a short radiative lifetime (τ_r). However, high doping may also lead to increased defect concentrations (and a correspondingly low τ_{nr}) and excessive free-carrier absorption of the photons generated by the LED.

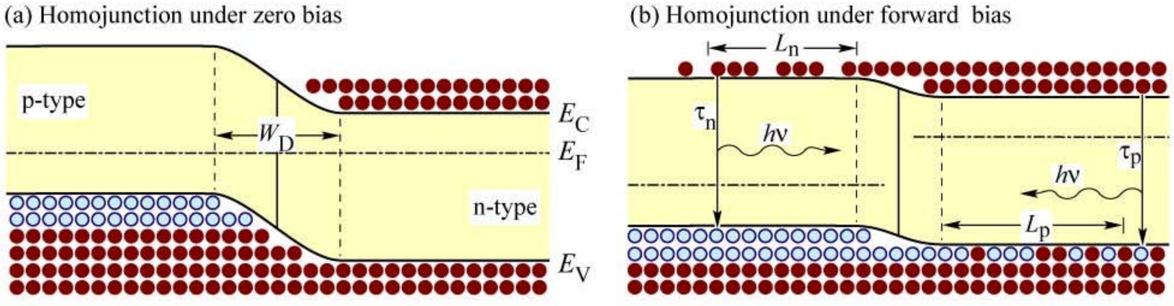

Figure 2.19: P-n homojunction under (a) zero and (b) forward bias.

The primary advantage of the homojunction LED structure is its ease of fabrication. It consists of only a single crystal composition. In the case of a binary such as GaP, there is no need to worry about the difficulties associated with lattice matching. This gratly simplifies the epitaxial growth process. However the structure has also several drawbacks. First, carrier injection is controlled by the doping near the p-m junction, and occurs for both electrons and holes. As a result, it becomes critical to mantain careful control over doping concentration and defect levels on both side of the junction. Second, there is no mechanism for confining the injected electrons or holes to the vicinity of the p-n junction, so they may diffuse a distance of up to several diffusion lengths (L_n or L_p) before recombination occurs. This makes it difficult to achieve a high injected minority carrier density and also means that defects located far from the junction may contribute to nonradiative recombination and reduced LED efficiency. Thus the "active region" (the region where radiative recobination may occur) is very thick. Third, in a direct gap semiconductor the emitted photons may be reabsorbed via band-to-band absorption before they have an opportunity to be extracted from the LED.

2.6.2 Single-Heterostructure LEDs

Structures composed of semiconductors that have different bandgaps due to different chemical composition are called *heterostrucure*.

An energy band diagram for a single-heterostructure (SH) LED is shown in figure 2.20. In this example, a wide-bandgap n-type layer forms a p-n heterojunction with a narrow-bandgap p-type layer. The bandgap difference between the two layers is $\Delta E_G = E_G(\text{n-type layer}) - E_G(\text{p-typelayer}) = \Delta E_c + \Delta E_v$. The conduction band offset ΔE_c provides an increase in the electron injection current under forward bias, while the valence band offset ΔE_v helps to supress the hole injection current. As a result, the ratio of electron current to hole current is enchanced by a factor of $exp(\Delta E_G/kT)$. Electron-hole recombination is essentially limited to only one side of the junction. In this example, the active layer conists only of the p-type layer.

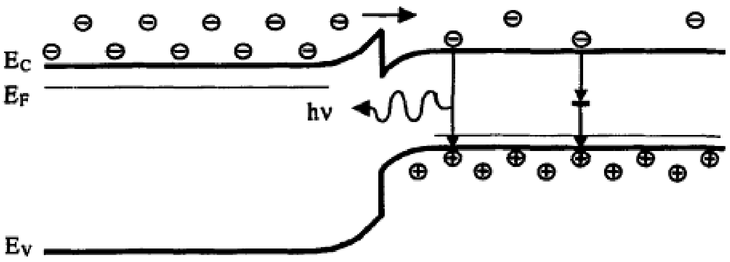

Figure 2.20: Band diagram for aforward-biased single-heterostrucure.

Use of an SH enables doping levels to be optimized with very little effect on the minority injection process (assuming $\Delta E_G \gg kT$). In figure 2.20 the n-type layer may be optimized for low resistance, and high defect concentrations will have little impact on LED efficiency since there are very few minority holes. The p-type layer doping level may be optimized solely for high radiative efficiency. Self-absorption is also reduced in this SH LED since E_G in the n-type layer is greater than the photon energy.

The fabrication of an SH LED requires an heteroepitaxial growth process capable of growth of low-defect-density alloys. In addition the p-n junction must be placed precisely at the location of the heterojunction, or the device becomes a homojunction and the advantages of the SH will be lost.

2.6.3 Double-Heterostructure LEDs

Practical high-brightness LEDs use a double hetero-structure (DH), which implements the benefits offered by band-gap engineering to a larger extent. The potential profile of a forward-biased DH LED is shown in Figure . The structure comprises a narrow-gap active p-type layer sandwiched between wide-gap conductive regions of n- and p-types, respectively. This allows for bidirectional injection of excess carriers into the active layer, where electrons and holes recombine. Moreover, the minority carriers that diffuse through one of the hetero-interfaces are trapped in the active layer by the second hetero-interface and cannot diffuse away. This increases the excess carrier density and, consequently, the rate of radiative recombination. Also, in such a structure, both conductive layers are transparent to the light emitted, and the reabsorption effect is minimized for both directions. However, reabsorption is still present in the active layer. It should be noted that both SH and DH LED structures require materials with good lattice matching. If lattice constant differ too much, a high density of defects (typically threading dislocation) is produced at the hetero-interfaces, giving rise to the non-radiative recombination. The requirement of lattice matching imposes severe limitations for the materials system used in hetero-junction LEDs.

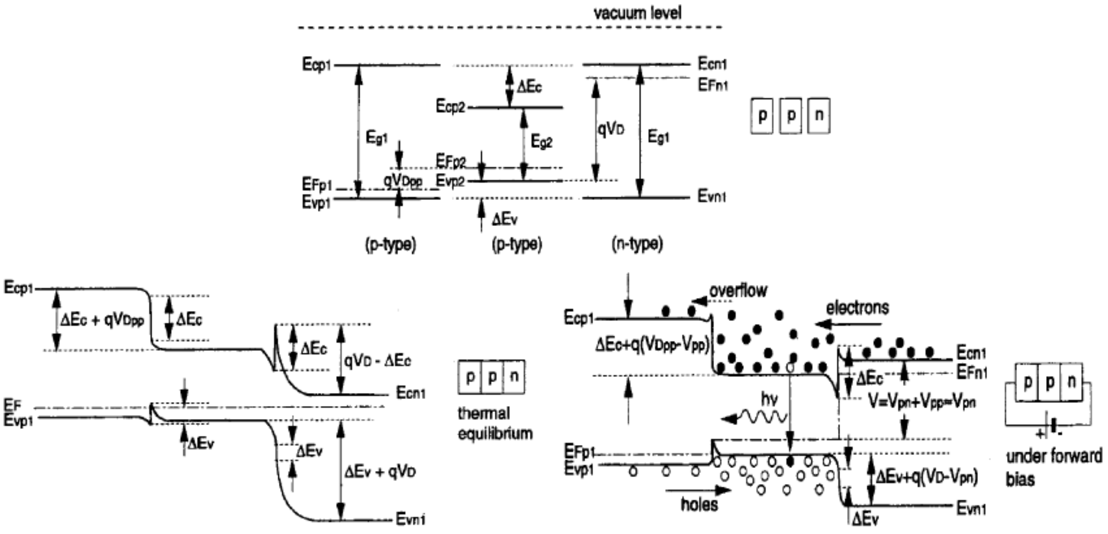

Figure 2.21: Band diagram of double ppn heterojunction with a forward bias applied.

2.6.4 Quantum-well structures

Thinning the active layer is the way to further increase the rate of radiative recombination and reduce the reabsorption. In addition, using very thin active layers enable one to overcome some lattice-matching problems, since such layers are able to conform to the thick confining layers without defect generation (pseudomorphic layers). However, when the thickness of the active layer becomes comparable or smaller than the de Broglie wavelength of electrons in the crystal, the energy spectrum of the carriers is modified (quantum confinement). Such double heterostructures are called *quantum wells* (QW) *structures.*

Optical properties of QWs differ from those of the bulk material in that instead of free motion along the perpendicular direction to the heterointerface (x) discrete energy levels, E_n, occur. For an infinitely deep rectangular quantum well, these levels split from the bottom of the conduction band, E_c, by

$$E_n - E_c = \frac{\pi^2 \hbar^2 n^2}{2 m_e a^2} \tag{2.51}$$

where n = 1, 2, 3,... (any positive integer number) is the quantum number, a is the width of the quantum well, and m_e is the electron effective mass. In the y-z plane, which is parallel to the heterointerface, the electronic motion is not quantized. In real device structures, the potential well is never infinitely deep. For a finite symmetrical potential well, the electron energy is given by

$$E = \frac{\hbar^2 k^2}{2 m_e} + \frac{\hbar^2 q_n^2}{2 m_e} \tag{2.52}$$

where the value of q_n is found from solutionof the following equation:

$$\frac{q_n a}{2} = \frac{n\pi}{2} - sin^{-1}\left(\frac{q_n \hbar}{\sqrt{2 m_n U_0}}\right). \tag{2.53}$$

Here U_0 is the depth of the well. The same considerations are valid for holes with the effective mass m_h.

The carrier state density is then a discrete function of energy as presented in figure 2.22.

If more quantum wells are placed one close to another (at less than 5 nm), in a regular structure, a Multi Quantum Well (MQW) is obtained. In a MQW structure a tunnel transport phenomenon sets up between quantum wells. This leads to the creation of a continuity of quantized energy levels through the entire structure.

Single quantum wells (SQWs) and multiple quantum wells (MQWs) offer the most versatile structures for high-brightness LEDs.

2.6.5 Effect of heterojunctions on device resistance

The employment of heterostructures allows one to improve the efficiency of LEDs by confining carriers to the active region, thereby avoiding diffusion of minority carriers over long distances. Although heterostructures allow for improved LED designs, there

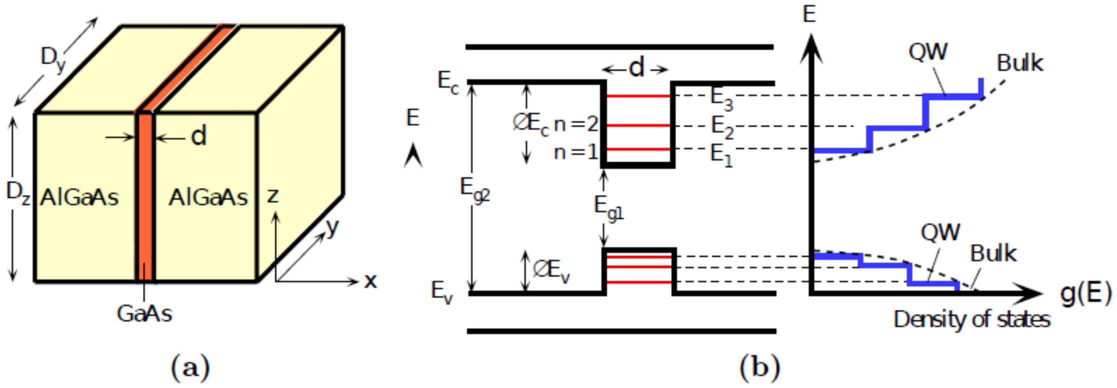

Figure 2.22: A Quantum Well device: (a) schematic illustration of a QW sctucture,(b) the conduction electron are confined in the x-direction to a small length d so that their energy is quantized and the DOS in a 2D QW is a discrete function of energy. The DOS is constant at each quantized energy level.

are also problems associated with heterojunctions.

One of the problems introduced by heterostructures is the resistance caused by the heterointerface. The origin of the resistance is illustrated in figure 2.23(a), which shows the band diagram of a heterostructure. The heterostructure consists of two semiconductors with different bandgap energy and it is assumed that both sides of the heterostructure are of n-type conductivity. Carriers in the large-bandgap material will diffuse over to the small-bandgap material where they occupy conduction band states of lower energy. As a result of the electron transfer, an electrostatic dipole forms, consisting of a positively charged depletion layer with ionized donors in the large-bandgap material, and a negatively charged electron accumulation layer in the small-bandgap material. The charge transfer leads to the band bending illustrated in figure 2.23(a). Carriers transferring from one semiconductor to the other must overcome this barrier by either tunneling or by thermal emission over the barrier. The resistance caused by heterojunctions can have a strong deleterious effect on device performance, especially in highpower devices. The thermal power produced by heterostructure resistances leads to heating of the active region, thereby decreasing the radiative efficiency.

It has been shown that heterostructure band discontinuities can be completely eliminated by grading of the chemical composition of the semiconductor in the vicinity of the heterostructure (Schubert et al., 1992). The band diagram of a graded heterostructure is shown in figure 2.23(b). Inspection of the figure reveals that there is no longer a spike in the conduction band which hinders the electron flow. It has been shown that the resistance of parabolically graded heterostructures is comparable to bulk material

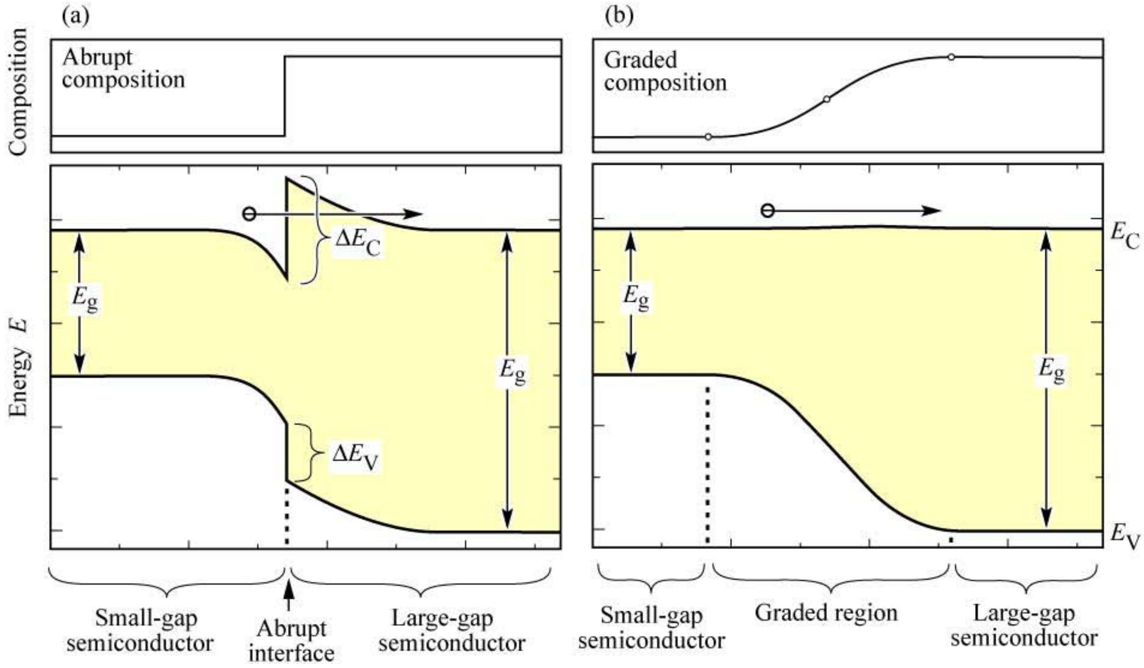

Figure 2.23

resistance. Thus, the additional resistance introduced by abrupt heterostructures can be completely eliminated by parabolic grading.

2.6.6 Carrier loss in double heterostructures

In an ideal LED, the injected carriers are confined to the active region by the barrier layers adjoining the active regions. By means of confinement of carriers to the active region, a high carrier concentration is attained resulting in a high radiative efficiency of the recombination process.

The energy barriers confining the carriers to the active region are typically of the order of several hundred meV, i.e. much larger than kT. Nevertheless, some carriers will succeed in escaping from the active region into the barrier layers. The concentration of the escaping carriers in the barrier layers will be rather low, resulting in a low radiative efficiency of carriers in the barrier layers.

Free carriers in the active region are distributed according to the Fermi–Dirac distribution and, as a result, some carriers have a higher energy than the height of the confining barrier. Thus some of the carriers escape from the active region into the barrier regions as illustrated in figure 2.24.

The number of escaping carriers is inversely dependent on the height of the energy barriers of the DH. Thus a high barrier height is required to minimize the leakage

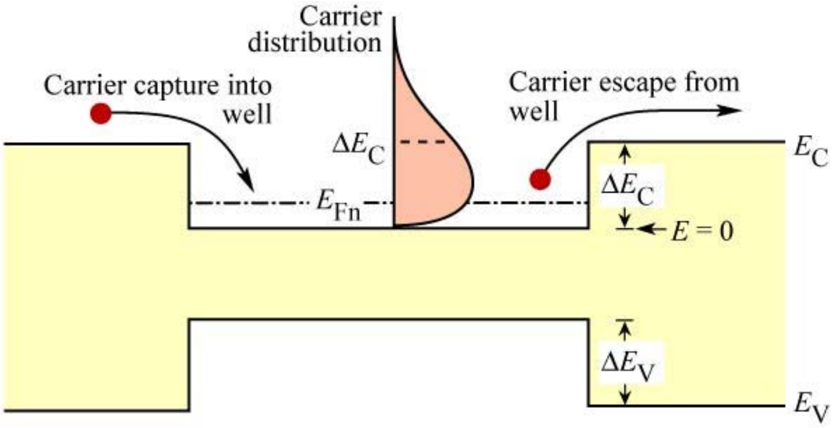

Figure 2.24: Carrier capture and escape in a DH. Also shown is the carrier distribution in the active layer.

current.

It is worth noting that the leakage increases exponentially with temperature. Thus, a decrease of the radiative efficiency of LEDs results as the temperature increases. To reduce the temperature dependence of the emission, high barriers are required. As we have seen, in addition to carrier leakage, other effects, such as SRH recombination also contribute to the lower radiative efficiency at high temperatures.

2.6.7 Carrier overflow in double heterostructures

Another loss mechanism present in DHs is the overflow of carriers from the active region into the confinement regions. Carrier overflow occurs at high injection current densities. As the injection current increases, the carrier concentration in the active region increases and the Fermi energy rises. For sufficiently high current densities, the Fermi energy will rise to the top of the barrier. The active region is flooded with carriers and a further increase in injection current density will not increase the carrier concentration in the active region. As a result, the optical intensity saturates. At high injection current densities, carrier overflow occurs, even if the barriers are sufficiently high, so the carrier leakage over the barriers at low injection current densities can be neglected.

Consider a double heterostructure LED with an active region of thickness W_{DH}, as shown in figure. The rate equation of carrier supply to (by injection) and removal from (by recombination) the active region is given by

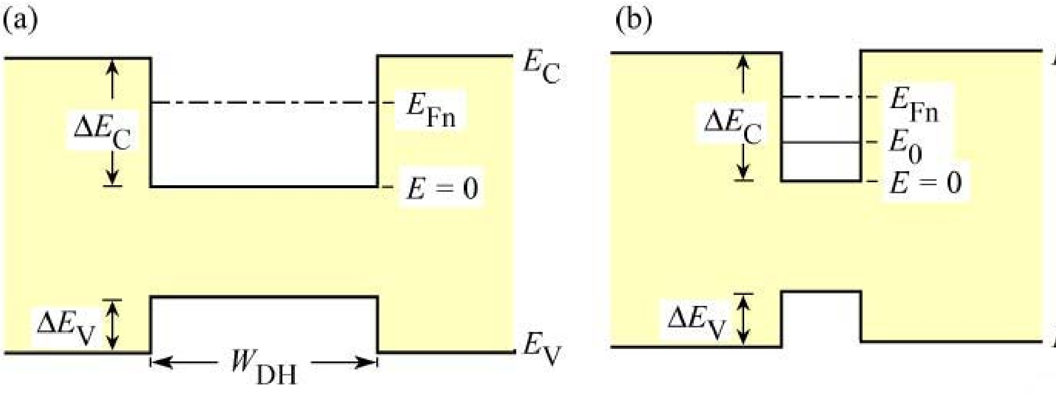

Figure 2.25

$$\frac{dn}{dt} = \frac{J}{eW_{DH}} - Bnp, \tag{2.54}$$

where B is the bimolecular recombination coefficient. In steady state condition and for high injection densities (p=n), equation 2.54 yields

$$n = \sqrt{\frac{J}{eBW_{DH}}}. \tag{2.55}$$

By increasing current injection, carrier densities increase, thus, Fermi energy rises. In the high-density approximation, the Fermi energy is given by

$$\frac{E_F - E_C}{kT} = \left(\frac{3\sqrt{\pi}}{4}\frac{n}{N_C}\right)^{2/3}. \tag{2.56}$$

At high injection levels, the Fermi energy rises and will eventually reach the top of the barrier. At that poin

t, it is $E_F - E_C = \Delta E_C$. Using this value, the current density at which the active region overflows can be calculated from equations 2.55 and 2.56 and one obtains

$$J_{overflow} = \left(\frac{4N_C}{3\sqrt{\pi}}\right)^2 \left(\frac{\Delta E_C}{kT}\right)^3 qBW_{DH.} \tag{2.57}$$

Either the conduction band or the valence band well may overflow first depending on the effective density of states (N_C, N_V) and the band discontinuities (ΔE_C, ΔE_V).

Generally, the problem of carrier overflow is more severe in structures with a small activeregion volume. In particular, single-quantum-well structures and quantum-dot active regions have an inherently small volume. At a certain current density, the active region is filled with carriers, and the injection of additional carriers will not lead to an increase in the emitted light intensity.

Experimental results of an LED structure with one, four, six, and eight quantum wells (QWs) are shown in figure 2.26. The light intensity for the single QW structure saturates at a low current level. As the number of quantum wells is increased, the current level at which saturation occurs increases, and the optical saturation intensity increases as well. The saturation of the light intensity displayed in figure 2.26 is caused by the overflow of carriers.

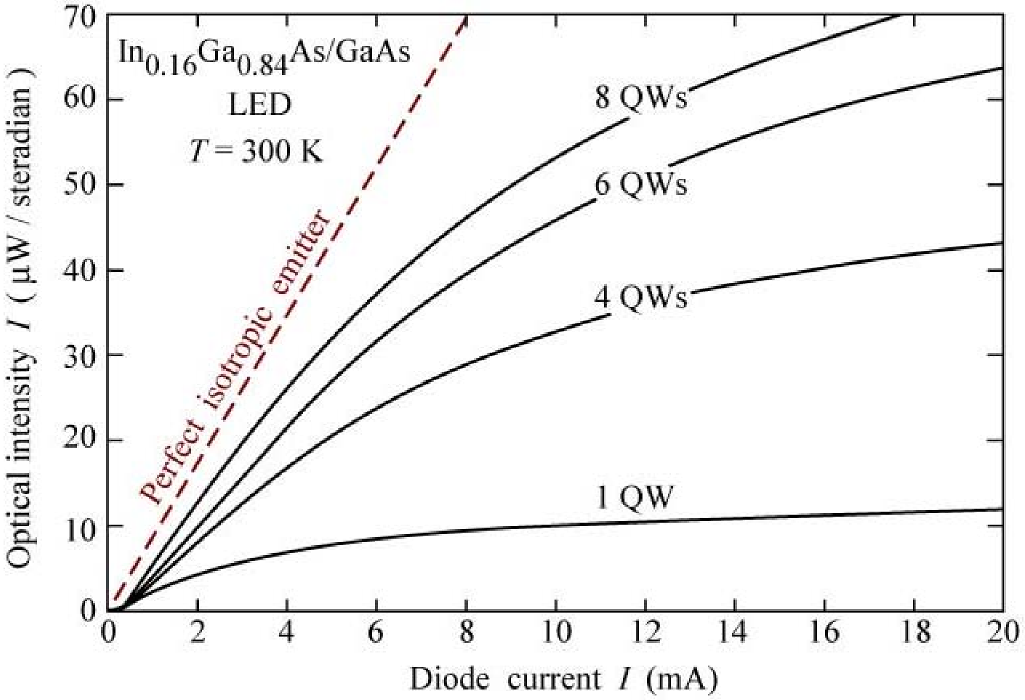

Figure 2.26: Optical intensity emitted by $In_{0.16}Ga_{0.84}As/GaAs$ LEDs with active regions consisting of one, four, six, and eight quantum wells and theoretical intensity of a perfect isotropic emitter (dashed line).

The calculation of the overflow current level is different for QW structures and bulk active regions. For QW structures, we must employ the 2D DOS, rather than the 3D DOS that was used in the above calculation. The Fermi level in a QW with one quantized state energy E_0 is given by

$$\frac{E_F - E_0}{kT} = \ln\left[\exp\left(\frac{n^{2D}}{N_C^{2D}}\right) - 1\right], \tag{2.58}$$

where n^{2D} is the 2D carrier density per cm^2 and N_C^{2D} is the effective density of states given by

$$N_C^{2D} = \frac{m^*}{\pi\hbar^2}kT. \tag{2.59}$$

Because we are dealing with high carrier densities, the high-degeneracy approximation can be employed and one obtains

$$E_F - E_0 = \frac{\pi\hbar^2}{m^*} n^{2D}. \tag{2.60}$$

Next, we write the rate equation for the quantum well. The rate equation of carrier supply to (by injection) and removal from (by recombination) the active region is given by

$$\frac{dn^{2D}}{dt} = \frac{J}{e} - B^{2D} n^{2D} p^{2D}, \tag{2.61}$$

where $B^{2D} \simeq B/W_{QW}$ is the bimolecular recombination coefficient for a 2D structure. In steady state condition and for high injection densities ($n^{2D} = p^{2D}$), equation 2.61 yields

$$n = \sqrt{\frac{J}{eB^{2D}}} = n = \sqrt{\frac{JW_{QW}}{eB}}. \tag{2.62}$$

At high injection levels, the Fermi energy will reach the top of the barrier. At that point, $E_F – E_0 = \Delta E_C – E_0$. The use of this value in equation 2.60 and subsequent elimination of n^{2D} from equations 2.60 and 2.62 yields the current density at which the active region overflows

$$J_{overflow} = \left[\frac{m^*}{\pi\hbar^2}(\Delta E_C – E_0)\right]^2 \frac{qB}{W_{QW}}. \tag{2.63}$$

Thus overflow of the active region is a potential problem in double heterostructures as well as quantum well structures. In order to avoid this problem, high-current LEDs must employ thick double heterostructure active regions, or many QWs of multiple QW (MQW) active regions, or a large injection (contact) area. By choosing these parameters, the volume of the active region can be designed in such a way that at the intended current density of operation, carrier overflow does not occur.

2.6.8 Electron-Blocking layer

Carriers tend to escape from the active layer of an LED into the confinement layers. The carrier escape can be substantial in DH with a low barrier height at the active-confinement interface. In addition, high temperatures promote carrier loss out of the active region due to the increase in carrier thermal energy.

The electron leakage current is larger than the hole leakage current due to the usually larger diffusion constant of electrons compared with holes in III-V semiconductors.

To reduce carrier leakage out of the active region, carrier-blocking layers are used. In partcular, *electron-blocking layers* or *electron blockers* are used in many LED structures to reduce electron escape out of the active region. Such electron blockers are regions with a high bandgap energy located at the confinement-active interface.

An example of the band diagram of a GaInN LED with an electron-blocking layer is shown in figure 2.27.

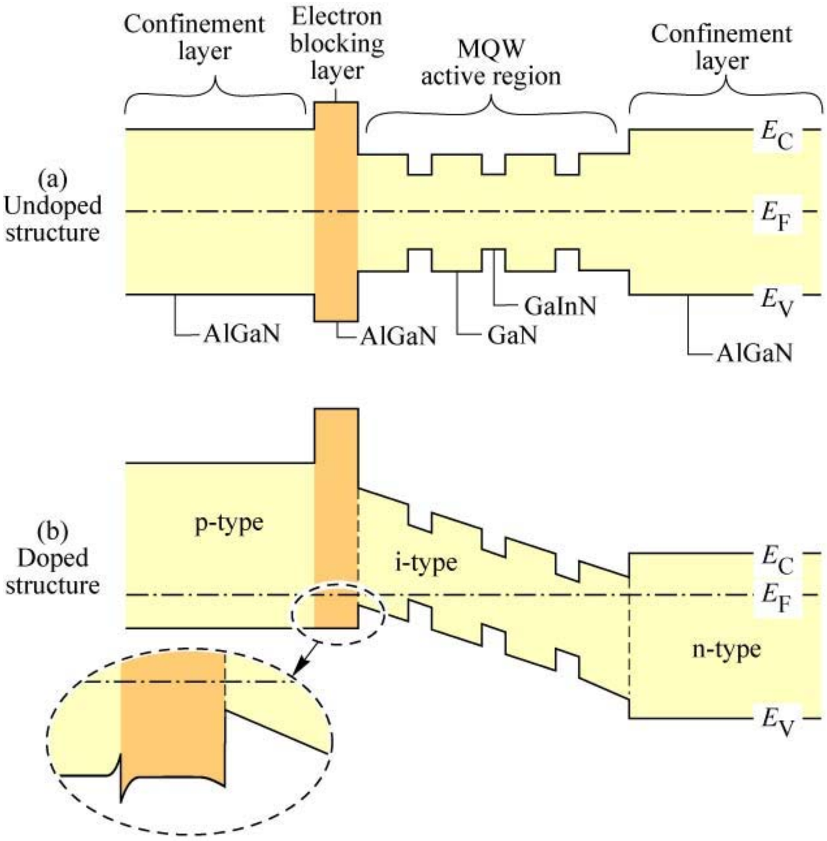

Figure 2.27: AlGaN current-blocking layer in an AlGaN/GaN/GaInN multi quantum well structure. (a) Band diagram without doping. (b) Band diagram with doping. The Al content in the electron-blocking layer is higher than in the p-type connement layer.

2.7 Thermal Model

The thermal management is one of the main issues concerning a LED device, and its improvement is one of the keys of a successful light source.

For what concerns this thesis work, the study of the thermal characteristics and behaviour for LEDs under stress conditions requires the construction of a valid thermal model in which we must base our consideration and evaluate our results. This model is represented in Figure 2.28 and deals with the thermal path that the heat has to follow. Each path can be represented with a thermal resistance that is not only peculiar for each device, but also vary with the disposition of one or more LEDs onto the Printed Circuit Board (PCB) and, obviously, with the applied thermal interfaces.

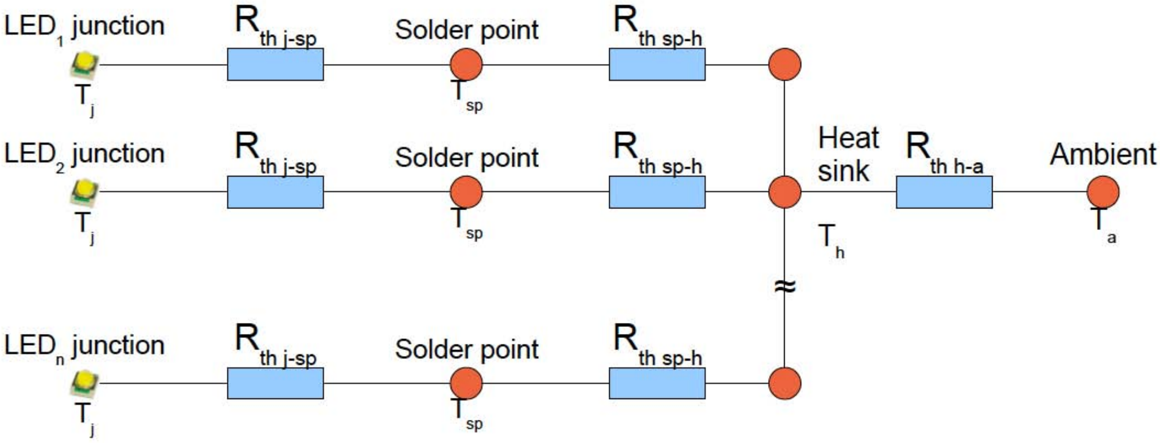

Figure 2.28: Thermal model used to represent the thermal path from the LED active region to the ambient.

Each thermal resistance, expressed in K/W, consists in the resistance of a certain material to the thermal flux, as the electrical resistance opposes to the current. As shown in Figure 3.6, if $T_A > T_B$, there will be a thermal power ux from the point A to B, and as a consequence a temperature gradient $\Delta T = T_A - T_B$. The relation between the power transferred, P_{th}, the thermal resistance R_{th} and temperature gradient is very similar to the Ohm's law:

$$\Delta T = P_{th} R_{th} \tag{2.64}$$

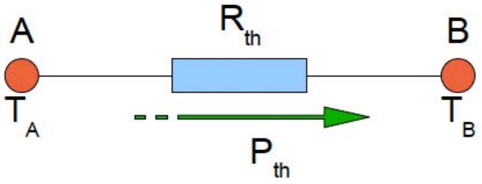

Figure 2.29

Using a measurement process that will be described later, the complexive thermal resistance (from junction to ambient) can be calculated. This is necessary not only because the device working and its ageing are very dependant from the thermal resistance, but also because the thermal resistance from junction to solder point, that is provided by the LED producer, is pretty useless: as a matter of fact we cannot simply add the new thermal resistances in the path to ambient (i.e. the resistance introduced by the PCB, the thermal interface and the heatsink), because once we change one of them, even the thermal flux does.

2.8 Optical properties

2.8.1 LED efficiency

The total efficiency of a LED is dependent on its ability to convert electrons into a luminous output, and can be conveniently divided into two factors. In an ideal LED, every single electron injected into the device should recombine radiatively, thus emitting a photon, so that its internal efficiency would be unitary. However, this is never true, and the internal quantum efficiency is calculated as

$$\eta_{int} = \frac{\text{photons emitted from active region per second}}{\text{photons injected into LED per second}} = \frac{P_{int}/(h\nu)}{I/q} \tag{2.65}$$

where P_{int} is the optical power emitted from the active region and I is the injected current.

Once a photon is emitted from the active region, it should reach the free space to contribute to the luminous flux. But, usually, only up to half of the photons are extracted from the die, due to several loss mechanisms. For example, photons with sufficient energy can be absorbed by the metallic contact surfaces or by the substrate material and recombine. Also, many photons remain trapped into the device beacuse of the total internal reflection phenomenon. The extraction efficiency takes account of these loss mechanisms, and is defined as

$$\eta_{extraction} = \frac{\text{photons emitted into free space per second}}{\text{photons emitted from active region per second}} = \frac{P/(h\nu)}{P_{int}/(h\nu)} \tag{2.66}$$

where P is the optical power emitted into free space.
The external quantum efficiency is then given by the product of the previous two:

$$\eta_{ext} = \frac{\text{photons emitted into free space per second}}{\text{photons injected into LED per second}} = \frac{P/(h\nu)}{I/q} = \eta_{int}\eta_{extraction}$$

It gives a measure of the capacity of the whole LED to convert the electrical current in light. A similar estimate is expressed by the power or “wallplug” efficiency defined as:

$$\eta_{power} = \frac{P}{IV}$$

where IV is the electrical power provided to the LED.

2.8.2 Emission spectrum

The ideal luminous flux from a LED is monochromatic, but in fact it comprises a certain wavelength range.

The physical mechanism by which semiconductor LEDs emit light is spontaneous recombination of electron–hole pairs and simultaneous emission of photons. The radiative electron-hole recombination process can be schematically described as in Figure 2.30 for a direct-bandgap semiconductor. Electrons in conduction band and holes in valence band have nearly parabolic dispersion. This means that their distribution in an $E - k$ space can be expressed as:

$$E = E_C + \frac{\hbar^2 k^2}{2m_e^*} \qquad \text{(for electrons)} \tag{2.67}$$

and

$$E = E_V - \frac{\hbar^2 k^2}{2m_h^*} \qquad \text{(for holes)} \tag{2.68}$$

where $m_e^*$and m_h^* are the electron and hole effective masses, k is the carrier wavenumber and E_V and E_C are the valence and conduction band edges respectively.

Energy conservation requires that the photon energy (E_{ph}) is given by the difference between the electron energy, E_e, and the hole energy E_h

$$E_{ph} = h\nu = E_e - E_h \approx E_g. \tag{2.69}$$

where the last approximation is only valid if the thermal energy kT is much smaller than the bandgap energy E_g. Thus the desired emission wavelength of an LED can be attained by choosing a semiconductor material with an appropriate bandgap energy.

As the electron momentum, equal to

$$p_e = m_e^* v = \sqrt{2m_e^* kT} \tag{2.70}$$

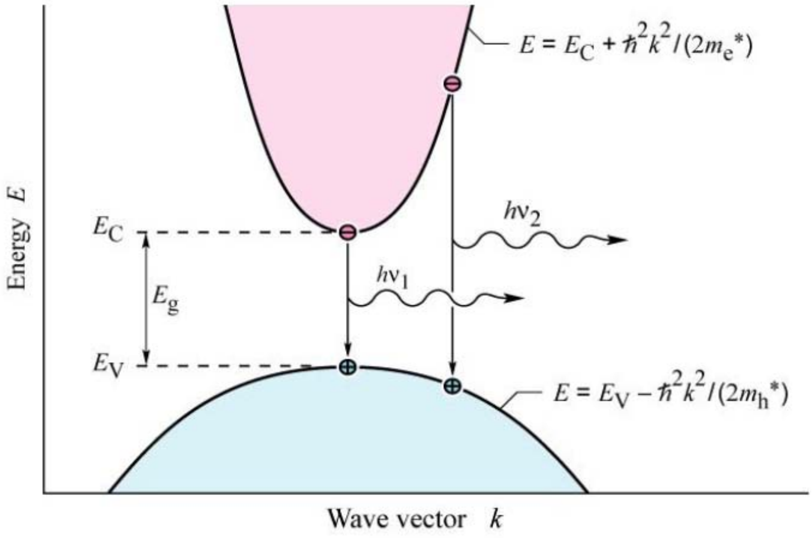

Figure 2.30: Parabolic electron and hole dispersion relations showing vertical electron-hole recombination and photon emission.

is much greater than photon momentum

$$p = \hbar k = \frac{h\upsilon}{c} = \frac{E_g}{c}$$

it cannot change significantly in the recombination process, so that the transitions can be considered to be "vertical".

By substituting the parabolic dispersion relations in Equation 2.69 and requiring that electron and hole momenta are the same, the photon energy can be expressed as the joint dispersion relation:

$$E_{ph} = h\nu = E_g + \frac{\hbar^2 k^2}{2m_r^*} \tag{2.71}$$

where $m_r^*$is called the reduced mass and is defined as

$$m_r^* = \left(\frac{1}{m_e^*} + \frac{1}{m_h^*}\right)^{-1}. \tag{2.72}$$

Using the joint dispersion relation, the joint density of states can be calculated as

$$\rho(E) = \frac{1}{2\pi^2}\left(\frac{2m_r^*}{\hbar^2}\right)^{\frac{3}{2}}\sqrt{E - E_g}. \tag{2.73}$$

Since the distribution of carriers in the bands is given by the Boltzmann statistics, i.e.

$$f_B(E) = e^{-E/(kT)}, \tag{2.74}$$

the *emission intensity* as a function of energy (emission spectrum), that is proportional to to the product of the two last equations, is

$$I(E) \propto \sqrt{E - E_g} e^{-E/(kT)} \tag{2.75}$$

that corresponds to the spectral shape shown in Figure 2.19, which is the theoretical emission spectrum for one LED. The peak emission energy is at $E = E_g + \frac{1}{2}kT$ and the full-width at half-maximum of the emission is $\Delta E = 1.8kT$ corresponding to $\Delta\lambda = \frac{1.8kT\lambda^2}{hc}$.

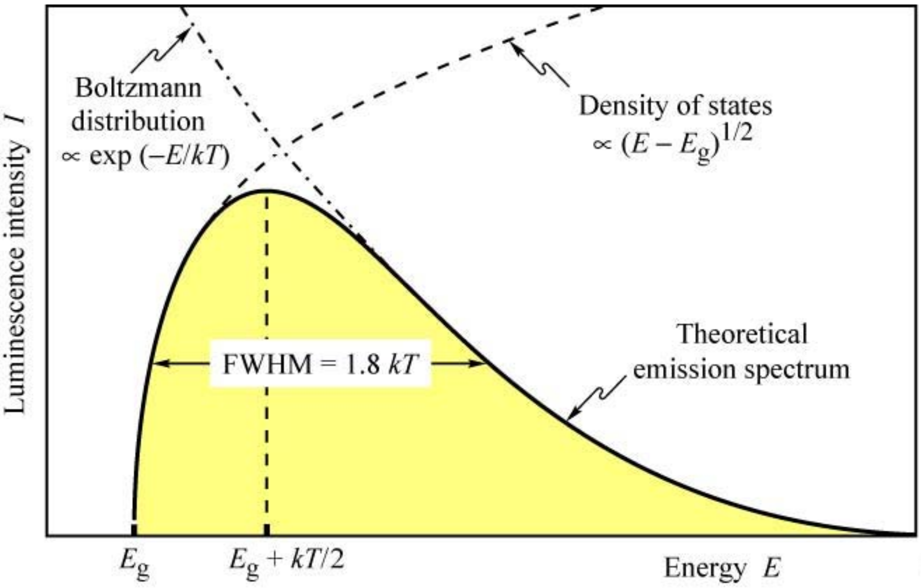

Figure 2.31: Theoretical intensity spectrum for a direct-bandgap semiconductor.

LED emission is narrower than the spectral widht of a single color as perceived by the human eye, so that it appears to be monochromatic.

The emission spectrum depends on the operating conditions of the LED. If the injection current is increased, more high-energy states will be occupied by the carriers, leading to higher energy recombinations and thus widening the spectrum.

The emission spectrum also varies with temperature. In fact the emission intensity of LEDs decreases with increasing temperature, as shown in Figure 2.32. This decrease of the emission intensity is due to several temperature-dependent factors such as non-radiative recombination via deep levels, surface recombination, and carrier loss over heterostructure barriers. Near room temperature, the temperature dependence of the

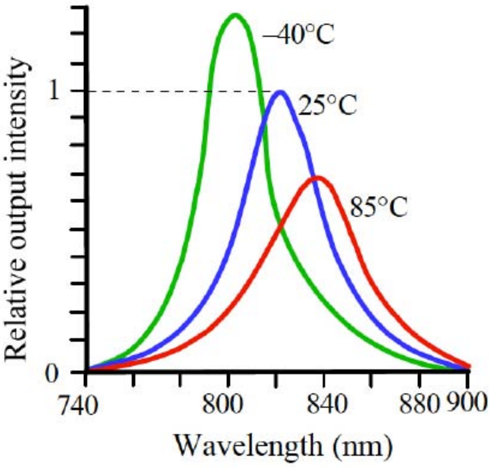

Figure 2.32: Effect of temperature on the spectral emission of a red AlGaAs LED, normalized to the peak emission at 25 °C.

LED emission intensity is frequently described by the phenomenological equation

$$I = I|_{300K} \exp\left(-\frac{T - 300K}{T_1}\right) \tag{2.76}$$

where T_1 is the characteristic temperature. A high characteristic temperature, implying a weak temperature dependence, is desirable. The dependence of the Boltzmann function with the temperature is also important and is remarkable onto the spectrum variation both when the device is put at different ambient temperatures and when its temperature rises under self-heating conditions. In particular, as shown in Figure 2.32, higher operating temperatures result in a broadening of the spectrum and in a shift towards longer wavelengths. Moreover is to be noted that the energy gap decreases with increasing temperature, and this involves an increase in the peak wavelength of emission.

2.8.3 Output power vs Current curves

As described at the beginning of this chapter, carrier recombination processes may be radiative and non-radiative. Radiative processes (governed by bimolecular coefficient B) therefore take place in parallel or in series with other processes, including SRH recombination (coefficient A), Auger recombination (coefficient C), electron and hole trapping processes, c_n and c_p and leakage current out of the active region. A schematic representation of these phenomena is given in Figure 2.33.

The most state-of-the-art LEDs have lightly doped p and n-side. Therefore, the

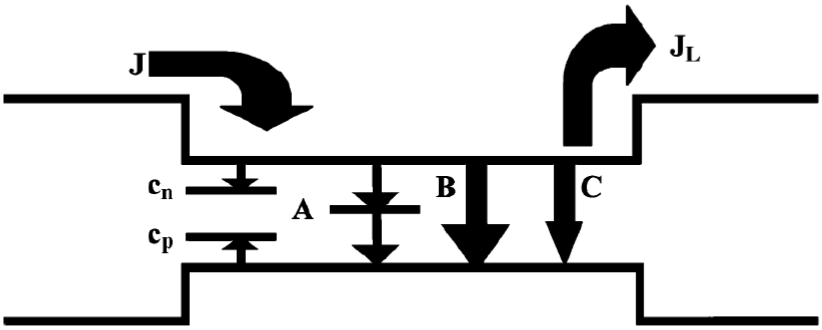

Figure 2.33: Schematic representation of the carriers recombination processes.

injected carrier concentration is higher than the background doping, and therefore we can assume that n = p. In this approximation, as described above, SRH, radiative and Auger recombination rate can be described by terms of the form An, Bn^2, Cn^3 respectively. Charge neutrality conditions impose that the rate equation can be expressed as

$$\frac{dn}{dt} = \frac{J}{ql} - An - Bn^2 - Cn^3 - \frac{J_L}{ql_1} \tag{2.77}$$

or, in other terms

$$\frac{dn}{dt} = \frac{J}{ql} - R_{SHR} - R_R\text{-}R_A\text{-}\frac{J_L}{ql_1} \tag{2.78}$$

where J_L is the leakage current density out of the active region. Converting recombination rate in lifetimes we finally obtain the following rate equation

$$\frac{dn}{dt} = \frac{J}{ql} - n\left(\frac{1}{\tau_{SHR}} - \frac{1}{\tau_R}\text{-}\frac{1}{\tau_A}\right)\text{-}\frac{J_L}{ql_1} \tag{2.79}$$

where l is the thickness of the active layer, l_1 is the minority carriers diffusion length.

Under steady-state regime, equation 2.79 becomes

$$\frac{J}{ql} = An + Bn^2 + Cn^3 + \frac{J_L}{ql_1}. \tag{2.80}$$

Under the condition $n = p$, the term Cn^3 depends on bandstructure through the relationship $np = n_i^2 e^{qV/kT}$ and $n_i^2 = N_C N_V e^{-Eg/kT}$. In wide-bandgap semiconductors, the term n_i^3 can be small, and therefore the Auger recombination term is usually neglected. Under this assumption, the rate equation simplies to

$$\frac{J}{ql} \approx An + Bn^2 + \frac{J_L}{ql_1}. \tag{2.81}$$

Remembering the expression of the SRH recombination rate explained at the beginning of this chapter

$$R_{SHR} = \frac{p_0\Delta n + n_0\Delta p + \Delta n\Delta p}{(N_T v_p \sigma_p)^{-1}(n_0 + n_1 + \Delta n) + (N_T v_n \sigma_n)^{-1}(p_0 + p_1 + \Delta_p)} \tag{2.82}$$

under the assumption that trap parameters are the same for electrons and holes and that $n = n_0 + \Delta n \approx p = p_0 + \Delta p$, i.e. that injected carrier concentration is higher than the background doping it can rewritten as

$$R_{SHR} = \frac{nv\sigma N_T}{2} \tag{2.83}$$

and neglecting the leakage current components we have

$$J' = qln\sigma vN_T/2 + qlBn^2. \tag{2.84}$$

At low current densities, the electron concentration n is low, and therefore $An \gg Bn^2$. For an intermediate current value the radiative and non-radiative recombination terms become equal ($An = Bn^2$), and

$$J' = 2qlAn_1 = qln_1\sigma vN_T \tag{2.85}$$

where n_1 is the value of n for which $An = Bn^2$. This last equation indicates that the current level necessary to saturate the non-radiative recombination components is proportional to the defect concentration. At higher current level, the quadratic term Bn^2 begins to dominate over the non-radiative term, leading to the complete saturation of non-radiative paths.

Light output L is only related to radiative recombination and therefore is proportional to Bn^2. On the basis of the previous calculation we can state that

$$L \propto Bn^2 = \frac{J'}{ql} - \frac{n\sigma vN_T}{2}. \tag{2.86}$$

On the other hand, for low current levels we have $An \gg Bn^2$ and

$$L \propto Bn^2 = \frac{B}{A^2}\left(\frac{J'}{qj}\right)^2. \tag{2.87}$$

Therefore, for low injection current levels, non-radiative processes dominate and light output has a parabolic dependence on injected current. For higher current levels non-radiative processes are saturated, and light output depends linearly on injected current. A further increase of the current renders a higher value of radiative decays but also a greater probability of carrier escaping and a grater self-heating, that leads the L-I curve to a sub-linear trend. Higher current levels saturate the decays number: this saturation is reflected by a pretty constant light output for very high currents. Obviously the carrier escaping strictly depends on the heterostructure and the number of quantum wells.

The balance between radiative and non-radiative process at the different current levels and the parabolic and linear behavior of the optical power vs injected current (L-I) curves are schematically represented in Figure 2.34 and 2.35 respectively

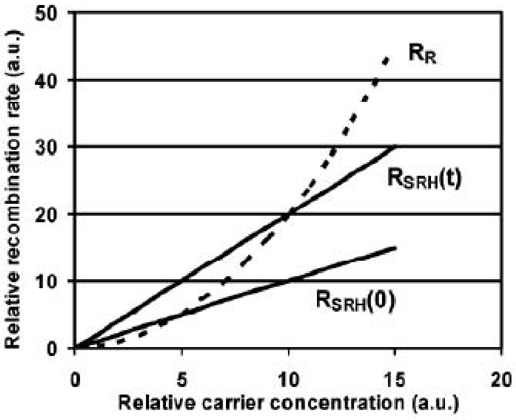

Figure 2.34: Schematic representation of the carriers recombination processes (radiative and non-radiative processes).

2.8.4 The escaping angle of light

In order to prevent the total internal reflection of the radiation inside the chip, an epoxy dome is often applied where the light has to be extracted, and because of this it is possible to estimate the escape angle, that gives origin to an escape cone, inside which light can succesfully irradiate in free space, and outside it is most likely trapped and then losed.

If we evaluate, as in Figure 2.36, the surface area of the spherical escaping cone with radius r and assuming that the light is emitted froma point-like source with power P_{source}, we obtain the relation:

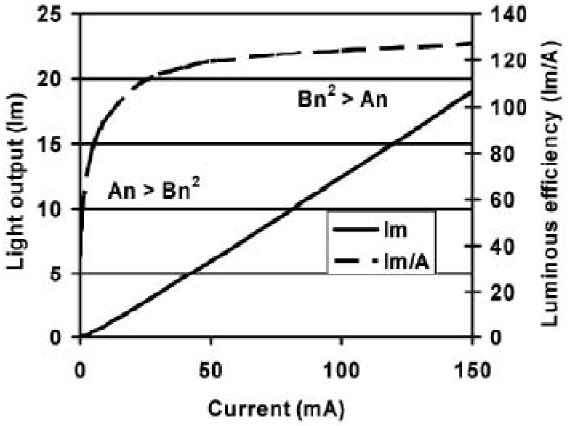

Figure 2.35: Schematic plot of the L-I curve of one LED, showing the parabolic and linear region. The luninous efficiency (L/I vs I) is also plotted for completness.

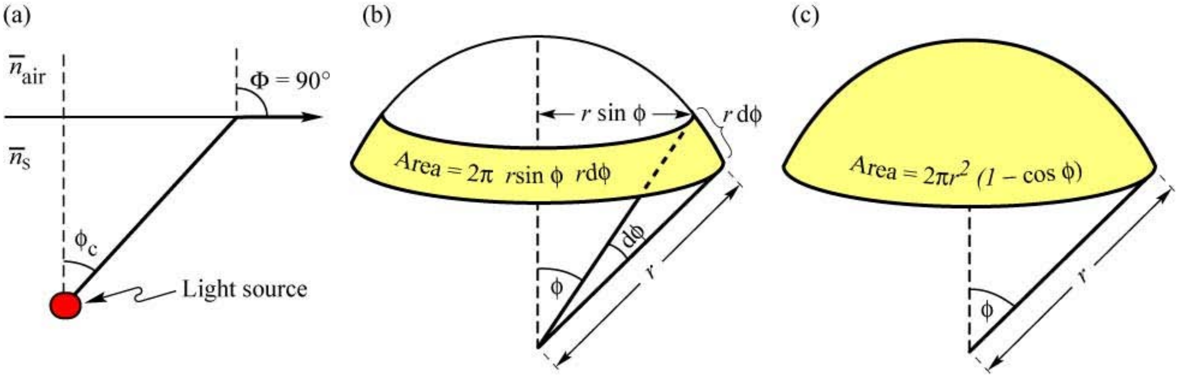

Figure 2.36: (a) Definition of the escape cone by the critical angle ϕ_c . (b) Area element dA. (c) Area of calotte-shaped section of the sphere defined by radius r and angle ϕ_c .

$$P_{escape} = P_{source} \frac{2\pi r^2(1-\cos\phi_c)}{4\pi r^2} = P_{source}\frac{1}{2}(1-\cos\phi_c), \tag{2.88}$$

which is stricly dependant from the critical angle ϕ_c :

$$\phi_c = \frac{n_{air}}{n_s}, \tag{2.89}$$

where $n_{air} \simeq 1$ is the air refractive index, $n_s > 1$ is the semiconductor's. Expanding in eq. 2.88 the cosine into a power series and combining this with eq.2.89, we arrive to

$$\frac{P_{escape}}{P_{source}} = \frac{1}{4}\phi_c^2 = \frac{1}{4}\frac{n_{air}^2}{n_s^2}. \tag{2.90}$$

Since the semiconductor's refrative index can be quite high ($ns > 2.5$), the quantity in eq. 2.90 can be signicantly increased with the application of an epoxy dome with an interediate refractive index over the chip top surface: this leads to a rising of the critical angle, thus a greater light escaping is achieved.

2.9 Generation of white light with LEDs

As we discussed in Chapter 1, light is perceived as white light if the three types of cones located on the retina of the human eye are excited in a certain ratio, namely with similar intensity. For the case of white light, the tristimulus values are such that the location of the chromaticity point is near the center of the chromaticity diagram.

White light can be achieved with LEDs in two main ways:

1. RGB systems, in which light from multiple monochromatic LEDs (red, green, and blue) is mixed, resulting in white light.
2. Phosphor conversion, in which a blue or near-ultraviolet (UV) chip is coated with phosphor(s) to emit white light.

The RGB approach produces white light by mixing the three primary colors: red, green, and blue. Hence the method is called *multi-color white LEDs* (sometimes referred to as *RGB LEDs*). Because these need electronic circuits to control the blending and diffusion of different colors, and because the individual color LEDs typically have slightly different emission patterns (leading to variation of the color depending on direction) even if they are made as a single unit, these are seldom used to produce white lighting. Nevertheless, this method is particularly interesting in many uses because of the flexibility of mixing different colors.

There are several types of multi-color white LEDs: di-, tri-, and tetrachromatic white LEDs (see Figure 2.37). Several key factors that play among these different methods, include color stability, color rendering capability, and luminous efficacy. Often, higher efficiency will mean lower color rendering, presenting a trade-off between the luminous efficiency and color rendering. For example, the dichromatic white LEDs have the best luminous efficacy (120 lm/W), but the lowest color rendering capability. However, although tetrachromatic white LEDs have excellent color rendering capability, they often have poor luminous efficiency. Trichromatic white LEDs are in between, having both good luminous efficacy (>70 lm/W) and fair color rendering capability.

However, before this type of LED can play a role on the market, several technical problems must be solved. As a matter of fact individual colored LEDs respond diferently to drive current, operating temperature, dimming, and operating time. Therefore feedback loop systems must be used for example with color sensors, to actively monitor and control the color output of multiple color mixing LEDs.

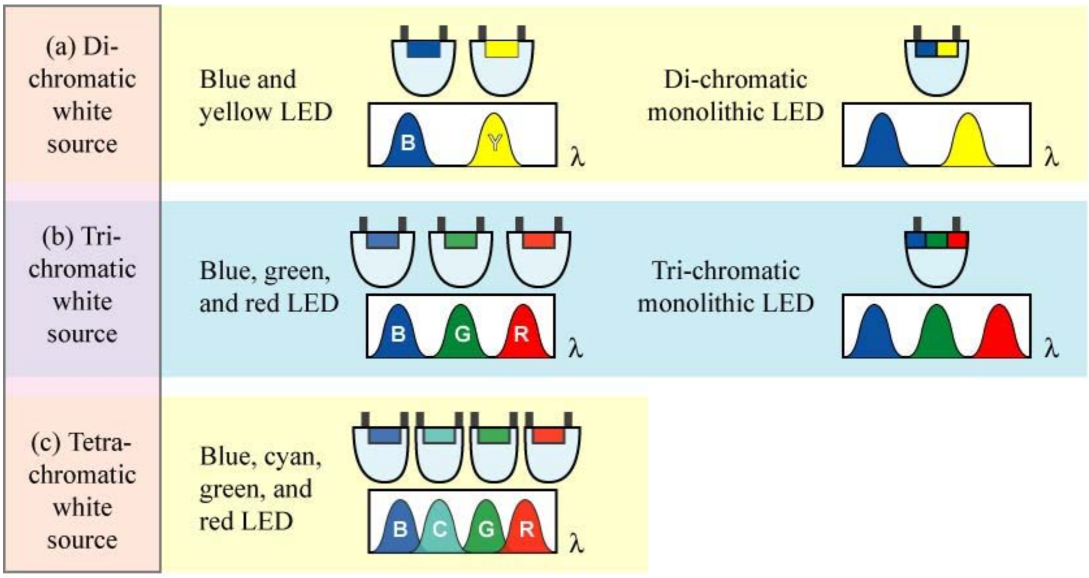

Figure 2.37: LED-based approaches for white sources including single-chip and multiple-chip, di-chromatic, tri-chroamtic, and tetra-chromatic approaches.

The phosphor conversion approach involves coating LEDs of one color with phosphors of different colors to form white light; the resultant LEDs are called *phosphor-converted white LEDs* (pc-LEDs). The cross-sectional structure of a white LED lamp based on phosphor conversion is shown in Figure 2.39(a).

Phosphors consist of an inorganic host material doped with an optically active element. They act as a wavelength converter; part of the light emitted by a LED excites the phosphors that then re-emit light at longer wavelengths, with very high conversion efficiency. The phosphor powder can be suspended in epoxy resin that sourrounds the die, so that all the light emitted must travel through this coating. There are several different approaches to generate white light based on phosphors excited by semiconductor LEDs, which are shown in Figure 2.38. They can be classified in dichromatic, trichromatic, and tetrachromatic approaches. These approaches use either UV-excitation sources or visible-spectrum-excitation sources (mostly blue semiconductor LEDs).

Generally, the luminous source efficiency decreases with increasing multi-chromaticity of the source. Thus, dichromatic sources have the highest luminous efficacy of radiation and also the highest potential luminous source efficiency. On the other hand, the color-rendering capability is lowest for dichromatic sources and it increases with the multi-chromaticity of the source. The color-rendering index can reach values very close

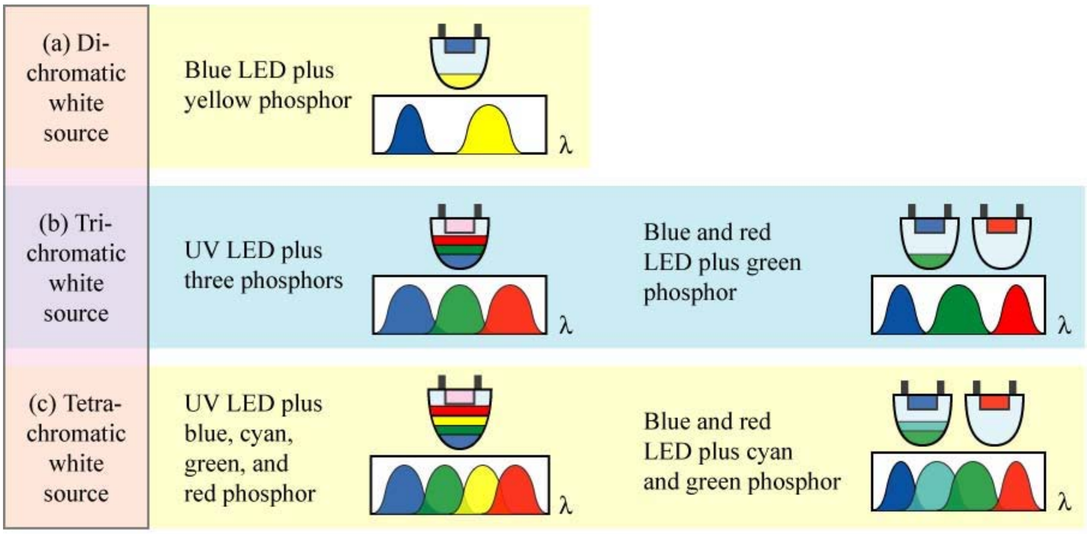

Figure 2.38: White sources using phosphors that are optically excited by UV or blue LEDs.

to $CRI = 100$ for tetrachromatic sources.

In assessing the merits of these LED architectures, we note that pc-LEDs may provide a simpler and lower cost solution. Requiring only one LED (tipically blue), the pc-LED avoids some of the complexities of multichip systems, including aspects of assembly, color mixing, and feedback circuitry to maintain color quality, given different thermal and degradation properties of the individual LEDs. However, in terms of energy efficiency, the multichip approach offers a clear advantage. By providing direct emission at the necessary visible wavelengths, multichip LEDs avoid the absorption and emission losses of the phosphor as well as down-conversion losses associated with generating lower energy phosphor emission from a higher energy blue source. The multichip approach also has greater potential for actively controlling the light's spectral distribution, providing "smart" lighting capabilities far beyond traditional lamp systems. Thus, although success of the multichip approach requires overcoming significant LED materials challenges, the compelling benefits have inspired concerted pursuit of that design [4].

2.9.1 Efficiency of wavelength-converter materials

The conversion efficiency of short wavelength light to long wavelength light by a wavelength converter (λ-converter) material is determined by two distinct factors, namely:

- the *external quantum efficiency* of the λ-converter;

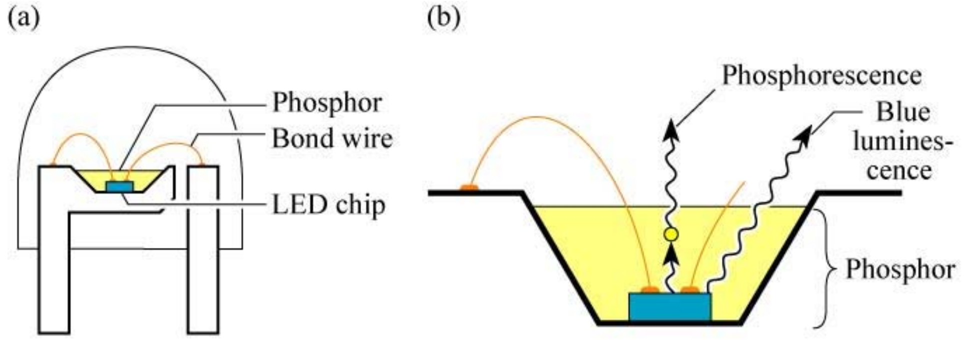

Figure 2.39: (a) Structure of white LED consisting of a GaInN blue LED chip and a phosphor encapsulating the die. (b) Wavelength-converting phosphorescence and blue luminescence.

- the *inherent energy loss* incurred in wavelength conversion.

The external quantum efficiency of the converter material, η_{ext}, is given by

$$\eta_{ext} = \frac{number\, of\, photons\, emitted\, into\, free\, space\, by\, \lambda - converter\, per\, second}{number\, of\, photons\, absorbed\, by\, \lambda - converter\, per\, second}. \tag{2.91}$$

The external efficiency originates in the internal efficiency and the extraction efficiency of the converter material according to $\eta_{ext} = \eta_{internal}\eta_{extraction}$. Note that the internal quantum efficiency depends on the inherent efficiency of the material whereas the extraction efficiency depends on the spatial distribution of the λ-converter material. Generally, thin films have high extraction efficiencies whereas lumpy aggregations of converter materials have lower extractionefficiency due to reabsorption. It is therefore desirable to employ λ-converter materials in the form of thin layers.

The inherent wavelength-conversion loss (sometimes called quantum deficit or Stokes shift) incurred when converting a photon with wavelength λ_1 to a photon with wavelength λ_2 ($\lambda_1 < \lambda_2$) is given by $\Delta E = h\nu_1 - h\nu_2 = \frac{hc}{\lambda_1} - \frac{hc}{\lambda_2}$ Thus the wavelength-conversion efficiency is given by

$$\eta_{(\lambda - conversion)} = \frac{(h\nu_2)}{(h\nu_1)} = \frac{\lambda_1}{\lambda_2} \tag{2.92}$$

where λ_1 is the wavelength of the photon absorbed by the phosphor and λ_2 is the wavelength of the photon emitted by the phosphor. Note that wavelength-conversion loss is fundamental in nature. The loss cannot be overcome with conventional λ-converter materials. The power-conversion efficiency of a wavelength converter is the product of this two efficiencies:

$$\eta_{(\lambda-converter)} = \eta_{(\lambda-conversion)}\eta_{ext}. \tag{2.93}$$

The inherent wavelength conversion energy loss is the main reason that λ- converter-based white light sources have a fundamentally lower efficiency limit than white-light sources based on RGB LEDs.

2.9.2 Phosphors types

Phosphors consist of an inorganic host material doped with an optically active element. Yttrium aluminum garnet (YAG), Y3Al5O12, is a particularly common host material. Phosphors having YAG as a host material are called YAG phosphors. The optically active dopant is a rare-earth element, a rare-earth oxide, or

2.10 Package

Virtually all LEDs are mounted in a package that provides two electrical leads, a transparent optical window for the light to escape, and, in power packages, a thermal path for heat dissipation. The chip-encapsulating material advantageously possesses high optical transparency, a high refractive index, chemical inertness, high-temperature stability, and hermeticity. The refractive index contrast between the semiconductor and air is reduced by including an encapsulant thereby increasing the light extraction efficiency. Virtually all encapsulants are polymers with a typical refractive index of 1.5 to 1.8. As stated in the previous section, a reduced index contrast at the semiconductor surface increases the angle of total internal reflection thereby enlarging the light escape cone and the extraction efficiency.

A power package is shown in Figure 2.12. Power packages have a direct, thermally conductive path from the LED chip, through the package, to a heat sink, e.g. a printed circuit board. The power package shown in the figure has several advanced features. Firstly, the package contains an Al or Cu heatsink slug with low thermal resistivity to which the LED submount is soldered by a metal-based solder. Secondly, the chip is encapsulated with silicone or epoxy resin. Because standard encapsulant retains mechanical softness in its cured state, the encapsulant is covered with a plastic cover that also serves as lens. Thirdly, the chip is directly mounted on a Si submount that includes electrostatic discharge protection (ESD).

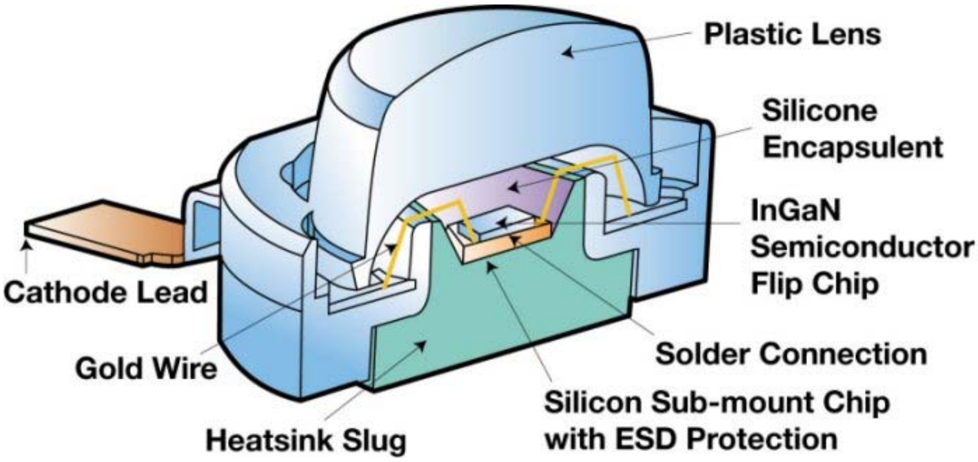

Figure 2.40: Cross section through high-power package.

2.11 Encapsulants

Encapsulants have several requirements including high transparency, high refractive index, chemical stability, high-temperature stability, and hermeticity. All encapsulants are based on polymers.

A common encapsulant is ***epoxy resin*** (also called epoxy), which remains transparent and does not show degradation over many years for long-wavelength visible-spectrum and IR LEDs. However, it has been reported that epoxy resins lose transparency in LEDs emitting at shorter wavelengths, i.e. in the blue, violet, and UV (Barton et al., 1998). . The refractive index of epoxy resin is near 1.6. Besides being transparent, epoxy resin is noted for its good mechanical properties and good thermal stability. However, prolonged exposure of the epoxy to temperatures exceeding 120 °C will lead to discoloration and loss of transparency (yellowing).

To overcome the limited thermal stability of epoxies, ***silicone*** encapsulants have been used since the early 2000s. Silicone is thermally stable up to temperatures of about 190 °C, significantly higher than epoxies (Crivello, 2004). Furthermore silicone is flexible (and remains flexible for decades) thereby reducing the mechanical stress on the semiconductor chip. Silicone is a polymer that contains Si and O thereby resembling SiO2 more so than epoxy resins. This resemblance suggests that silicone encapsulants are chemically and thermally stable and do not lose transparency as easily as epoxy resins. It may be desirable to develop encapsulants that are SiO2-like because SiO2 has excellent thermal and chemical stability and very high transparency (Crivello, 2004). On the other hand, silica lacks the flexibility that silicones offer.

Poly methyl methacrylate or briefly ***PMMA*** is a less common encapsulant used for LEDs. PMMA is also known under the name of acrylic glass and under the product name Plexiglas. The relatively low refractive index of PMMA (n = 1.49 in the wavelength range 500– 650 nm) results in a limited extraction efficiency when used with high-index semiconductors.

2.12 Material of choice

The most-important semiconductors for LED applications are listed in Figure 2.41, where the relative luminosity for the human eye is also added for reference [5]. The spectrum covers most of the visible and extends into the infrared region. In general, all of these semiconductors are direct-bandgap materials except for some of the alloy composition in the GaAsP system. Direct-bandgap semiconductors, as discussed before, are particularly important for electroluminescent devices, because the radiative recombination is a first-order transition process (no phonon involved) and the quantum efficiency is expected to be much higher than that for an indirect-bandgap semiconductor, where a phonon is involved.

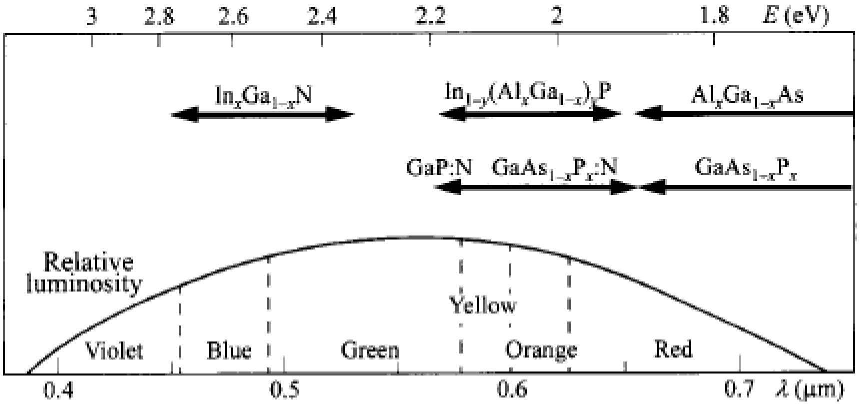

Figure 2.41: Semiconductors of interest for LEDs, including the relative luminosity function of the human eye.

AlGaAs The $Al_xGa_{1-x}As$ systems covers a wide range of wavelengths from red to infrared. In the form of GaAs, it is the earliest material used for high-efficiency LEDsin the 1960s. For higher A1 composition,≈ 45%, its bandgap becomes indirect, so the wavelength is limited to about $0.65\mu m$. The advantages of this material system include excellent heterojunction growth capability for making double-heterojunction LEDs, and it has a good lattice match to GaAs substrates. GaAs has the mostadvanced material technology of all the compound semiconductors. The AlGaAs material system is suited for high-brightness visible-spectrum LEDs emitting in the red wavelength range.

ALInGaP This material system has higher energy than AlGaAs, and it covers a wide range of the visible spectrum, i.e., red, orange, yellow, and green. The direct-bandgap range limits this material system to wavelengths longer than $0.56\mu m$. This system also has good lattice match to GaAs substrate.

InGaN This most-recent technological breakthrough in InGaN epitaxial growth gives an important addition to LED applications. This material has a wide spectrum covering green, blue, and violet. More importantly, it is the sole provider for blue and violet which had been difficult from a material point of view. For longer wavelengths extending to the rest of the visible spectrum, higher In percentage is needed to decrease the energy gap. But higher In percentage is accompanied by more misfit dislocations because of increased lattice mismatch. Therefore, this material is not used for the rest of the visible spectrum. The substrate materials can be sapphire, Sic, or GaN, but the high cost of the latter two substrates encourages the use of sapphire.

GaAsP As shown in Figure 2.41, the $GaAs_{1-x}P_x$ system covers a very wide range of spectrum, from the infrared to the middle of the visible spectrum but the efficiency is very low. However, an efficient radiative recombination center can be introduced by incorporating specific impurities such as nitrogen.

2.13 Degradation mechanism

In this section, we give an overview on the degradation mechanisms that limit the lifetime of GaN-based LEDs.

Over the last few years, several authors have demonstrated that the optical efficiency of GaN-based LEDs can significantly decrease during operation time. A number of mechanisms have been identified as responsible for LED degradation, including the following [6]:

1. the decrease in the internal quantum efficiency due to the generation of nonradiative centers in the active region of the devices;
2. the decrease in the acceptor concentration at the p-side of the diodes due to the generation of magnesium–hydrogen complexes;

3. changes in the processes responsible for the injection of the carriers in the active region of the devices (e.g., trap-assisted tunneling);
4. the shortening of the p-n semiconductor junction as a consequence of an ESD event;
5. the degradation of the plastic lens due to the high temperatures reached by the devices and/or to the interaction of the plastic materials with the short-wavelength radiation emitted by the LEDs;
6. the browning of the phosphorous material (for white LEDs) as a consequence of high-temperature treatment.

These degradation mechanisms can be triggered or accelerated by the current flowing in the active region of the devices, by the high temperatures reached during operation, or by exposure to reverse-bias or to ESD events. All these factors can be present during the normal operation of an LED.

2.13.1 The increase of nonradiative recombination centers

Among the causes, that involve a decrease of the optical output power, there is the increment of nonradiative centers that renders a minor number of radiative recombinations and a lowering of the internal quantum efficiency. The mechanisms responsible of the nonradiative centers increment are surely accentuated during a high temperature operation, but are demonstrated to be present even during a normal low-current operation, so it is very important to understand the involved dynamics, in order to design the right improvements to this technology. The effects of this degradation can be clearly observed both by I-V and L-I measurements: as a matter of fact, the generation of defects within the active region can leads to an increase of the parallel resistance of the diode and to a lowering of the optical power for low current densities as well.

Observing the L-I relation it is possible to point out the creation of the nonradiative centers, since the nonradiative processes commonly prevail for low currents injections over the radiative ones, and the total light output is affected by their increment. Nonetheless the nonradiative recombination paths can saturate for high current injection, and their effect on the overall light output is limited.

The creation of nonradiative centers has been noticed to be current-activated, thus a great current flow towards the active layer can induce the diffusion of defects in there and the generation of nitrogen vacancies in the whole active region. These imperfections represent a discontinuity in the regular semiconductor lattice and they promote the nonradiative decays.

2.13.2 The ohmic contacts worsening

The increase of the serial resistance, or in general a significant change of the electrical properties can be related to a degradation of the electrical bondings of the LED chip: this is noticed both by an increase of the operating voltage and by a complexive lowering of the optical power. The electrical characteristics significantly change during a high temperature or high current operation, and these can influence the chip structure in several ways, like increasing the resistivity of the metal-semiconductor contacts and of the p-type neutral regions, or worsening the current distribution over the active region due to current crowding effects.

The high-temperature operation of the chip can increase the chemical interaction between Mg-acceptor atoms and Hydrogen which involves a lowering of the effective carrier concentration, the increase of resistivity of the metal-semiconductor interface and of the p-type neutral region, together with a broadening of the Schottky barrier at the p-type ohmic contact. All these effects can lead to a general worsening of the current distribution over the active region, with the subsequent lowering of the current injection inside the active layer and the lowering of the optical power. Since the release of Hydrogen is due to imperfections inside the lattice and is impoved by a high-temperature operation of the device, an improvement of the heterointerfaces is necessary to reduce the presence of hydrogen defects inside the semiconductor structure.

As well as the high temperature operation, high currents lead to a morphological degradation of the ohmic contacts: some works [7] reveal the detachment of the bondings as a consequence of high current conditions, that is probably due to a poor adhesion and/or to a thermal mismatch between different metal layers inside the chip.

2.13.3 The degradation of the chromatic properties

The luminous flux lowering is partially explained by the increase of nonradiative decays, while a more detailed analysis about the quality of the light can be conducted in order to quantify, for example, chromatic shifts or in general significant changes in the optical behaviour of the devices. The white LEDs are structured by a blue pumping LED chip below a yellow phosphors mix, in order to render a wider spectrum radiation. This double conformation obviously leads to a double degradation, as the blue LED can suffer of a lowering of its output power due to a worsening of the chip structure, and a yellow radiation decrease can be ascribed to a browning of the material used for the encapsulation of the phosphors/chip system, or to the pure worsening of the phosphors: both these elements contribute to a changing of the chromatic coordinates. Under exceptional degrading conditions this changing can lead to a radical variation of the perceived radiation color.

A worsening of the package itself is often caused by high temperatures operation, and consists in a partial carbonization of the rflective surface of the chip, which introduces a decrease of the light extraction efficiency and a complexive lowering of the efficiency of the device.

An overall worsening of the light output can be added by a degrading or browning of the epoxy lens over the chip, which in some cases is observed to be crashed. The parameters monitored in this work concerning the optical quality of the light are the x and y chromaticity coordinates, the CRI index and the CCT: the comments about the changing of these indexes are postponed to the presentation of the results.

CHAPTER 3

Devices

In this chapter we report the more relevant characteristics of the devices analyzed in this thesis work, taken from their respective datasheets. As a matter of fact, once the working of a common LED has been fully understood, it is important to see how its variants are implemented and what are their features. This descriptive chapter is important because it either provides a direct and practical application of the notions previously presented and it introduces the measurements applied and explained in the next chapters.

The market of high-power LEDs presents a large number of big and small manufacturers each of which has many types of devices in its catalog. The most reasonable procedure to select the LEDs to test is to refer to the most important manufacturers, whose products represent the state-of-the-art of modern LED technology and the basis on which the future devices will be developed. The six companies chosen are Cree, Philips Luxeon, Osram, Samsung, LG and Seoul Semiconductor Semiconductor. For the first three we have tested both color (blue, green and red/amber) and white devices, whereas for the last three only white LEDs. In particular the devices that have been analyzed are:

- CREE XLamp XP-E High-Efficiency White LEDs
- CREE XLamp XP-E color LEDs: Blue, Green and Red LEDs;
- OSRAM OSLON SSL 80: White, Blue and Reds LEDs ;

- OSRAM OSLON SX Green LEDs;
- PHILIPS LUXEON REBEL: White, Blue, Green and Reds LEDs;
- Samsung LH351A-3535 Ceramic White LEDs;
- LG 3535 Ceramic Type White LEDs;
- SEOUL SEMICONDUCTOR Z5M White LEDs;
- SEOUL SEMICONDUCTOR Z5P White LEDs.

3.1 CREE XLamp XP-E

3.1.1 CREE XLamp XP-E color LEDs

The XLamp XP-E LED, introduced in late 2008, continues Cree's history of innovation in LEDs for lighting applications with wide viewing angle, symmetrical package (3.45x3.45mm), unlimited floor life and electrically neutral thermal path. Cree XLamp LEDs bring high performance and quality of light to a wide range of lighting applications, including color-changing, portable and personal, outdoor, indoor-directional, transportation, stage and studio, commercial and emergency-vehicle lighting.

The devices is available in white, outdoor white, royal blue, blue, green, amber, red and red-orange. This LED is composed by the *EZ-Bright 1000* chip, mounted on a ceramic package sealed by a lens made with plastic materials.

In this work we have used blue, green and red devices, whose characteristics are reported below.

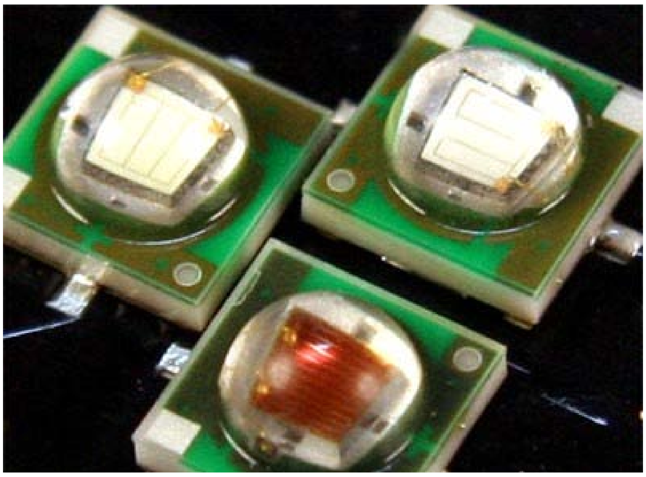

Figure 3.1: CREE XP-E color LEDs.

3.1.1.1 CREE XP-E Blue LED

The main characteristics of the CREE XP-E Blue, as given in the datasheet [8], have been reported in Table 3.1. This LED allows a maximum continuous current of 1A. Its nominal current is set to 350 mA, corresponding to a typical forward voltage drop of 3.2 V (at ambient temperature), thus dissipating approximately 1 watt. The current-voltage characteristic is shown in Figure 3.2. In Figure 3.3 (blue line) is reported the relative spectral power distribution of this device.

Typical luminous flux	30.6lm (350mA)
Dominant Wavelength Range	465-485nm (350mA)
Typical forward voltage	3.2V (350mA)
Maximum DC forward current	1A
Typical thermal resistance	9°C/W
Maximum junction temperature	150°C
Viewing angle (FWHM)	130°
Order Code	XPEBLU-L1-0000-00Y01

Table 3.1: Main features of CREE XP-E Blue LEDs.

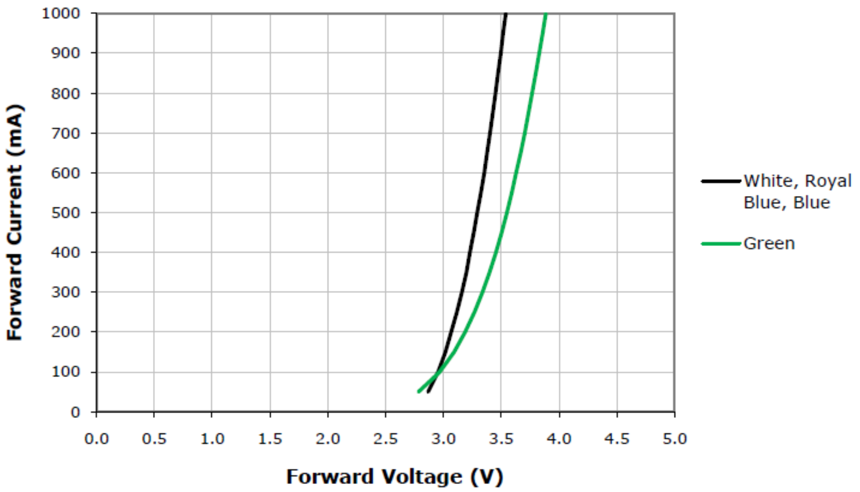

Figure 3.2: Current-voltage characteristics ($Tj = 25°C$) of CREE XP-E devices: White,Blue and Green LEDs.

3.1.1.2 CREE XP-E Green LED

Table 3.2 reports the main characteristics for the XP-E GREEN LED, that are very similar to those of the blue device. The current-voltage characteristic and the relative spectral power distribution are reported in Figure 3.2 and 3.3 (green line), respectively.

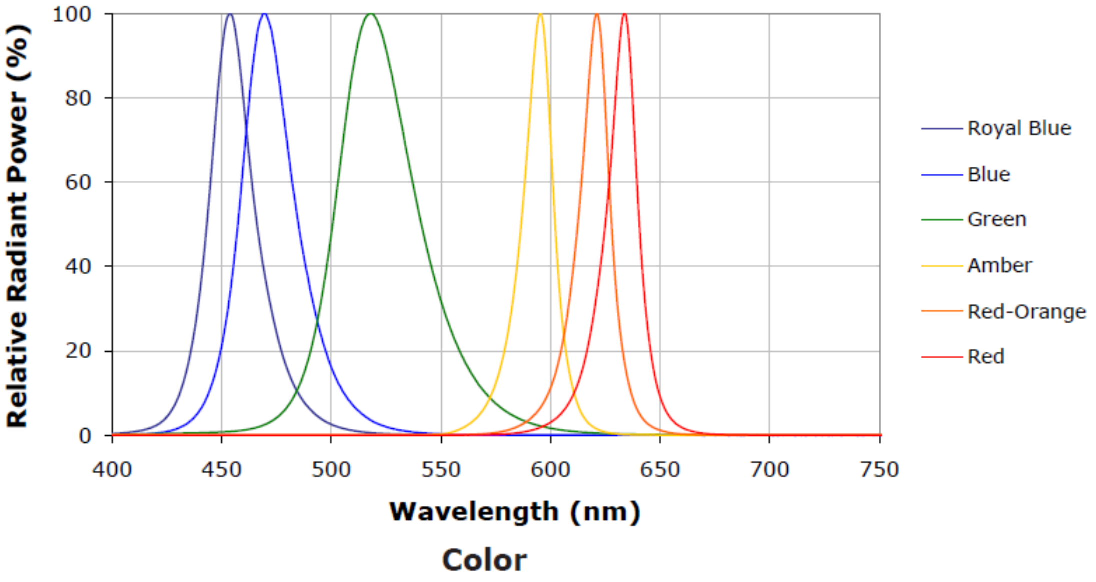

Figure 3.3: The relative spectrum intensity for the CREE XP-E color LEDs.

Typical luminous flux	80.6lm (350mA)
Dominant Wavelength Range	520-535nm (350mA)
Typical forward voltage	3.4V (350mA)
Maximum DC forward current	1A
Typical thermal resistance	15°C/W
Maximum junction temperature	150°C
Viewing angle (FWHM)	130°
Order Code	XPEGRN-L1-0000-00901

Table 3.2: Main features of CREE XP-E GREEN LEDs.

3.1.1.3 CREE XP-E Red LED

The key features of the CREE XP-E Red LED, as given in the datasheet [8], have been reported in Table 3.1. Unlike the previous, this LED allow a maximum continuous current of 700mA. Its nominal current is set to 350 mA, corresponding to a typical forward voltage drop of 2.4 V (at ambient temperature). The current-voltage characteristic of the device is shown in Figure 3.2. In Figure 3.3 (red line) is reported the relative spectral power distribution of this LED.

3.1.2 CREE XLamp XP-E High-Efficiency White LED

XLamp XP-E High Efficiency White LEDs extend the light output and efficacy of the XLamp XP-E LED family, enabling luminaire designs that use up to 50 percent fewer

Typical luminous flux	51.7lm (350mA)
Dominant Wavelength Range	620-630nm (350mA)
Typical forward voltage	2.1V (350mA)
Maximum DC forward current	700mA
Typical thermal resistance	10°C/W
Maximum junction temperature	150°C
Viewing angle (FWHM)	130°
Order Code	XPERED-L1-0000-00401

Table 3.3: Main features of CREE XP-E Red LEDs.

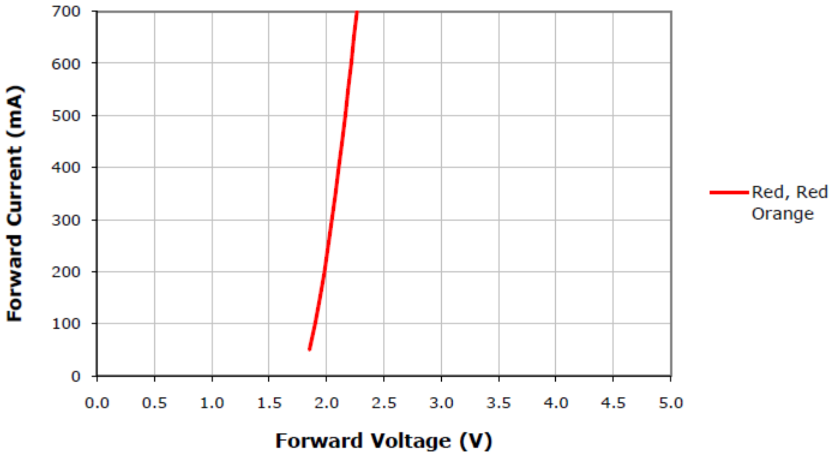

Figure 3.4: Current-voltage characteristics of CREE XP-E Red LED.

LEDs for a lower system cost.

XLamp XP-E High Efficiency White LEDs deliver up to 148 lumens in cool white (6500K) and 114 lumens in warm white (3000K) at 1W. In addition to light output and efficacy improvements, XP-E HEW LEDs feature a reduced thermal resistance of 6 °C/W. XP-E High Efficiency White LEDs are available in the same white variations as XP-E LEDs, including Standard White, Outdoor White and 80-CRI White. The one that has been used is the 80-CRI White.

In table 3.4 are reported the main characteristic of this devices, as given in the datasheet [9]. The current-voltage characteristic and the relative spectral power distribution of the device are shown in Figure 3.6.

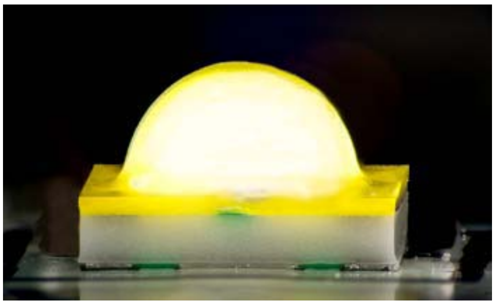

Figure 3.5: Picture of the CREE XP-E HEW LED.

Typical luminous flux	100lm (350mA)
CCT Range	2600-4300K
CRI	80 (min.)
Typical forward voltage	3V (350mA)
Maximum DC forward current	1A
Typical thermal resistance	6°C/W
Maximum junction temperature	150°C
Viewing angle (FWHM)	120°
Order Code	XPEHEW-H1-0000-00CE7

Table 3.4: Main features of CREE XP-E HEW LEDs.

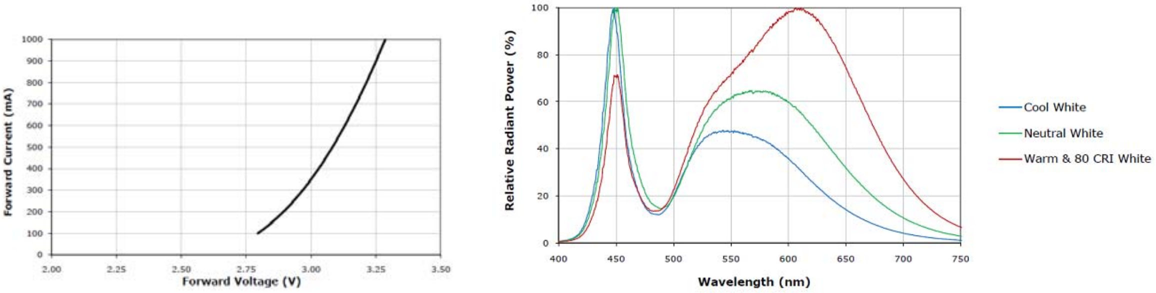

(a) (b)

Figure 3.6: a)Current-Voltage characteristics and b)relative spectral power distribution of CREE XPE HEW LED.

3.2 OSRAM OSLON SSL 80 and SX

3.2.1 OSRAM OSLON SSL 80

The OSRAM OSLON SSL LED is an exceptionally small light source (3x3mm) with a narrow radiation pattern that is designed to maximize application efficiencies. The design of the OSLON SSL is based on a joint package concept comprising a ceramic base with integrated contacts (bottom only-terminated) and a hard silicone cast as a lens (Figure 3.7). The ceramic base has the decisive advantage that it has stable degradation characteristics in regard to light, regardless of the wavelength. In addition, it has sufficiently good thermal conductivity and enables thermal connection to the p.c. board to be designed electrically neutral. The OSLON SSL 80 features an 80º viewing angle that delivers directed light with outstanding efficiency from an incredibly small source. This device is available in different color temperatures from 2700 to 6500 K and RGB-colors. Highly efficient semiconductor chips with the latest thin-film technology from OSRAM Opto Semiconductors are used as light sources in the OSLON SSL. The chip technology (ThinGaN or UX:3) uses the semiconductor material composition indium gallium nitride for the colors deep blue, true green and white, and the material composition aluminum indium gallium phosphides (ThinFilm) for the colors amber, yellow and red.

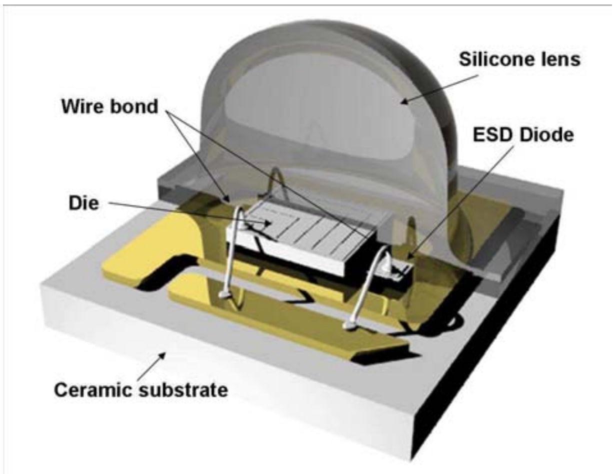

Figure 3.7: Construction of the OSLON SSL and OSLON Square product family (from [10]).

Here we report the principal characteristics of the devices analyzed in this work.

3.2.1.1 OSLON SSL 80 Warm White LED

Compared to the white LEDs of the other manufacturers, this device is characterized by the highest CRI, typical 95, obtained using a multi-phosphor approach. The main characteristics of the device, as given in the datasheet [11], have been reported in Table 3.5. The current-voltage characteristic and the relative spectral emission of the device are reported in Figure 3.9.

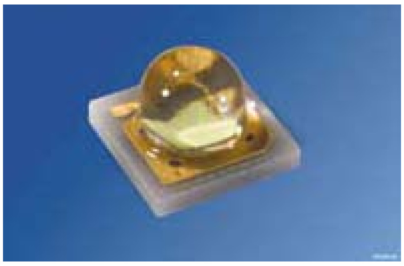

Figure 3.8: Picture of the OSLON SSL 80 Warm White LED.

Typical luminous flux	71-89.2 lm (350mA)
CCT	3000K
CRI	95 (typ.)
Typical forward voltage	3.2V (350mA)
Maximum DC forward current	800mA
Typical thermal resistance	7°C/W
Maximum junction temperature	125°C
Viewing angle (FWHM)	80°
Technology	ThinGaN
Order Code	LCW CQ7P.CC-KPKR-5R8T

Table 3.5: Principal characteristics of OSLON SSL 80 Warm White LED.

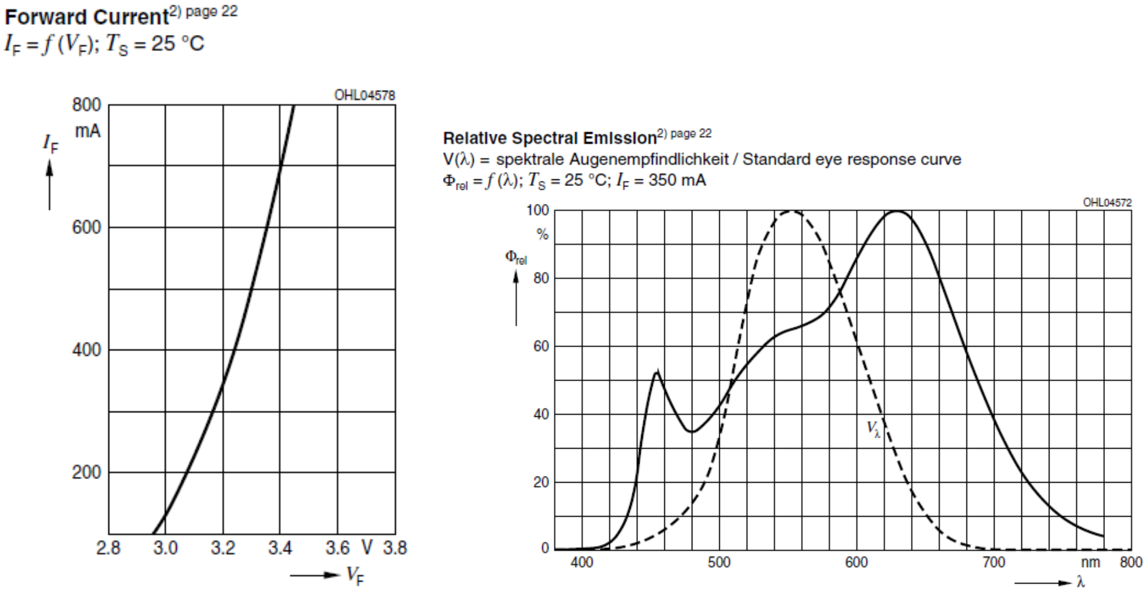

(a)

(b)

Figure 3.9: a)Current-Voltage characteristics and b)relative spectral power distribution of OSRAM OSLON SSL 80 Warm White LED.

3.2.1.2 OSRAM OSLON SSL 80 Blue LED

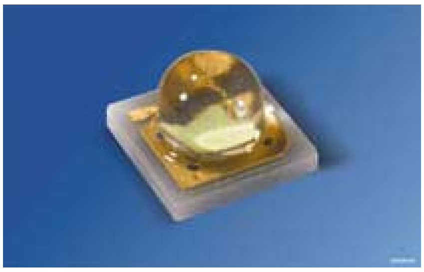

Figure 3.10: Picture of the OSLON SSL 80 Blue LED.

The key features of the OSLON SSL 80 Blue LED, as reported in the datasheet [12], have been listed in Table 3.6. In Figure 3.11 are shown the current-voltage characteristic and the relative spectral emission of this LED.

Typical luminous flux	21-39 lm (350mA)
Dominant Wavelength Range	464-476nm (350mA)
Typical forward voltage	3.2V (350mA)
Maximum DC forward current	1A
Typical thermal resistance	7°C/W
Maximum junction temperature	135°C
Viewing angle (FWHM)	80°
Technology	InGaN
Order Code	LB CP7P-GYHY-35

Table 3.6: Principal characteristics of OSLON SSL 80 Blue LED.

3.2.1.3 OSRAM OSLON SSL 80 Amber LED

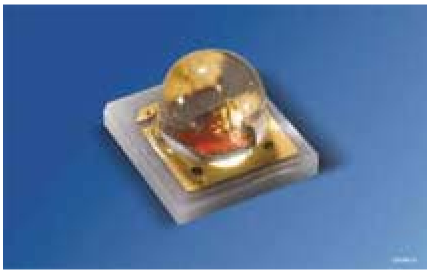

Figure 3.12: Picture of the OSLON SSL 80 Red LED.

Table 3.7 reports the main characteristics for the OSLON SSL 80 Amber LED [13]. The current-voltage characteristic and the relative spectral power distribution are reported in Figure 3.13.

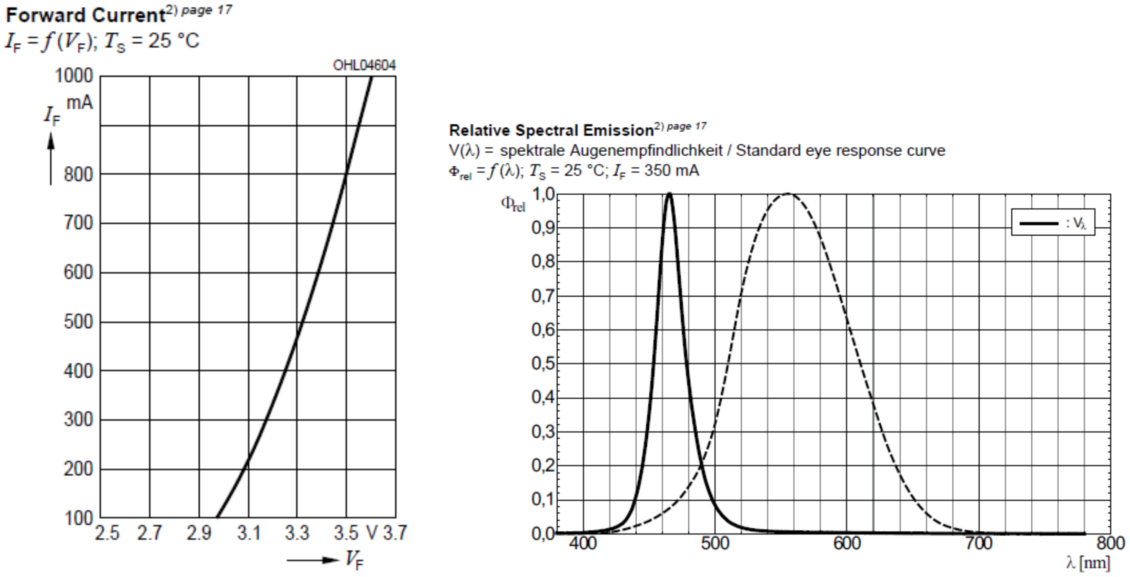

(a) (b)

Figure 3.11: a)Current-Voltage characteristics and b)relative spectral emission of OSRAM OSLON SSL 80 Blue LED.

Typical luminous flux	45-82 lm (400mA)
Dominant Wavelength Range	612-625nm (400mA)
Typical forward voltage	2.2V (400mA)
Maximum DC forward current	1A
Typical thermal resistance	7°C/W
Maximum junction temperature	125°C
Viewing angle (FWHM)	80°
Technology	AlInGaN
Order Code	LA CP7P-JXKX-24

Table 3.7: Principal characteristics of OSLON SSL 80 Amber LED.

3.2.2 OSRAM OSLON SX

The OSRAM OSLON SX LED delivers directed light with outstanding efficiency from an incredibly small source. The OSRAM OSLON SX is a 3x3 mm device mounted in a new LED ceramic package specially engineered to enable slim and compact lighting designs, with silicone resin and lens. The OSRAM OSLON SX is highly bright, lasts at least 50,000 hours, and provides a 60º focused beam ideal for signal and warning lights. This reliable lighting solution allows for cost-efficient, resource-saving designs with fewer LEDs and fewer and smaller peripheral components. The device is available in amber, deep blue, true green, ultra white, and yellow. For our purpose we have used only the true green LED, whose characteristic are reported below.

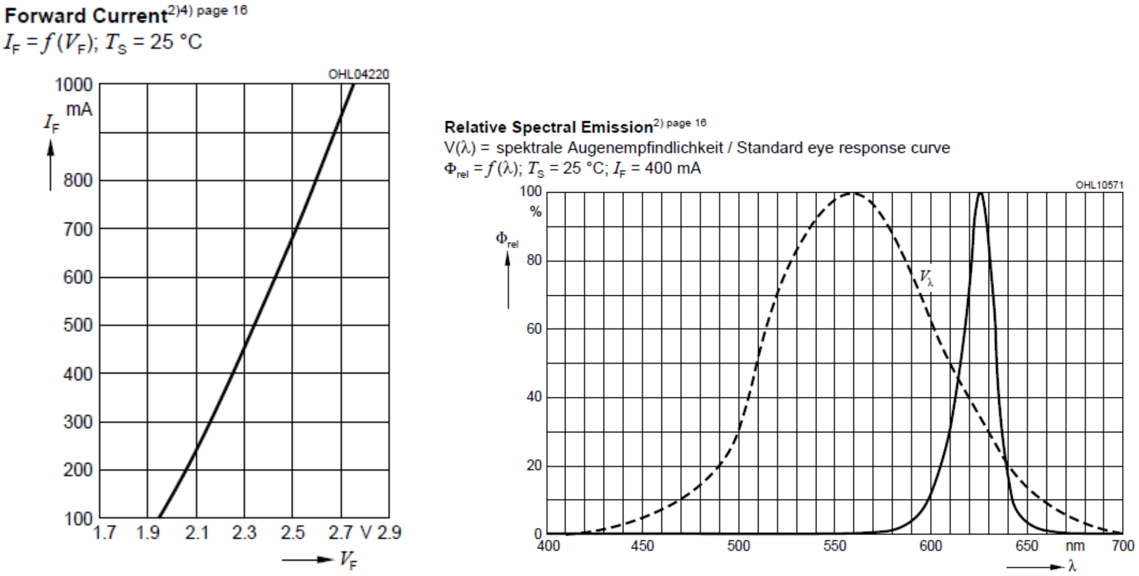

(a) (b)

Figure 3.13: a)Current-Voltage characteristics and b)relative spectral emission of OSRAM OSLON SSL 80 Amber LED.

3.2.2.1 OSRAM OSLON SX GREEN LED

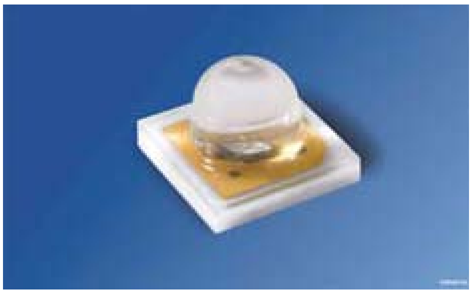

Figure 3.14: Picture of the OSLON SX Green LED.

The main characteristics of the OSLON SX Green LED, as given in the datasheet [14], have been reported in Table 3.8. This LED allows a maximum continuous current of 250mA. Its nominal current is set to 140 mA, corresponding to a typical forward voltage drop of 3.3 V (at ambient temperature). The reported thermal resistance from junction to solder point is $R_{thj-sp} = 27K/W$, which is very high compared to the others probably because of the reduced dimensions of the device, that is certainly the smallest among the ones considered in this work. The current-voltage characteristic and the relative spectral power distribution of the device are shown in Figure 3.15.

Typical luminous flux	18-45 lm (140mA)
Dominant Wavelength Range	513-543nm (140mA)
Typical forward voltage	3.3V (140mA)
Maximum DC forward current	250mA
Typical thermal resistance	27°C/W
Maximum junction temperature	150°C
Viewing angle (FWHM)	60°
Technology	ThinGaN
Order Code	LT CN5M-GAHB-25-1

Table 3.8: Main features of OSLON SX Green LED.

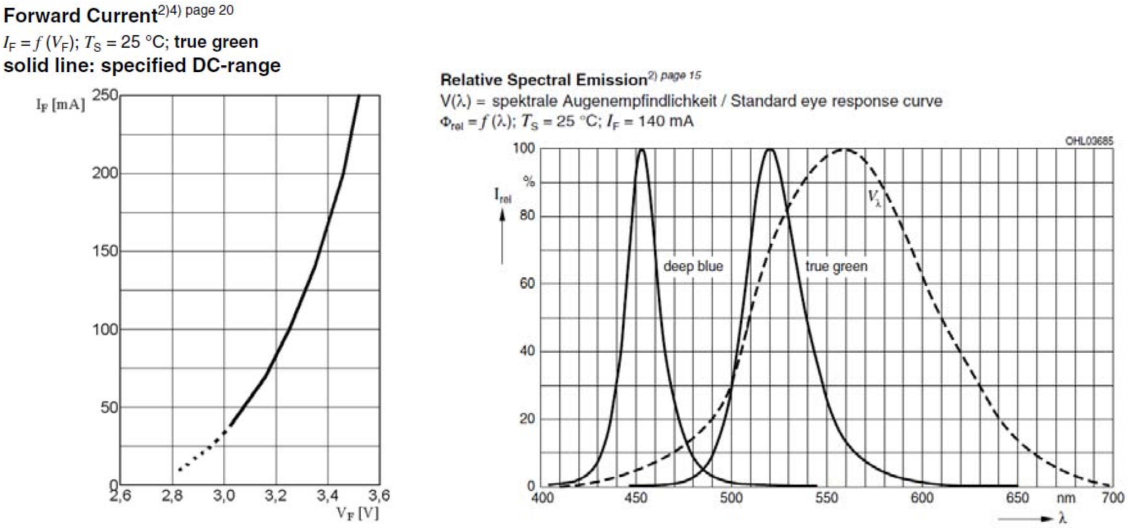

(a) (b)

Figure 3.15: a)Current-Voltage characteristics and b)relative spectral emission of OSRAM OSLON SX Green LED.

3.3 PHILIPS LUXEON Rebel

The LUXEON Rebel devices, described by the manufacturer as the most widely used power LED today, are ultracompact (just 3x4.5mm), surfacemount, highpower LEDs that deliver elevated standards for light output, flux density and manufacturability. LEDs from the LUXEON Rebel White Portfolio are available in a number of CCT/CRI combinations, different flux and CCT ranges. LUXEON Rebel Direct Color Portfolio and Phosphor Converted colors are available in a wide range of colors. Both white and colored LEDs share the same footprint making it easy to mix LUXEON Rebel LEDs to get the exact lighting effect desired.

The fundamental packaging philosophy of LUXEON Rebel attaches the LED chip

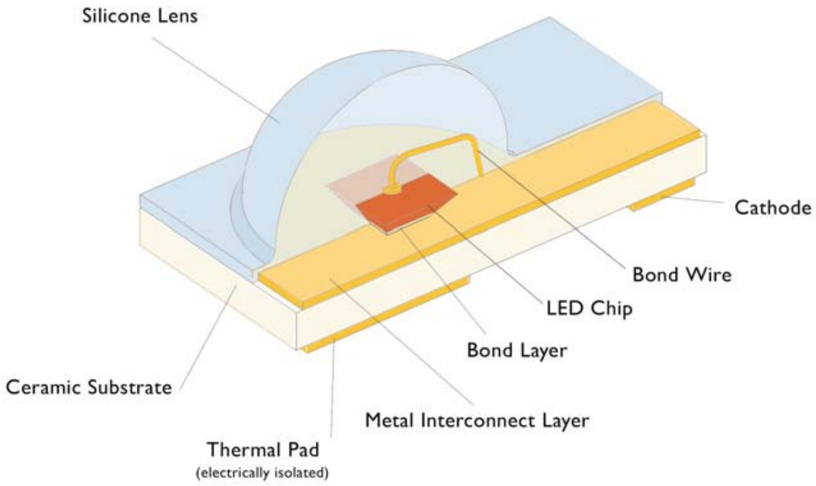

Figure 3.16: Internal construction of the AlInGaP LUXEON Rebel package.

to a metallized ceramic substrate that provides a high efficiency thermal path to extract heat from the active region of the LED. Metal pads on the underside of the ceramic substrate are designed to be reflow soldered to printed circuit pads with high thermal conductivity, which in turn conduct the heat generated within the LED chip to an external heatsink. Hence, the LUXEON Rebel has a 3-pad package comprising an anode pad, a cathode pad and an electrically insulated thermal pad. The primary electrical connections from the LED chip are connected to the anode and cathode pads. On the top of the package is a soft, clear silicone lens.

Two different LED fabrication technologies are used in the LUXEON Rebel product family. The red, red-orange, and amber LUXEON Rebel packages use Aluminum Indium Gallium Phosphide (AlInGaP) chip technology. The white, green, cyan, blue and royal blue LUXEON Rebel packages use Indium Gallium Nitride (InGaN) chip technology. These two distinct fabrication technologies require somewhat different packaging.

Figure 3.16 illustrates the internal construction of the AlInGaP LUXEON Rebel package. The LED chip is bonded to the metallized ceramic substrate using a high-temperature, Pb-free eutectic bond. Note that AlInGaP LUXEON Rebel has the cathode on the top of the die, which is connected to the metallized ceramic substrate using a gold wire. A clear silicone lens is molded over the LED chip and gold wire.

Figure 3.17 illustrates the internal construction of the InGaN LUXEON Rebel package. Note that the LED chip is mounted on top of the metallized ceramic substrate

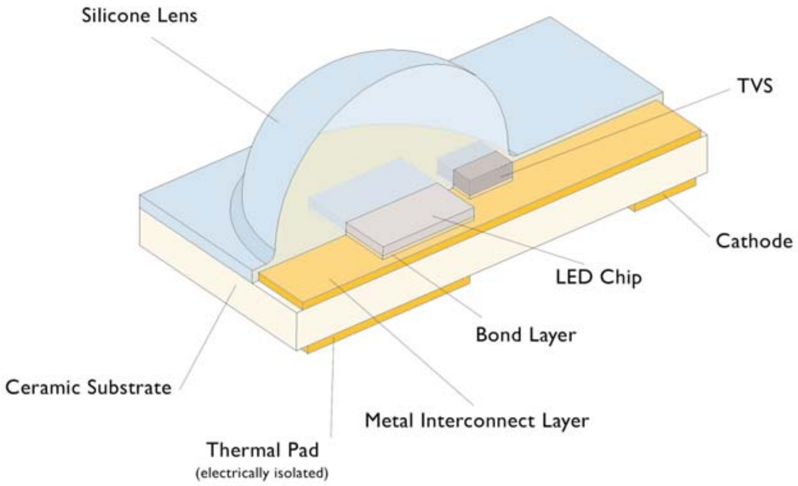

Figure 3.17: Internal construction of the InGaN LUXEON Rebel package.

using gold to gold interconnects. A separate silicon chip is also mounted on the metallized ceramic substrate. This chip protects the LED chip from electrostatic discharge (ESD). A clear silicone lens is molded over the LED and silicon chips.

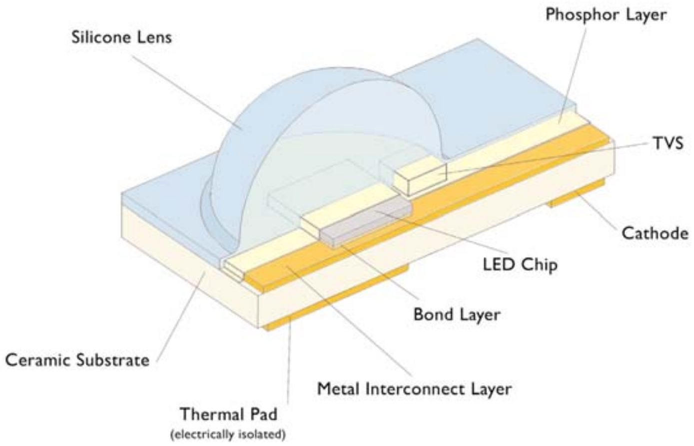

Figure 3.18: Internal construction of the white LUXEON Rebel package.

Figure 3.18 illustrates the internal construction of the white LUXEON Rebel package. A white LUXEON Rebel uses a blue InGaN chip. Then a yellow phosphor conformal coating is applied over the LED chip.

The main features of the devices analyzed in this work are reported in the next sections.

3.3.1 LUXEON Rebel White LED

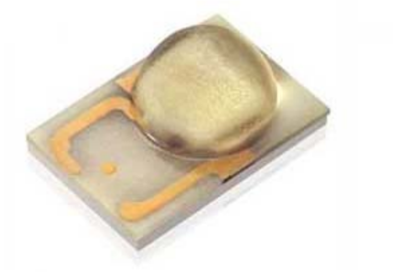

Figure 3.19: LUXEON Rebel White LED.

The key features of the LUXEON Rebel White LED, as reported in the datasheet [15], have been listed in Table 3.9. In Figure 3.20 are shown the current-voltage characteristic and the relative spectral power distribution of this LED.

Typical luminous flux	66 lm (350mA)
CCT Range	2870-3220K
CRI	85 (typ)
Typical forward voltage	3V (350mA)
Maximum DC forward current	1A
Typical thermal resistance	10°C/W
Maximum junction temperature	150°C
Viewing angle (FWHM)	120°
Technology	InGaN
Order Code	LXM3-PW71

Table 3.9: Main features of the LUXEON Rebel White LED.

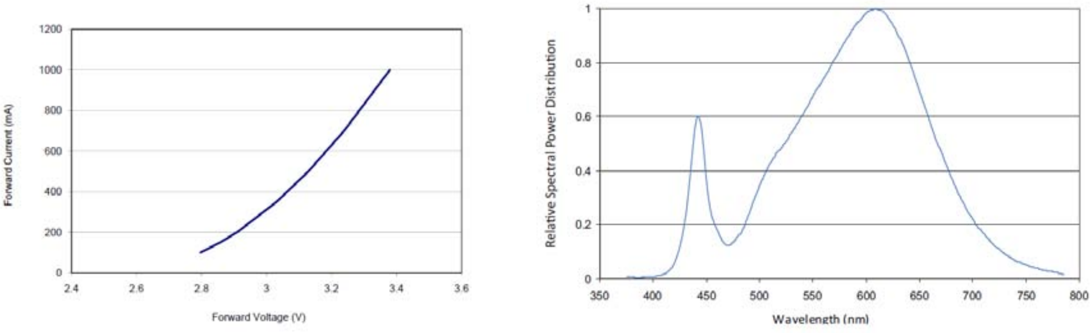

(a) (b)

Figure 3.20: a)Current-Voltage characteristics and b)relative spectral power distribution of LUXEON Rebel White LED.

3.3.2 LUXEON Rebel Blue LED

Figure 3.21: Picture of the LUXEON Rebel Blue LED.

Table 3.10 reports the principal characteristics for the LUXEON Rebel Blue LED [15]. The I-V characteristic is shown in Figure 3.22. In Figure 3.24 (blue line) is reported the relative spectral power distribution of this device.

Typical luminous flux	28lm (350mA)
Dominant Wavelength range	460-480nm (350mA)
Typical forward voltage	2.95V (350mA)
Maximum DC forward current	1A
Typical thermal resistance	10°C/W
Maximum junction temperature	150°C
Viewing angle (FWHM)	125°
Technology	InGaN
Order Code	LXML-PB01-0023

Table 3.10: Principal characteristics for the LUXEON Rebel Blue LED.

3.3.3 LUXEON Rebel Green LED

The main properties of the OSLON SX Green LED, as given in the datasheet [16], have been reported in Table 3.11. The current-voltage characteristic and the relative spectral power distribution are reported in Figure 3.22 and 3.24 (green line), respectively.

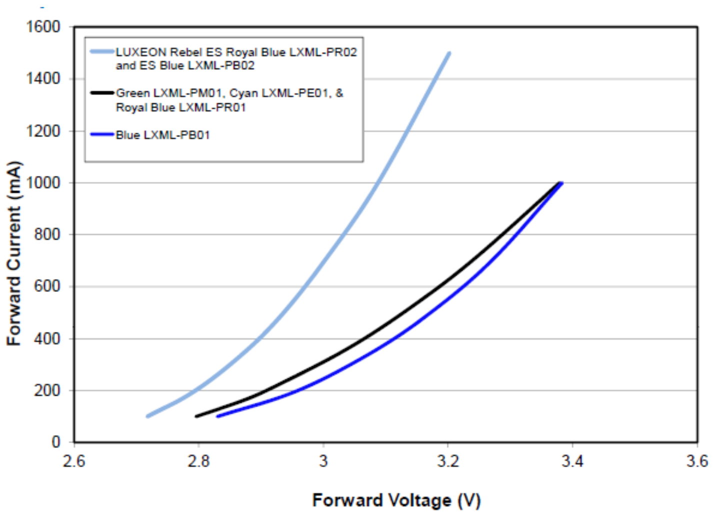

Figure 3.22: Forward current vs. forward voltage for green, blue, royal blue LEDs.

Figure 3.23: Luxeon Rebel Green LED.

Typical luminous flux	102lm (350mA)
Dominant Wavelength range	520-540nm (350mA)
Typical forward voltage	2.9V (350mA)
Maximum DC forward current	1A
Typical thermal resistance	10°C/W
Maximum junction temperature	150°C
Viewing angle (FWHM)	125°
Technology	InGaN
Order Code	LXML-PM01-0100

Table 3.11: Principal characteristics for the LUXEON Rebel Green LED.

3.3.4 LUXEON Rebel RED LED

The key features of the LUXEON Rebel Red LED are listed in Table 3.1. Unlike the previous, this LED allows a maximum continuous current of 700mA. Moreover it presents an higher thermal reisistance and a maximum junction temperature of 135°C,

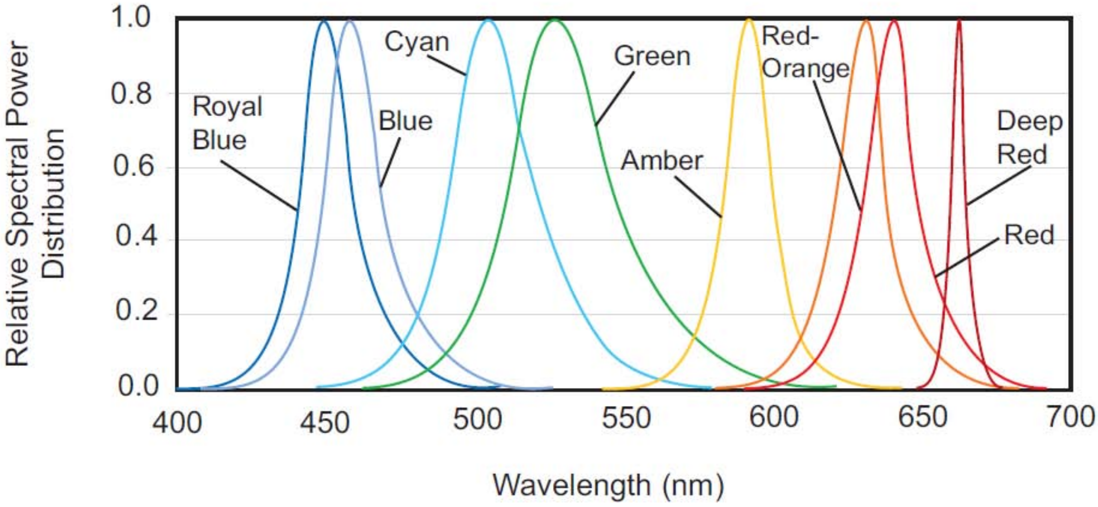

Figure 3.24: Relative intensity vs. wavelength of LUXEON Rebel Color Portfolio LEDs.

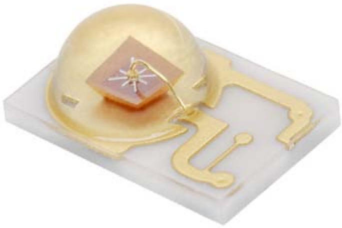

Figure 3.25: Luxeon Rebel Green LED.

which is lower compared to the others of the same manufacturer. The current-voltage characteristic of the device is shown in Figure 3.26. The linear trend of this plots is probably due to an high parasitic serial resistance. In Figure 3.24 (red line) is reported the relative spectral power distribution for this LED.

3.4 Samsung LH351A-3535

The LH351A-3535 ceramic SMD LED by Samsung is an extremely efficient SMD Power-LED with a luminosity of up to 448 lumens and a good color rendering index of at least 80. The ceramic package provides effective heat dissipation and low thermal resistance. The application areas are enormously diverse, ranging from lighting of individual objects to the illumination of entire areas. The principal characteristics for the device used in this work are reported in table 3.13. Figure 3.28 shows the I-V characteristic and the spectrum distribution of this LED.

Typical luminous flux	46lm (350mA)
Dominant Wavelength range	620-645nm (350mA)
Typical forward voltage	2.9V (350mA)
Maximum DC forward current	700mA
Typical thermal resistance	12°C/W
Maximum junction temperature	135°C
Viewing angle (FWHM)	125°
Technology	AlInGaP
Order Code	LXML-PD01-0040

Table 3.12: Principal characteristics for the LUXEON Rebel Red LED.

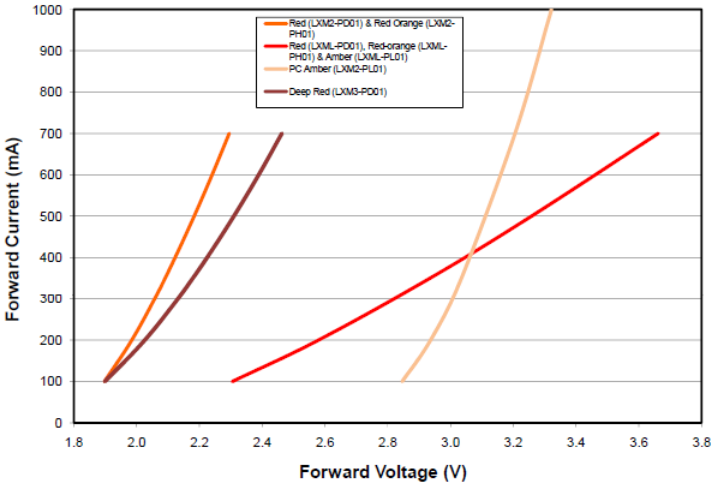

Figure 3.26: Forward current vs. forward voltage for red, deep red, red-orange, amber, and PC amber.

Typical luminous flux	110lm (350mA)
CCT	3000K
CRI	80 (min.)
Typical forward voltage	2.95V (350mA)
Maximum DC forward current	1.5A
Typical thermal resistance	4°C/W
Maximum junction temperature	150°C
Viewing angle (FWHM)	125°
Order Code	SPHWHTL3D305E6V0H3

Table 3.13: Principal characteristics for Samsung LH351A-3535 (from [17]).

Figure 3.27: Picture of the Samsung LH351A-3535.

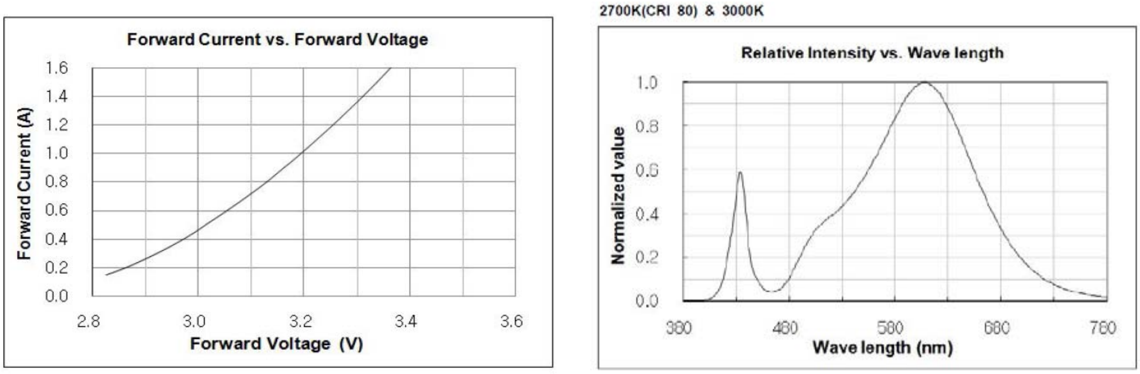

(a)

(b)

Figure 3.28: a)Current-Voltage characteristics and b)spectrum distribution of Samsung LH351A-3535.

3.5 LG 3535 Ceramic Type White LED

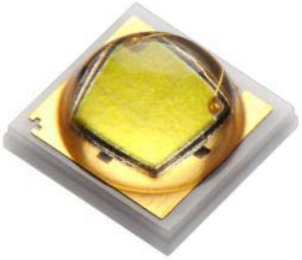

Figure 3.29: LG 3535 Ceramic Type White LED

Figure **??** shows the I-V characteristc and the relative spectrum of the device tested in this work.

Typical luminous flux	92-122lm (350mA)
CCT	2700K
CRI	80 (min.)
Typical forward voltage	2.98V (350mA)
Maximum DC forward current	1.5A
Typical thermal resistance	6°C/W
Maximum junction temperature	150°C
Viewing angle (FWHM)	112°
Technology	InGaN
Order Code	LEMWA33X80MW00

Table 3.14: Principal characteristics for LG 3535 Ceramic Type White LED (from [18]).

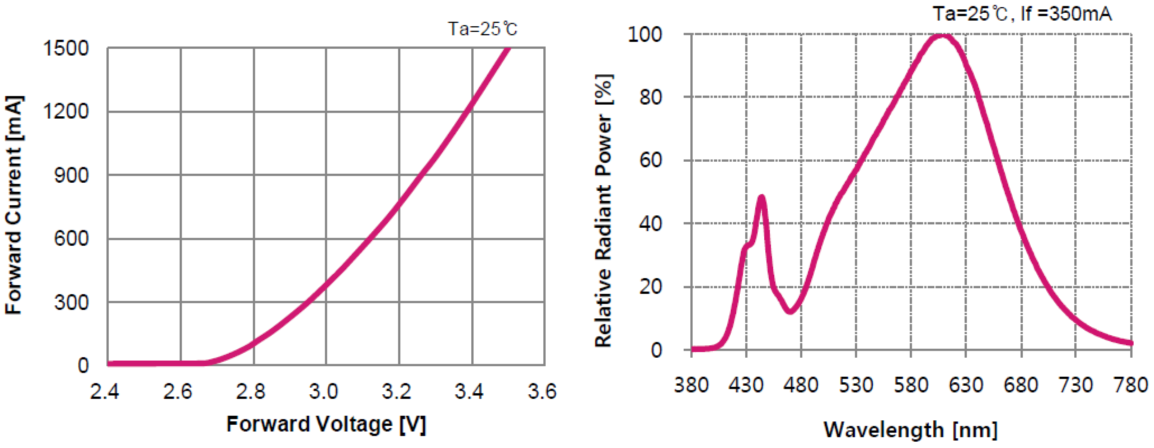

(a) (b)

Figure 3.30: a)Current-Voltage characteristics and b)spectrum distribution of the LG 3535 White LED.

3.6 SEOUL Z Power White LED

Seoul Semiconductor Z5 Power Series LEDs are designed for high current operation and high flux output applications. Z5 LEDs incorporate state of the art SMD design and thermal emission material. These Seoul Semiconductor power LEDs are ideal for light sources for general applications, custom-designed solutions, and automotive large LCD backlights. The Z5 series has a very small size (3.5x3.5x2.0mm, it is designed to fit on the Cree XPE footprint), a ceramic-based package, and a large radiation plate that make heat management easy. The Z5 series includes the Z5, Z5P and the Z5M devices. The Z5 has the smallest LED die at 1.0*1.0mm and can be driven up to

700mA. The Z5P has a 1.2*1.2mm LED die and can be driven up-to 1A. The Z5M has the Seoul Semiconductors largest LED die inside, it measures 1.4*1.4mm and can be driven up to 1.2A. The Seoul Semiconductor Z5 series includes white, red, green, and blue color options.

Here we report a brief description of the devices used in this work.

3.6.1 SEOUL Z5M White LED

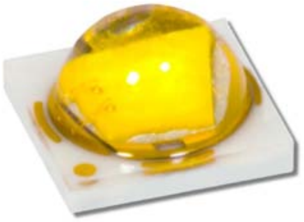

Figure 3.31: Picture of the SEOUL Z5M White LED.

The main properties of the SEOUL Z5M White LED, as given in the datasheet [19], are listed in Table 3.15. The current-voltage characteristics and the relative spectral power distribution are reported in Figure 3.32.

Typical luminous flux	116lm (350mA)
CCT	3000K
CRI	80 (min.)
Typical forward voltage	3.1V (350mA)
Maximum DC forward current	1.2A
Typical thermal resistance	4.5°C/W
Maximum junction temperature	145°C
Viewing angle (FWHM)	120°
Order Code	SSC-SZ5-M0-WW-C8

Table 3.15: Principal characteristics for SEOUL Z5M White LED.

3.6.2 SEOUL Z5P White LED

Table 3.10 reports the principal characteristics for the SEOUL Z5P White LED, while Figure 3.34 shows the I-V characteristics and the relative spectrum of the device.

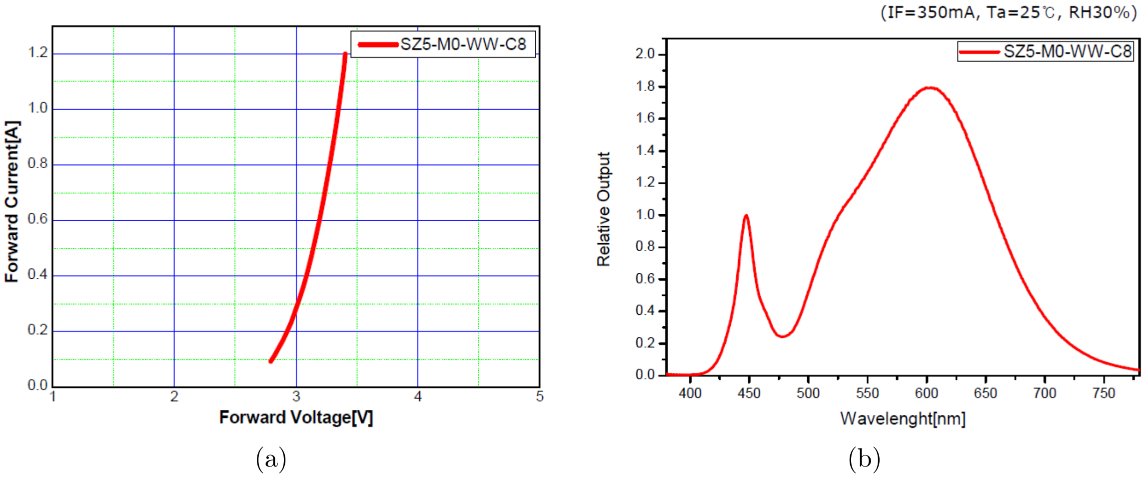

(a) (b)

Figure 3.32: a)Current-Voltage characteristics and b)spectrum distribution of SEOUL Z5M.

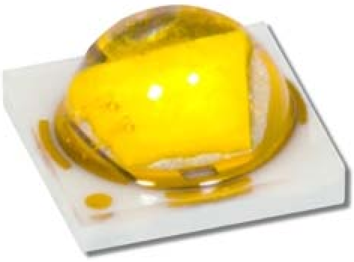

Figure 3.33: SEOUL Z5P White LED.

Typical luminous flux	112lm (350mA)
CCT	3000K
CRI	80 (min.)
Typical forward voltage	3.2V (350mA)
Maximum DC forward current	1A
Typical thermal resistance	5.5°C/W
Maximum junction temperature	145°C
Viewing angle (FWHM)	120°
Order Code	SSC-SZ5-M0-WW-C8

Table 3.16: Principal characteristics for SEOUL Z5P White LED (from [20]).

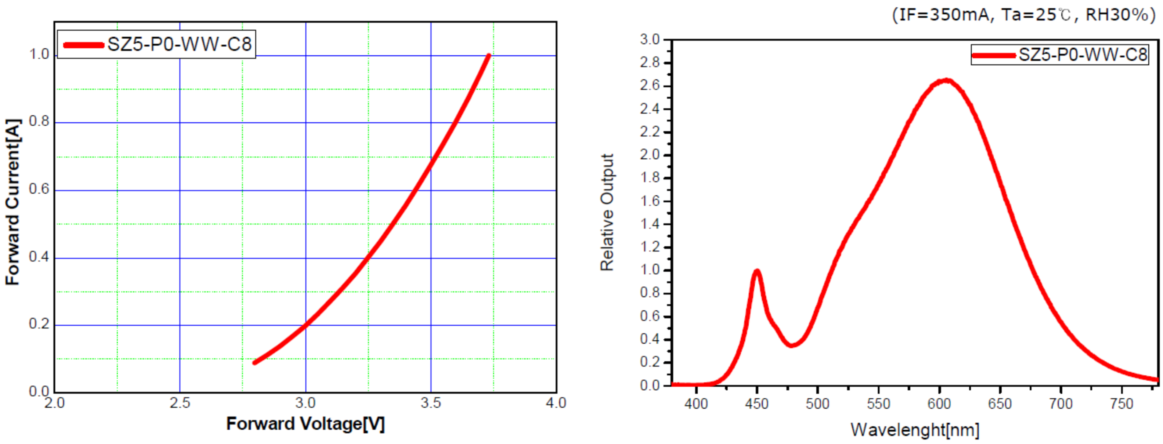

(a) (b)

Figure 3.34: a)Current-Voltage characteristics and b)spectrum distribution of SEOUL Z5P.

3.7 Summary

In this section we report a comparison between the characteristics of the LEDs of the various manufacterers . In particular, we report, for each color, the I-V characteristics, the spectra, the optical power (luminous flux) and the efficiency for the different manufacturers.

3.7.1 Blue LEDs

	Flux (lm, nominal current)	Voltage (V, nominal current)	$R_{thJ-SP}(W/K)$	T_{jmax}(°C)	$I_{max}(A)$
XP-E	30.6	3.2	9	150	1
OSLON	21-39	3.2	7	135	1
REBEL	28	2.95	10	125	1

Table 3.17: Comparison between the characteristics of the blue LEDs, as reported in their respective datasheets.

Observing Figure 3.35, we can note the XP-E device emits the highest optical power and presents also the highest efficiency.

3.7.2 Red LEDs

	Flux (lm, nominal current)	Voltage (V, nominal current)	$R_{thJ-SP}(W/K)$	T_{jmax}(°C)	$I_{max}(A)$
XP-E	51.7	2.1	10	150	0.7
OSLON	45-82	2.2	7	125	1
REBEL	46	2.9	12	125	0.7

Table 3.18: Comparison between the characteristics of the red LEDs, as reported in their respective datasheets.

Even in this case, Figure 3.36 shows that the XP-E device emits the highest optical power and presents also the highest efficiency. However in this case the worst efficiency is presented by the REBEL LED, probably due the high series resistance of this device as showed in 3.36 a).

3.7.3 Green LEDs

Observing Figure 3.37, we can note the REBEL device shows the highest values of luminous flux and luminous efficiency. However at high current injection the XP-E values of luminous flux are very to the ones shown by the REBEL LED. The OSLON

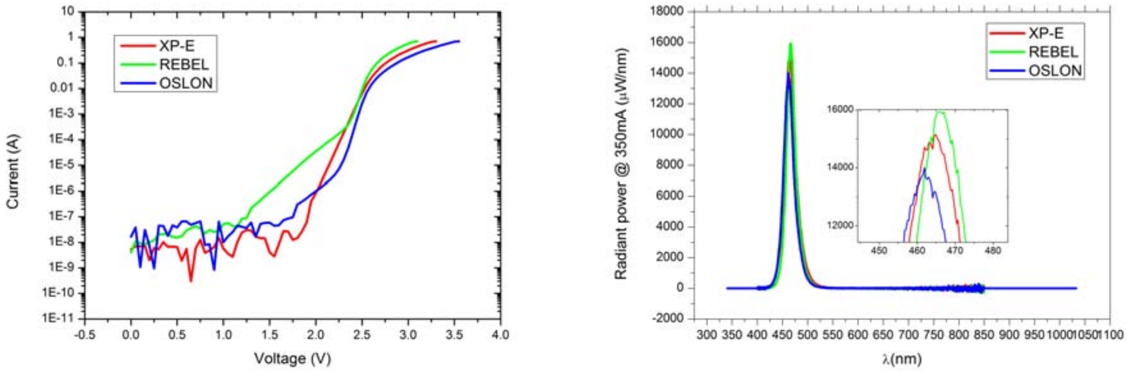

(a) I-V characteristics

(b) Spectra

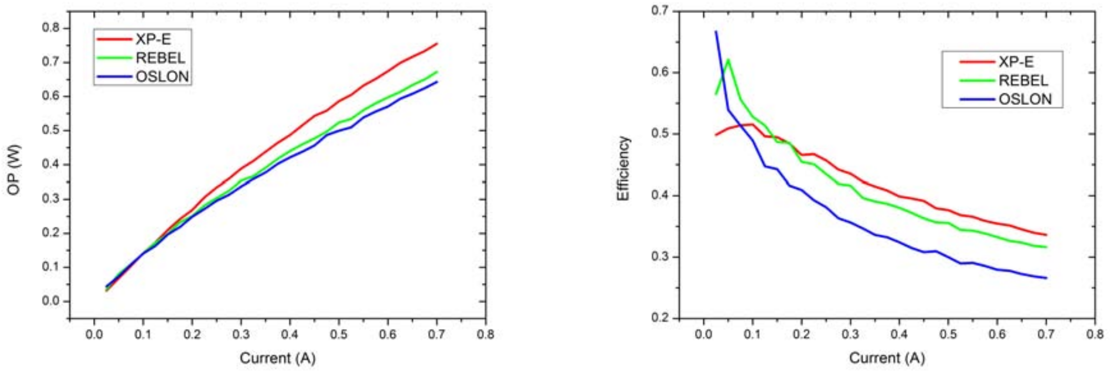

(c) Optical Power-Current

(d) Efficiency-Current

Figura 3.35: Characteristics of the blue LEDs.

device is the samallest among the ones considered in this work. This explains the very low values of luminous flux and maximum current of this device.

3.7.4 White LEDs

Observing Figure 3.38, we can note the Samsung LED shows the highest values of luminous flux and luminous efficiency (at high current values). However the XP-E, LG ans SEOUL M devices show values very similar to it. Even in this case, the OSLON device shows the worst values of luminous flux and efficiency. Nevertheless it present the highest value of CRI, obtained using a multi-phosphor approach.

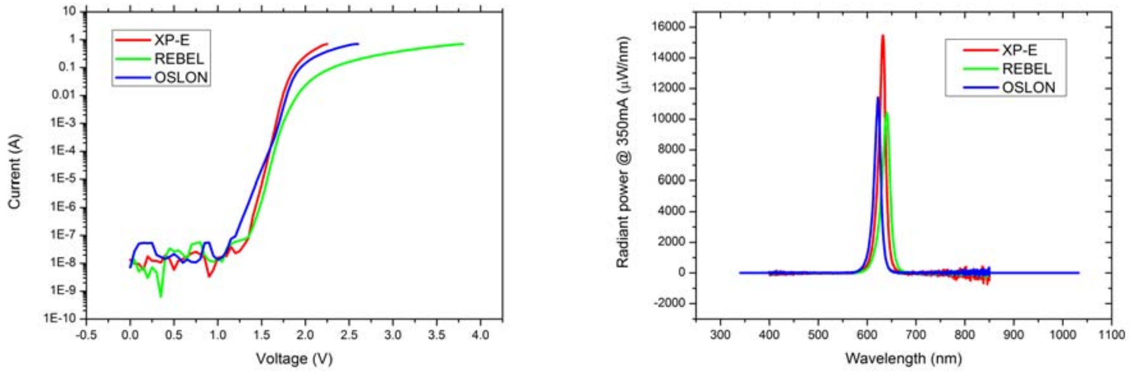

(a) I-V characteristics

(b) Spectra

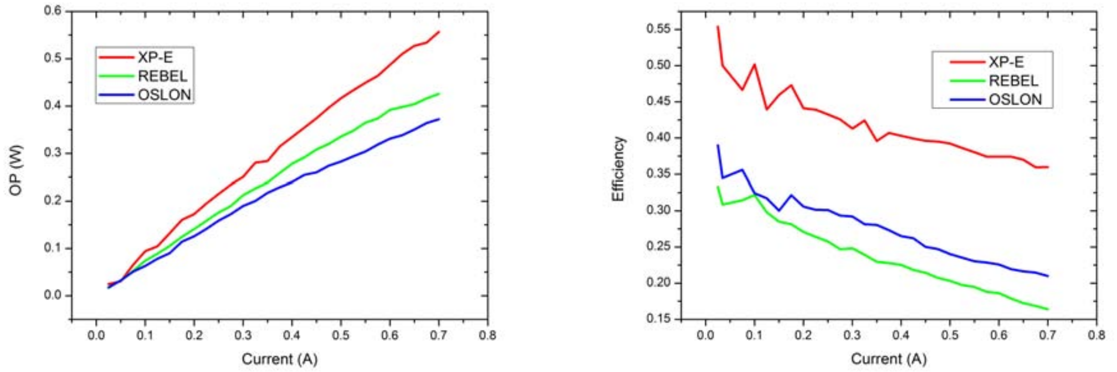

(c) Optical Power-Current

(d) Efficiency-Current

Figura 3.36: Characteristics of the red LEDs.

	Flux (lm, nominal current)	Voltage (V, nominal current)	$R_{thJ-SP}(W/K)$	T_{jmax}(°C)	$I_{max}(A)$
XP-E	80.6	3.4	15	150	1
OSLON	18-45	3.3	27	150	0.25
REBEL	102	2.9	10	150	1

Table 3.19: Comparison between the characteristics of the green LEDs, as reported in their respective datasheets.

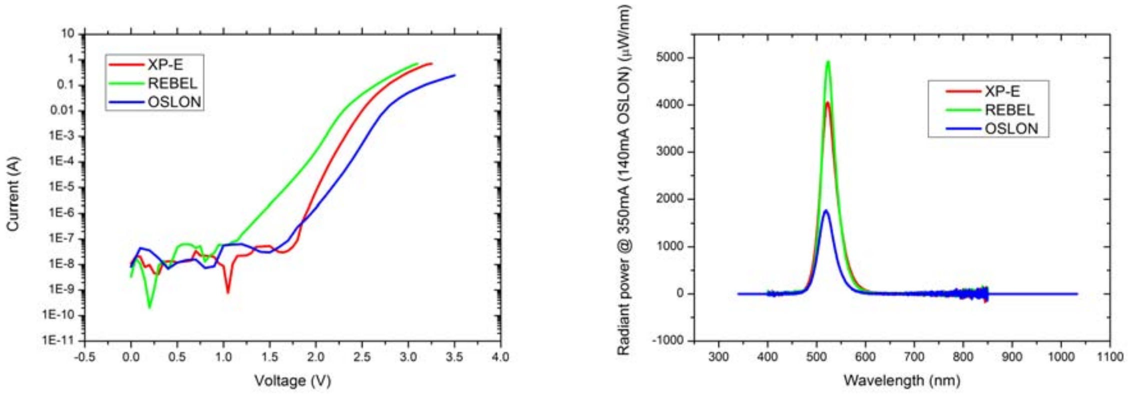

(a) I-V characteristics (b) Spectra

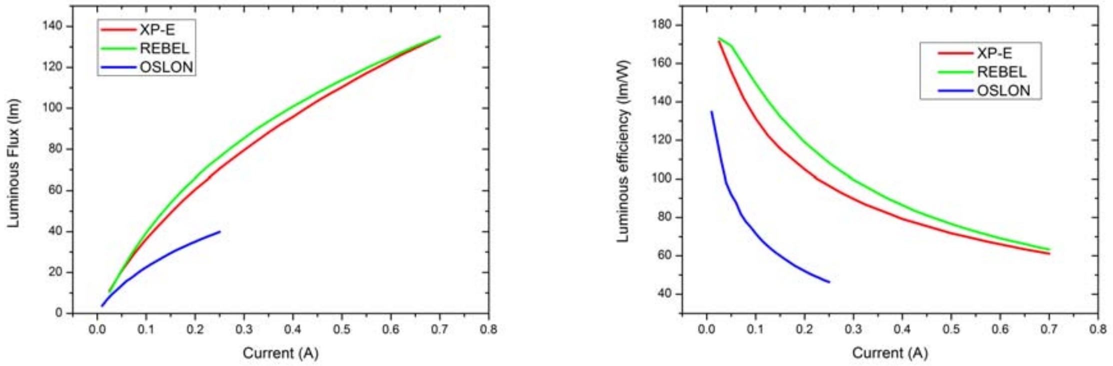

(c) Luminous Flux-Current (d) Luminous Efficiency-Current

Figura 3.37: Characteristics of the green LEDs.

	Flux (lm, nominal current)	CCT (K)	CRI	Voltage (V, nominal current)	$R_{thJ-SP}(W/K)$	T_{jmax}(°C)	$I_{max}(A)$
XP-E	100	3000	80(min)	3	6	150	1
OSLON	71-89.2	3000	95	3.2	7	125	0.8
REBEL	66	2870-3220	85	3	10	150	1
Samsung	110	3000	80(min)	2.95	4	150	1.5
LG	92-122	2700	80(min)	2.98	6	150	1.5
SEOUL Z5M	116	3000	80(min)	3.1	4.5	145	1.2
SEOUL Z5P	112	3000	80(min)	3.2	5.5	145	1

Table 3.20: Comparison between the characteristics of the white LEDs, as reported in their respective datasheets.

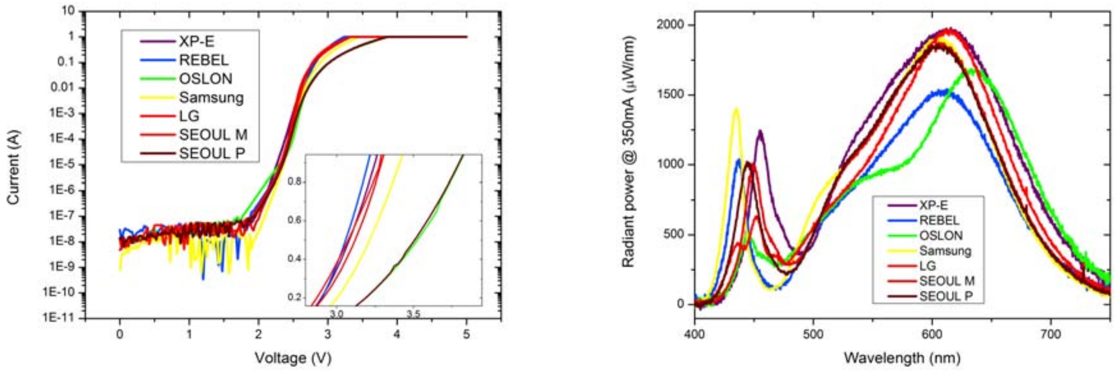

(a) I-V characteristics

(b) Spectra

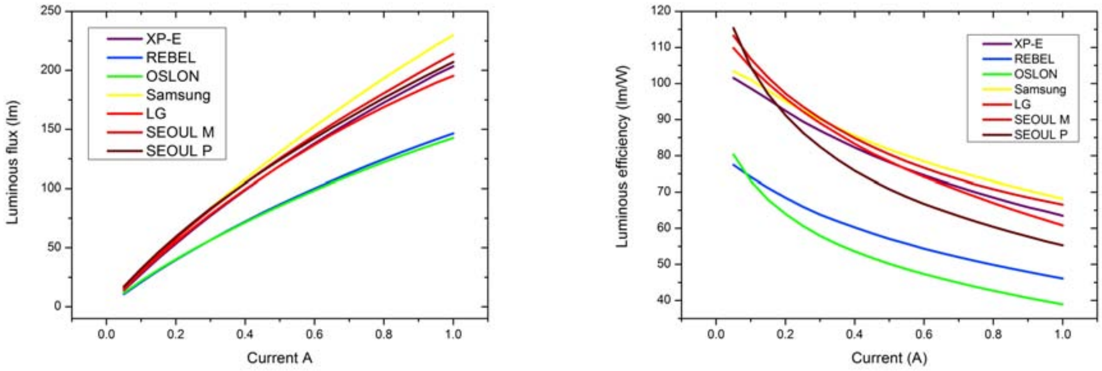

(c) Luminous Flux-Current

(d) Luminous Efficiency-Current

Figura 3.38: Characteristics of the white LEDs.

CHAPTER 4

Characterization techniques

In this chapter the laboratory equipment used for the devices characterization are described, as well as the applied methodologies and processes.Once the theoretical basis are set we point out the phases of the measurements and the used media in order to fully understand the experimental results: the various types of characterizations implemented are presented, each explained as in details as possible.

The main instrument used are definitely the SourceMeter, because as we will see in this chapter almost the investigations are conduced via electrical measurements. The second is the Integrating Sphere, that, used in association with the spectrometer and the sourcemeter, provides the main optical data needed to verify the stress results.

4.1 Electrical characterization

As it has already been mentioned, the electrical measurements are the basis of all the others, so it is useful to start from the description of the sourcemeter, the switch unit and the 4-wire measurement method and some measurements examples.

4.1.1 Keithley Series 2600 and 2600A System SourceMeter

Sourcemeters are instruments that can be used as stand-alone current or voltage sources and stand-alone voltmeters or ammeters, but they also allow to supply current to a device under test while simultaneously measuring the voltage drop across it (or vice

Figure 4.1: Keithley 2612 source measurement unit

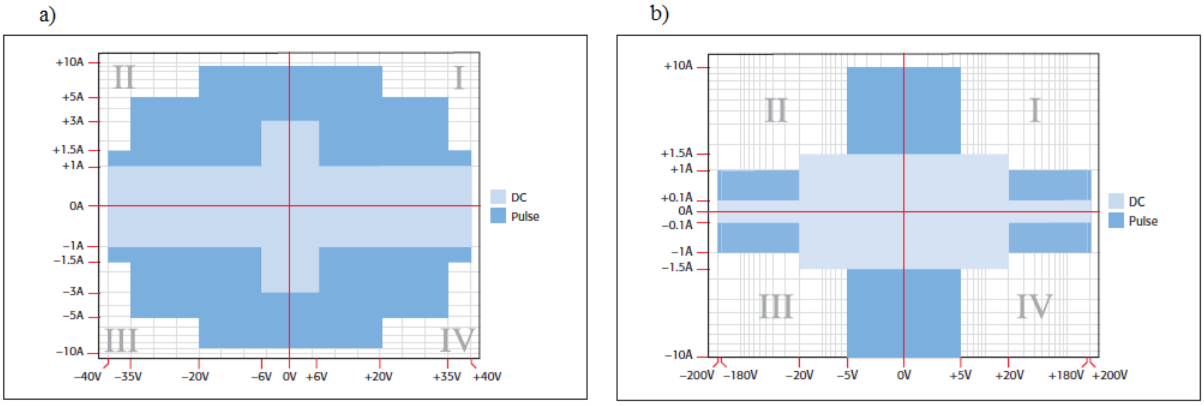

Figure 4.2: I-V capability of the 2602A a), and 2612A b) SourceMeter, as provided in [21].

versa), characteristics that we widely exploited in our tests.

For electrical measurements we adopted the instruments of the Keithley Series 2600 and 2600A System SourceMeter. In particular we used the 2612, 2612A and 2602A SourceMeter, which present very similar performance.

This dual-channel devices, obviously adapted for the 4-wire measurement, has been controlled by a Labview software developed for the required measurements, throught the GPIB interface: in most of the cases the instrument was used synchronized with the Switch Unit in order to obtain more efficient and rapid measurements.

In Figure 4.2 is reported the I-V capability of the instruments, both in pulsed and DC operation: the low DC voltage of each LED makes this instrument suitable to our purposes.

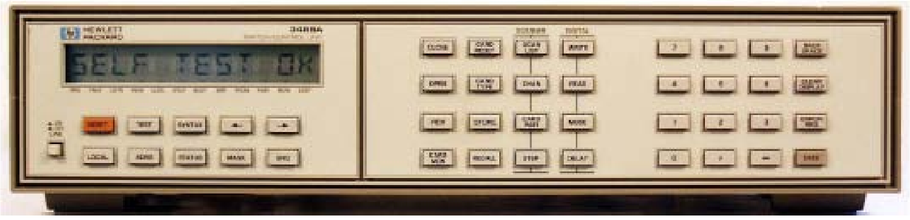

Figure 4.3: HP 3488A switch/control unit.

4.1.2 The HP 3488A Switch Unit

The HP 3488A switch/control unit, equipped with two 44470A 10-channel general purpose relay, is a very simple instrument used to speed up the measurements, indeed when it is used with the sourcemeter it allows a fast metering of each LED onto each board. It consists in a passive matrix of switches controlled via the GPIB interface, and it is capable to switch an input channel between several outputs, so that the same source or metering signal can be applied to two or more devices one by one.

Each of the measured PCB contains eight LEDs , so a single input (based on a 4-wire setting) was switched to eight outputs. The switching scheme is represented in Figure 4.4: the multiplexer provides a control of ten devices, but we have used just the first eight of them. The use of the switching matrix has obvious drawbacks: an increase in the noise that affects the measure, and also an increase in the series resistance of the cables, thus the use of a 4-Wire Kelvin connection was due.

The sourcemeter and the switch matrix have been combined in order to perform measurements concerning thermal (transients, thermal maps and supertransients) and optical characterization (together with the integrating sphere and spectrometer), as we will discuss in the next sections.

4.1.3 The 4-wire Kelvin measurement

When characterizing the electrical properties of a device, current must be sourced to it and the resulting voltage drop at its terminals needs to be measured. When this is done on the same two wires, as in Figure 4.5 (a), the voltage sensed by the instrument is affected by the parasitic resistance of the cables, thus degrading the quality of the measurement.

This problem is overcome by using the 4-wires Kelvin measurement setup. As shown in Figure 4.5 (b), this setup is based on a four wire connection; two of them are used

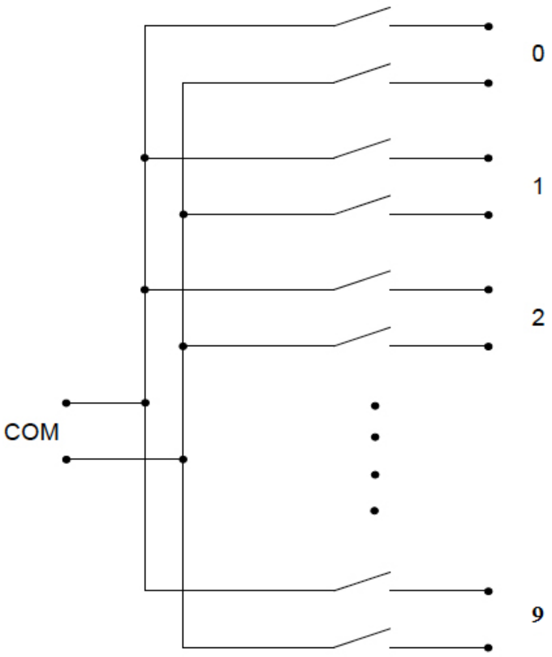

Figure 4.4: The relay multiplexer scheme of the switch matrix, in a 2-wire configuration. The 4-wire setting is obtained using two of multiplexers in parallel, as provided in [22].

to supply current to the device (Force) while the other two are employed to measure the voltage (Sense). In this way, no current passes through the Sense connections and the measurement is not degraded. In order to increase the efficiency of this method, the wires should be connected as close as possible to the device.

Therefore the measurement setup requires 4 different wires connected to each device: two for the voltage sensing circuit (high and low) and two for the current forcing circuit (high and low). All the wires of the eight LEDs of each sensing/forcing circuit of one PCB are grouped and soldered to one 15-way rectangular connector. Thus we have 4 15-way connectors for each PCB we can connect each device to the apposite Source/Meter using the 4-Kelvin conguration using the Switch Unit.

4.1.4 The V-I and I-V measurements

The simplest electrical measurement is the one in which a current is applied and the voltage is measured, this is called he V-I measurement, conversely it is possible to polarize the device with the voltage and then measure the owing current, obtaining the I-V. Since the devices are usually driven in current, the V-I measurement is the more obvious because it renders the voltage reached for a certain current and a certain auto-heating condition, as we will see in the thermal characterization. In Figure 4.6 is

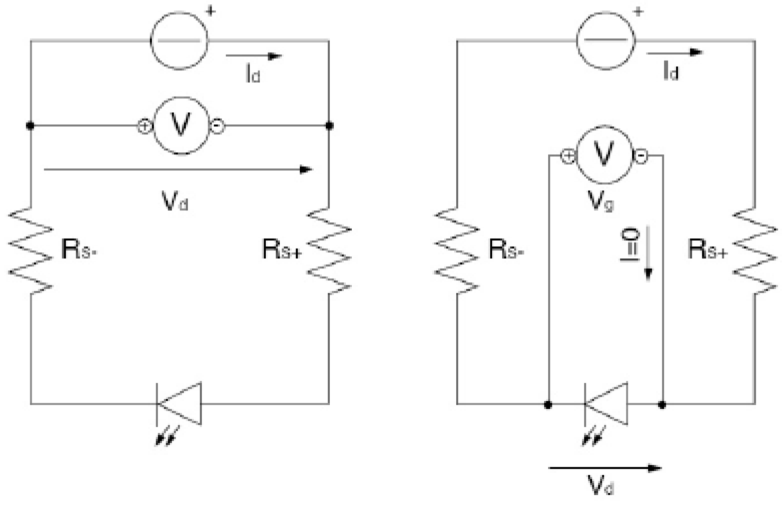

(a) 2-Wire (b) 4-Wire

Figure 4.5: (a) 2-Wire configuration and (b) 4-Wire Kelvin configuration.

reported an example of V-I measurement for four different XPE White LEDs.

Let's notice how for a certain current each LED presents a peculiar V(I) curve; the voltage difference among devices of the same type is actually the reason why they are polarized in current: since the voltage difference is directly due to the built-in voltage of each LED , the same current driving for all the chips assures a homogeneous current injection into the active region and so the same light output power among the LEDs[1].

The complementary measurement, the I-V one, is done during the stress in order to confirm the right electrical operation of the chip. With the data it provides it is evident the diode nature of the device: as a matter of fact, the I-V plots, as the ones reported in Figure 4.7, are similar to the ones reported in the section that deals with the diode.

4.1.5 Arroyo 5310 temperature controller

In the initial characterization of the CREE, OSLON and REBEL devices, both the electrical and optical measurements have been carried out at different temperatures, from 10 °C to 80 °C with steps of 10 °C. In order to heat and cool the LEDs, they have been mounted on a star PCB[2] applied to a Peltier cell driven by the Arroyo 5310. A Peltier cell is a thermoelectric device that uses the Peltier effect to create a heat flux

---

[1] This homogeneity of the light radiation is just nominal and it does not take into account the differences concerning the electron injection, the photon extraction and other chip-peculiar characteristics that can still vary among the retail LEDs .

[2] That is a simple commercial circuit board designed to provide the contacts to a single LED device.

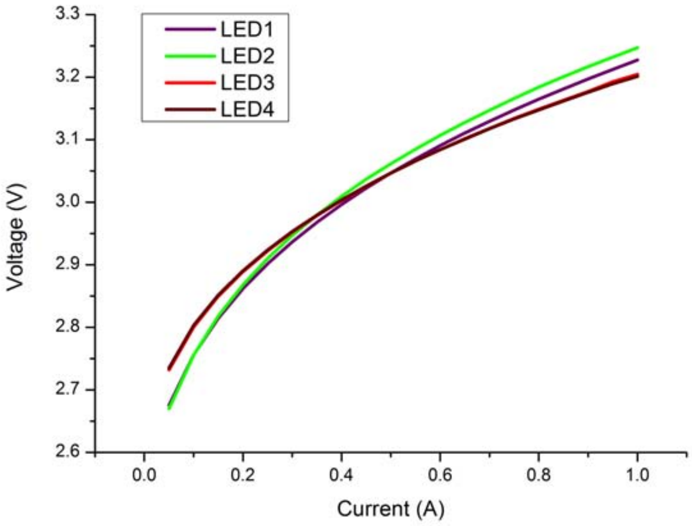

Figure 4.6: The V-I measurement for four XPE White LEDs.

between its two sides, depending on the direction of the current. The Arroyo 5310 is a temperature controller that provides power, regulating it through a feedback system, to the Peltier cells and in order to keep them at a constant temperature which is set by the user. The instrument provides up to 120W (12V/10A) of output power and is compatible with all common temperature sensor inputs (thermistor, RTD, AD590, and LM335). It also and has a 4-wire RTD (resistance temperature detector) mode to eliminate connector resistances. In this work, a thermistor has been employed as the temperature sensor in a classical 2-wire configuration.

4.2 Optical characterization

In this section we present the optical measurement system used for the optical characterization of the LED devices under stress, describing in detail each of the used instruments. Among these the integrating sphere is certainly the most important because it can ensure the quality, repeteability and reliability of the optical measurements, that, being the sphere just a passive enclosure, have been possible by the use of the spectrometer, an important instrument that will be described as well.

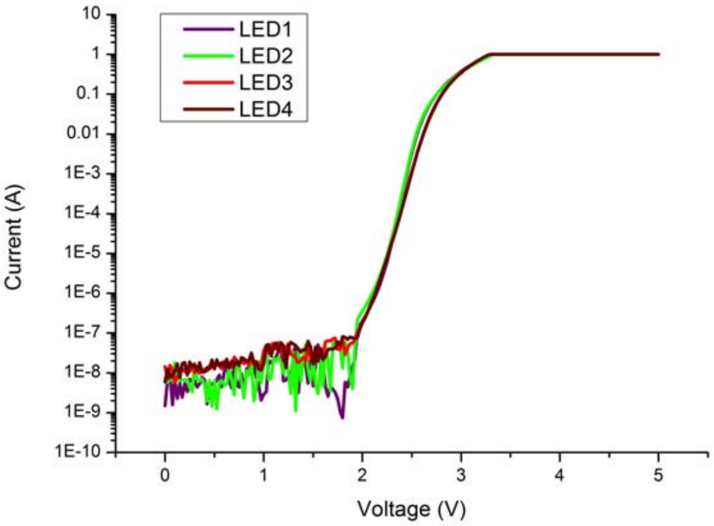

Figure 4.7: The I-V measurement for four XPE White LEDs. The current axis is logaritmic to put in evidence the low voltages for which the diode is not conducting.

Figure 4.8: Arroyo 5310.

4.2.1 LabSphere LMS-650 light integrating sphere

The LMS-650 is a light measurement sphere that spatially integrates a radiant flux. If a radiant source e.g. an LED is placed inside such a sphere (for some spheres it must be placed just outside it) the light emitted is reflected by the internal reflective coating until it can be considered to be uniformely distributed all over the internal surface, so that the flux that hits the photodetector (see Figure 4.10) gives correct information about its source. Only a small part of the radiant flux is absorbed by the sphere. A baffle is interposed between the source and the photodetector, to prevent direct optical connection. Therefore the optical measurements conducted using the sphere allow the complete ignorance of the spatial distribution of the light radiation from the sample, since it is put inside the sphere and a little portion of the light is gathered.

Figure 4.9: LabSphere LMS-650 light integrating sphere.

The employed sphere has a diameter of 65 inch, with two ports, one for the detector and the other for the auxiliary lamp. The sphere has one of its hemispheres blocked while the other can roll on a rail guide to allow internal access to the sphere, in order to easily change lamps or perform a mesurement. The inner surface of the sphere is totally covered with a high-reflective coating, the declared reflectance is of 98%. The sphere houses a pedestal where the device is mounted: this can be moved up and down, in order to align the device with the center of the sphere, and that is doted of all the electrical contacts needed for the measurements.

In our setup we used an optical fiber system instead of a photodetector because we wanted to obtain not only the optical power emitted by the device, but also a more detailed spectrum. This is possible if we connect the fiber end to the spectrometer, a very important instrument that will be described in the next section.

As we have just seen, the integrating sphere together with the spectrometer allows the measurement of the total irradiated luminous flux that comes from a lamp put inside it. The whole apparatus needs to be calibrated either with and without the device inserted in it. The two calibrations are called respectively the *sphere calibration* and the *self-absorption correction*:

- The sphere calibration is performed with no device mounted and using a special

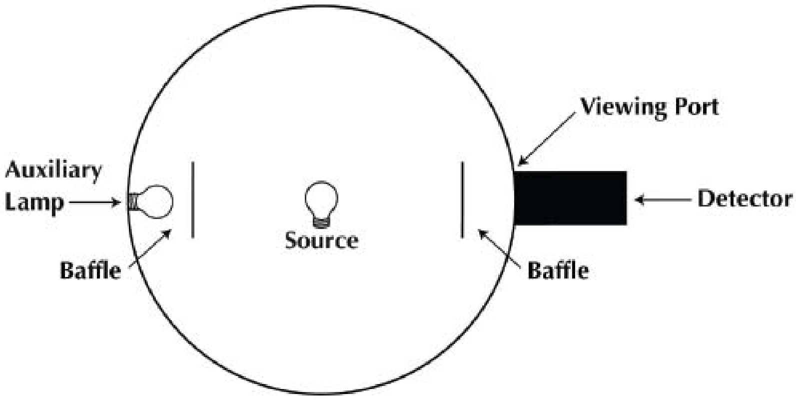

Figure 4.10: Structure of an integrating sphere.

halogen lamp, the spectrometer and the SpectraSuite software. The used lamp is halogen because of the continuity of its spectrum, that is very near to the one of a black body. As a matter of fact the halogen spectrum, in the wavelength region in which the spectrometer operates, is monotonically continous and this feature allows an accurate detection for all the wavelenghts. Furthermore the lamp's spectrum has been carefully measured by the producer and saved in the software: once the calibration lamp is applied to a suitable aperture on the sphere surface, its spectrum is registered and every difference between the measured and the provided one is reported in a special file, that will be read during the successive spectrum acquisitions. These differences are principally due to the reflective substrate imperfections, scale factors introduced by the fiber and the spectrometer, and the normal aging of the sphere.

- While the sphere calibration has to be done once a while, just to verify that the structural and optical characteristics of the apparatus are not signically changed, the self-absorption correction must take place whenever a different lamp is put inside the sphere. Indeed, while the sphere calibration gives a range of corrections due to perfectioning the whole system response, the self-absorption correction accounts for the light absorptions of the shape of the lighting device that is put inside the sphere, and so it provides the corrections that should be applied to the final results, concerning that particular device. This calibration is performed by turning off the device inside the sphere and mounting an auxiliary halogen lamp (different from the previous one) onto the aperture. The lamp is switched on and the final output from the fiber is registered once it is reached the steady-state spectrum. This result is written again in an apposite file, that must be read and compared with the results of the same measurement without the light source.

For more information about the sphere functioning see [23].

4.2.2 Ocean Optics USB2000+ spectrometer

The Ocean Optics USB2000+ spectrometer, manufactured by Ocean Optics, is the device that provides the radiometric, photometric and color characteristics of the light source under test. It receives light from the integrating sphere through an optical fiber and an acquisition trigger signal from the sourcemeter and sends the results to a PC via an USB port. Its spectral range is declared to be from 200 to 1150 nm but the specfiic range and resolution depends on grating.

Figure 4.11: Ocean Optics USB2000+ spectrometer.

The main components of the USB2000+ are (see Figure 4.12) :

1. A **SMA 905 connector,** through which the light from the optical fiber go inside the optical bench-
2. A **slit**, whose size regulates the amount of light that enters the optical bench and controls spectral resolution-
3. An **optical filter** that restricts optical radiation to pre-determined wavelength regions. Light passes through the Filter before entering the optical bench. Both bandpass and longpass filters are available to restrict radiation to certain wavelength regions.
4. A **collimating mirror** that focuses light entering the optical bench towards the grating of the spectrometer.

5. A **diffraction grating** that diffracts light from the Collimating mirror and directs the diffracted light onto the focusing mirror. Gratings are available in different groove densities, allowing you to specify wavelength coverage and resolution in the spectrometer.

6. A **focusing mirror** that receives light reflected from the Grating and focuses first-order spectra onto the detector plane.

7. **A Detector Collection Lens**, which is sn optional component that attaches to the Detector to increase light-collection efficiency. It focuses light from a tall slit onto the shorter Detector elements.

8. A **CCD detector** that collects the light received from the focusing mirror or detector collection lens and converts the optical signal to a digital signal. Each pixel on the Detector responds to the wavelength of light that strikes it, creating a digital response.

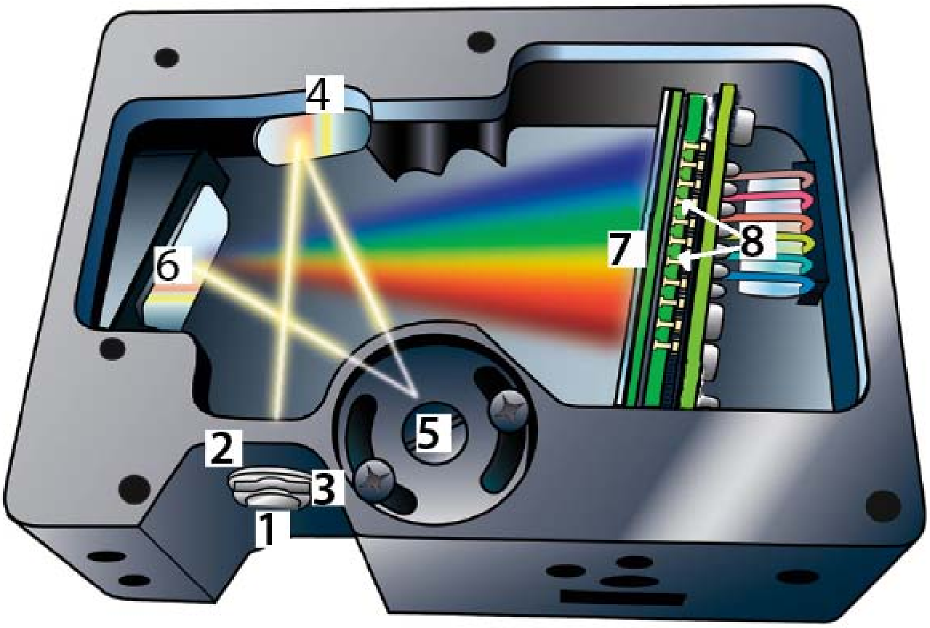

Figure 4.12: Ocean Optics USB2000+ spectrometer components.

For the optical characterization of the LED devices under stress, the measurement system, consisting of a sourcemeter, the switch matrix, the integrating sphere and the spectrometer, has been controlled by a Labview software developed for the required measurements, through the GPIB interface. The sourcemeter, combined with the switch unit, has been used to bias each LED on the same PCB inside the sphere at different current values and to send the measurement trigger to the spectrometer. The light emitted by each LED has been collected by the integrating sphere and sent through the optical fiber to the spectrometer.

The optical data taht can be extrapolated mathematically with these measurements are:

- the optical power and luminous, expressed in W and in lm;
- the efficacy (luminous flux /electrical power), expressed in lm/W;
- the correlated color temperature (CCT);
- the color rendering index (CRI);
- the chromatic coordinates x and y;

each of them has been measured for a sequence of forward currents, in most cases from 50 mA to 1A with a 50 mA step. Together with the optical measurements, the used software provides also some electrical information, very useful to verify the right functioning of the device:

- forward voltage;
- electrical absorbed power, that is obtained from the imposed current and measured voltage, and that allows the efficacy calculus.

4.3 Thermal characterization

As we pointed out in section 2.7, one of the most crucial aspects in the development of a solid state light source is the thermal management. As a matter of fact, the junction temperature of LED affects internal efficiency, maximum output power, lifetime, and other parameters. Junction temperature is determined by ambient temperature, driving current and also by the devices thermal properties. In particular, electrical power dissipated by the device and optical power of the photons that cannot escape from the device result in the heating of the device.

The first step in a LED device characterization consists in estimating its *thermal resistance* R_{th}. We can not assume valid the thermal resistance value provided by the manufacturer because of the particular setup of the stress condition, so the R_{th} of our devices was calculated: this is principally due to the fact that the datasheet-provided R_{th} is the one from the junction to the solder point. In our assembly the LED is put rstly onto the Metal Core (MC) PCB cnd then upon the heatsink, thus the R_{th} value results to be extremely increased.

Postponing the measurement results to the next chapter, we analize here the methodology used in order to obtain the thermal resistance value [24]. This process is principally divided into three steps: the *transients*, the *thermal maps* and the elaboration of the results derived from both of them. The first two steps imply the use of the sourcemeter and a controlled climatic chamber (or a Peltier cells driven by the Arroyo 5310) and all the measurements are exclusively electrical thanks to the fact that, once a certain current is applied, the LED operating voltage is strictly dependant from the junction temperature. The basic idea of this measurement process is to fix the ambient temperature and, making simple electrical measurements, retrieve the junction temperature during the subsequent stress condition.

4.3.1 The transients

If the device is biased with a certain and constant current, the self-heating triggers an exponential lowering of the voltage, until the heatsink and the junction reach a steady state during which the temperature remains constant, because the thermal flux and its dissipation are constant too. This dynamics is called here *transients* and can be characterized by measuring the voltage at steady state V_f . In this case the effective junction temperature is still unknown, but the ambient temperature can be imposed: the devices are put inside an oven or a temperature controlled room, and, after some temperature-stabilization ripples, the measurement is done by noting the device voltage for 30[3] seconds with a step of 0.5 seconds.

Our goal is to find the thermal resistance, that, as seen in section 2.7, is

$$R_{th} = \frac{T_{junction} - T_{ambient}}{P_{th}} \tag{4.1}$$

which is actually a ratio between unknown values, thus we will realize different transients, varying the current in order to change the thermal power flux, as will be explained in the third step of this analysis. Figure 4.13 shows a single transient, realized with a XP-E White LED for a current of $I = 350mA$ (left), and different transients

---

[3] In order to have a reliable datasets we must obtain a transient that is stable in its final part: this stabilization can be reached after at least 30 seconds of working.

carried out for currents from 100mA to 1 A with a step of 100 mA (right).

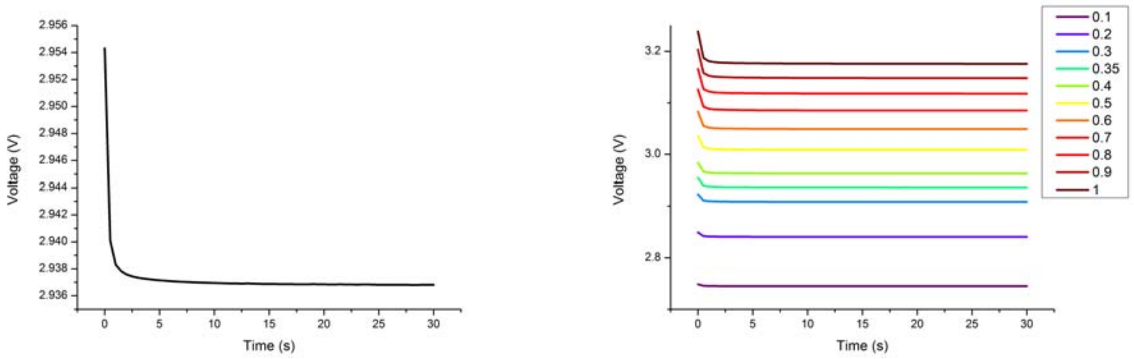

(a) *Current of 350mA.* (b) *Currents from 100mA to 1A*

Figure 4.13: Example of transients obtained from the thermal evaluation of a XP-E White LEDs.

Once the measurement is done, the data are fitted in order to find the necessary steadystate voltage V_f : the used fitting function is a third-order decay exponential, namely:

$$V(t) = V_f + A_1 e^{-t/t_1} + A_2 e^{-t/t_2} + A_3 e^{-t/t_3} \tag{4.2}$$

where V_f is the quantity we need.

4.3.2 The thermal maps

The second step is the measurement of a set of data called *thermal maps* for each LED , that will be elaborated with the transients.

Even in this case using electrical measurements we will retrieve the effective operational junction temperature by imposing the ambient one: this measurement is performed by varying not only the current but also the ambient temperature. The device is put inside the climatic chamber (or on the peltier cell) and, for various steps of temperature, the V-I characteristic is measured. An example is reported in Figure 4.14

The climatic chamber temperature has been varied from 25°C to 95°C with a step of 10°C. As soon as the temperature inside the chamber is stable, the sourcemeter proceeds biasing the device with the same set of currents as the ones used during the transients, and then it measures the voltage. To avoid self-heating of the devices these measurement has been performed with short pulses and low duty-cycle. In this

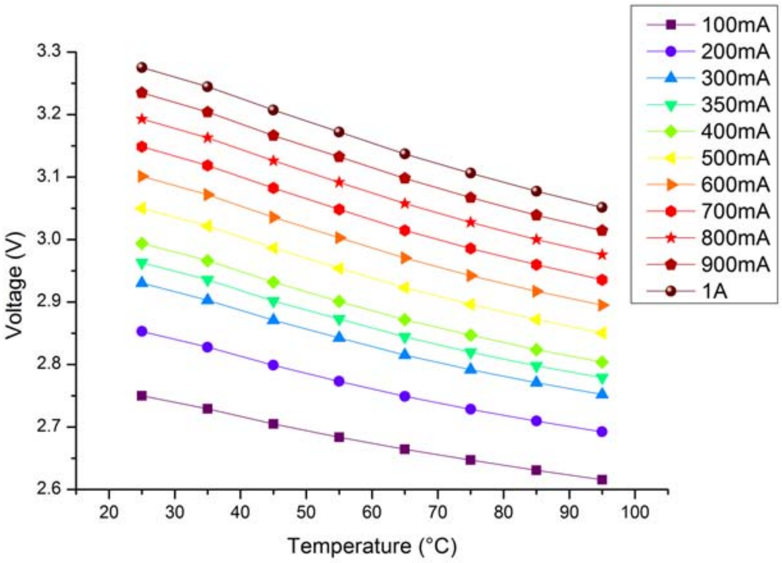

Figure 4.14: Thermal maps for a set of seven temperatures and for the same currents used in the transients. The plot refers to the measurement of the same device of Figure 4.13.

way we can neglect the self-heating contribution during the measurement and we can approximate the junction temperature with the ambient one, that corresponds to the chamber temperature.

After the measurement, once again the data are fitted in order to retrieve the needed values: the voltage is a function of the junction temperature T, more precisely:

$$V(T) = V_0 + A_1 e^{-T/t_1}. \tag{4.3}$$

Hence, fitting each curve that represents the varying of the measured voltage with the junction temperature at a fixed current, we obtain the three parameters (V_0; A_1; t_1) that describe the thermal-electrical dependence for a LED device, as is stated by eq. 4.3.

4.3.3 The thermal resistance extrapolation

At this point we can evaluate the junction temperature for the transients steady state condition, because we know all parameters useful to satisfy eq. 4.3. Thus replacing $V(T)$ with V_f we obtain:

$$T_j = -t_1 \ln\left(\frac{V_f - V_0}{A_1}\right). \tag{4.4}$$

If this proceeding is repeated for all the currents that have been applied, we find, as expected, that the higher is the current, the higher is the temperature of the junction.

The thermal resistance is obtained referring to equation 4.1, where the unknown term is just P_{th}, because the $T_{junction}$ has been just found and the $T_{ambient}$ can be set equal to the chamber (or temperature controlled room) temperature during the transient. If we impose a certain current to the device and measure the voltage, the electrical power is known: a part of it, the Joule power (P_{th}), will be lost in heat, and the other in optical radiation (P_{opt}), so the following holds:

$$P_{tot} = IV = P_{th} + P_{opt}. \tag{4.5}$$

Thus measuring the optical power emitted by the device we can determine the Joule power P_{th} and the relation of the thermal resistance becomes

$$T_{junction} = T_{heatsink} + R_{th}P_{th}. \tag{4.6}$$

From this linear relation we can obtain both R_{th} and $T_{heatsink}$ by simply linearly fitting the Temperature vs. Power relation. The first parameter, i.e. the slope, is finally the thermal resistance while the second one, i.e. the intercept, is nothing more than the ambient temperature that should be equal to the one set on the device.

4.3.4 The junction temperature: supertransients

In addition to the determination of the thermal resistance, the thermal maps are useful to find the junction temperature during the stress of the devices, that is hardly retrievable with other methods.

To determine the junction temperature during the stress we must first determine the steady-state voltage reached by the device in the stress condition, and then use this value in eq. 4.3 .

This is done using either the channel A of the sourcemeter, that measures the voltage of each device, and the channel B that provides the forward current at which we want to know the junction temperature and putting the devices into an oven at the stress temperature for an appropriate period of time (1200 seconds in our case). The result of this measurement is here called *supertransient*. Since the feeding current is supplied for all the LEDs using the serial connection, the devices mutually heat when they are turned on during the measurement: this fact will be kept into account during the discussion of the experimental results.

Once the measurement is done, the data are fitted in order to find the necessary

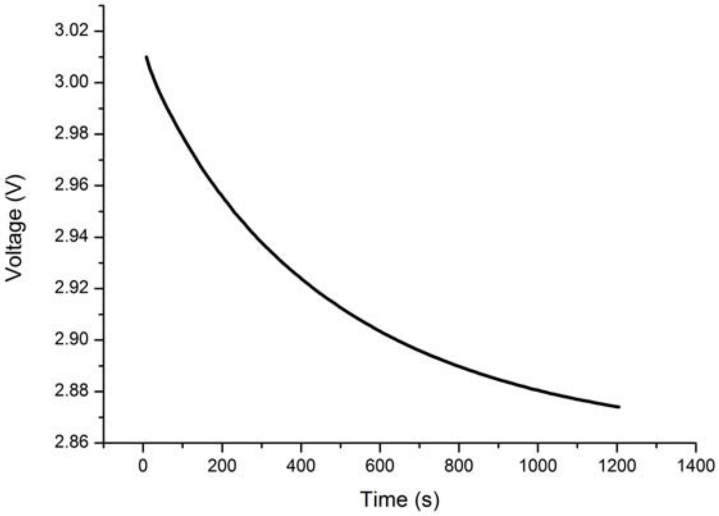

Figure 4.15: Example of supertransient realtive to a XP-E White LEDs stressed at 1A and T=125°C.

steadystate voltage $V_{supertransients}$: the used fitting function is a third-order decay exponential, namely:

$$V(t) = V_{supertransient} + A_1 e^{-t/t_1} + A_2 e^{-t/t_2} + A_3 e^{-t/t_3} \tag{4.7}$$

where $V_{supertransient}$ is the quantity we need.

In Figure 4.15 is reported the supertransient relative to the same device of Figure 4.13, stressed at 1A at the ambient temperature of 125°C.

CHAPTER 5

Stress methodology and thermal characterization results

In this chapter we will report the temperature and biasing conditions chosen for each stress. The LEDs setup onto the MCPCB and the whole structure of the device that has been measured will be also described, including the applied heatsink and the thermal interfaces. The results concerning the thermal characterization will be presented as well.

5.1 Stress conditions

The Cree, Philips and Osram LEDs have been stressed at four different temperature and biasing conditions, as shown in table 5.1. As far as the devices of the other manufactures are concerned , we have stressed them only at the last three conditions. The Oslon green LEDs are characterized by a maximum forward current of 250mA, therefore they have been stressed at 250mA and at 350mA during the first two and the third stress, respectively.

For each temperature and biasing condition we have stressed two LEDs for each type of device described in chapter 3. Thus for every stress we have used 6 colored (2 blue, 2 green and 2 red/amber) and 2 white LEDs for Cree, Philips and Oslon, 2 LEDs for Samsung and LG and 4 devices for SEOUL (2 Z5M and 2 Z5P).

As it will be explained in the next section, we have mounted the devices onto a

Oven temperature (°C)	Forward current (mA)	Stress name
105	700 (250 Oslon greens)	Stress 105-700
125	700 (250 Oslon greens)	Stress 125-700
125	1000 (350 Oslon greens)	Stress 125-1000
170	-	Pure thermal stress 170

Table 5.1: Temperature and biasing stress conditions.

MCPCB on which can be soldered 8 LEDs. Hence, for every stress, we used a different PCB for each manufacteur, except for Samsung, LG and SEOUL, whose devices have been mounted in the same one. Therefore each LED has been named through the following parameters:

- block name: XP-E, OSLON, REBEL or WHITE_LEDs (for Samsung, LG and SEOUL);
- stress temperature: 105, 125, 170;
- stress current: 700, 1000;
- color (for Cree, Osram and Philips devices)/name: B (blue), G (green), R (red), W (white); Samsung, LG, SEOUL M and SEOUL P;
- LED number: 1, 2.

For example: “XP-E_105_700_W1”; “WHITE_LEDs_125_1000_SEOUL P2”.

The adopted stress conditions are slightly over the maximum nominal operating values declared by the manufacturer, thus the performed stress can be considered to be an *accelerated lifetime stress*, as the standard operating conditions are not satisfied and the final results obtained in this way are expected to be reached only after a much longer operation under nominal values.

5.2 The LEDs mounting onto the MCPCB

The electrical configuration of the devices inside the PCB is reported in Figure 5.1, while the picture of Figure 5.2 shows the mounted LEDs : the eight LEDs in the same PCB are connected in series, with an access to the anode and cathode of each one provided by a special contact. In order to provide a direct link to each LED , for both the sense and the force contacts, four wires were soldered on each device: two on the anode contact and two on the cathode contact. We used four 15-pin D-sub connectors to gather the 32 wires of each group of LEDs so that it has been possible to easily connect and disconnect each device from the measuring system.

Since during the stress all eight LEDs onto a single board must be turned on, the series has been connected to a constant-current power supply (Agilent 3649A or Mean Well LPC-60) .

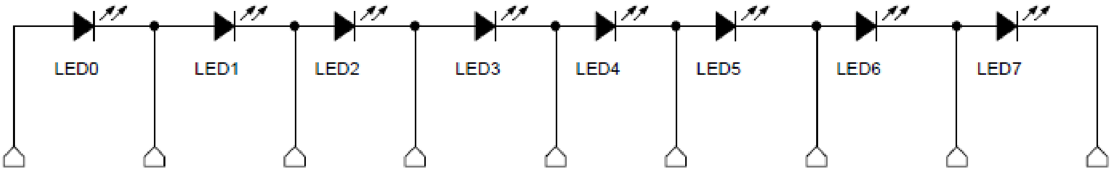

Figure 5.1: Electrical configuration of the LEDs inside the PCB.

The soldering of the LEDs is probably the most delicate procedure of the LED mounting, because of the tiny size of the packages and the proximity of the anode, cathode and thermal pad. It was made using a special soldering paste that, once put upon the contacts between the chip and the PCB, liquees inside the oven and realizes the soldering. In this way the LEDs and the whole PCB are not overheated because of the small time that they spend into the oven (5-6 minutes) and the temperature to which they are exposed (210°C maximum). Once this procedure is completed, the LEDs are perfectly soldered and can be still considered as virgin as before and the board can be fitted on the heat sink.

In order to obtain an effective mechanical and thermal contact between the MCPCB and the heatsink a thermal interface[1] and four screws were used. The used heatsink, that is reported in Figure 5.2, consists of an aluminium block of about 600 g of weight, measuring 115x60x80 mm and equipped with a comb of ten plates in order to better dissipate the heat.

The whole setup of the measured devices is represented in Figure 5.3: providing four different stress conditions, and disposing of six sets of devices to analyze, a total of 122 LEDs were mounted onto sixteen PCBs. We used only twelve heatsinks beacuse during the pure-thermal stress the use of them has not been necessary. As a matter of fact, all the measurements carried out on the devices during the stress are pulsed, thus the effects of self heating can be neglected.

---

[1] Keratherm pink standard film provided by Kerafol-Keramische Folien GmbH-

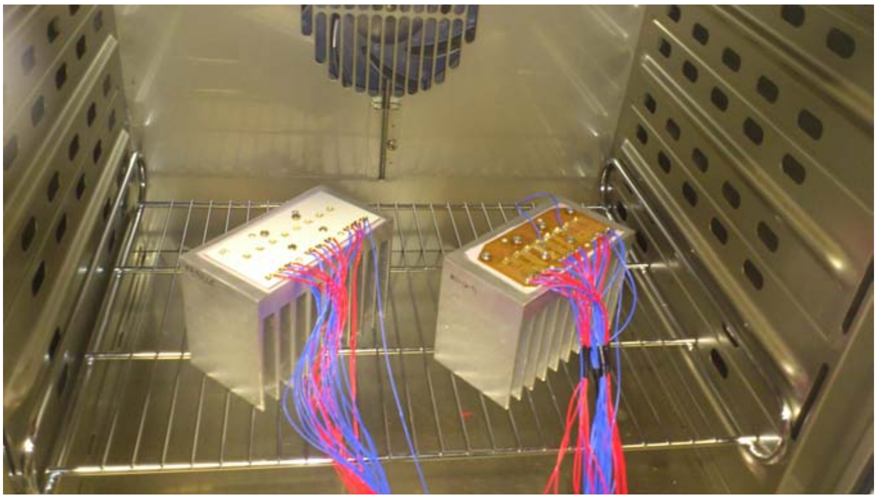

Figure 5.2: Picture of the whole mounted device, including the heat sink.

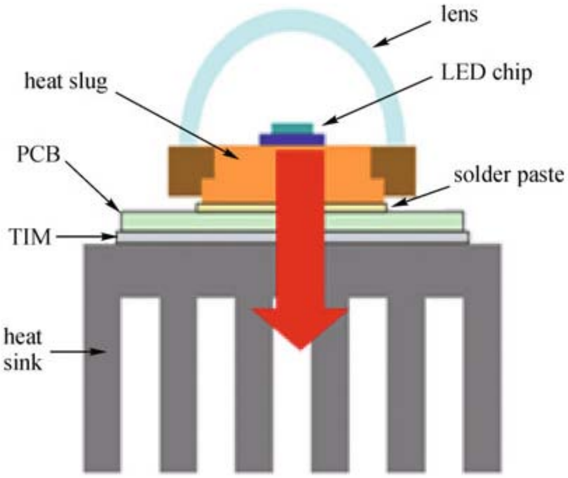

Figure 5.3: The final devices setup, highlighting the LED chip and all the introduced thermal interfaces in the thermal path from the active region to ambient.

5.3 The thermal characterization results

5.3.1 The LEDs Stressed at 105°C-700mA

In this stress we have used two different types of MCPBC: one for the Cree and Osram devices and the other for the Philips LEDs.

The thermal maps have been evaluated mounting the PCBs on a peltier cell driven by the Arroyo 5310, while the transients have been carried out at a temperature of 25°C. Both the thermal maps and the transients have been evaluated for a set of 8 forward currents (except for the Oslon green LEDs), i.e. from 0.1 to 0.7A with a 0.1A step, including the 350 mA point to represent the traditional operating current of such devices. As regards the green LEDs of Osram, that are characterized by a maximum forward current of 250mA, the thermal maps and the transients have been evaluated from 0.1 to 0.25A with a step of 25mA.

The supertransients have been evaluated at the stress conditions, feeding the devices at a current of 700mA (250mA for the Oslon green LEDs) in an oven at 105°C for 1200 seconds.

5.3.1.1 XP-E

In Table 5.2 are reported the thermal resistance R_{th} values and the ambient temperature $T_{ambient}$ extrapolated by the linear fitting of the Temperature-Power relation: the relative plots are reported in Figure 5.4.

	$R_{th}(\frac{K}{W})$	$T_{ambient}$(°C)	R_{thJ-SP} declared in the datasheet ($\frac{K}{W}$)
XP-E_105_700_R1	14.95	25.2	10
XP-E_105_700_R2	14.91	24.6	10
XP-E_105_700_B1	13.68	225	9
XP-E_105_700_B2	14.11	24.9	9
XP-E_105_700_G1	15.54	26.2	15
XP-E_105_700_G2	14.23	26.4	15
XP-E_105_700_W1	11.15	25.3	6
XP-E_105_700_W2	11.48	25.2	6

Table 5.2: The thermal properties of the measured XP-E_105_700 devices.

In Table 5.3 are reported the junction temperatures provided by the supertransients analysis and the temperature that each LED is expected to reach once it is biased by a current of 700 mA at an ambient temperature of 105°C using the thermal reistance values reported in table 5.2 . Notice that in the final results, that should be close

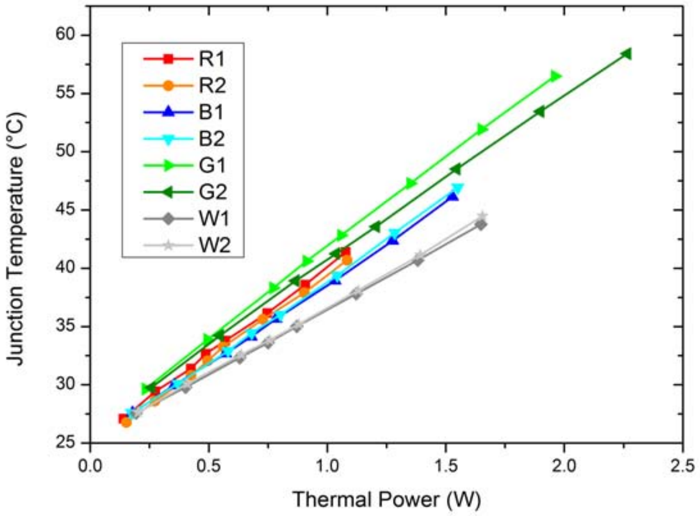

Figure 5.4: The junction temperature vs. thermal power of the XP-E_105_700 board.

to the values found with the supertransients, the injected power was calculated at ambient temperature, and the mutual heating of the LEDs onto the same PCB was not taken into account: as a matter of fact this quantity, that is not simple to estimate, should be the actual difference between the theoretical predictions and the experimental results. However the values reported in table 5.3are smaller than the maximum junction temperature declared by the manufacturer: 150°C.

	$T_{junction-supertransient}$ (°C)	$T_{junction-estimated}$ (°C)
XP-E_105_700_R1	139	121
XP-E_105_700_R2	146	121
XP-E_105_700_B1	136	126
XP-E_105_700_B2	138	127
XP-E_105_700_G1	149	135
XP-E_105_700_G2	142	137
XP-E_105_700_W1	133	123
XP-E_105_700_W2	126	123

Table 5.3: The junction temperatures provided by the supertransients analysis and evaluated referring only to the thermal resistance and power value for the XP-E_105_700 LEDs.

5.3.1.2 OSLON

An analogous characterization has been done for the OSLON devices mounted onto the same board: the resulting thermal resistances are reported in Table 5.4, while in Figure 5.5 the plots of temperature versus power are provided.

	$R_{th}(\frac{K}{W})$	$T_{ambient}$(°C)	R_{thJ-SP} declared in the datasheet ($\frac{K}{W}$)
OSLON_105_700_R1	15.24	25.5	7
OSLON_105_700_R2	15.48	25.1	7
OSLON_105_700_B1	16.27	27.3	7
OSLON_105_700_B2	15.96	25.4	7
OSLON_105_700_G1	19.75	26.3	27
OSLON_105_700_G2	18.43	27.8	27
OSLON_105_700_W1	15.26	27.6	7
OSLON_105_700_W2	16.96	27.5	7

Table 5.4: The thermal properties of the measured CREE_105_700 devices.

Observing Table 5.4 one can notice that for green LEDs the thermal resistance is much lower than the one declared in the datasheet. This may be due to the use of the peltier, that maintains constant only the board temperature and not the ambient one. As will be shown in section 5.3.3.2 the use of the climatic chamber in place of the peltier will lead to more sensible values.

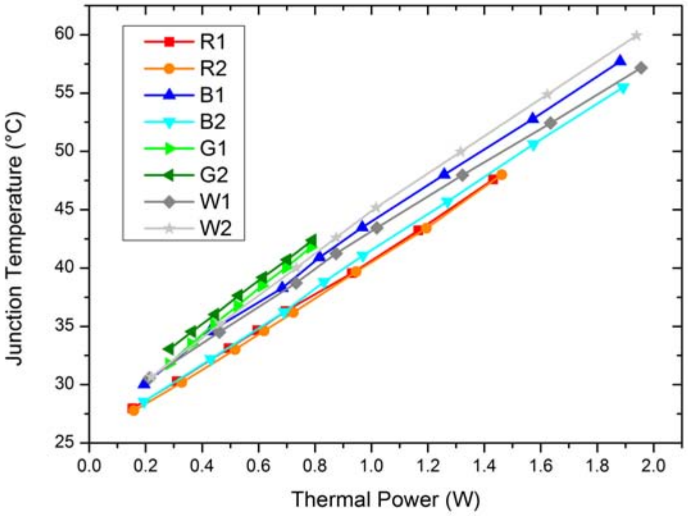

Figure 5.5: The junction temperature vs. thermal power of the OSLON_105_700 board.

In Table 5.5 are reported the junction temperatures provided by the supertransients analysis and the ones calculated using the values of thermal resistance values of table 5.4. Expect for red LEDs, these values are comparable with the maximum junction temperature declared by the manufacturer.

	$T_{junction-supertransient}$ (°C)	$T_{junction-estimated}$ (°C)
OSLON_105_700_R1	163	127
OSLON_105_700_R2	163	128
OSLON_105_700_B1	142	136
OSLON_105_700_B2	140	135
OSLON_105_700_G1	133	121
OSLON_105_700_G2	134	120
OSLON_105_700_W1	144	135
OSLON_105_700_W2	142	138

Table 5.5: The junction temperatures provided by the supertransients analysis and evaluated using the thermal resistance for the OSLON_105_700 LEDs.

5.3.1.3 REBEL

The REBEL thermal performances are reported in Table 5.6 while the plots of the junction temperature versus thermal power are shown in Figure 5.6. As stated before, for this stress we have used a different MCPCB than the one used for the Cree and Osram devices.

	$R_{th}(\frac{K}{W})$	$T_{ambient}$(°C)	R_{thJ-SP} declared in the datasheet ($\frac{K}{W}$)
REBEL_105_700_R1	20.23	28.9	12
REBEL_105_700_R2	20.73	28.4	12
REBEL_105_700_B1	15.38	28.11	10
REBEL_105_700_B2	15.83	27.9	10
REBEL_105_700_G1	14.24	28.6	10
REBEL_105_700_G2	14.7	28.5	10
REBEL_105_700_W1	16.31	29	10
REBEL_105_700_W2	17.36	29	10

Table 5.6: The thermal properties of the measured REBEL_105_700 devices.

In Table 5.7 are reported the junction temperatures provided by the supertransients analysis and the ones estimated using the values of thermal resistance in table 5.6.

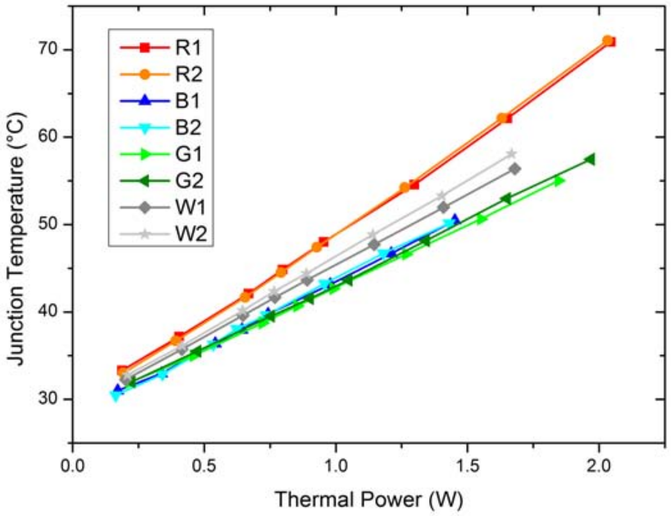

Figure 5.6: The junction temperature vs. thermal power of the REBEL_105_700 board.

	$T_{junction-supertransient}$ (°C)	$T_{junction-estimated}$ (°C)
REBEL_105_700_R1	184	146
REBEL_105_700_R2	198	147
REBEL_105_700_B1	153	127
REBEL_105_700_B2	154	128
REBEL_105_700_G1	162	131
REBEL_105_700_G2	167	134
REBEL_105_700_W1	166	132
REBEL_105_700_W2	163	134

Table 5.7: Comparison between the junction temperatures provided by the supertransients analysis and evaluated for the REBEL_105_700 LEDs.

Observing Table 5.7 one can notice that the Rebel LEDs are reach much higher temperature than the other manufacturers' devices. This may be due to the different board used, which could have an higher thermal conductivity, causing a greater mutual heating of the LEDs.

5.3.2 The LEDs stressed at 125°C-700mA

For the XP-E, OSLON and REBEL boards the thermal maps have been evaluated mounting the PCBs on a peltier cell driven by the Arroyo 5310, while the transients have been made placingthe boards in an oven at 45°C. In the WHITE_LEDs board case instead, the thermal maps have been obtained exploting a climatic chamber, whereas the transients have been made at a temperature of 25°C. The thermal characterization of this board has been made after 500 hours of stress because an initial characterization had not brought meaningful results.

Since the stress current is the same of the previous, the thermal maps and the transients have been evaluated using the same set of currents. The supertransients have been carried out at the stress conditions, feeding the devices at a current of 700mA (250mA for the Oslon greens) in an oven at 125°C for 1200 seconds.

As it will be show, the junction temperatures reached by the devices in this stress conditions are quite higher than the ones declared by the manufacturer.

5.3.2.1 XP-E

In Table 5.8 are reported the thermal resistance R_{th} and the ambient temperature $T_{ambient}$ found during the linear fitting of the Temperature-Power relation: the relative plots are reported in Figure 5.7.

	$R_{th}(\frac{K}{W})$	$T_{ambient}$(°C)	R_{thJ-SP} declared in the datasheet ($\frac{K}{W}$)
XP-E_125_700_R1	14.32	45.1	10
XP-E_125_700_R2	13.67	44.7	10
XP-E_125_700_B1	11.68	46.1	9
XP-E_125_700_B2	11.90	46.4	9
XP-E_125_700_G1	12.04	47.1	15
XP-E_125_700_G2	12.85	46.9	15
XP-E_125_700_W1	9.32	47	6
XP-E_125_700_W2	9.87	47.1	6

Table 5.8: The thermal properties of the measured XP-E_125_700 devices.

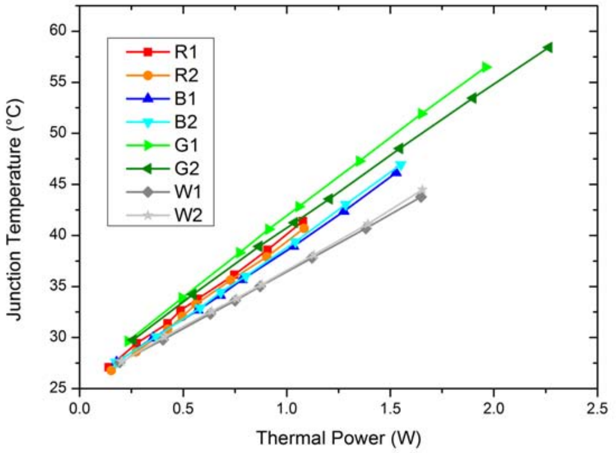

Figure 5.7: The junction temperature vs. thermal power of the XP-E_125_700 board.

In Table 5.9 are reported the junction temperatures provided by the supertransients analysis and the temperatures estimated using the thermal reistance values of Table 5.8.

	$T_{junction-supertransient}$ (°C)	$T_{junction-estimated}$ (°C)
XP-E_125_700_R1	219	140
XP-E_125_700_R2	224	139
XP-E_125_700_B1	182	142
XP-E_125_700_B2	189	142
XP-E_125_700_G1	173	151
XP-E_125_700_G2	165	150
XP-E_125_700_W1	176	140
XP-E_125_700_W2	228	141

Table 5.9: The junction temperatures provided by the supertransients analysis and evaluated referring only to the thermal resistance and power value for the XP-E_125_700 LEDs.

5.3.2.2 OSLON

The results of the thermal characterization for the Oslon devices are reported in Table 5.10, while in Figure 5.8 the plots of temperature versus power are provided.

In Table 5.11 are reported the junction temperatures provided by the supertransients analysis and the ones calculated using the values of thermal resistance in table 5.10. However, as regards the red LEDs, the supertransients analysis has not led to

	$R_{th}(\frac{K}{W})$	$T_{ambient}$(°C)	R_{thJ-SP} declared in the datasheet ($\frac{K}{W}$)
OSLON_125_700_R1	14.88	44.75	7
OSLON_125_700_R2	14.86	45.11	7
OSLON_125_700_B1	12.30	47.43	7
OSLON_125_700_B2	13.71	46.54	7
OSLON_125_700_G1	17.97	45.72	27
OSLON_125_700_G2	19.27	46.37	27
OSLON_125_700_W1	18.89	46.99	7
OSLON_125_700_W2	13.85	49.38	7

Table 5.10: The thermal properties of the measured OSLON_125_700 devices.

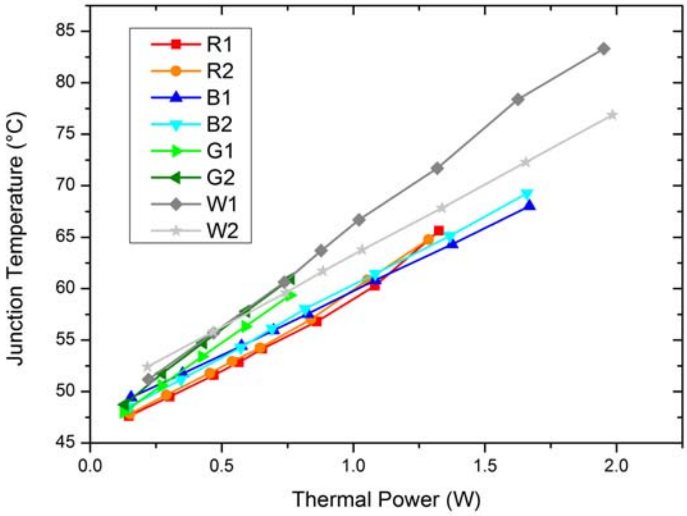

Figure 5.8: The junction temperature vs. thermal power of the OSLON_125_700 board.

meaningful results. Thus the temperatures reported in table 5.11 , have been obtained using the values of its right coloumnand adding to them a term relating to the mutual heating of the LEDs. This had been calculated by averaging the difference between the temperature obtained with the supertransients and the one calculated using the thermal resistances for the other LEDs.

5.3.2.3 REBEL

The REBEL thermal performances are reported in Table 5.12 while the plots of the junction temperature versus electrical power are shown in Figure 5.9.

In Table 5.13 are compared the junction temperatures provided by the supertran-

	$T_{junction-supertransient}$ (°C)	$T_{junction-estimated}$ (°C)
OSLON_125_700_R1	182	145
OSLON_125_700_R2	181	144
OSLON_125_700_B1	177	145
OSLON_125_700_B2	199	148
OSLON_125_700_G1	169	139
OSLON_125_700_G2	179	140
OSLON_125_700_W1	199	162
OSLON_125_700_W2	189	152

Table 5.11: The junction temperatures provided by the supertransients analysis and evaluated referring only to the thermal resistance and power value for the OSLON_125_700 LEDs.

	$R_{th}(\frac{K}{W})$	$T_{ambient}$(°C)	R_{thJ-SP} declared in the datasheet ($\frac{K}{W}$)
REBEL_125_700_R1	15.31	44.67	12
REBEL_125_700_R2	14.10	44.12	12
REBEL_125_700_B1	10.85	46.90	10
REBEL_125_700_B2	11.68	46.47	10
REBEL_125_700_G1	11.04	45.99	10
REBEL_125_700_G2	10.63	46.40	10
REBEL_125_700_W1	12.56	46.64	10
REBEL_125_700_W2	14.24	46.55	10

Table 5.12: The thermal properties of the measured REBEL_125_700 devices.

sients analysis and the ones estimated using the values of thermal resistance of Table 5.12.

5.3.2.4 WHITE_LEDs

An analogous characterization has been done for the Samsung, LG and SEOUL devices, which have been mounted on the same board. The results of this characterization are reported in Table 5.14 while the plots of the junction temperature versus electrical power are shown in Figure 5.10. In Table 5.15 table are reported the junction temperatures provided by the supertransients analysis and the ones estimated using the values of thermal resistance of table 5.14.

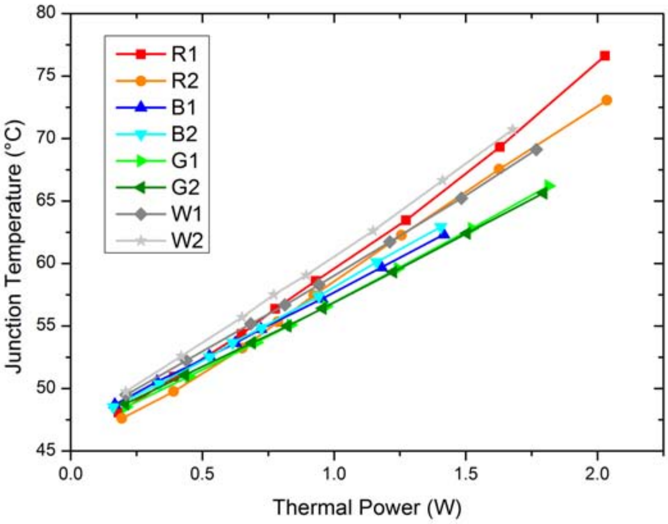

Figure 5.9: The junction temperature vs. thermal of the REBEL_125_700 board.

	$T_{junction-supertransient}$ (°C)	$T_{junction-estimated}$ (°C)
REBEL_125_700_R1	218	156
REBEL_125_700_R2	223	154
REBEL_125_700_B1	182	140
REBEL_125_700_B2	173	141
REBEL_125_700_G1	183	145
REBEL_125_700_G2	187	144
REBEL_125_700_W1	195	147
REBEL_125_700_W2	192	149

Table 5.13: The junction temperatures provided by the supertransients analysis and evaluated referring only to the thermal resistance and power value for the REBEL_125_700 LEDs.

	$R_{th}(\frac{K}{W})$	$T_{ambient}$(°C)	R_{thJ-SP} declared in the datasheet ($\frac{K}{W}$)
WHITE_LEDs_125_700_Samsung1	21.39	25.3	4
WHITE_LEDs_125_700_Samsung2	21.93	24.4	4
WHITE_LEDs_125_700_LG1	14.54	27.60	6
WHITE_LEDs_125_700_LG2	14.64	27.2	6
WHITE_LEDs_125_700_SEOUL M1	19.68	20.4	4.5
WHITE_LEDs_125_700_SEOUL M2	18.33	23.0	4.5
WHITE_LEDs_125_700_SEOUL P1	18.52	24.1	5.5
WHITE_LEDs_125_700_SEOUL P2	21.16	20.2	5.5

Table 5.14: The thermal properties of the measured WHITE_LEDs_125_700 devices.

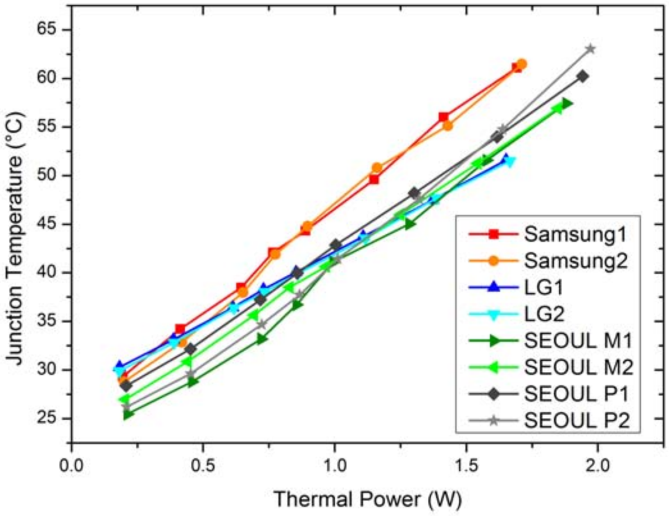

Figure 5.10: The junction temperature vs. thermal power of the WHITE_LEDs_125_700 board.

	$T_{junction-supertransient}$ (°C)	$T_{junction-estimated}$ (°C)
WHITE_LEDs_125_700_Samsung1	206	161
WHITE_LEDs_125_700_Samsung2	210	163
WHITE_LEDs_125_700_LG1	223	149
WHITE_LEDs_125_700_LG2	213	149
WHITE_LEDs_125_700_SEOUL M1	166	162
WHITE_LEDs_125_700_SEOUL M2	164	159
WHITE_LEDs_125_700_SEOUL P1	172	161
WHITE_LEDs_125_700_SEOUL P2	159	167

Table 5.15: The junction temperatures provided by the supertransients analysis and evaluated referring only to the thermal resistance and power value for the Samsung, LG and SEOUL LEDs.

5.3.3 The LEDs stressed at 125°C-1A

The thermal maps have been obtained using the climatic chamber, while the transients have been carried out at a temperature of 25°C. Both the thermal maps and the transients have been evaluated for a set of 11 forward currents (except for the Oslon green LEDs), i.e. from 0.1 to 1 A with a 0.1 A step, including the 350 mA point to represent the traditional operating current of such devices. As regards the Oslon green LEDs, the thermal maps and the transients have been evaluated from 0.1 to 0.35 A with a step of 50mA. The supertransients have been realized feeding the devices at a current of 1A (350mA for the Oslon green LEDs) in an oven at 125°C for 1200 seconds.

As it will be show, the junction temperatures reached by the devices in this stress conditions are quite higher than the ones declared by the manufacturer.

5.3.3.1 XP-E

In Table 5.16 are reported the thermal resistance R_{th} and the ambient temperature $T_{ambient}$ found during the linear fitting of the Temperature-Power relation: the relative plots are reported in Figure 5.11.

	$R_{th}(\frac{K}{W})$	$T_{ambient}$(°C)	R_{thJ-SP} declared in the datasheet ($\frac{K}{W}$)
XP-E_125_1000_R1	16.20	21.3	10
XP-E_125_1000_R2	16.06	21.7	10
XP-E_125_1000_B1	15.57	22.5	9
XP-E_125_1000_B2	15.50	23.4	9
XP-E_125_1000_G1	15.20	24.9	15
XP-E_125_1000_G2	16.95	24.6	15
XP-E_125_1000_W1	11.19	25.2	6
XP-E_125_1000_W2	11.61	25.4	6

Table 5.16: The thermal properties of the measured XP-E_125_1000 devices.

Table 5.17 shows the junction temperatures provided by the supertransients analysis and the temperature that each LED is expected to reach once it is biased by a current of 1000 mA at an ambient temperature of 125°C using the thermal reistance values reported in Table 5.16.

5.3.3.2 OSLON

The results of the thermal characterization for the Oslon devices are reported in Table 5.18, while in Figure 5.12 the plots of temperature versus power are provided. In this case the thermal resistances of the green LEDs are comparable with those reported in

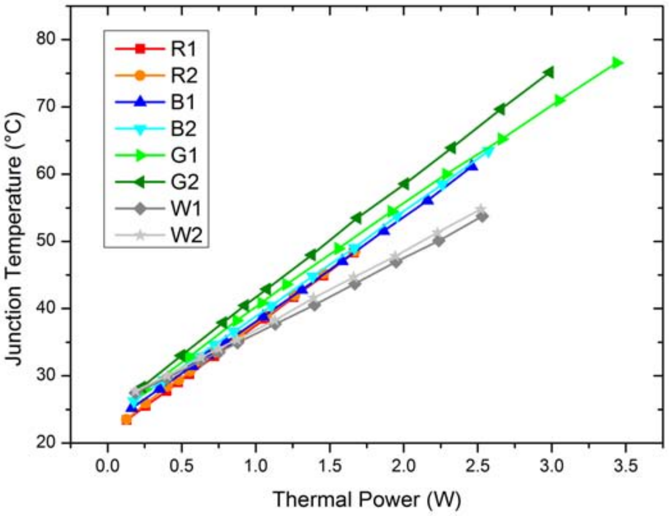

Figure 5.11: The junction temperature vs. thermal power of the XP-E_125_1000 board.

datsheet. This leads us to state that the use the climatic chamber is more reliable than the use of the peltier cell driven by the Arroyo.

In Table 5.19 are reported the junction temperatures provided by the supertransients analysis and the ones calculated using the values of thermal resistance in table 5.18. The junction temperatures of the red LEDs have been calculated in the same manner described in section 5.3.3.2.

5.3.3.3 REBEL

The REBEL thermal performances are reported in Table 5.20 while the plots of the junction temperature versus electrical power are shown in Figure 5.13.

In Table 5.21 are compared the junction temperatures provided by the supertransients analysis and the ones estimated using the values of thermal resistance of table 5.20. However the supertransients analysis has not led to meaningful values for the red LEDs. Thus the junction temperatures of these devices have been calculated using the same method described for the Osoln red LEDs.

5.3.3.4 WHITE_LEDs

The results of the thermal characterization for the Samsung, LG and SEOUL devices are reported in Table 5.22, while the plots of the junction temperature versus electrical

	$T_{junction-supertransient}$ (°C)	$T_{junction-estimated}$ (°C)
XP-E_125_1000_R1	253	152
XP-E_125_1000_R2	264	152
XP-E_125_1000_B1	178	163
XP-E_125_1000_B2	191	165
XP-E_125_1000_G1	191	177
XP-E_125_1000_G2	177	176
XP-E_125_1000_W1	173	153
XP-E_125_1000_W2	173	154

Table 5.17: The junction temperatures provided by the supertransients analysis and evaluated referring only to the thermal resistance and power value for the XP-E_125_700 LEDs.

	$R_{th}(\frac{K}{W})$	$T_{ambient}$(°C)	R_{thJ-SP} declared in the datasheet ($\frac{K}{W}$)
OSLON_125_1000_R1	17.82	25.1	7
OSLON_125_1000_R2	16.72	26.6	7
OSLON_125_1000_B1	15.71	27.7	7
OSLON_125_1000_B2	17.49	27.9	7
OSLON_125_1000_G1	31.33	28.8	27
OSLON_125_1000_G2	30.37	29.3	27
OSLON_125_1000_W1	17.83	28.4	7
OSLON_125_1000_W2	20.08	28.9	7

Table 5.18: The thermal properties of the measured OSLON_125_1000 devices.

power are shown in Figure 5.14.

Table 5.23 reports the junction temperatures provided by the supertransients analysis and the ones estimated using the values of thermal resistance of table 5.22. As far as the Samsung and LG devices are concerned, the junction temperatures reported in the central coloumn have been calculated using the corresponding values of the right coloumn to which have been added a term accounting for the mutaul heating of the LEDs. This had been calculated by averaging the difference between the temperature obtained with the supertransients and the one calculated using the thermal resistances for the other LEDs.

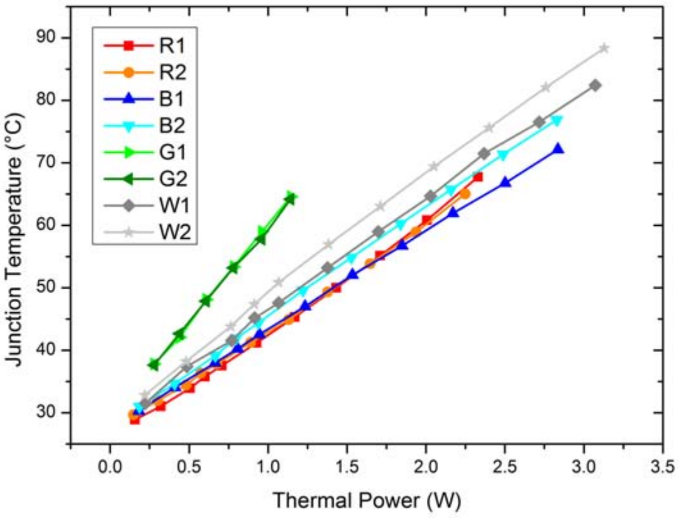

Figure 5.12: The junction temperature vs. thermal power of the OSLON_125_1000 board.

	$T_{junction-supertransient}$ (°C)	$T_{junction-estimated}$ (°C)
OSLON_125_1000_R1	183	166
OSLON_125_1000_R2	179	163
OSLON_125_1000_B1	179	170
OSLON_125_1000_B2	183	174
OSLON_125_1000_G1	181	161
OSLON_125_1000_G2	195	160
OSLON_125_1000_W1	195	180
OSLON_125_1000_W2	197	188

Table 5.19: The junction temperatures provided by the supertransients analysis and evaluated referring only to the thermal resistance and power value for the OSLON_125_1000 LEDs.

	$R_{th}(\frac{K}{W})$	$T_{ambient}$(°C)	R_{thJ-SP} declared in the datasheet ($\frac{K}{W}$)
REBEL_125_1000_R1	18.07	23.3	12
REBEL_125_1000_R2	17.91	23.9	12
REBEL_125_1000_B1	13.67	25.4	10
REBEL_125_1000_B2	13.96	25.4	10
REBEL_125_1000_G1	14.52	25.1	10
REBEL_125_1000_G2	14.1	25	10
REBEL_125_1000_W1	15.38	27	10
REBEL_125_1000_W2	16.14	26.7	10

Table 5.20: The thermal properties of the measured REBEL_125_1000 devices.

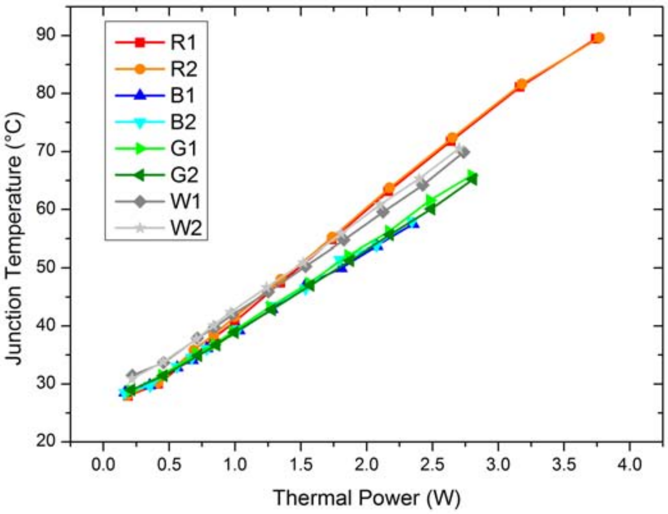

Figure 5.13: The junction temperature vs. thermal of the REBEL_125_1000 board.

	$T_{junction-supertransient}$ (°C)	$T_{junction-estimated}$ (°C)
REBEL_125_1000_R1	239	193
REBEL_125_1000_R2	238	192
REBEL_125_1000_B1	207	157
REBEL_125_1000_B2	209	158
REBEL_125_1000_G1	223	166
REBEL_125_1000_G2	199	165
REBEL_125_1000_W1	218	167
REBEL_125_1000_W2	198	169

Table 5.21: The junction temperatures provided by the supertransients analysis and evaluated referring only to the thermal resistance and power value for the REBEL_125_1000 LEDs.

	$R_{th}(\frac{K}{W})$	$T_{ambient}$(°C)	R_{thJ-SP} declared in the datasheet ($\frac{K}{W}$)
WHITE_LEDs_125_1000_Samsung1	22.14	27.6	4
WHITE_LEDs_125_1000_Samsung2	22.97	28.6	4
WHITE_LEDs_125_1000_LG1	12.93	26	6
WHITE_LEDs_125_1000_LG2	13.56	26.9	6
WHITE_LEDs_125_1000_SEOUL M1	16.62	26.3	4.5
WHITE_LEDs_125_1000_SEOUL M2	16.99	26.7	4.5
WHITE_LEDs_125_1000_SEOUL P1	19.01	27.2	5.5
WHITE_LEDs_125_1000_SEOUL P2	21.77	25.1	5.5

Table 5.22: The thermal properties of the measured WHITE_LEDs_125_1000 devices.

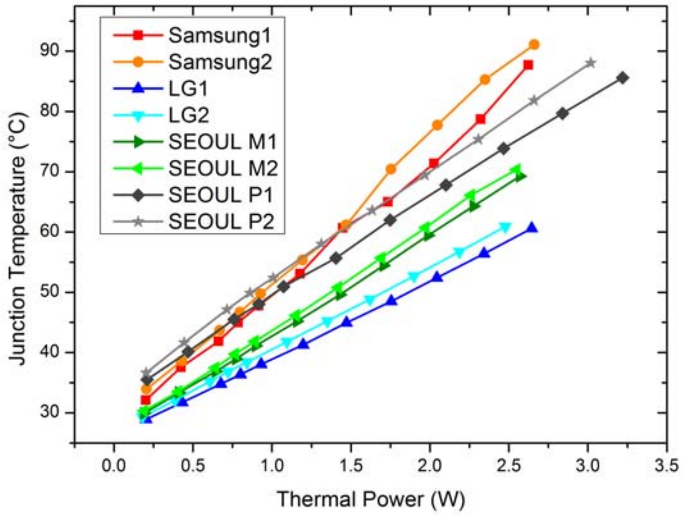

Figure 5.14: The junction temperature vs. thermal power of the WHITE_LEDs_125_1000 board.

	$T_{junction-supertransient}$ (°C)	$T_{junction-estimated}$ (°C)
WHITE_LEDs_125_1000_Samsung1	206	184
WHITE_LEDs_125_1000_Samsung2	209	186
WHITE_LEDs_125_1000_LG1	182	159
WHITE_LEDs_125_1000_LG2	181	159
WHITE_LEDs_125_1000_SEOUL M1	192	168
WHITE_LEDs_125_1000_SEOUL M2	195	168
WHITE_LEDs_125_1000_SEOUL P1	192	189
WHITE_LEDs_125_1000_SEOUL P2	225	191

Table 5.23: Comparison between the junction temperatures provided by the supertransients analysis and evaluated referring only to the thermal resistance and power value for the Samsung, LG and SEOUL LEDs stressed at 125°C-1A.

5.3.4 The comparison of the stress conditions

Figures 5.15 to 5.22 show the thermal resistances and the junction temperatures for each manufactures at the various stress conditions.

Observing figures 5.16, 5.18, 5.20 and 5.22 we can notice, that contrary to what we expected, the junction temperatures reached during the stress at 125°C-1A seem comparable to the ones reached during the stress at 125°C-700mA. This mistake may be do the different setups used for evaluating the thermal maps for the 2 stress conditions. As a matter of fact we have used the climatic chamber in the first case and the peltier in the second one. Therefore, in order to obtain comparable data, it would had to be used the same setup for the different stress conditions.

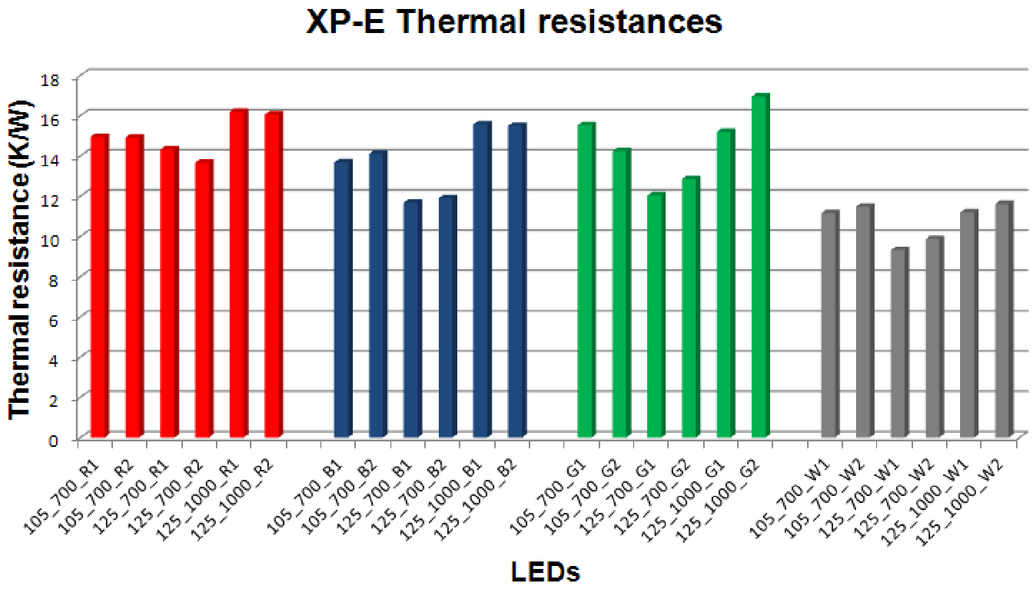

Figure 5.15: Thermal resistances of the XP-E devices for the three different stress conditions.

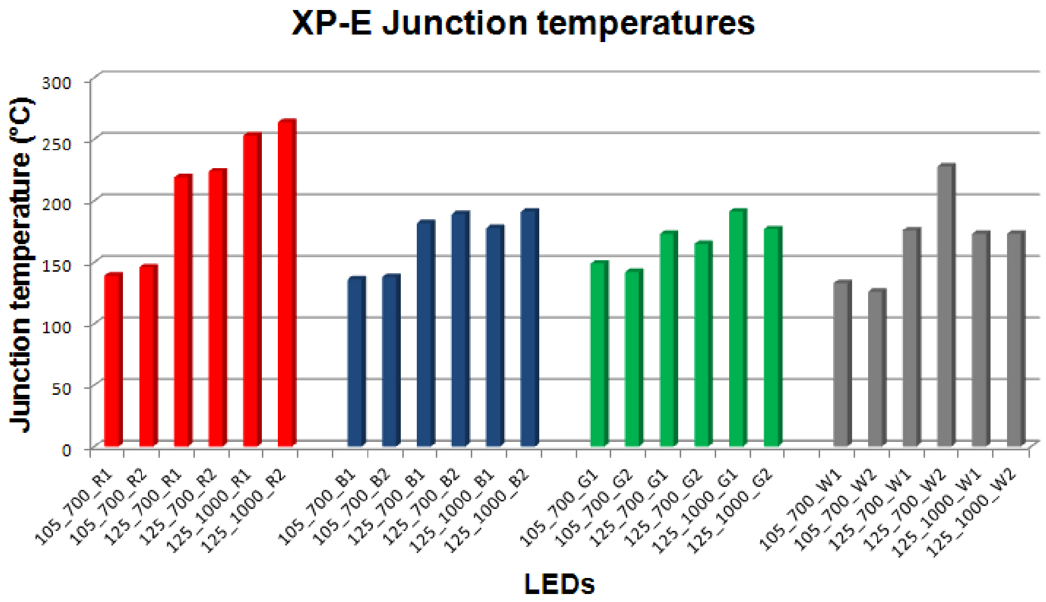

Figure 5.16: Junction temperatures of the XP-E devices for the three different stress conditions.

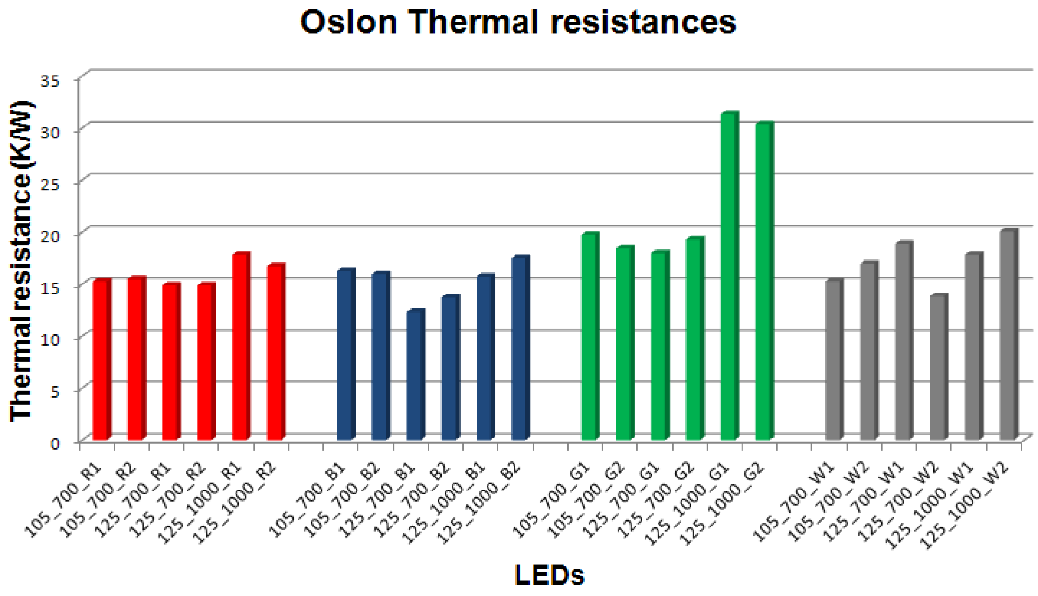

Figure 5.17: Thermal resistances of the Oslon devices for the three different stress conditions.

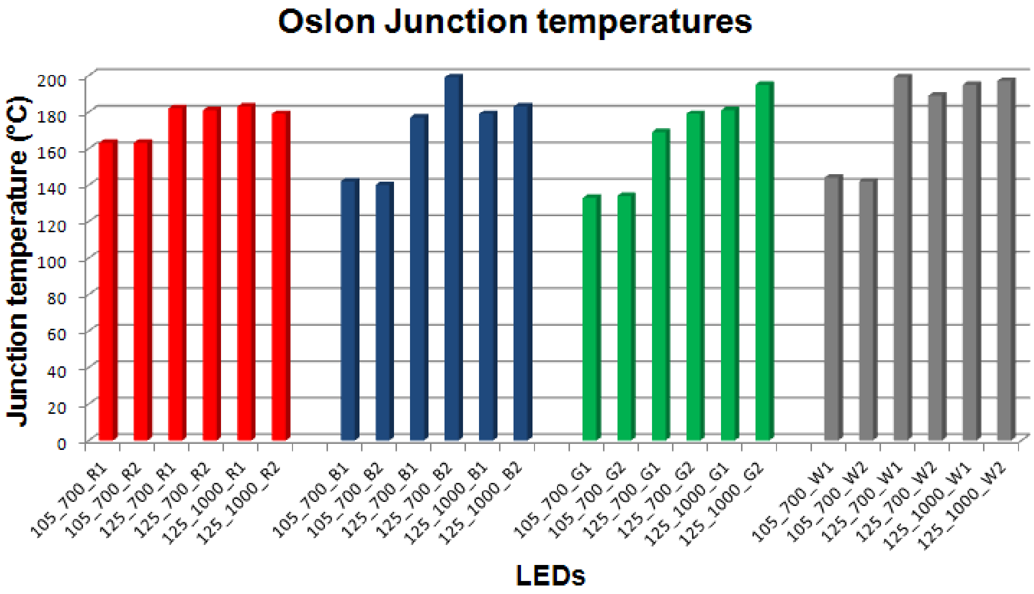

Figure 5.18: Junction temperatures of the Oslon devices for the three different stress conditions.

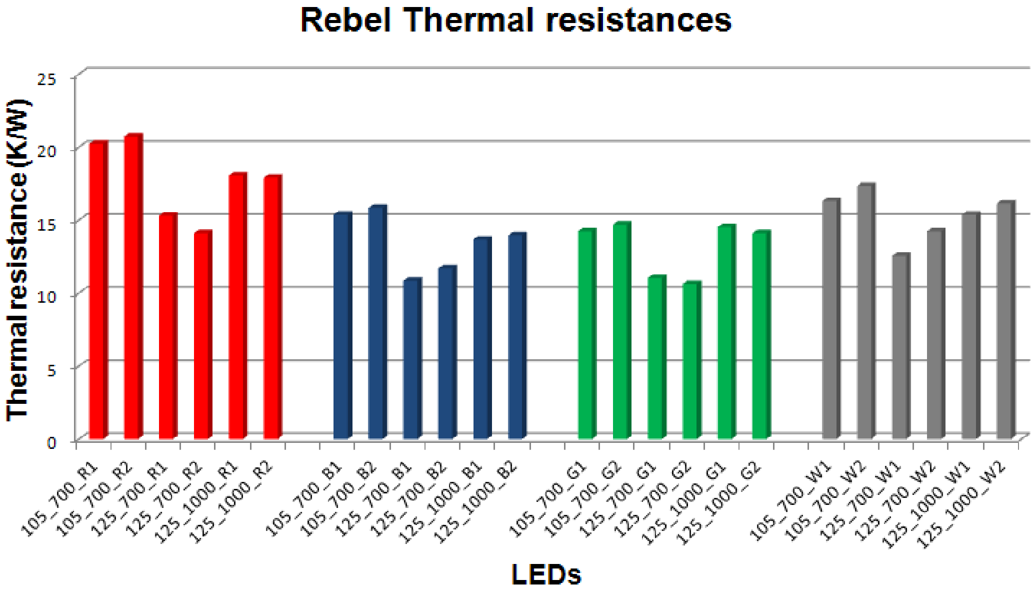

Figure 5.19: Thermal resistances of the Rebel devices for the three different stress conditions.

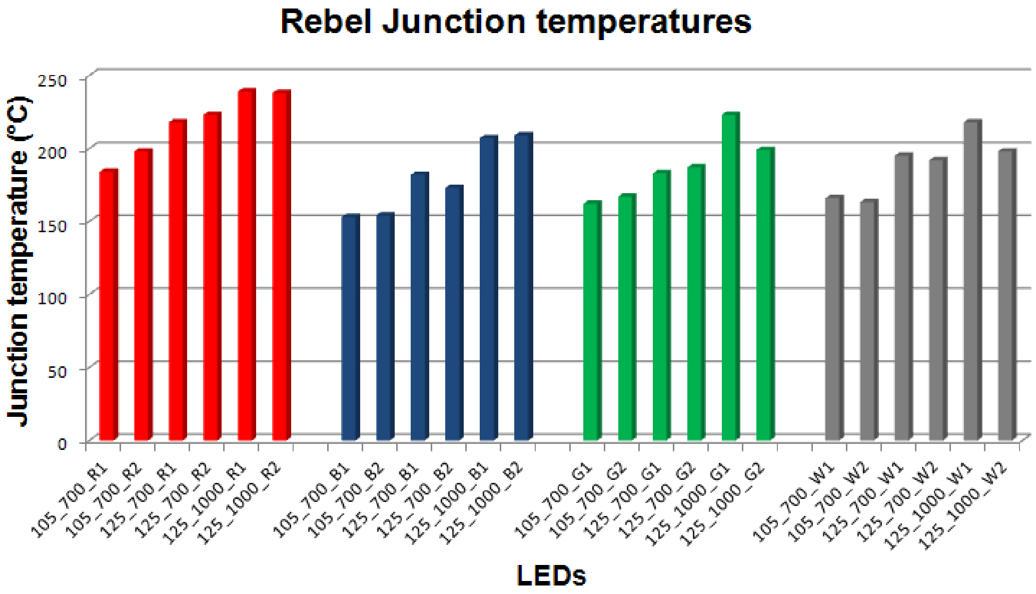

Figure 5.20: Junction temperatures of the Rebel devices for the three different stress conditions.

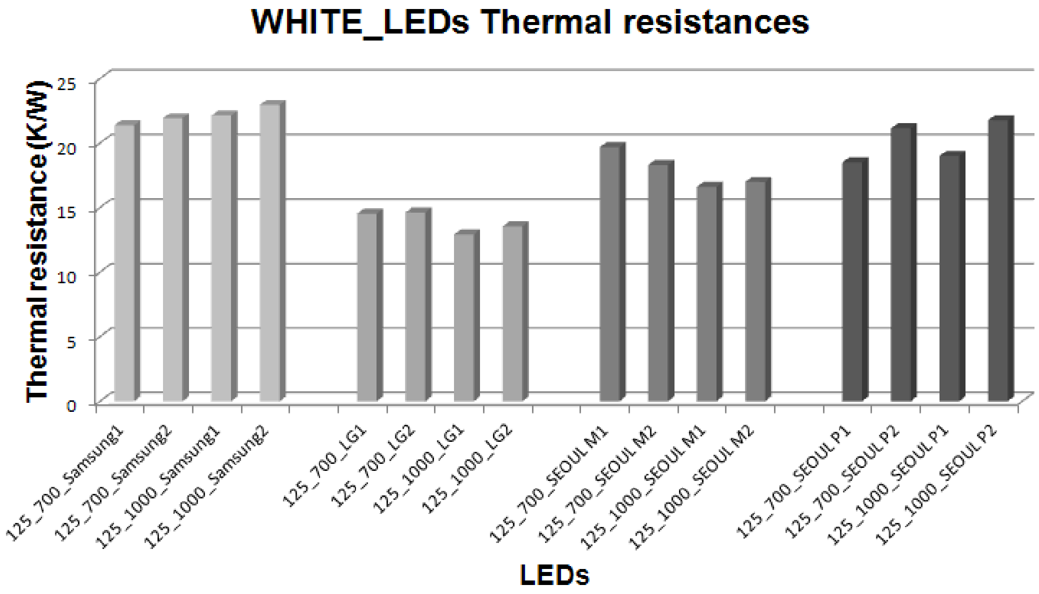

Figure 5.21: Thermal resistances of the Samsung, LG and SEOUL devices for the two different stress conditions.

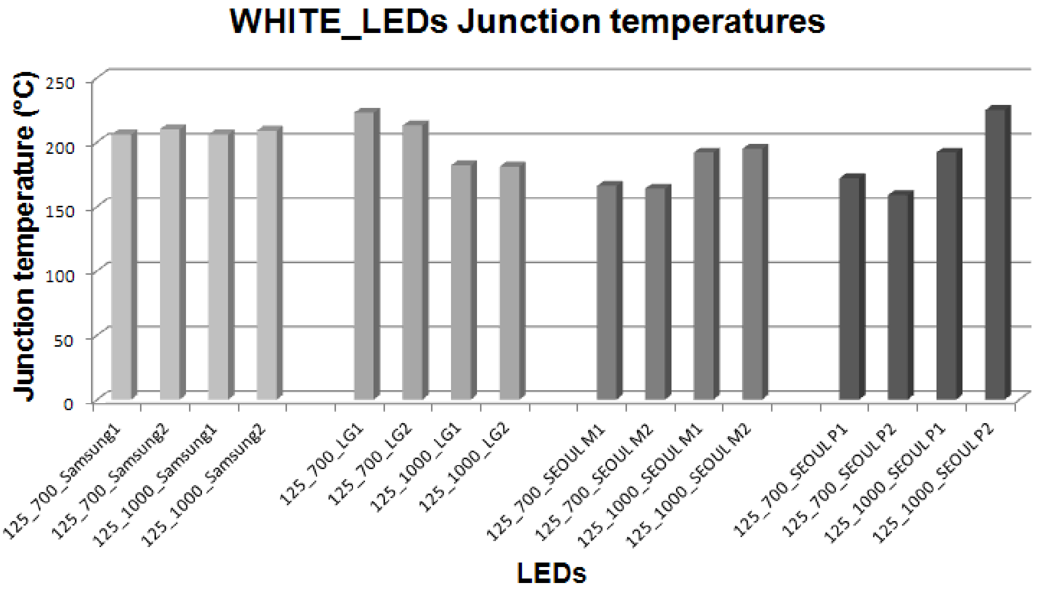

Figure 5.22: Junction temperatures of the Samsung, LG and SEOUL devices for the two different stress conditions.

CHAPTER 6

Stress results

In this chapter we will discuss the results of the various stress conditions for each manufacturer. At the end of each section it will be presented a comparison beetween the devices of the different manufactures, while at the end of the chapter the effects of different stress condition on the degradation mechanisms will be analyzed.

6.1 Stress 105_700

6.1.1 XP-E LEDs

The optical power behaviour measured at 350mA is reported in Figure 6.1. The trend is normalized to the initial value. The devices do not suffer of a considerable decay of the OP after 2750 hours of operation. However, as regards the white LEDs, they show an increase of the OP during the first hours, that could be a result of the activation of dopant inside the lattice that leads to the increase of the devices optical efficiency, while the subsequent measurements report a gradually decay of the OP. This decay may be due to a progressive darkening of the incapsulation material, as showed in Figure 6.3. This is hypothesis is supported by the decreasing in the yellow/blue ratio of these devices, as showed in Figure. Figure 6.4 a) shows the spectrum of the XP_E_105_700_W1 at 350mA, which confirm the OP decay after the first hours of stress.

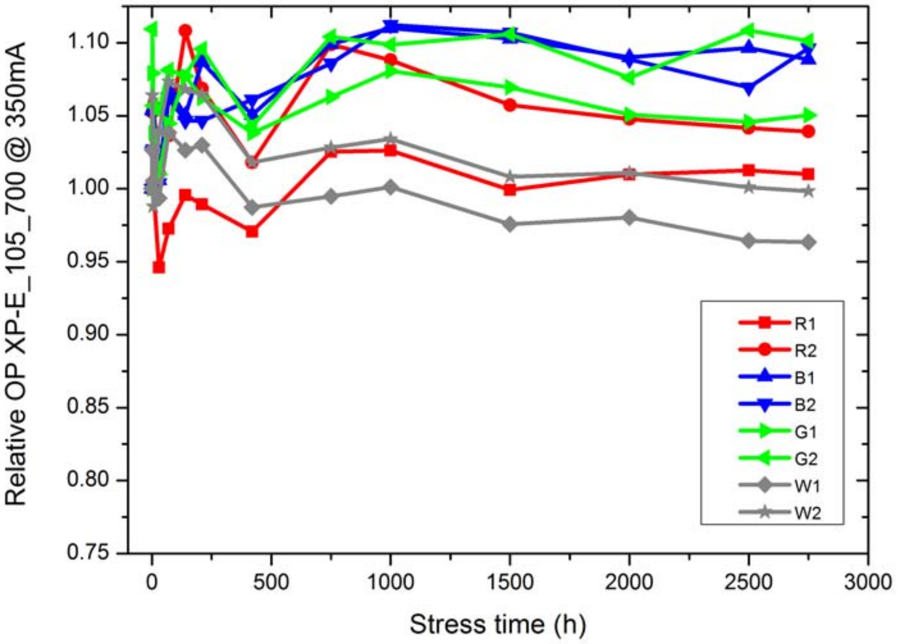

Figure 6.1: The OP trend for the first 2750 hours of operation of the XP-E devices, measured for a forward current of 350 mA.

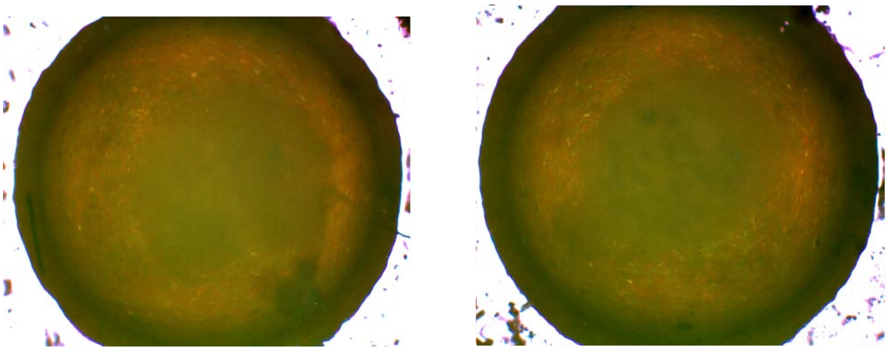

(a) XP-E_105_700_W1

(b) XP-E_105_700_W1

Figura 6.3: White LEDs after 2750 hours.

The I-V characteristics are in accordance with these result, because no sensible variation is noticed. However the I-V measurements show an increase on the series resistance of the white LEDs, as pointed out in Figure 6.4 b). This could be due to the worsening of the ohmic contacts and translates into a decline in the LEDs efficacy. Moreover, an increase in the series resistance can lead to higher junction temperatures during operation at high current, shortening the devices lifetime.

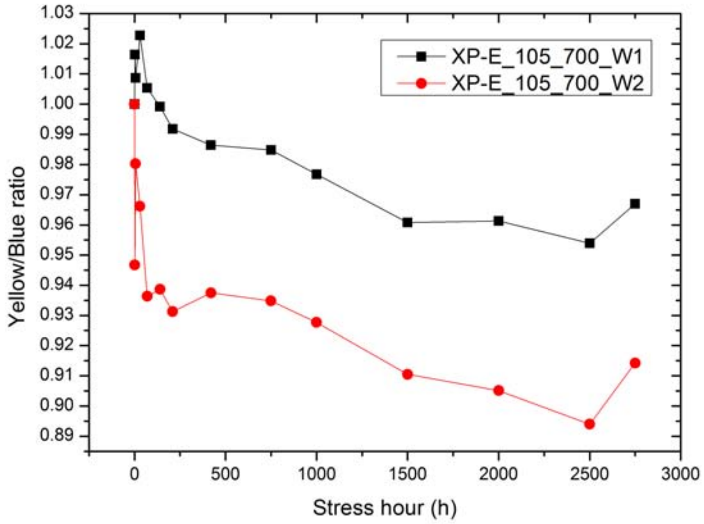

Figure 6.2: Yellow/Blue ratio of the XP-E_105_700 white LEDs.

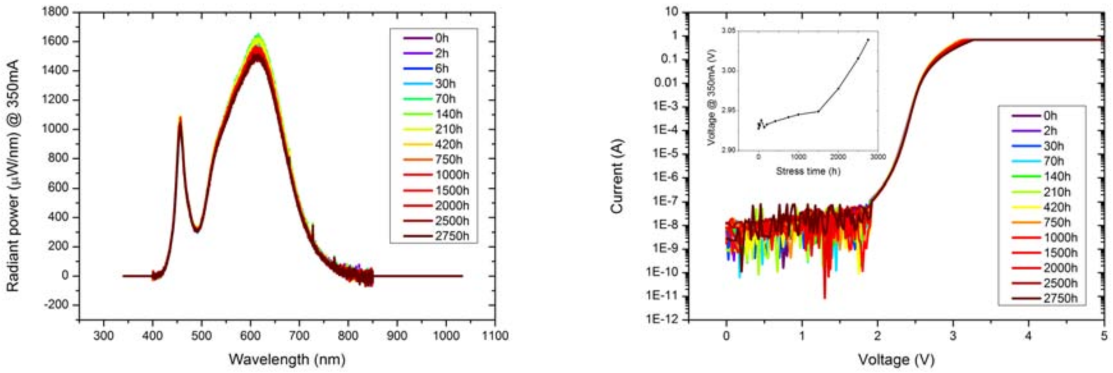

(a) Spectrum

(b) I-V characteristic

Figura 6.4: a) Spectrum at 350mA and b) I-V characteristic of the XP-E_105_700_W1.

In Figure 6.5 are reported the x,y coordinate and CCT measurements. They are the average of the two white LEDs values at 350mA. The variations are limited and the CCT shows a slight increase (i.e. a shift toward cooler color).

6.1.2 OSLON LEDs

Figure 6.6 shows the trend of the normalized optical power at 350 and 100mA. The two blue and one white LEDs suffer of a strong OP decay depending from the hours

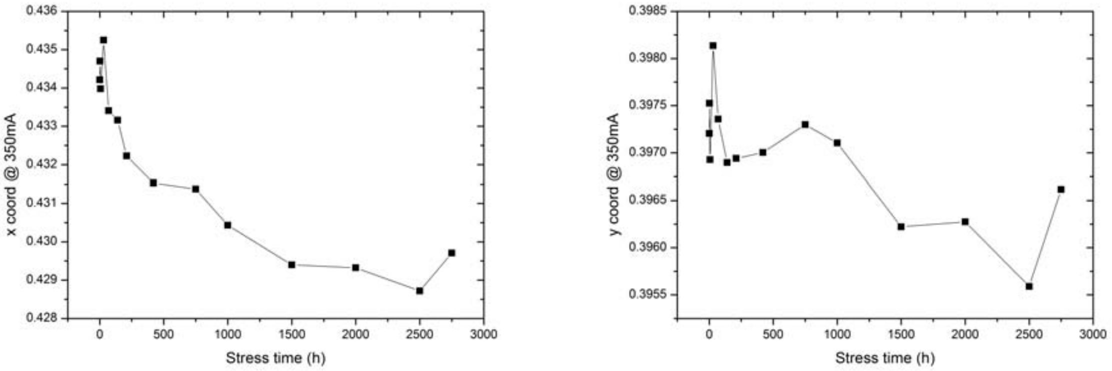

(a) x coordinate (b) y coordinate

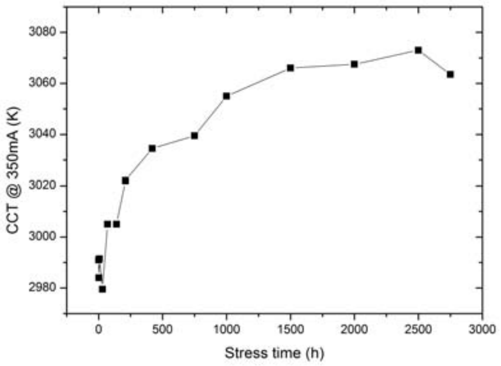

(c) CCT

Figura 6.5: The x,y coordinate and CCT measuraments for the XP-E_105_700 white LEDs.

of operation at which they were submitted. This decay may be due to a progressive increase of the nonradiative centers during operation. The presence of nonradiative centers is confirmed by the lower OP value reached by the plots in 6.6 b) , with respect of the values obtained for higher current operation. Figure 6.7 shows the spectrum of the OSLON_105_700_W1 and OSLON_105_700_B1 at 350mA, which confirm the OP decay.

The I-V characteristic of the green, blue and white LEDs show to suffer of a relevant changing during the device operation: Figure 6.8 clearly points out the creation of a preferential path for the current flow, which is highlighted by the non-neglible current absorption below the threshold voltage and the increase of the current for higher voltage. This is due to a parallel resistance that is represented by the non radiative

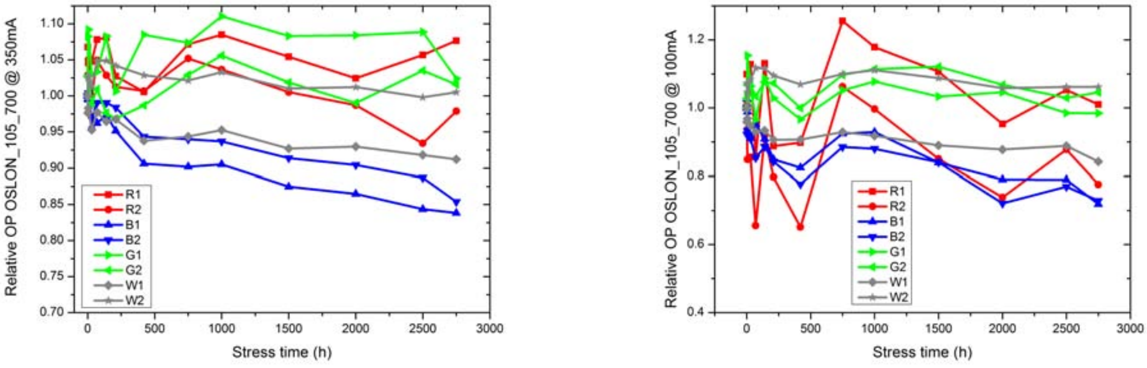

(a)

(b)

Figura 6.6: OP trend at a) 350mA and b) 100mA of the OSLON_105_700 devices.

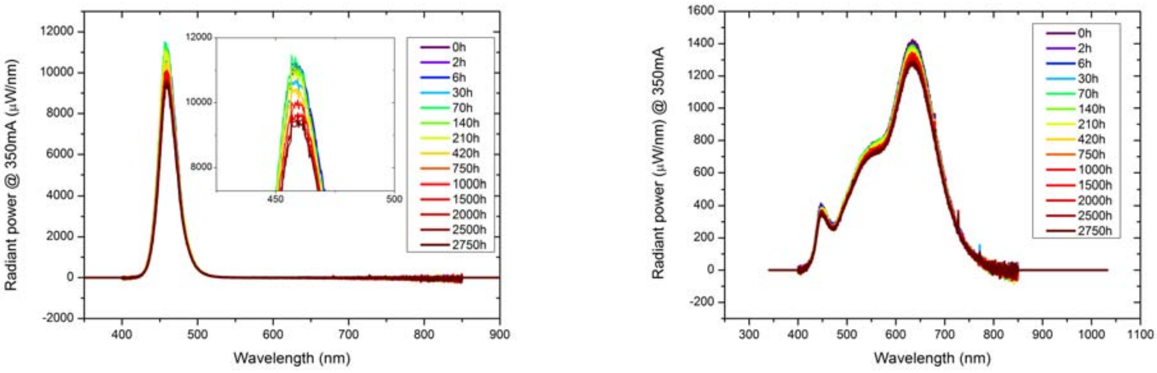

(a)

(b)

Figura 6.7: Spectrum of the: a) OSLON_105_700_B1 and b) OSLON_105_700_W1.

centers and other impurities trapped inside the lattice, whose presence has already been noticed with the L-I curves. Because of the presence of the parallel resistance in the electrical behavoiur of the OSLON devices, the presence of a series one has not been noticed: as a matter of fact, the parallel electrical path yields to an increase of the current that could hide the effect of the eventual worsening of the ohmic contacts, or in general of the electric changes of the chip.

In Figure 6.9 are reported the x,y coordinates and CCT measurements. They are the average of the two white LEDs values at 350mA. The colorimetric characteristics are not changing at all: the variations of the coordinates are below the 1% of the initial value.

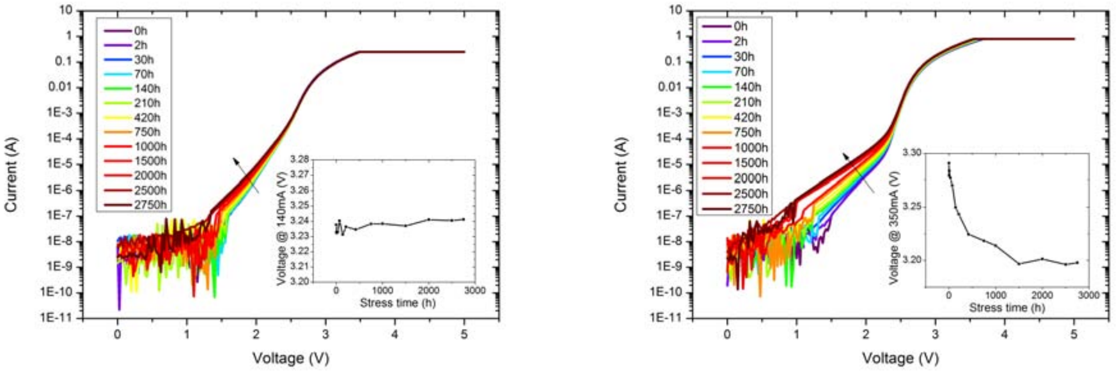

(a) OSLON_105_700_G2

(b) OSLON_105_700_B1

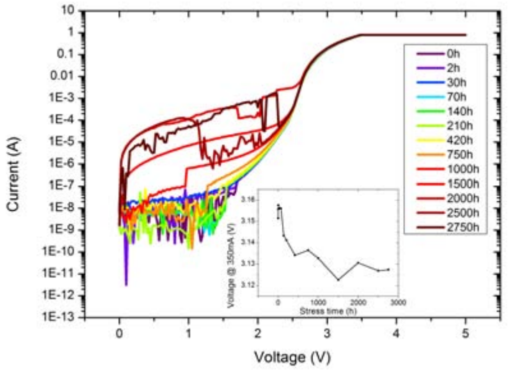

(c) OSLON_105_700_W2

Figura 6.8: I-V characteristics of the OSLON_105_700 devices.

6.1.3 REBEL LEDs

Even in this case the OP trend for a current of 100mA and 350mA is reported in Figure 6.10. The red and white LEDs have demonstrated to suffer of a strong OP decay. The decay is more evident at low-current injection thus it should be due to the increase of the nonradiative centers during operation. Figure 6.7 shows the spectrum of the REBEL_105_700_W1 and REBEL_105_700_R1 at 350mA, which confirm the OP decay in these devices.

As concerns the I-V measurements, two important phenomena have been verified: firstly, the threshold voltage has demonstred to shift towards lower values as the operation time increase, while for higher voltages the current absorption is lowered. The former is due to a gradual creation of a parallel resistance (according to the increase in the nonradiative centers), while the latter can be ascribed to the increase of the

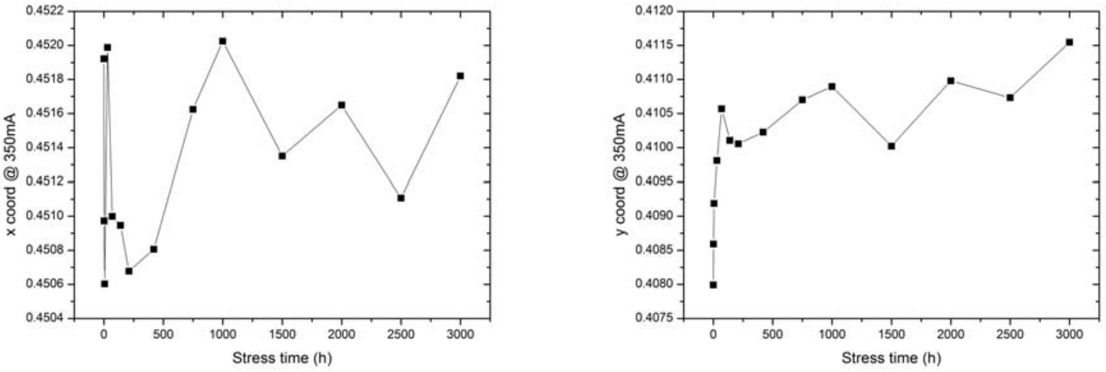

(a) x coordinate (b) y coordinate

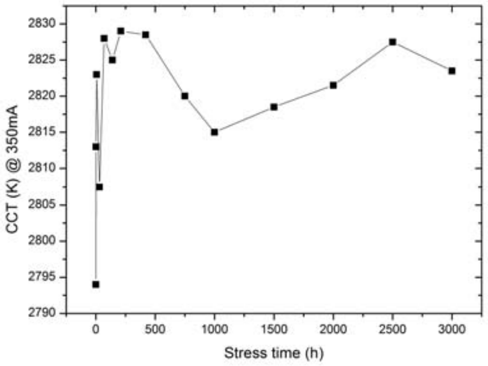

(c) CCT

Figura 6.9: The x,y coordinate and CCT measuraments for the OSLON_105_700 white LEDs.

series resistance. The parallel resistance is certainly caused by changes into the semiconductor lattice, while a worsening of the ohmic contacts can lead to the increase of the serial one. In Figure 6.13 are reported the x,y coordinate and CCT measurements. They are the average of the two white LEDs values at 350mA. Even in this case, the variations are very low and the CCT shows a slight increase (i.e. a shift toward cooler white point).

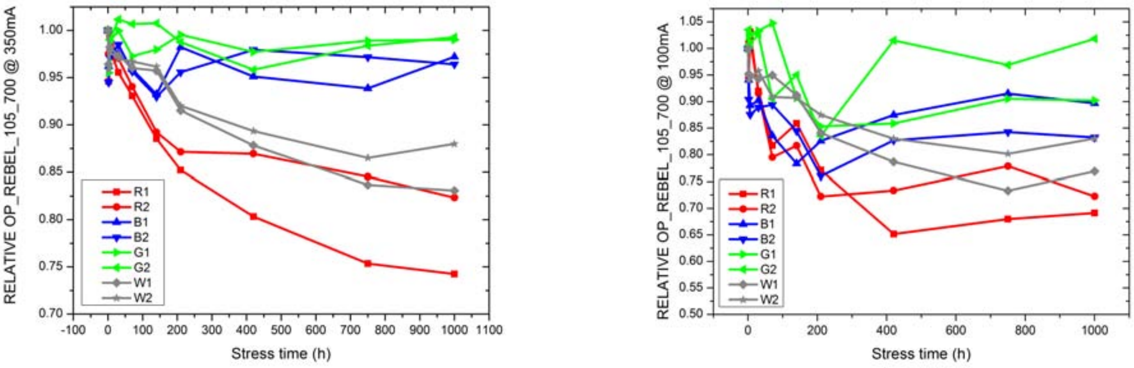

(a) (b)

Figura 6.10: OP trend at a) 350mA and b) 100mA of the REBEL_105_700 devices.

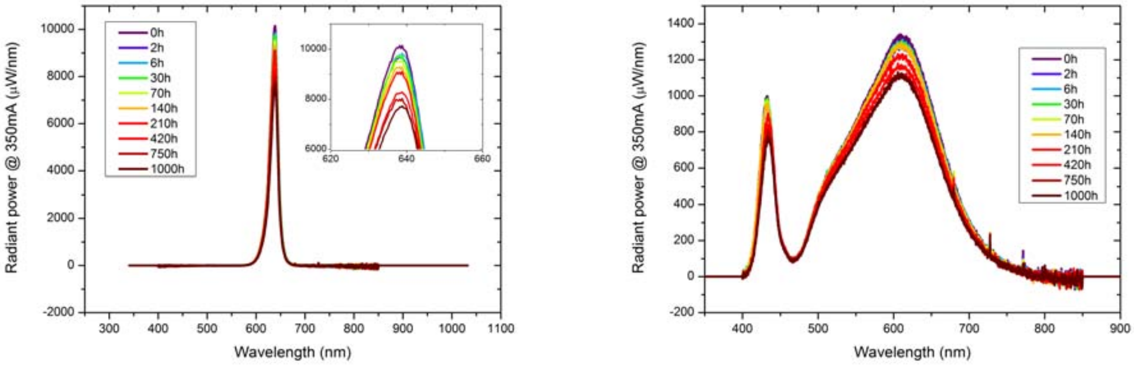

(a) (b)

Figura 6.11: Spectrum of the: a) REBEL_105_700_R1 and b) REBEL_105_700_W1.

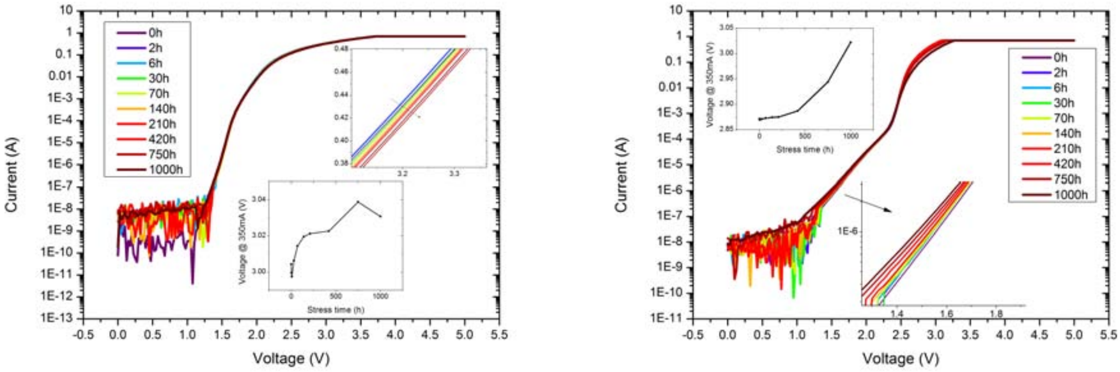

(a) REBEL_105_700_R1

(b) REBEL_105_700_B2

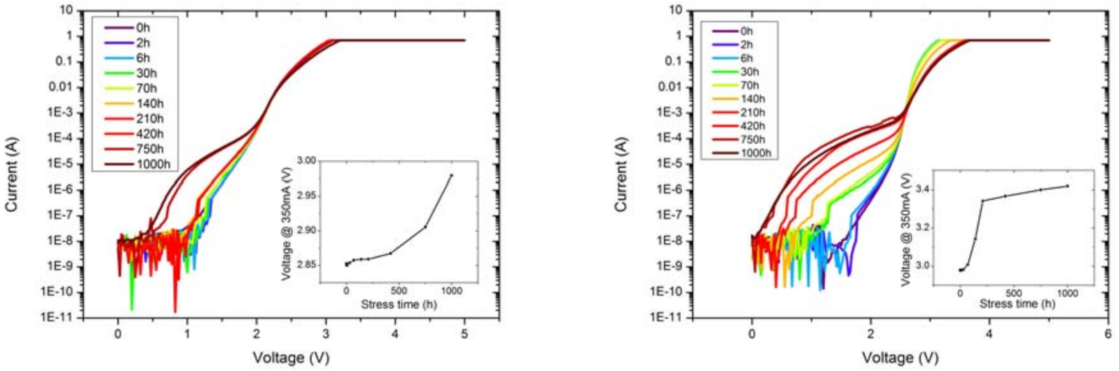

(c) REBEL_105_700_G1

(d) REBEL_105_700_W1

Figura 6.12: I-V characteristics of the REBEL_105_700 devices.

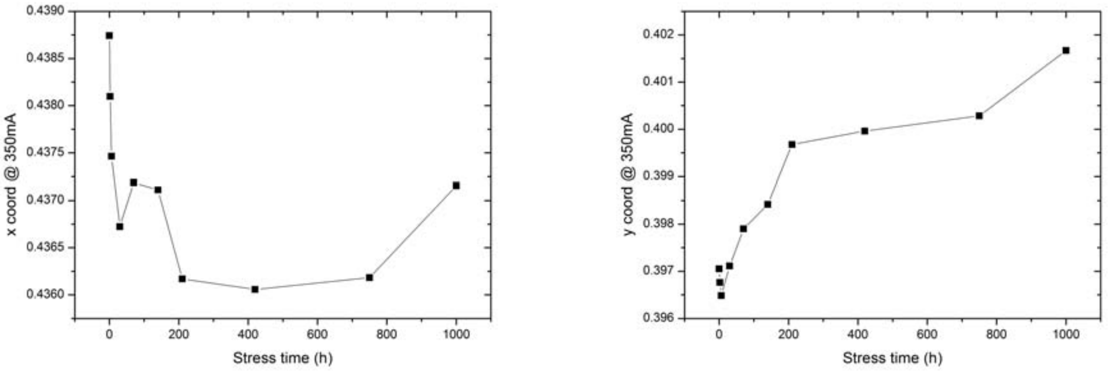

(a) x coordinate

(b) y coordinate

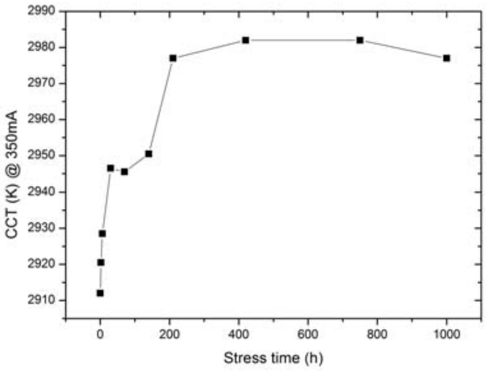

(c) CCT

Figura 6.13: The x,y coordinate and CCT measuraments for the REBEL_105_700 white LEDs.

6.1.4 Summary

LED name	OP(%)
XP-E_105_700_R1	1.01
XP-E_105_700_R2	3.922
XP-E_105_700_B1	8.86
XP-E_105_700_B2	9.61
XP-E_105_700_G1	5.04
XP-E_105_700_G2	10.13
OSLON_105_700_R1	7.67
OSLON_105_700_R2	-2.12
OSLON_105_700_B1	-16.17
OSLON_105_700_B2	-14.62
OSLON_105_700_G1	2.41
OSLON_105_700_G2	1.59
REBEL_105_700_R1	-23.98
REBEL_105_700_R2	-17.38
REBEL_105_700_B1	-1.92
REBEL_105_700_B2	-1.525
REBEL_105_700_G1	0.66
REBEL_105_700_G2	2.51

(a) Monochromatic LEDs.

LED name	OP(%)	x coord (%)	y coord (%)	CCT (K)
XP-E_105_700_W1	-3.65	-0.81	-0.13	2991-3045
XP-E_105_700_W2	-0.16	-1.26	-0.16	2991-3082
OSLON_105_700_W1	-8.801	-0.38	1.44	2784-2814
OSLON_105_700_W2	0.513	-0.34	0.89	2804-2839
REBEL_105_700_W1	-12.565	-0.11	0.81	2946-3022
REBEL_105_700_W2	-12.14	0.06	0.94	2878-2932

(b) White LEDs.

Tabella 6.1: Optical characteristics of the LEDs stressed at 105°C and 700mA.

In table 6.1 are presented the OP levels reached for every single LED stressed, together with the x,y percent variation and the initial and final CCT for the white LEDs.

These results highlight the fact that the optical power and the electrical characteristics given by the XP-E devices do not suffer this stress condition, while some of the OSLON (blue) and REBEL (red) devices show a relevant decay in the OP and degradation from the electrial point of view. However the REBEL devices have been mounted onto a different PCB, which leads to an higher mutual-heating of the LEDs. Thus a comparison with the devices of the oteher manufactures is not very useful.

Observing the I-V characteristics of the OSLON and REBEL devices are evident the generation of nonradiative center, which does not seem to occur in the CREE devices. The REBEL devices show a considerable increase in the series resistance that may be due to a worsening of the ohmic contacts.

As far as the white LEDs are concerned, only the CREE devices seem to show a phosphor degradation. However the OP decay is higher in the REBEL LEDs. This may be be due to the worse electrical characteristics of these devices than the ones of the other manufacturers. Finally, we note that the green LEDs of all the manufacturers don't suffer of any optical degradation in this stress condition.

6.2 Stress 125_700

6.2.1 XP-E LEDs

The optical power behaviour measured at 350mA is reported in Figure 6.14. The trend is normalized to the optical measurement conducted before the stress.

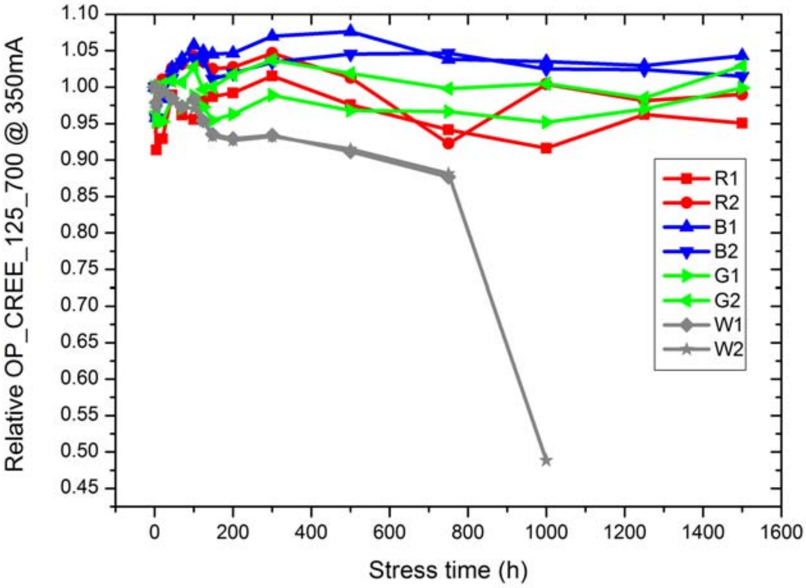

Figure 6.14: The OP trend for the first 1500 hours of operation of the XP-E devices, measured for a forward current of 350 mA.

The two white LEDs, running the 1000th and 1250th hour of stress, catastrophically crashed into a short circuit. Thus the devices were analyzed by the microscope and the obtained images are reported in Figure 6.15. It is evident the darkenening of the incapsulation material, which can lead to a worsening of the optical properties but is surely not responsible of the electrical short. On the other hand the bondings are not even melted or collapsed: the breaking is probably happened inside the package, and the short circuit could involve the whole active region. An electrical characterization via I-V measurements did not give any signicant response, as they behaved like perfect short, and so further investigation are recommended to fully understand what happened to them.

Observing Figure 6.14, one can notice that the white devices show a considerable OP decay until they crashed into a short circuit. Figure 6.16 a) shows that the yellow/blue

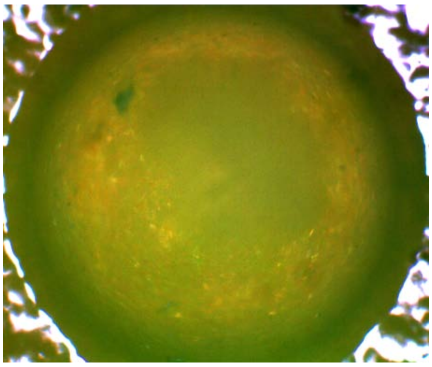

Figure 6.15: XP-E_125_700_W1 after 1000 hours.

ratio[1] presents an exponential decay during the stress: this is correlated to a decreased phosphor conversion efficiency. Therefore we can associate a significant part of the optical power decay of this devices to that phosphor degradation. In Figure 6.17 are reported the x,y coordinate and CCT measurements. They are the average of the two white LEDs values at 350mA. The x coordinate shows a slight decrease while the CCT shows a slight increase, i.e. a shift toward cooler color, which confirms the hypotehesis of the phosphor degradation .

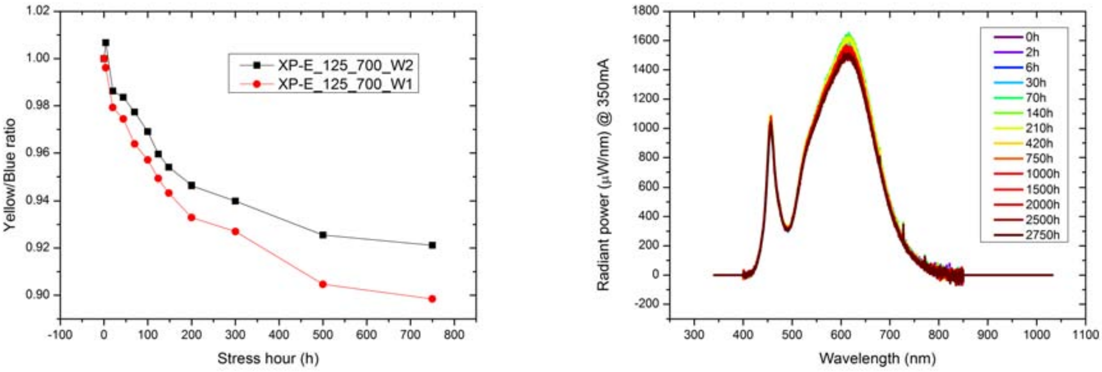

(a)

(b)

Figure 6.16: a) Yellow/blue ratio for the XP-E_125_700 white LEDs and b) Spectrum of the XP-E_127_700_W1.

As far as the electrical characteristics are concerned the I-V curves in Figure 6.18 show an increase on the diode series resistance, which is particularly evident in the white devices.

---

[1] The yellow/blue ratio is the ratio between the area rlative to the the phosphor emission and that relative to the blue peak.

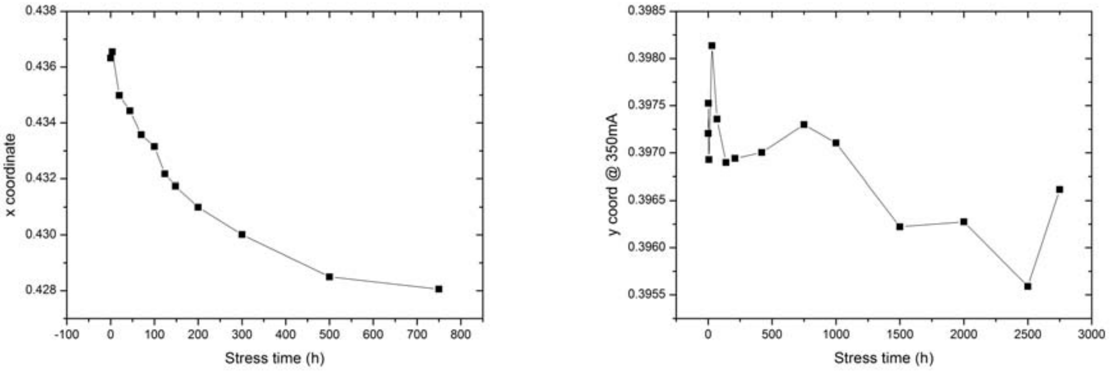

(a) x coordinate (b) y coordinate

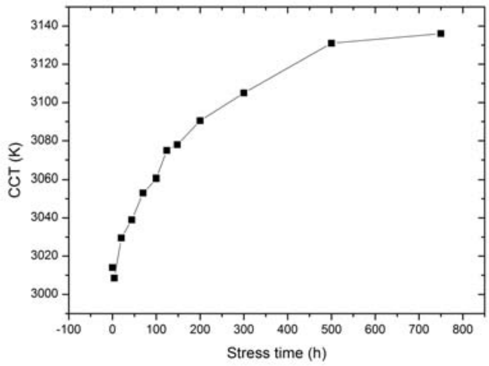

(c) CCT

Figura 6.17: The x,y coordinates and CCT measuraments for the XP-E_125_700 white LEDs.

6.2.2 OSLON LEDs

Figure 6.19 a) shows the trend of the normalized optical power at 350mA. The two white and one red LEDs suffer of a relevant OP decay. As concerns the white LEDs, the decay is under 5% of the initial value until the 1000th hour of stress and then show a substantial drop up to 15%. This may be due to a high decrease in the conversion efficiency of the phosphor. As proof of it, figure 6.19 b) shows the normalized trend of the blue, yellow and red peak of the spectrum (these devices uses a multi-phosphor approach for producing white light) of the OSLON_125_700_W2 LED. It is evident that after 1000 hours of stress the blue peak icreases while the others suffer of a strong decay. This phenomenon is also well visible in the spectrum of Figure 6.20.

The OP decay of the OSLON_125_700_R2 may be due to a progressive darkening

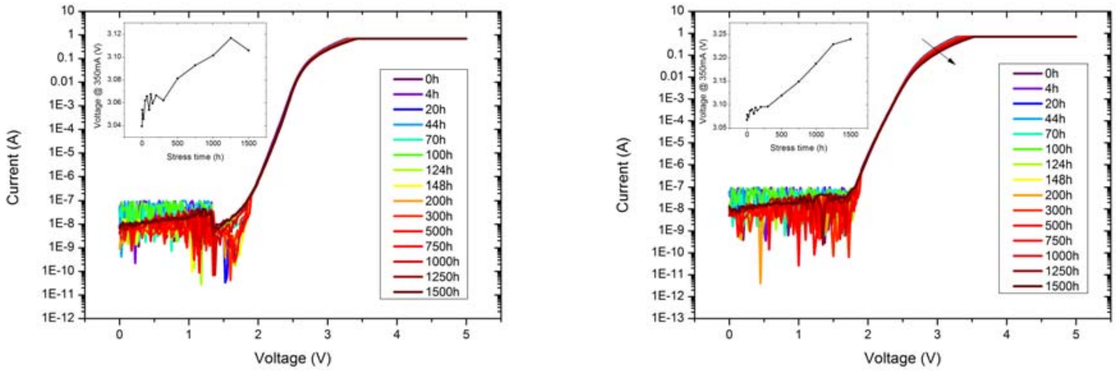

(a) XP-E_125_700_B1

(b) XP-E_125_700_G2

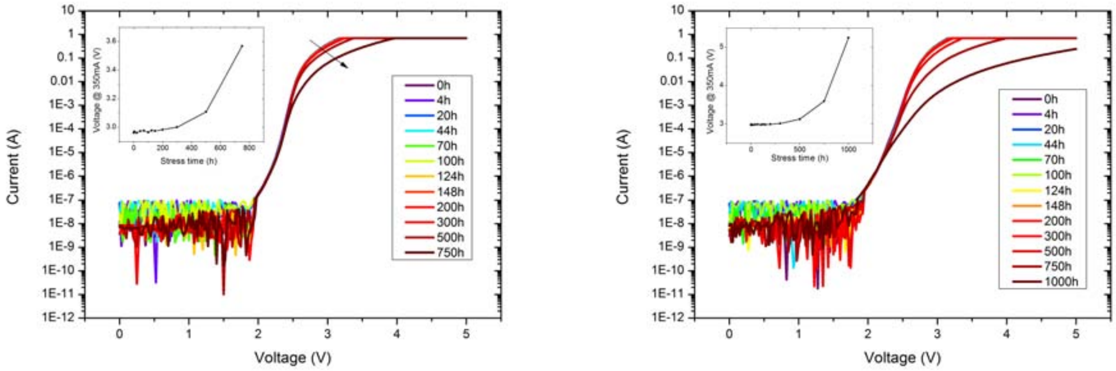

(c) XP-E_125_700_W1

(d) XP-E_125_700_W2

Figura 6.18: I-V characteristics of the XP-E_125_700 devices.

of the encapsulation material.

In Figure 6.17 are reported the x,y coordinates and CCT measurements at 350mA. The x and y coordinates show a slight decrease in both devices.

The I-V characteristic of the green, blue and white LEDs show to suffer of a relevant changing during the device operation: Figure 6.22 clearly points out the creation of a preferential path for the current flow, which is highlighted by the non-neglible current absorption below the threshold voltage and the increase of the current for higher voltage. This is due to a parallel resistance that is formed by lattice defects which act as non-radiative recombination centers.

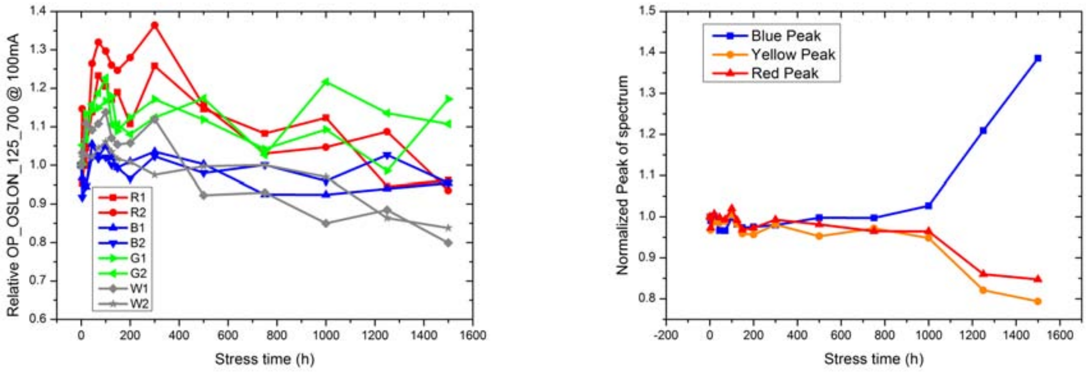

(a) OSLON_125_700_W1

(b) OSLON_125_700_W2

Figura 6.19: a) OP trend at 350mA of the OSLON_125_700 devices, b) Normalized trend of the blue, yellow and red peak of the OSLON_125_700_W2..

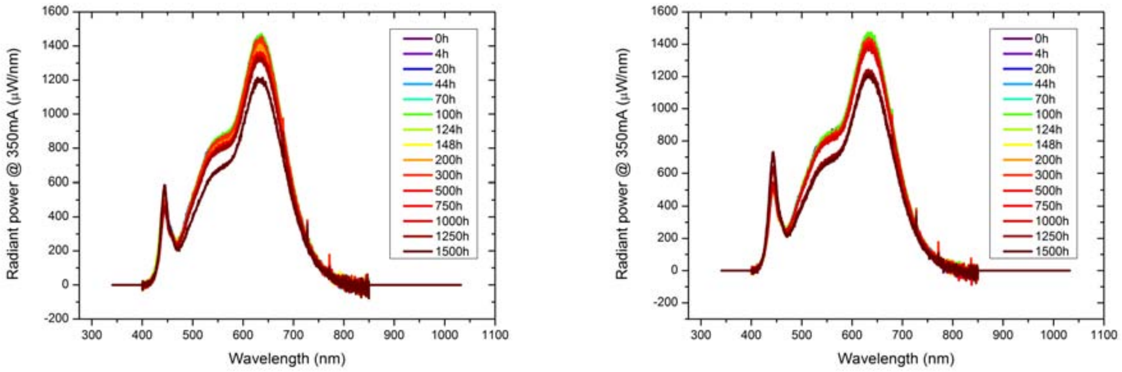

(a) OSLON_125_700_W1

(b) OSLON_125_700_W2

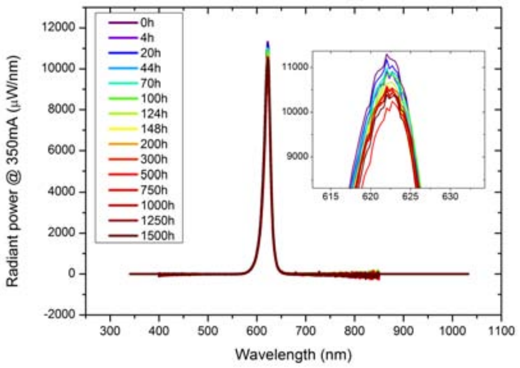

(c) OSLON_125_700_R2

Figura 6.20: Spectrum of the OSLON_125_700 devices.

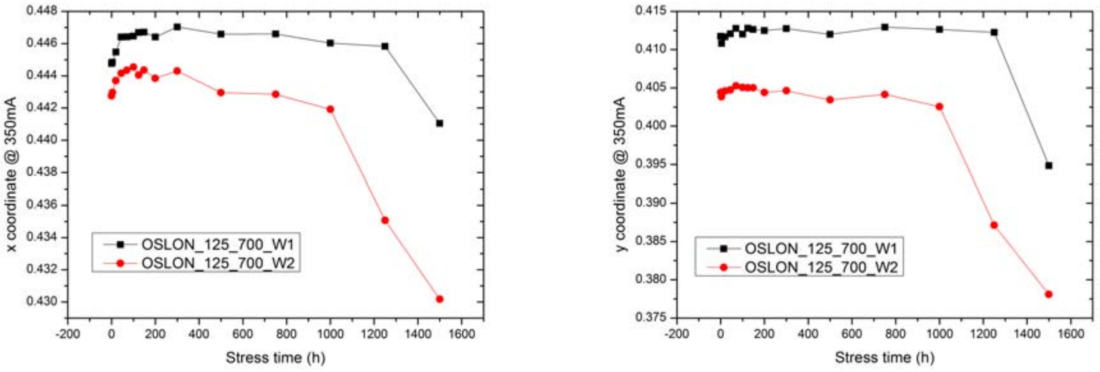

(a) x coordinate

(b) y coordinate

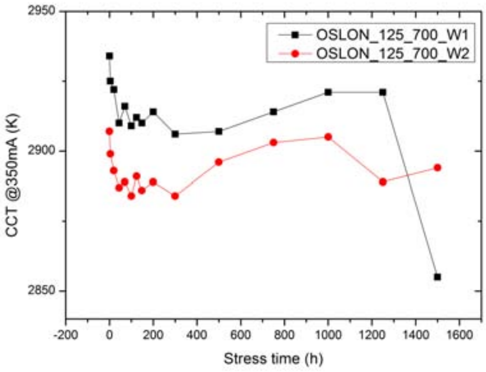

(c) CCT

Figura 6.21: The x,y coordinates and CCT measuraments for the OSLON_125_700 white LEDs.

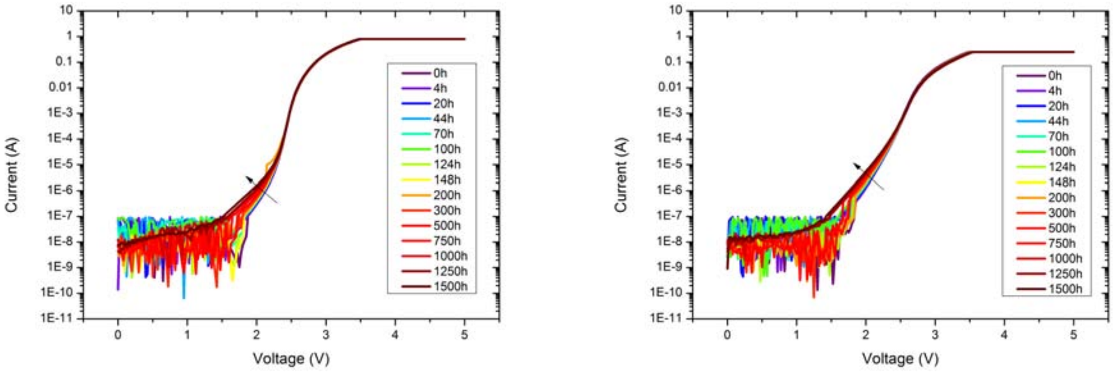

(a) OSLON_125_700_B2

(b) OSLON_125_700_G1

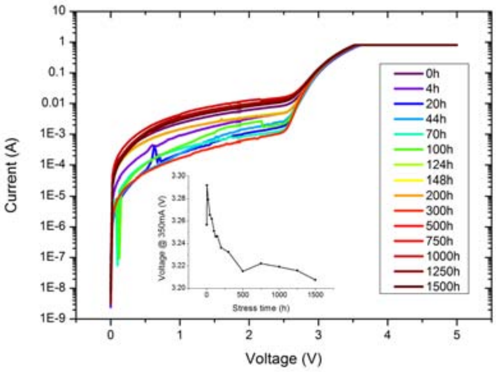

(c) OSLON_125_700_W1

Figura 6.22: I-V characteristics of the OSLON_125_700 devices.

6.2.3 REBEL LEDs

The OP trend for a current of 100mA and 350mA is reported in Figure 6.23. The REBEL_125_700_R1 device shows a lens breaking (see Figure 6.24) after 100 hours of operation that leads to a high drop in the OP. This may be due to the high temperature reached by the device during the stress. As a matter of fact the I-V characteristics of the REBEL red LEDs show a high serial resistance that can lead to a not neglible self-heating of the devices.

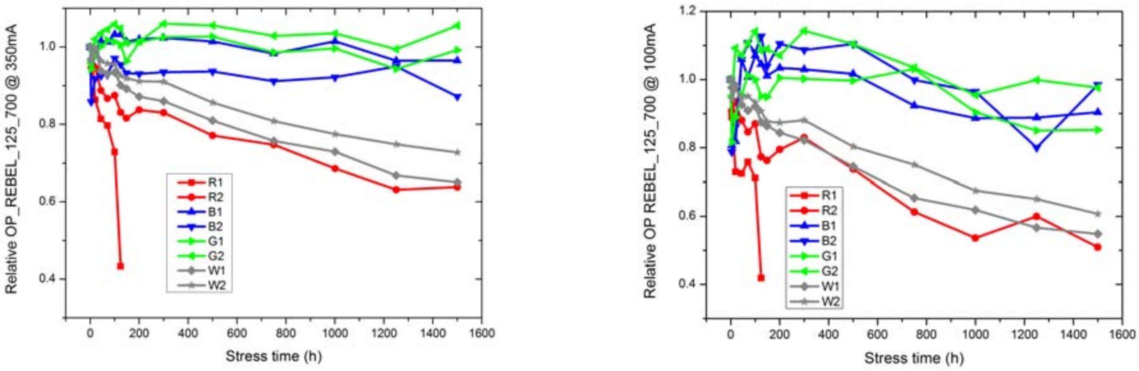

(a) (b)

Figura 6.23: OP trend at a) 350mA and b) 100mA of the REBEL_125_700 devices.

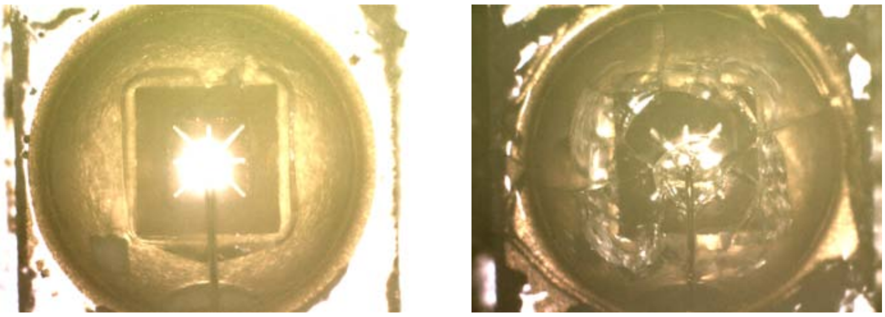

(a) REBEL_125_700_R1 at 0-hour.

(b) REBEL_125_700_R1 at 100-hour.

Figura 6.24: Pictures of the REBEL_125_700_R1.

The REBEL_125_700_R2 and the white LEDs have demonstrated to suffer of a strong OP decay. The decay is more evident in the low current operation thus it should be due to the increase of the nonradiative centers during operation. However, after 1500 hours, the white LEDs show some cracks on the lens (see Figure

6.25) that can contribute to the OP decay. Moreover the breaking of the lens for the REBEL_125_700_R1 suggest that a degradation of the lens could contribute to the OP decay of the REBEL_125_700_R2.

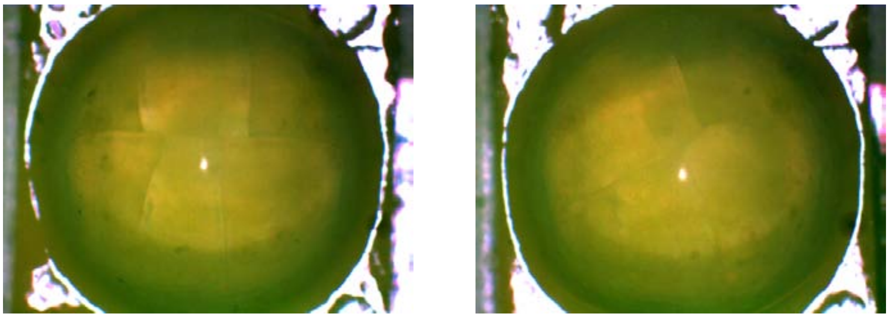

(a) REBEL_125_700_W1.

(b) REBEL_125_700_W2.

Figura 6.25: Pictures of the REBEL_125_700 white LEDs at 1500-hour.

Figure 6.7 shows the spectrum of the REBEL_125_700_W1 and REBEL_125_700_R2 at 350mA, which confirm the OP decay in these devices.

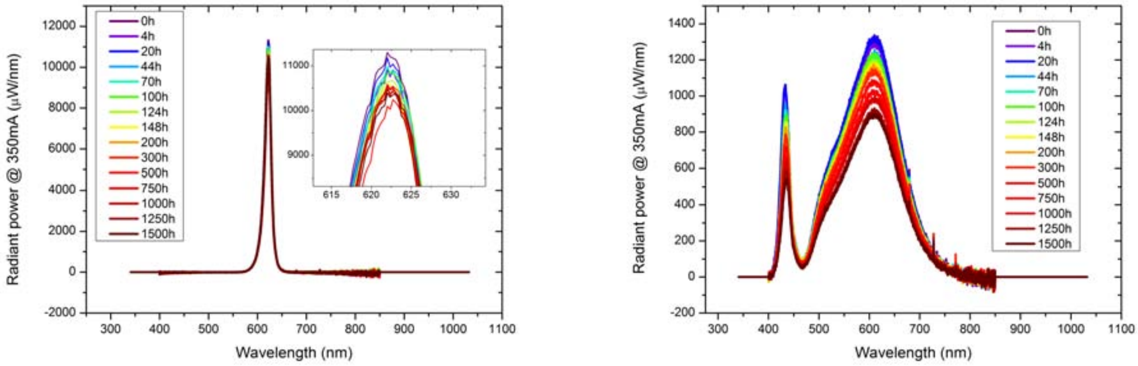

(a)

(b)

Figura 6.26: Spectrum of the: a) REBEL_125_700_R1 and b) REBEL_125_700_W1.

As concerns the I-V measurements, two important phenomena have been verified: firstly, the creation of a parallel resistance (according to the increase in the nonradiative centers), secondly the presence of a serial resistance. The parallel resistance is certainly caused by changes into the semiconductor lattice, while a worsening of the ohmic contacts can lead to the increase of the serial one.

In Figure 6.28 are reported the x,y coordinate and CCT measurements at 350mA. The CCT shows a slight decrease (i.e. a shift toward warmer color).

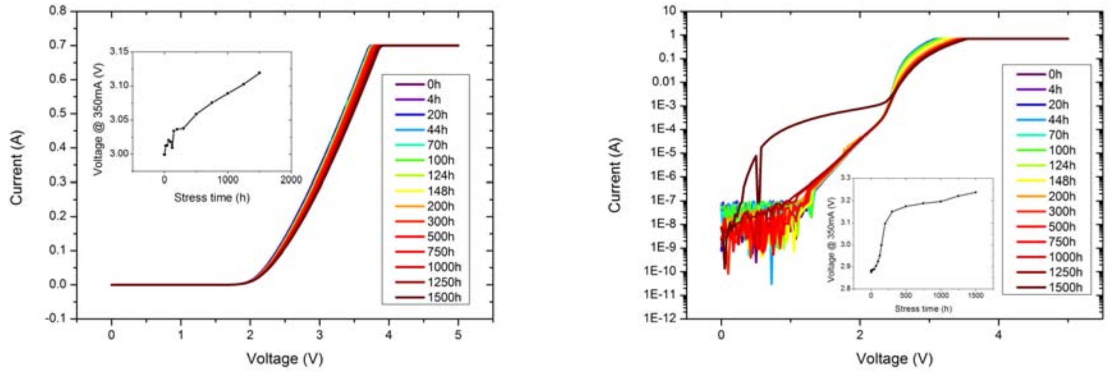

(a) REBEL_125_700_R2 (b) REBEL_125_700_B1

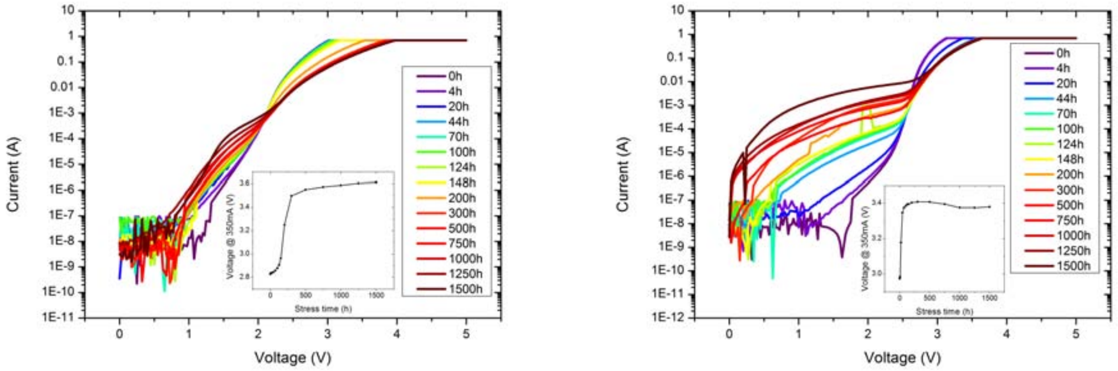

(c) REBEL_125_700_G2 (d) REBEL_125_700_W1

Figura 6.27: I-V characteristics of the REBEL_125_700 devices.

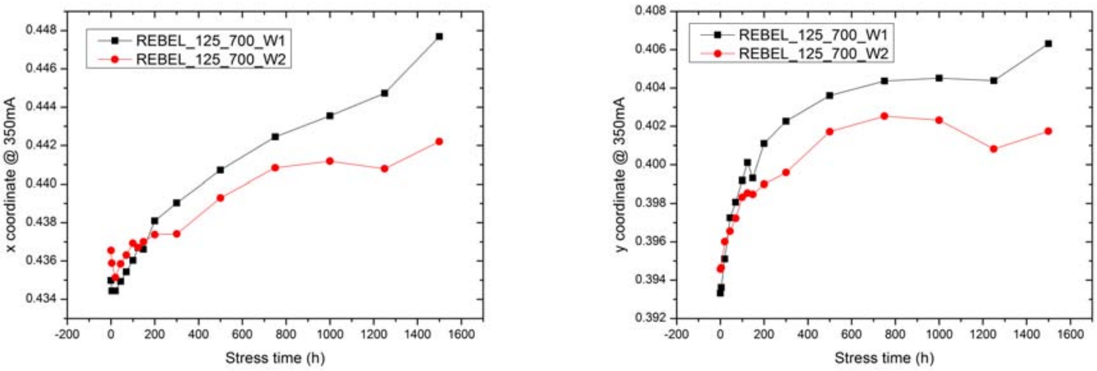

(a) x coordinate

(b) y coordinate

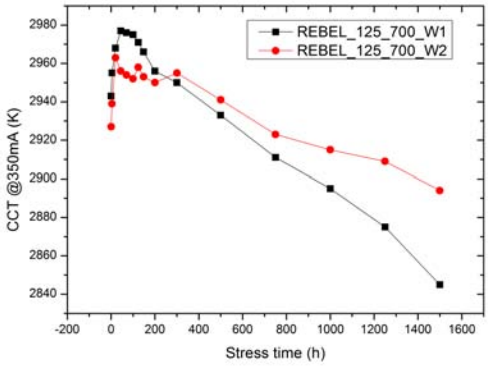

(c) CCT

Figura 6.28: The x,y coordinate and CCT measurements for the REBEL_125_700 white LEDs.

6.2.4 Samsung, LG and SEOUL LEDs

Figure 6.29 shows the trend of the normalized optical power at 350mA after 750 hours of operation. The SEOUL devices suffer of a strong OP decay. Since it is note visible any kind of yellowing or deterioration of the package, degradation of optical characteristics can be attributed only to changes of electrical nature. Figure 6.30 shows the spectra of these LEDs at 350mA, which confirm the strong OP decay in the SEOUL devices.

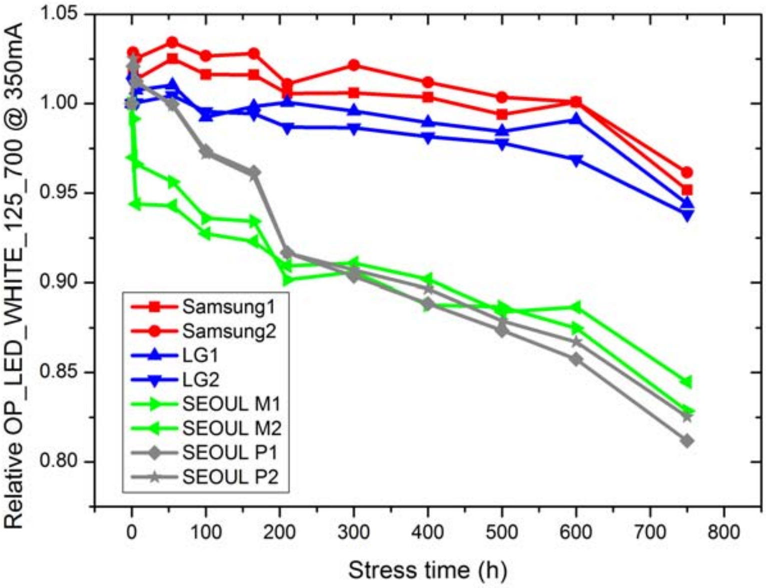

Figura 6.29: OP trend at 350mA of the WHITE_LEDs_125_700 devices.

As concerns the I-V measurements, the LG and SEOUL M devices show the growth of a parasitic shunt resistance, which substract current to the active zone of the devices, and an increase in the series one, while the Samsung and SEOUL M show the presence of only the first effect.

In Figures 6.32 to 6.35 are reported the x,y coordinates and CCT measurements. They are the average of the two LEDs values at 350mA. For the SEOUL devices, especially for Z5P, the x,y coordinates show a moderate increase and the CCT shifts toward warmer white point while for the samsung devices the CCT increases. Insteatd for the LG LEDs the colorimetric characteristics remain virtually constant.

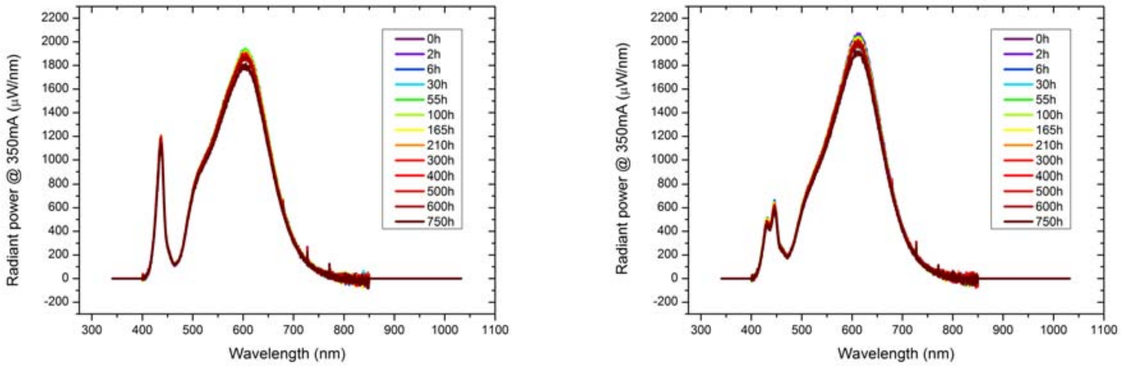

(a) WHITE_LEDs_125_700_Samsung1 (b) WHITE_LEDs_125_700_LG1

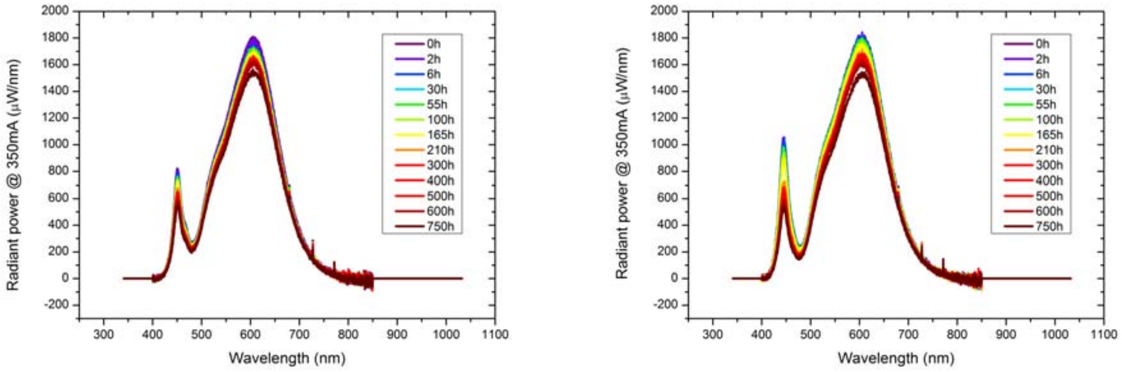

(c) WHITE_LEDs_125_700_SEOUL M1 (d) WHITE_LEDs_125_700_SEOUL P1

Figura 6.30: Spectrum of the WHITE_LEDs_125_700 devices.

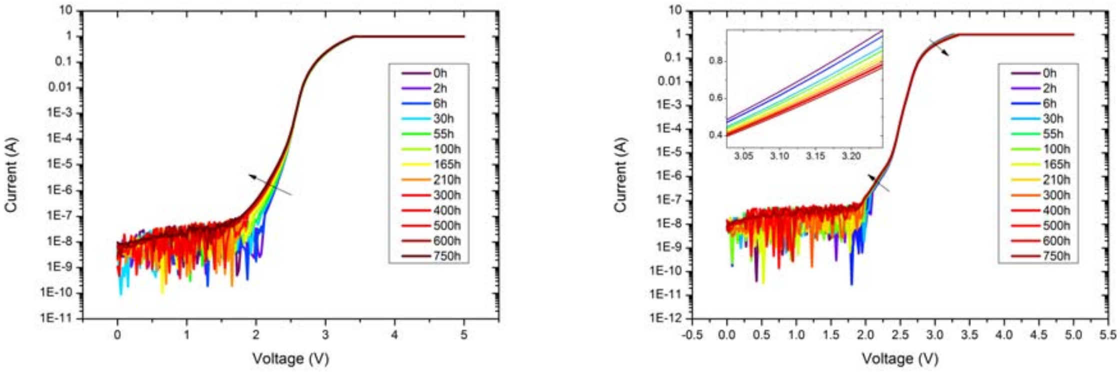

(a) WHITE_LEDs_125_700_Samsung1

(b) WHITE_LEDs_125_700_LG1

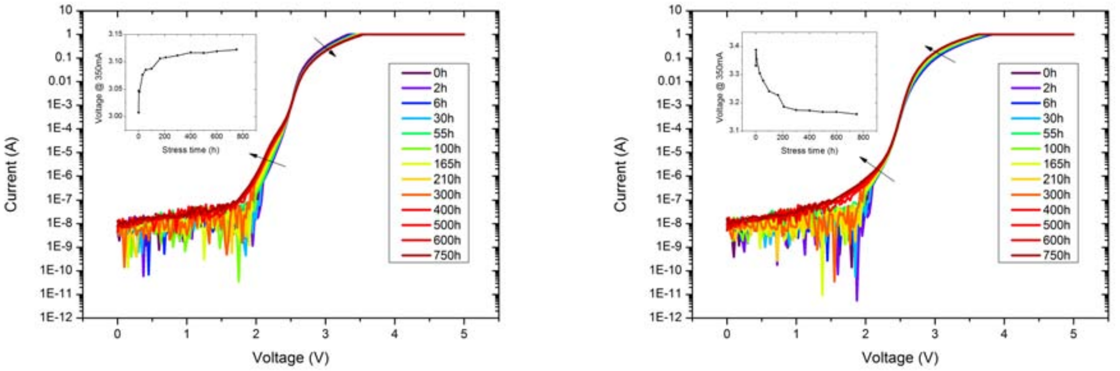

(c) WHITE_LEDs_125_700_SEOUL M1

(d) WHITE_LEDs_125_700_SEOUL P1

Figura 6.31: I-V characteristics of the WHITE_LEDs_125_700 devices.

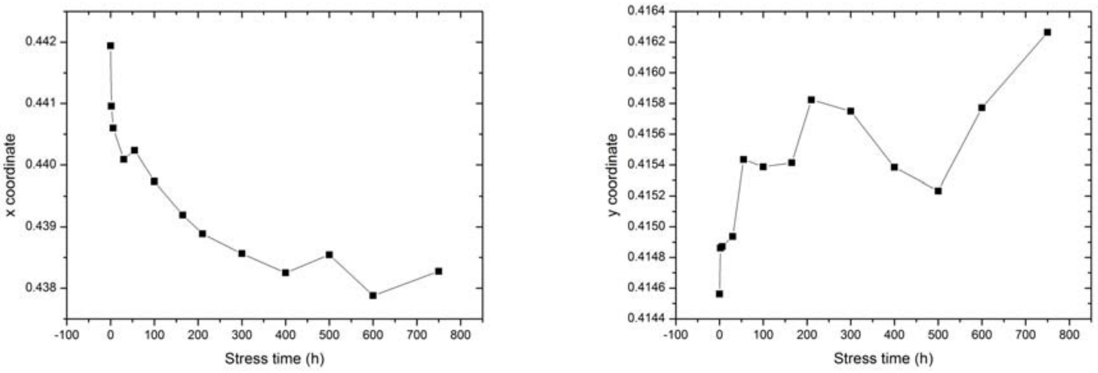

(a) x coordinate

(b) y coordinate

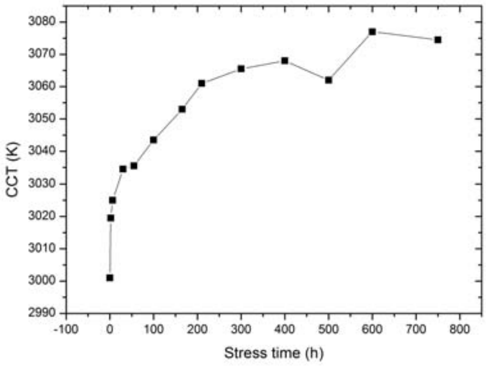

(c) CCT

Figura 6.32: The x,y coordinates and CCT measuraments for the Samsung LEDs.

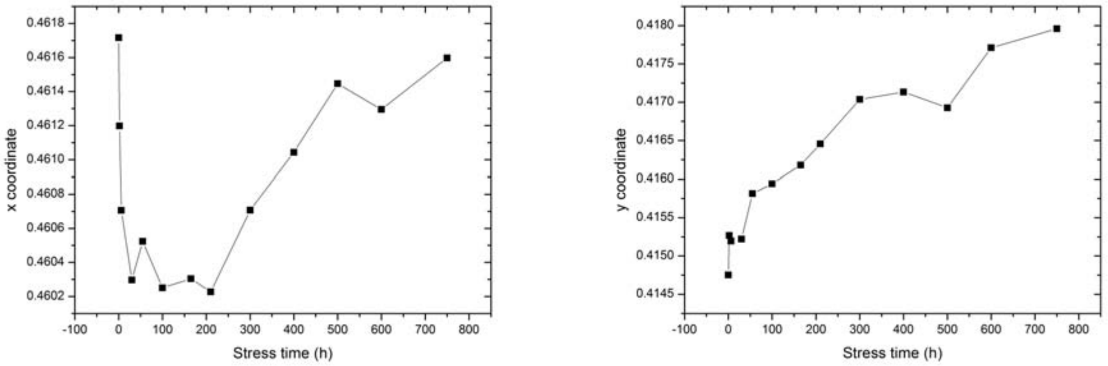

(a) x coordinate (b) y coordinate

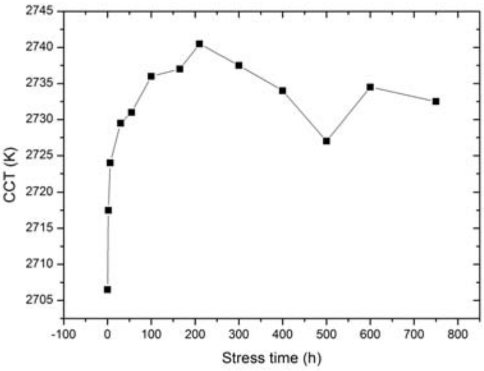

(c) CCT

Figura 6.33: The x,y coordinates and CCT measuraments for the LG LEDs.

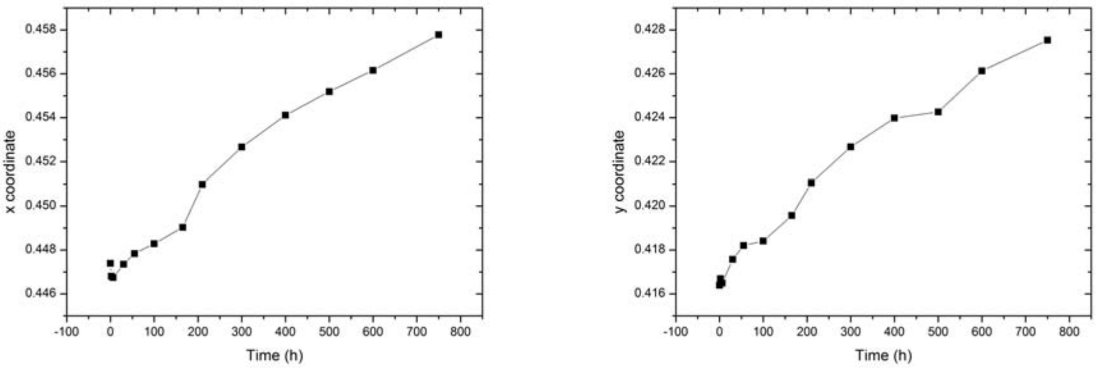

(a) x coordinate (b) y coordinate

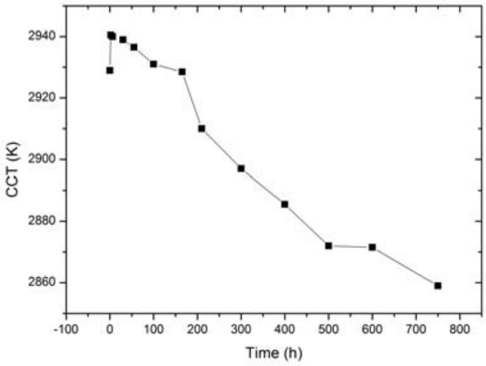

(c) CCT

Figura 6.34: The x,y coordinates and CCT measuraments for the SEOUL M LEDs.

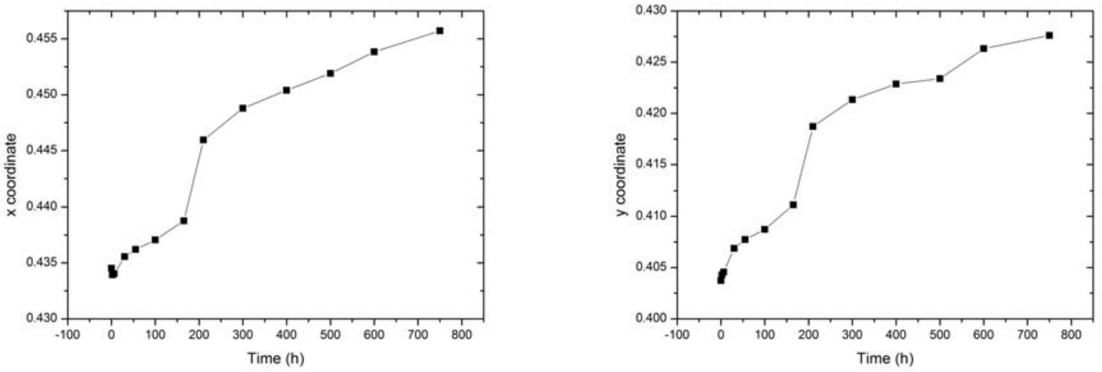

(a) x coordinate

(b) y coordinate

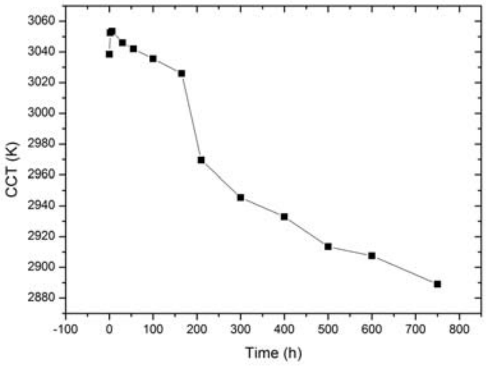

(c) CCT

Figura 6.35: The x,y coordinates and CCT measuraments for the SEOUL P LEDs.

6.2.5 Summary

In table 6.2 are presented the OP levels reached for every single LED stressed, together with the x,y percent variation and the initial and final CCT for the white LEDs.

These results highlight the fact that the white LEDs of all manufactures suffer of a strong OP decay in this stress conditions. For the OSLON and CREE devices this seem to be due to a phosphor degradation, for the REBEL to the formation of nonradiative centers and to a degradation of the lens, while for the other manufacturers the decay can be attributed to changes in the electrical characteristics of the devices. However the CREE devices catastrophically crashed into a short circuit after 1000 and 1250 hours of operation. This suggests that the OP decay can also be due to a worsening of the electrical characteristics of the LEDs.

As far a s the coloured LEDs are concerned, the results highlight that the optical characteristics of the CREE devices are more stable that the other manufacturers. Again the green LEDs of all the manufacturers don't suffer of any optical degradation in this stress condition.

Even in this case the REBEL and OSLON devices show the creation of nonradiative centers, that is confirmed by the presence of a parallel resistance in the I-V characteristics. The CREE and REBEL devices show a high increase in the series resistance. The REBEL red LEDs suffer of degradation and breaking of the lens that may be due to the high series resistance that could lead to a considerable self-heating of the devices.

LED name	OP(%)
XP-E_125_700_R1	-4.96
XP-E_125_700_R2	-1.01
XP-E_125_700_B1	4.3
XP-E_125_700_B2	1.49
XP-E_125_700_G1	-0.11
XP-E_125_700_G2	2.91
OSLON_125_700_R1	4.35
OSLON_125_700_R2	-10.77
OSLON_125_700_B1	-1.03
OSLON_125_700_B2	-3.21
OSLON_125_700_G1	-1.78
OSLON_125_700_G2	1.18
REBEL_125_700_R1	-56.68 (after 124h)
REBEL_125_700_R2	-36.19
REBEL_125_700_B1	-3.48
REBEL_125_700_B2	-12.79
REBEL_125_700_G1	-0.77
REBEL_125_700_G2	5.57

(a) MonochromaticLEDs.

LED name	OP(%)	x coord (%)	y coord (%)	CCT (K)
XP-E_125_700_W1	-12.33 (after 750h then crashed)	-2.15	-0.90	3015-3145
XP-E_125_700_W2	-51.52 (after 1000h then crashed)	-1.71	-0.44	3013-3127
OSLON_125_700_W1	-15.46	-0.84	-4.28	2934-2855
OSLON_125_700_W2	-15.46	-2.92	-6.97	2907-2894
REBEL_125_700_W1	-34.92	2.84	3.20	2943-2845
REBEL_125_700_W2	-27.22	1.28	1.78	2927-2894
WHITE_LEDs_125_700_Samsung1	-4.82	-0.82	0.44	3030-3104
WHITE_LEDs_125_700_Samsung2	-4.821	-0.85	0.38	2972-3045
WHITE_LEDs_125_700_LG1	-5.59	-0.07	0.71	2707-2734
WHITE_LEDs_125_700_LG2	-6.19	0.02	0.83	2706-2731
WHITE_LEDs_125_700_SEOUL M1	-17.16	2.16	2.53	2905-2841
WHITE_LEDs_125_700_SEOUL M2	-15.53	2.37	2.68	2953-2877
WHITE_LEDs_125_700_SEOUL P1	-18.82	5.00	5.93	3042-2879
WHITE_LEDs_125_700_SEOUL P2	-17.48	4.30	5.24	3035-2899

(b) White LEDs.

Tabella 6.2: Optical characteristics of the LEDs stressed at 125°C and 700mA.

6.3 Stress 125-1000

The conditions of this stress have proved to be very thrusts. In fact some devices catastrophically crashed into a short or a open circuit during this stress and and the lenses of some LEDs show cracks and damage.

6.3.1 XP-E LEDs

The behaviour of the Optical power for a current of 350mA is reported in Figure 6.36. The trend is normalized to the initial value.

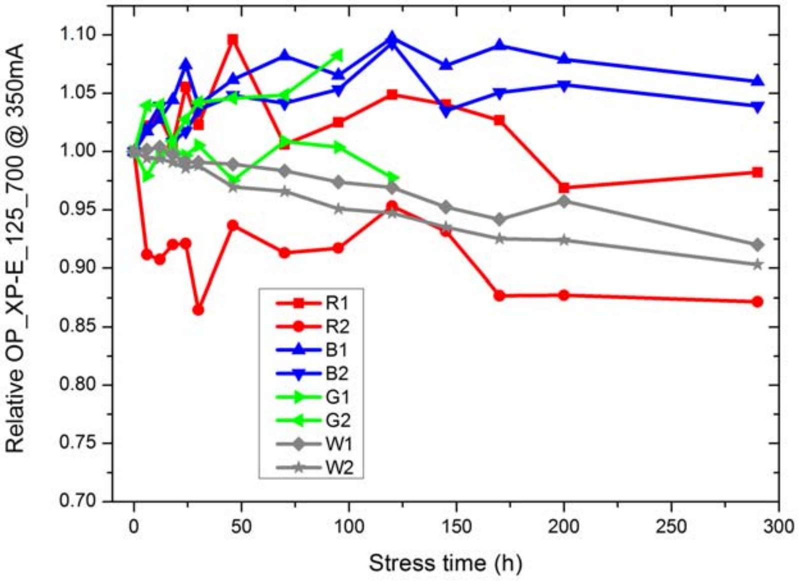

Figure 6.36: OP trend at 350mA of the XP-E_125_1000 devices.

The two green LEDs, running the 95th and 120th hour of stress, catastrophically crashed into a short circuit. Thus the devices were analyzed by the microscope but no damages on the lens, the package and the bondings were noticed. Therefore the breaking is probably related to the lattice fusion inside the active area of the chip which causes the junction shortening. An electrical characterization via I-V measurements show a high increase in the series resistance of the devices until they crashed into a short (see Figure 6.39 b)).

Observing Figure 6.36, one can notice that the XP-E_125_1000_R2 and white LEDs show a considerable OP decay. Figure 6.37 a) shows that the yellow/blue ratio presents an exponential decay during the stress: this is correlated to a decrease of the efficiency of the phosphor. Therefore we can associate a significant part of the optical power decay of the white devices to that phosphor degradation. In Figure 6.38 are

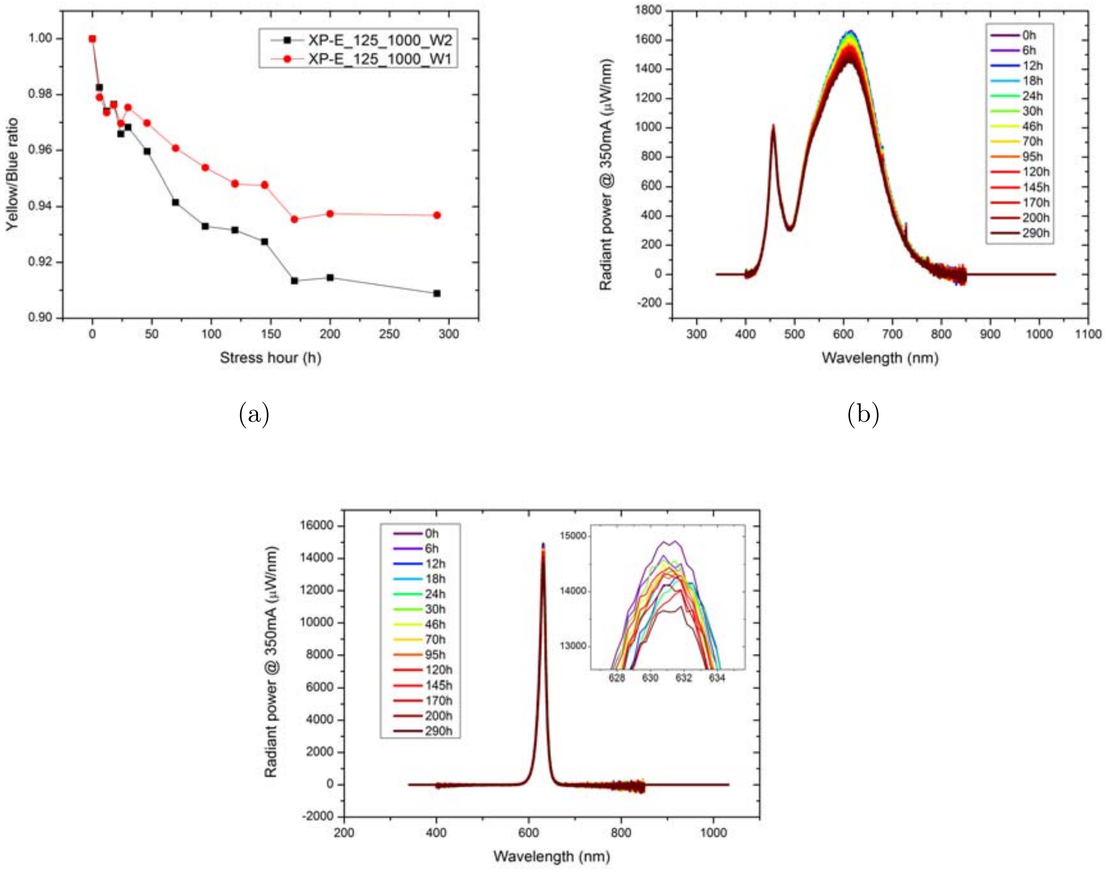

(a)

(b)

(c)

Figure 6.37: a) Yellow/blue ratio for the XP-E_125_1000 white LEDs, b) Spectrum of the XP-E_127_1000_W1 and c) Spectrrum of the XP-E_125_1000_R2.

reported the x,y coordinates and CCT measurements. They are the average of the two white LEDs values at 350mA. The x and y coordinates show a slight decrease while the CCT shows a slight increase, i.e. a shift toward cooler color, which confirms the hypotehesis of the phosphor degradation. .

As far as the electrical characteristics the I-V curves show an increase on the diode series resistance, which is particularly evident in the white and green devices.

6.3.2 OSLON LEDs

Figure 6.40 shows the trend of the normalized optical power at 350mA.

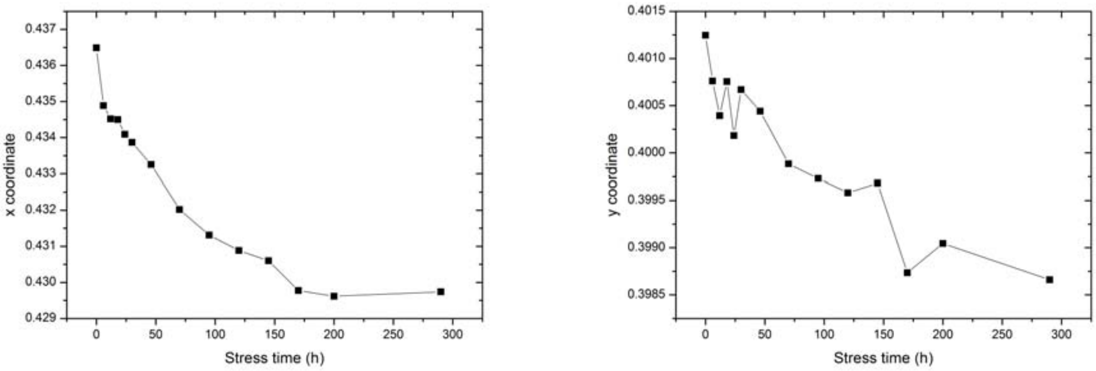

(a) x coordinate

(b) y coordinate

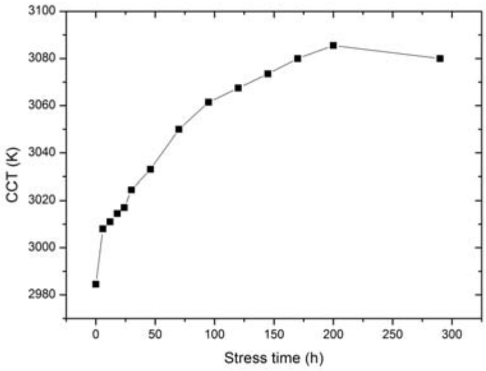

(c) CCT

Figura 6.38: The x,y coordinates and CCT measuraments for the XP-E_125_1000 white LEDs.

The OSLON_125_1000_B2 and two red LEDs crashed into a short circuit during the 145th hour of operation. As reported for the Cree devices, the LEDs fail can be exclusively associated to a shortening of the active area of the chip due to over-heating. Because the three devices crashed at the same istant we can hypothesize that it could be due to an accidal over-current or over-voltage event.

As concerns the white LEDs, they show a catastrophic breaking of the e lens (see Figure 6.41) after 120 and 200 hours. This may be due to the high temperature reached by the device during the stress. The OP decay before the catastrophic braking of the lens, may be due to a decrease in the conversion efficiency of the phosphor, and to the degradation of the lens obviously .

The OP decay of the OSLON_125_1000_B1 may be due to a progressive increase of the nonradiative centers during operation as confirmed by the I-V characteristic

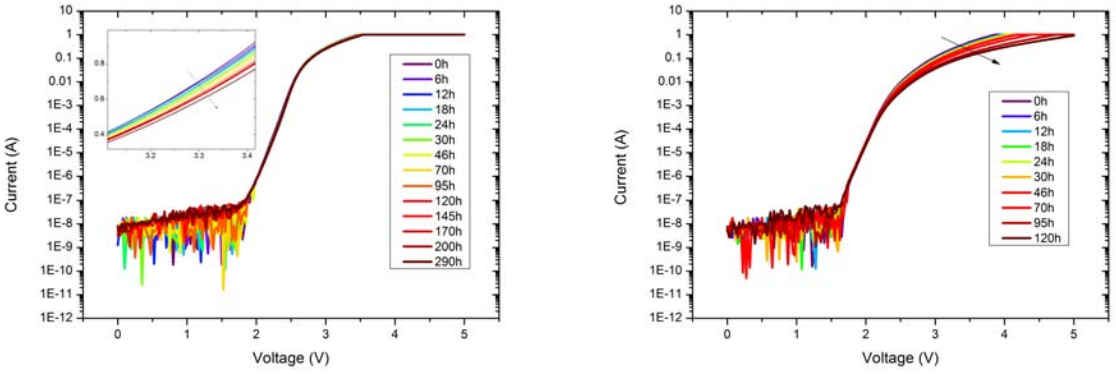

(a) XP-E_125_1000_B1

(b) XP-E_125_1000_G1

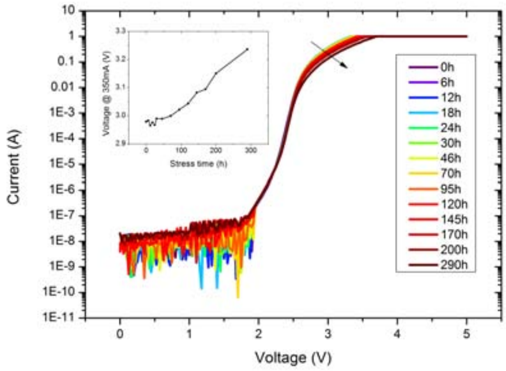

(c) XP-E_125_1000_W1

Figura 6.39: I-V characteristics of the XP-E_125_1000 devices.

showed in Figure 6.43 a), which points out the presence of a parallel resistance.

In Figure 6.38 are reported the x,y coordinates and CCT measurements at 350mA of the OSLON_125_1000_W1 until the 200th hour. The I-V characteristic of the green, blue and white LEDs show to suffer of a relevant changing during the device operation: Figure 6.43 clearly points out the creation of a preferential path for the current flow, which is highlighted by the non-neglible current absorption below the threshold voltage and the increase of the current for higher voltage. This is due to a parallel resistance formed by lattice defects which act as nonradiative recombination centers.

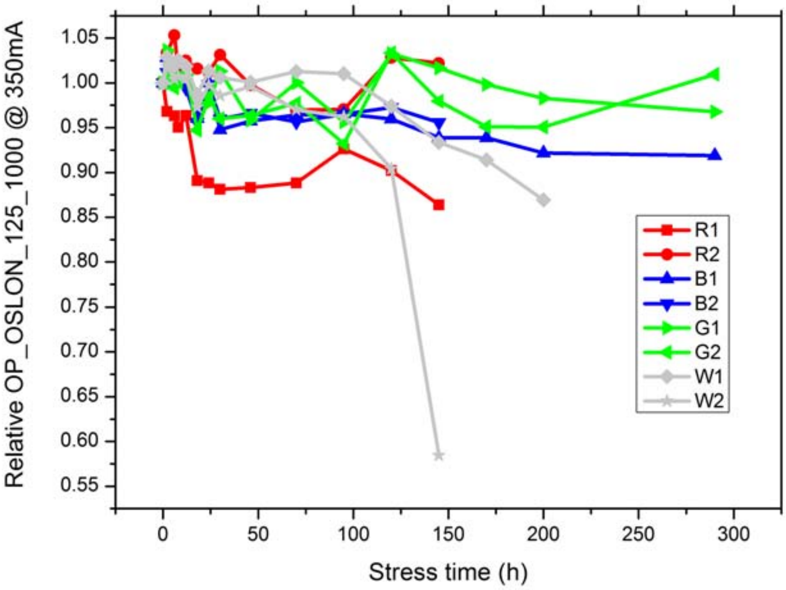

Figura 6.40: a) OP trend at 350mA of the OSLON_125_1000 devices.

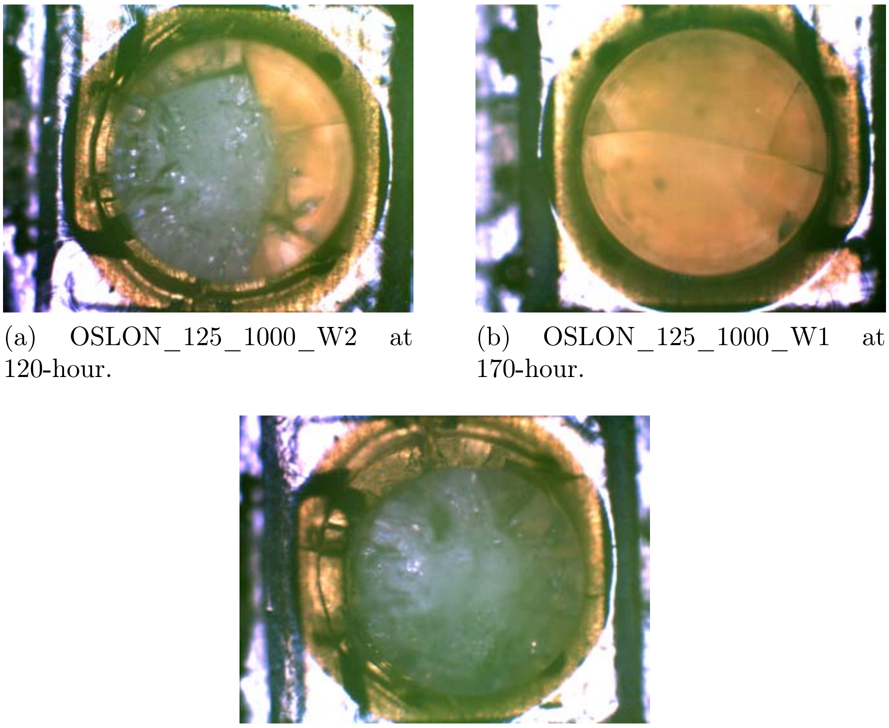

(a) OSLON_125_1000_W2 at 120-hour.

(b) OSLON_125_1000_W1 at 170-hour.

(c) OSLON_125_1000_W1 at 200-hour.

Figura 6.41: Pictures of the OSLON_125_1000 white LEDs.

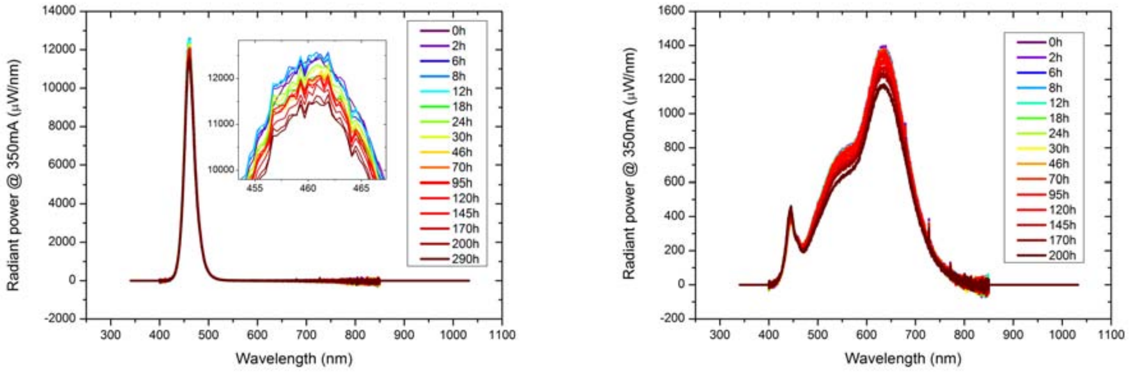

(a) OSLON_125_1000_B1 (b) OSLON_125_1000_W1

Figura 6.42: Spectrum of the OSLON_125_1000 devices.

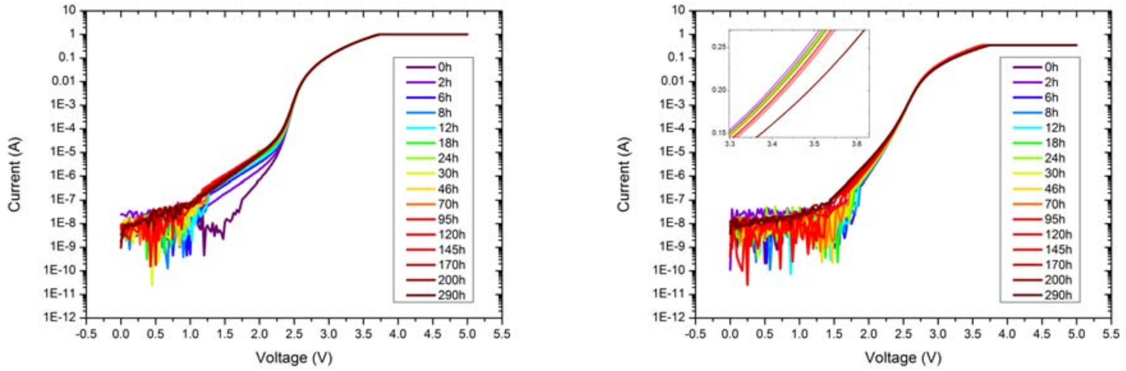

(a) OSLON_125_1000_B1 (b) OSLON_125_1000_G1

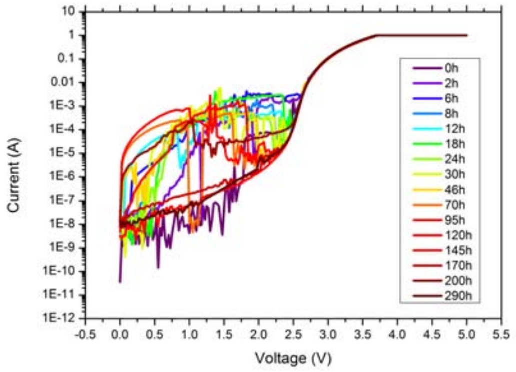

(c) OSLON_125_1000_W1

Figura 6.43: I-V characteristics of the OSLON_125_1000 devices.

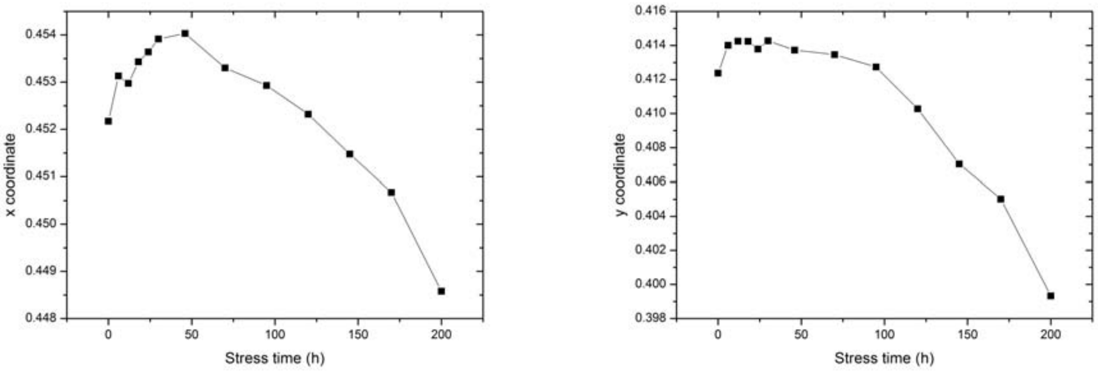

(a) x coordinate (b) y coordinate

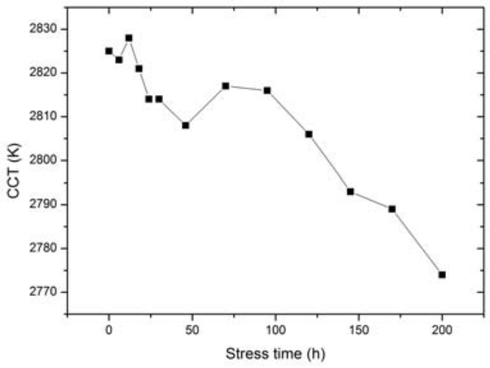

(c) CCT

Figura 6.44: The x,y coordinates and CCT measurements for the OSLON_125_1000_W1.

6.3.3 REBEL LEDs

The OP trend for a current of 100mA and 350mA is reported in Figure 6.45. The red LEDs show a breaking of the epoxy lens after 95 hours of operation that leads to a high drop in the OP. As stated before, this may be due to the high temperature reached by the devices during the stress.

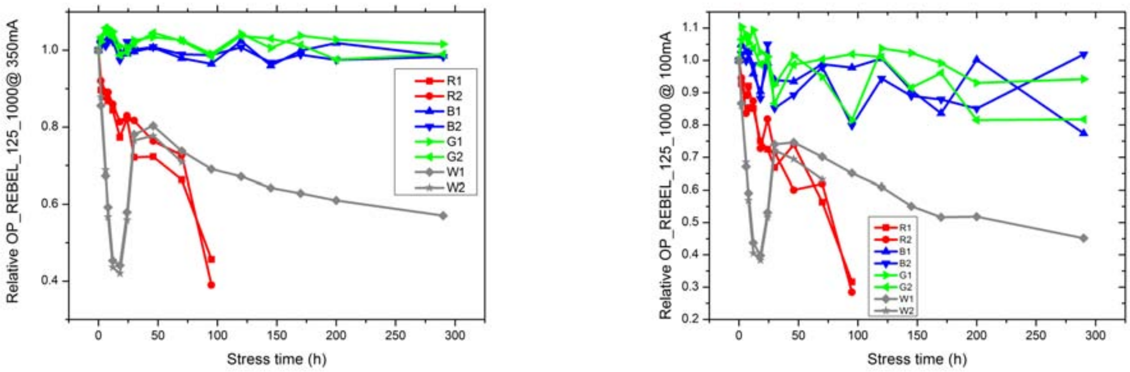

(a) (b)

Figura 6.45: OP trend at a) 350mA and b) 100mA of the REBEL_125_1000 devices.

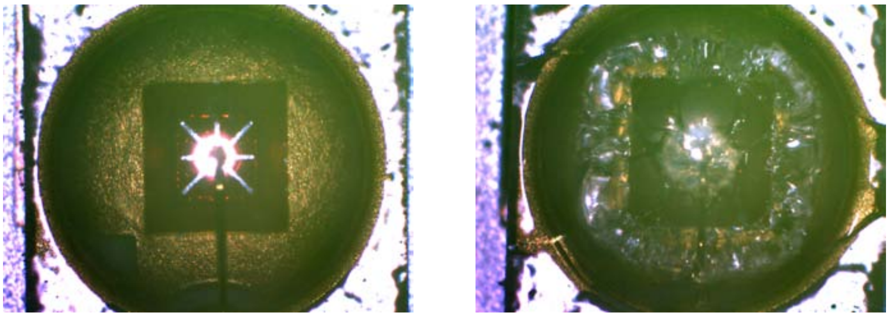

(a) REBEL_125_1000_R1 at 0-hour.

(b) REBEL_125_1000_R1 at 100-hour.

Figura 6.46: Pictures of the REBEL_125_1000_R1.

The white LEDs show an unsual OP trend. In the first hours it shows a strong decay, until 40% of the initial value. Then it starts to increase and reaches a value about 80% of the initial one, and then at 50th hour returns to decrease. Since this phenomenon has been noticed also in the SEOUL P devices, it will be explained in the next section. The REBEL_125_1000_W2 crashed into a short circuit after 70 hours of operation.

As concerns the I-V measurements, two important phenomena have been verified: firstly, the growth of a parasitic shunt resistance, secondly the increase of the series resistance. The parallel resistance is represented by the low resistance paths formed by lattice defects (this presence is confirmed by the lower OP value reached by the plots in 6.45 b) , with respect of the values obtained for higher current operation.), while a worsening of the ohmic contacts can lead to the increase of the serial one. The increase in the series resistance is very high in the white devices. This can lead to higher junction temperatures during operation that can cause irreversible damage to the device. In Figure 6.48 are reported the x,y coordinate and CCT measurements at

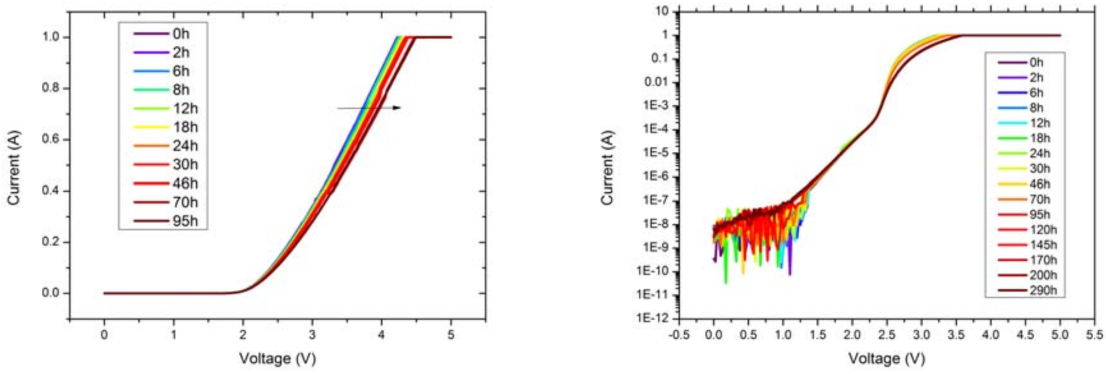

(a) REBEL_125_1000_R1 (b) REBEL_125_1000_B2

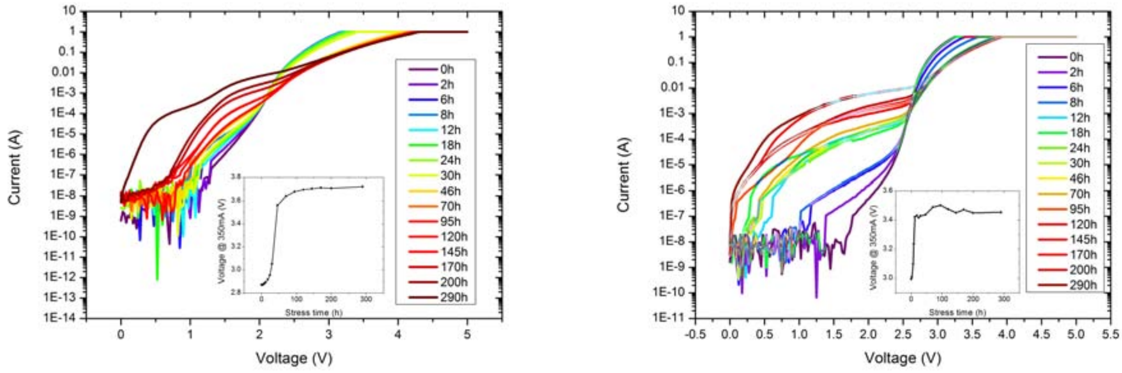

(c) REBEL_125_1000_G2 (d) REBEL_125_1000_W1

Figura 6.47: I-V characteristics of the REBEL_125_1000 devices.

350mA for the REBEL_125_1000_W1.

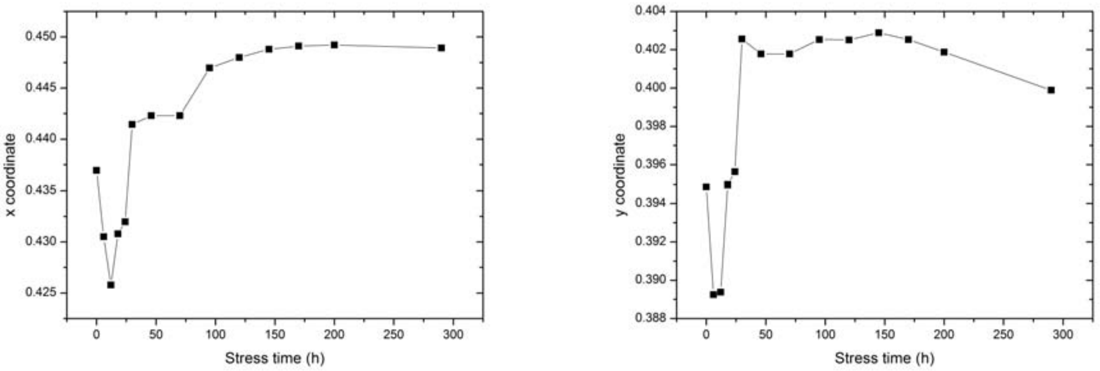

(a) x coordinate

(b) y coordinate

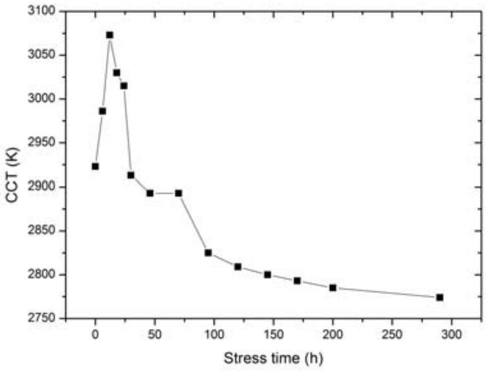

(c) CCT

Figura 6.48: The x,y coordinate and CCT measuraments for the REBEL_125_1000_W1.

6.3.4 Samsung, LG and SEOUL LEDs

Figure 6.49 shows the trend of the normalized optical power at 350mA after 290 hours of operation. The SEOUL P devices present an unsual OP trend. In the first 25 hours it shows a strong decay, until 35% of the initial value. Then it starts to increase and reaches a value about 85/90% of the initial one, and then at 70th hour returns to decrease. The WHITE_LEDs_125_1000_SEOUL P1 crashed into an open circuit after 200 hours of operation.

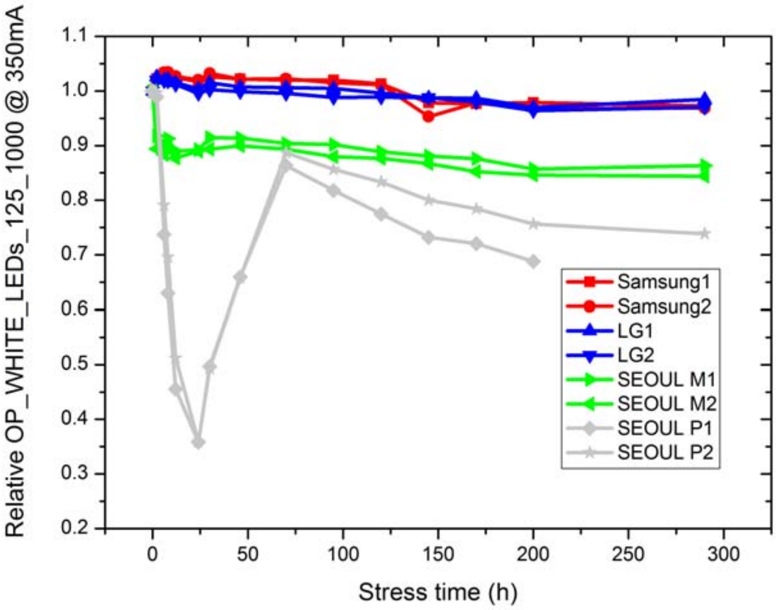

Figura 6.49: OP trend at 350mA of the WHITE_LEDs_125_1000 devices.

To understand the reason for this trend we have stressed a SEOUL Z5P LED for 40 hours with a step of 4 hours between measures. The results of this stress and pictures obtained using the microscope are reported in Figure 6.50 and 6.51respectively.

We can note the occurring of a darkening which then tends to disappear over stress time. This darkening catastrophically limit the devices emission, thus when it starts to dissepear the OP start to increase. As described in [25], this phenomenon can be explained as follows. Any VOCs (volatile organic compounds, like solder flux and residual chemistry) present in an SSL system can diffuse into the gas permeable silicone lens and encapsulants of the LED. Within the molecular structure of these silicone materials, the VOCs will occupy a free space in the interwoven silicone polymer. With subsequent exposure to high photon energy emitted from the LED, along with the heat

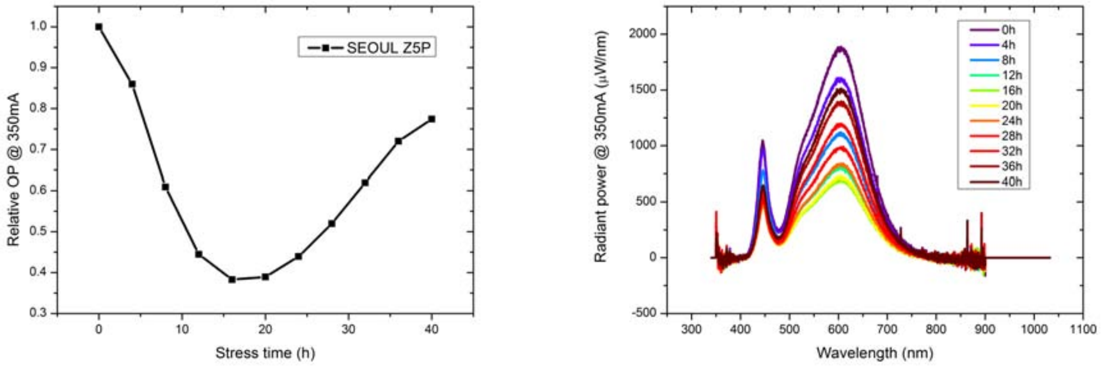

(a) OP trend at 350mA

(b) Spectrum at 350mA

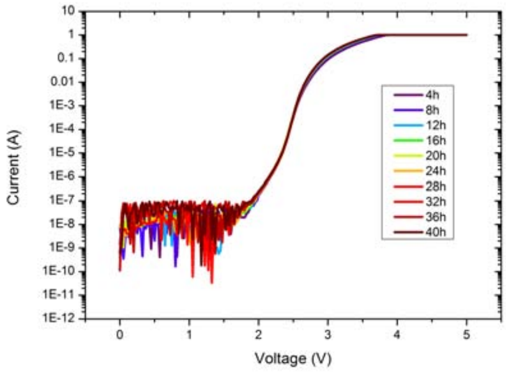

(c) I-V characteristic

Figura 6.50: Electrical and optical characteristich of the SEOUL Z5P stressed for 40 hour.

from the lighting system and the environment, the volatile compounds trapped in the LED‘s lens or encapsulants can discolor. This discoloration of the trapped VOCs can degrade the light emitted from the LED. This discoloration of the encapsulants is on the top of the LED chip, localized to the area just above the chip surface, closest to the source of heat and high photon energy. The VOCs occupying a free space within the lens or encapsulant typically do not cause permanent damage to the silicone material or the LED chip. Thus if this VOCs are allowed to outgas this darkening can disappear and the LED can recover virtually all of the lost luminous flux output.

The OP decay of the SEOUL P devices after this phenomenon may be due to a degradation and a cracking of the lens as showed in Figure 6.53.

The SEOUL M devices show a slight OP decay. Since it is note visible any kind of darkening or deterioration of the package, degradation of optical characteristics can be

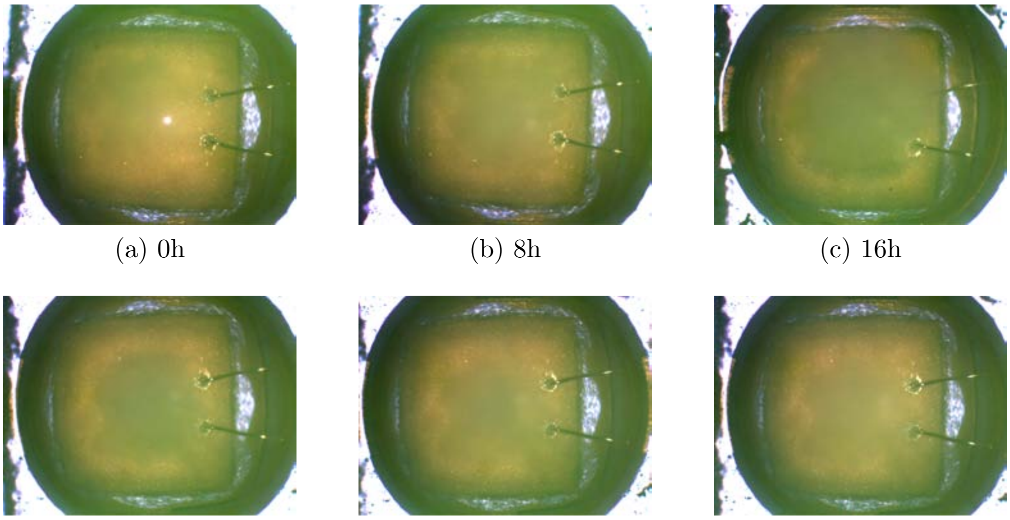
(a) 0h (b) 8h (c) 16h

(d) 24h (e) 32h (f) 40h

Figura 6.51: Pictures of the SEOUL Z5P stressed for 40 hour.

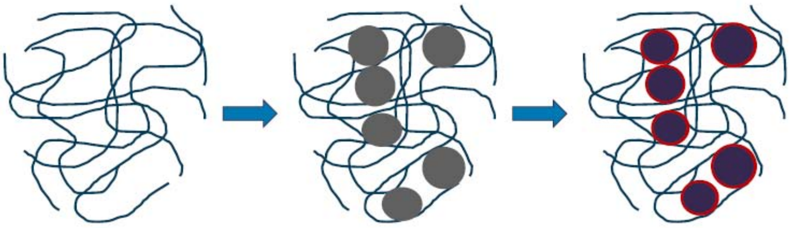
Figure 6.52: Left to right - Silicone chains; VOCs occupying free spaces in the silicone; VOC discoloration as a result of exposure to heat and photonic energy

attributed only to changes of electrical nature.

As concerns the I-V measuraments (see Figure 6.54), the LG and SEOUL M devices show the growth of a parasitic shunt resistance, which substract current to the active zone of the devices, and an increase in the series one, while the Samsung and SEOUL P show the presence of only the first effect.

In Figures 6.55 to 6.58 are reported the x,y coordinates and CCT measurements. They are the average of the two LEDs values at 350mA (except for the SEOUL P). For the SEOUL devices, especially for the Z5P, the x,y coordinates show a strong increase and the CCT shifts toward warmer white point while for the samsung devices the CCT increases. Insteatd for the LG LEDs the colorimetric characteristics remain virtually constant.

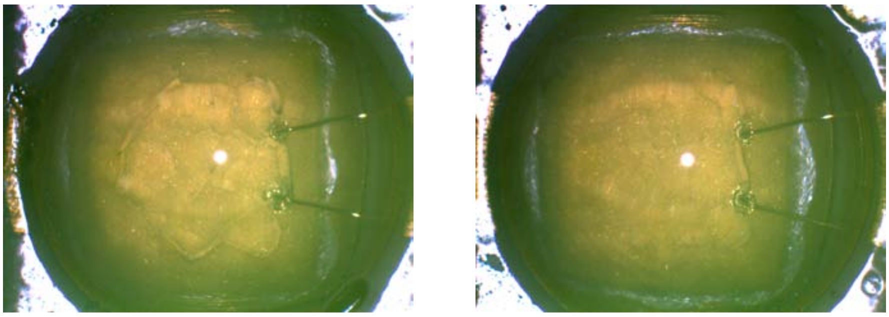

(a)
WHITE_LEDs_125_1000_SEOUL
P1 at 170h

(b)
WHITE_LEDs_125_1000_SEOUL
P2 at 170h

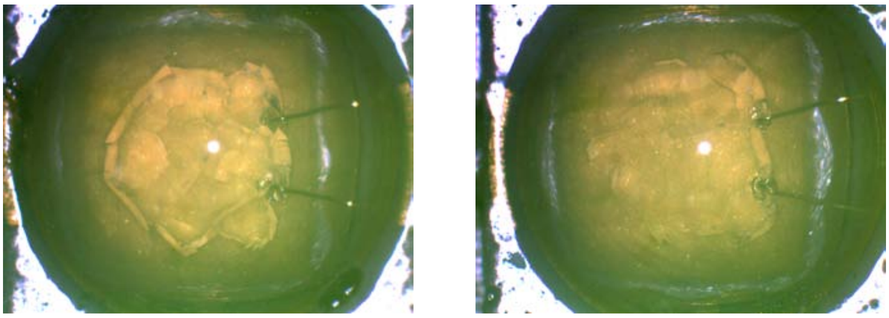

(c)
WHITE_LEDs_125_700_SEOUL
M1

(d)
WHITE_LEDs_125_700_SEOUL
P1

Figura 6.53: Pictures of the WHITE_LEDs_125_1000_SEOUL P1 and WHITE_LEDs_125_1000_SEOUL P2 .

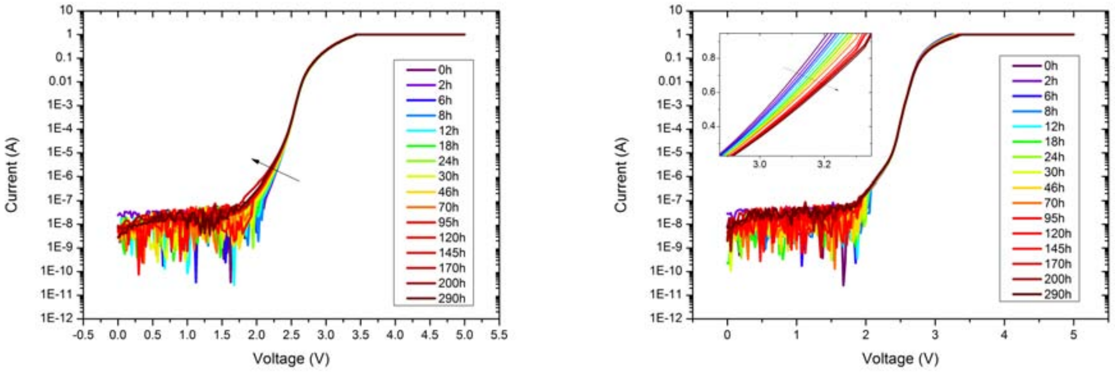

(a) WHITE_LEDs_125_1000_Samsung2 (b) WHITE_LEDs_125_1000_LG1

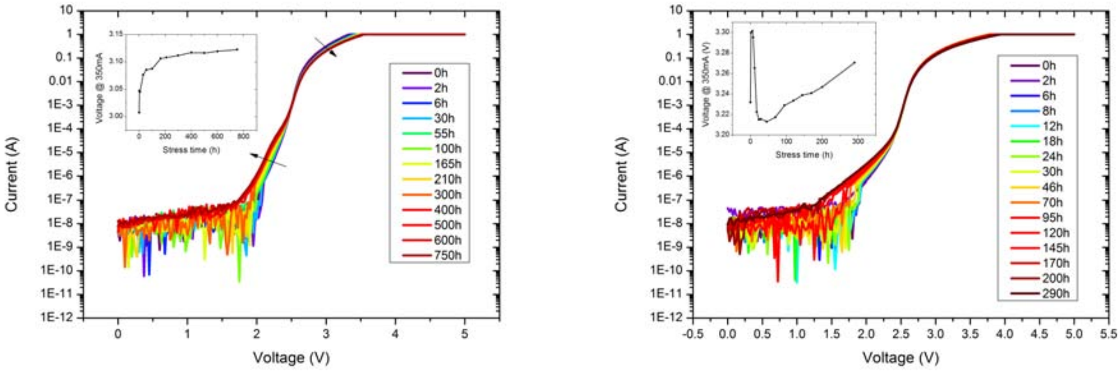

(c) WHITE_LEDs_125_1000_SEOUL M1 (d) WHITE_LEDS_125_1000_SEOUL P2

Figura 6.54: I-V characteristics of the WHITE_LEDs_125_1000 devices.

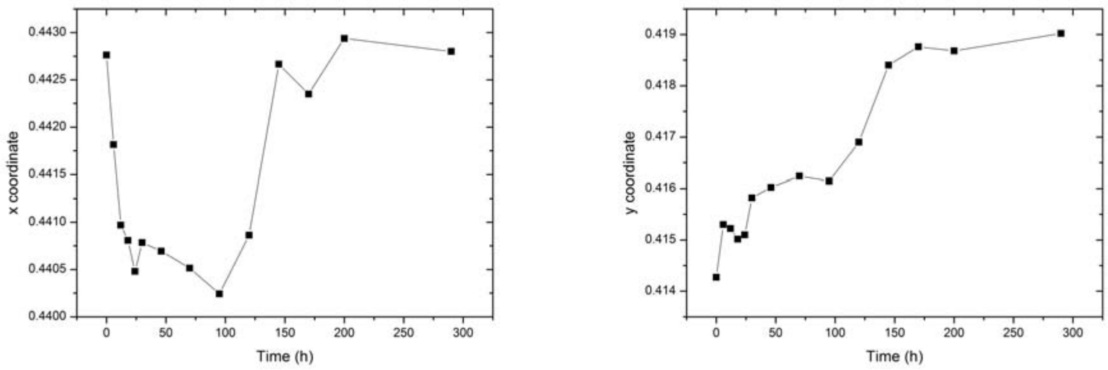

(a) x coordinate

(b) y coordinate

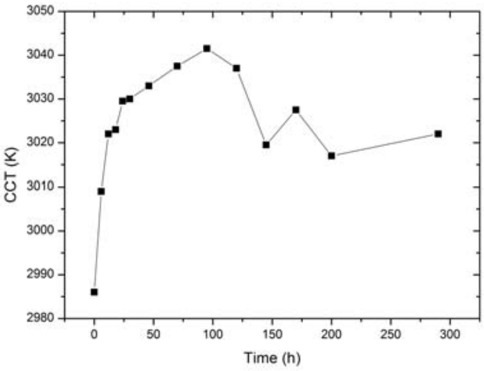

(c) CCT

Figura 6.55: The x,y coordinate and CCT measuraments for the Samsung LEDs.

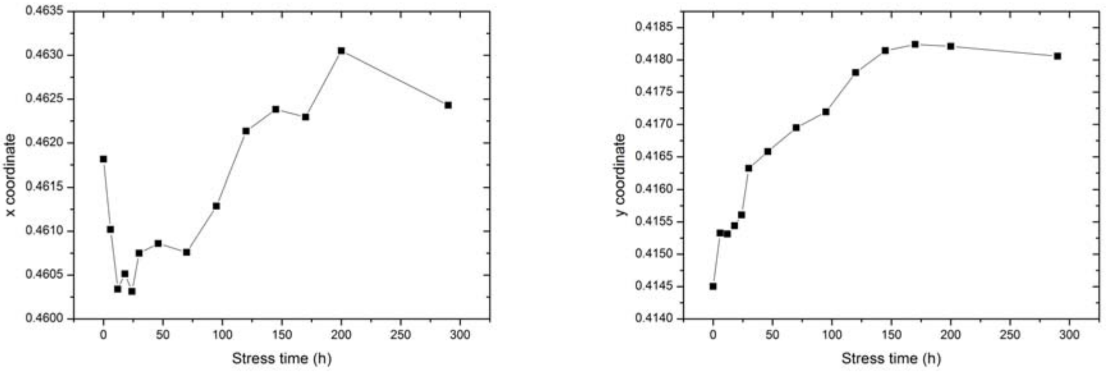

(a) x coordinate

(b) y coordinate

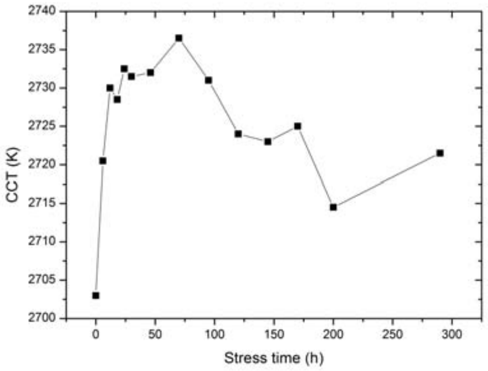

(c) CCT

Figura 6.56: The x,y coordinate and CCT measuraments for the LG LEDs.

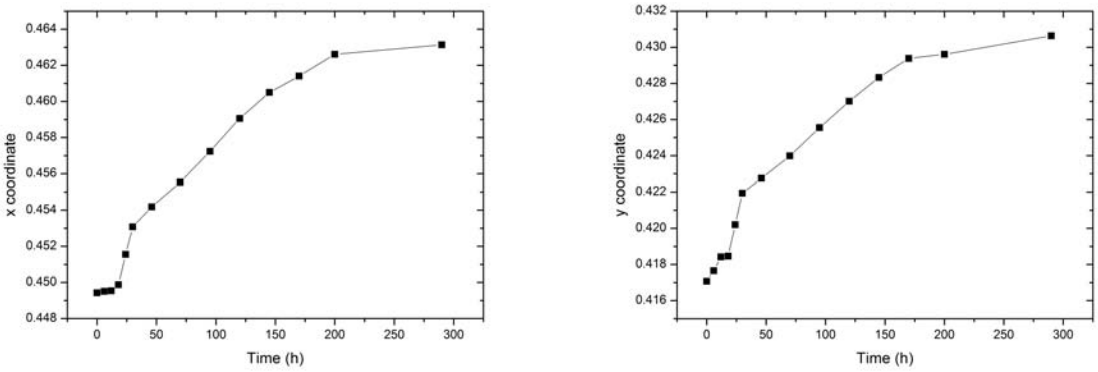

(a) x coordinate

(b) y coordinate

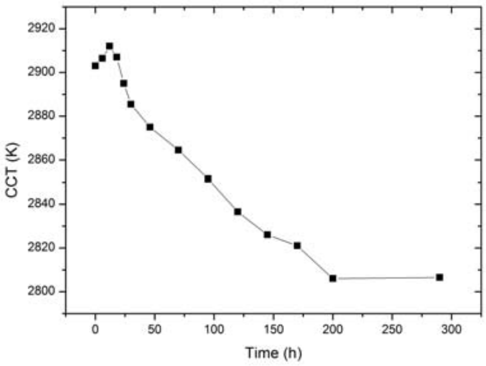

(c) CCT

Figura 6.57: The x,y coordinate and CCT measuraments for the SEOUL M LEDs.

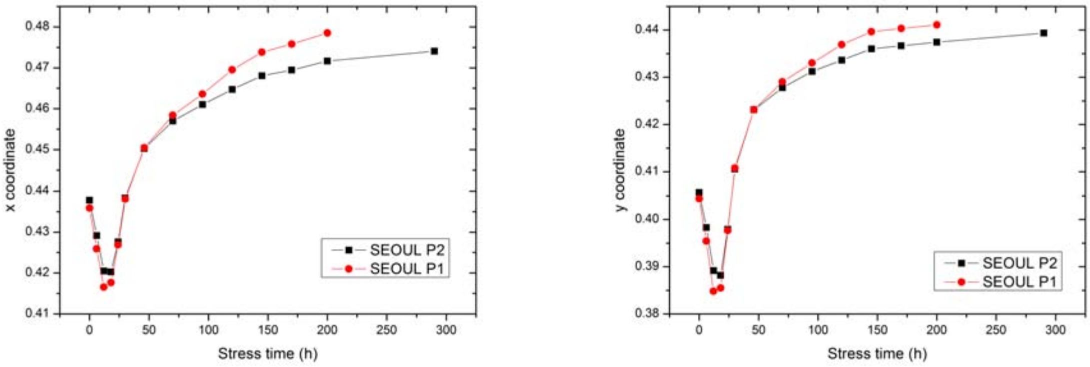

(a) x coordinate

(b) y coordinate

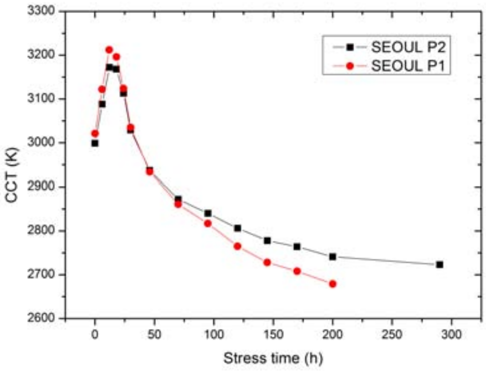

(c) CCT

Figura 6.58: The x,y coordinate and CCT measuraments for the SEOUL P LEDs.

6.3.5 Summary

In table 6.3 are presented the OP levels reached for every single LED stressed, together with the x,y percent variation and the initial and final CCT for the white LEDs.

A comparison between the devices of the various manufacturers is quite difficult because this stress has proved to be very thrusts, possibly due to the high temperatures reached by the devices during operation. As a matter of fact some LEDs catastrophically crashed into a short or a open circuit during this stress and and the lenses of some LEDs show very obvious cracks and damage.

However we can state that, as concerns the white LEDS, the LG and Samsung devices show the most stable electrical and optical properties.

LED name	OP(%)
XP-E_125_1000_R1	-1.77
XP-E_125_1000_R2	-12.83
XP-E_125_1000_B1	6.02
XP-E_125_1000_B2	3.92
XP-E_125_1000_G1	2.23 (after 120h then crashed)
XP-E_125_1000_G2	8.28 (after 95h then crashed)
OSLON_125_1000_R1	-13.62 (after 145h then crashed)
OSLON_125_1000_R2	2.20 (after 145h then crashed)
OSLON_125_1000_B1	-8.12
OSLON_125_1000_B2	-4.43 (after 145h then crashed)
OSLON_125_1000_G1	-3.24
OSLON_125_1000_G2	0.97
REBEL_125_1000_R1	-54.37 (after 95 h)
REBEL_125_1000_R2	-61.01 (after 95 h)
REBEL_125_1000_B1	-1.45
REBEL_125_1000_B2	-1.73
REBEL_125_1000_G1	1.59
REBEL_125_1000_G2	-1.02

(a) Monochromatic LEDs.

LED name	OP(%)	x coord (%)	y coord (%)	CCT (K)
XP-E_125_1000_W1	-8.00	-1.27	-0.57	3004-3082
XP-E_125_1000_W2	-9.69	-1.82	-0.72	2965-3078
OSLON_125_1000_W1	-13.08 (after 200h)	-0.79	-3.16	2825-2774
OSLON_125_1000_W2	-9.57 (after 120h)	-0.33	-2.26	2826-2774
REBEL_125_1000_W1	-42.94	2.74	1.27	2923-2774
REBEL_125_1000_W2	-29.11 (after 70h)	2.16	2.20	2948-2867
WHITE_LEDs_125_1000_Samsung1	-2.75	-0.08	1.09	3001-3032
WHITE_LEDs_125_1000_Samsung2	-3.14	0.10	1.21	2971-3012
WHITE_LEDs_125_1000_LG1	-1.53	0.05	0.78	2711-2732
WHITE_LEDs_125_1000_LG2	-2.99	0.21	0.94	2695-2711
WHITE_LEDs_125_1000_SEOUL M1	-13.64	3.03	3.15	2888-2791
WHITE_LEDs_125_1000_SEOUL M2	-15.60	3.07	3.35	2918-2822
WHITE_LEDs_125_1000_SEOUL P1	-31.21 (after 200h)	9.78	9.07	3021-2679
WHITE_LEDs_125_1000_SEOUL P2	-26.12	8.28	8.30	2999-2723

(b) White LEDs.

Tabella 6.3: Optical characteristics of the LEDs stressed at 125°C and 1A.

6.4 Pure thermal stress

6.4.1 XP-E LEDs

The behaviour of the OP for a current of 350mA after 300 hours of operation is reported in Figure 6.59. The trend is normalized to the optical measurement conducted before the stress. Observing Figure 6.59, one can notice that the white devices show a considerable OP, until the 87% of the initial value. Figure 6.60 a) shows that the yellow/blue ratio presents an exponential decay during the stress: this is correlated to a decrease of the efficiency of the phosphor. Therefore we can associate a significant part of the optical power decay of this devices to that phosphor degradation. The phosphor conversion degedradation can be noted also from the spectrum measurements as showed in Figure 6.60 b). In Figure 6.61 are reported the x,y coordinates and CCT measurements. They are the average of the two white LEDs values at 350mA. The x and y coordinates show a slight decrease while the CCT shows a slight increase, i.e. a shift toward cooler color, which confirms the hypotehesis of the phosphor degradation.

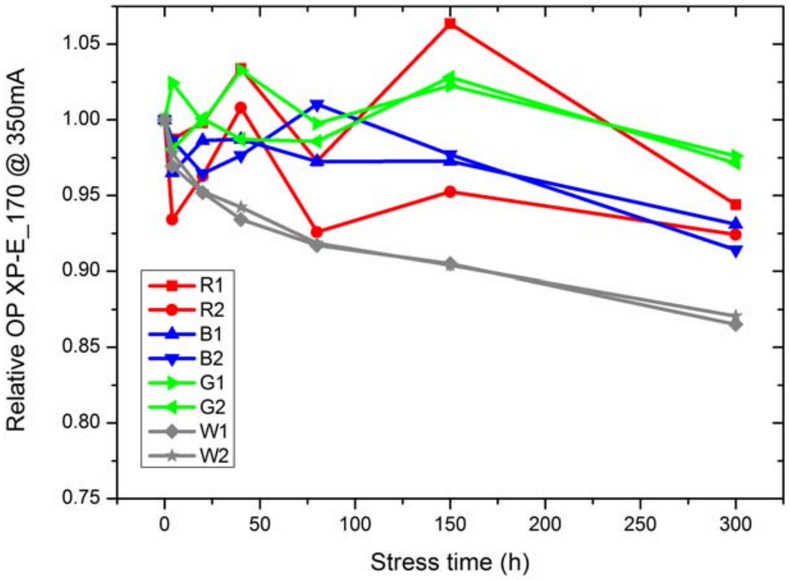

Figure 6.59: The OP trend for the first 300 hours of operation of the XP-E devices, measured for a forward current of 350 mA.

.

As far as the electrical characteristics are concerned the I-V curves (see Figure 6.62) show an slight increase on the diode series resistance, which is more evident in the white

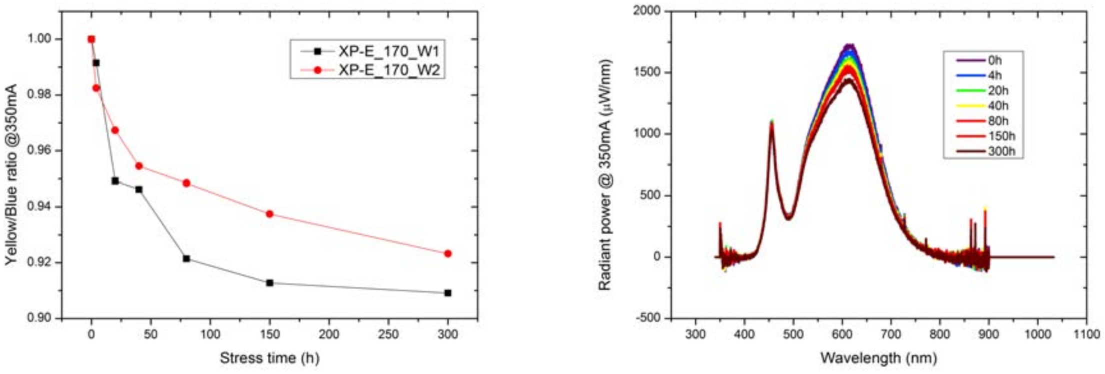

(a)

(b)

Figure 6.60: a) Yellow/blue ratio for the XP-E_170 white LEDs and b) Spectrum of the XP-E_170_W1.

and green devices. However no variation of threshold voltage has been noticed and the current no suffer of a great changing during the stress. This is in accordance with the absence of a substantial creation of nonradiative centers that can influence the electrical characteristic of the devices.

6.4.2 OSLON LEDs

Figure 6.63 a) shows the trend of the normalized optical power at 350mA. . The devices do not suffer of a considerable decay of the OP after 300 hours of operation.

In Figure 6.61 are reported the x,y coordinates and CCT measurements at 350mA. They are the average of the two white LEDs values at 350mA. The colorimetric characteristics remain virtually constant.

Figure 6.65 shows the I-V characteristics of these devices. For the green and white devices we can note the cration of a parallel resistance that tend to disappear over the stress time. This may be due to the instability of the parasitic path inside the active region.

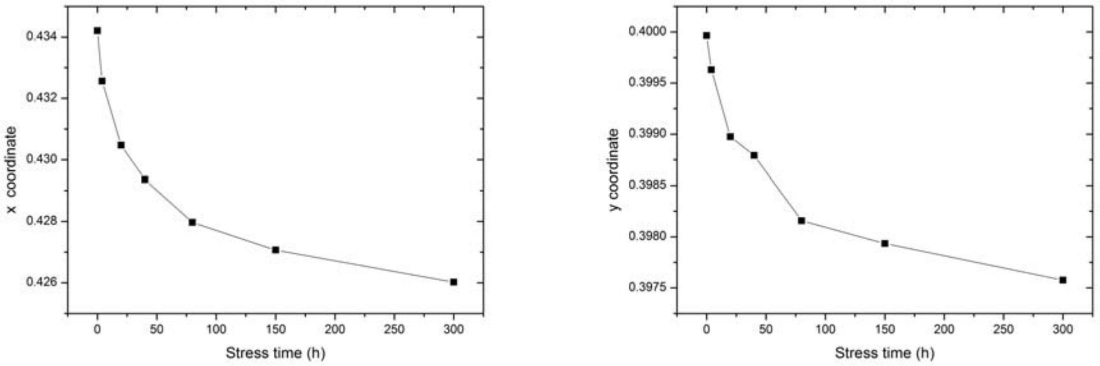

(a) x coordinate (b) y coordinate

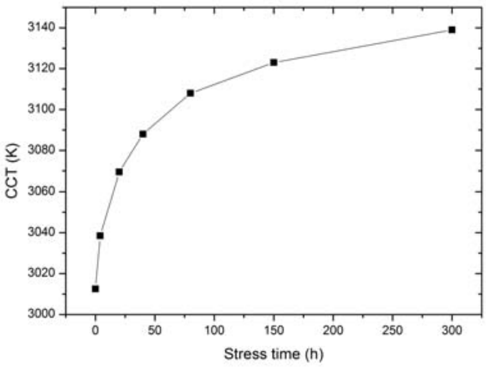

(c) CCT

Figura 6.61: The x,y coordinates and CCT measurements for the XP-E_170 white LEDs.

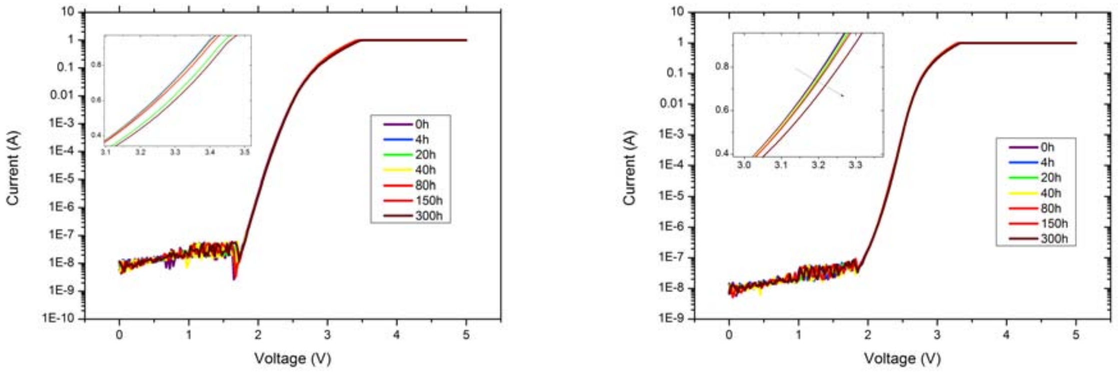

(a) XP-E_170_G2 (b) XP-E_170_W1

Figura 6.62: I-V characteristics of the XP-E_170 devices.

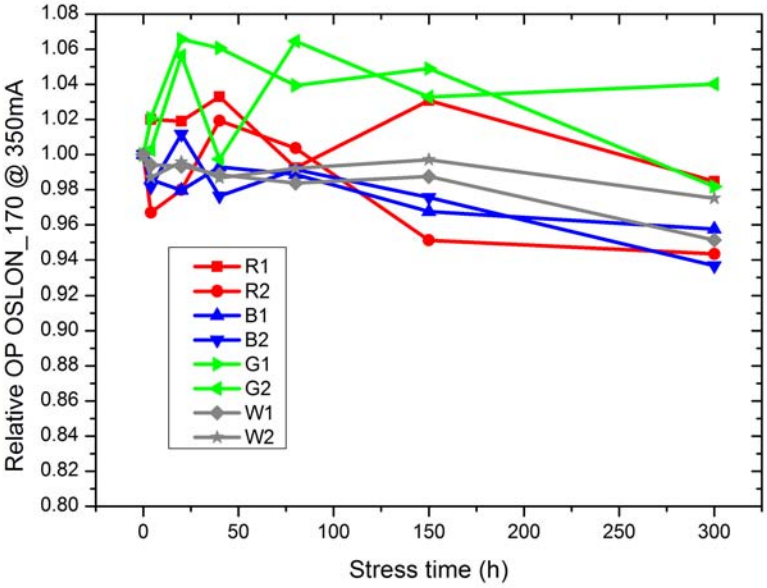

Figura 6.63: OP trend at 350mA of the OSLON_170 devices.

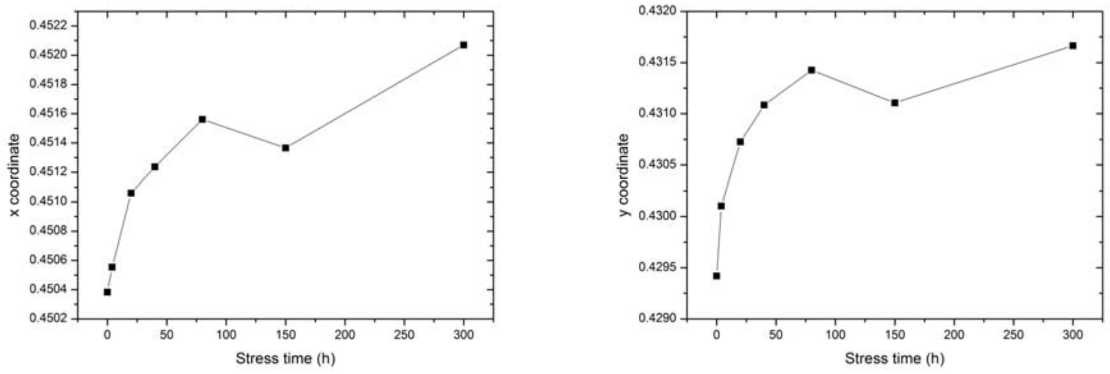

(a) x coordinate

(b) y coordinate

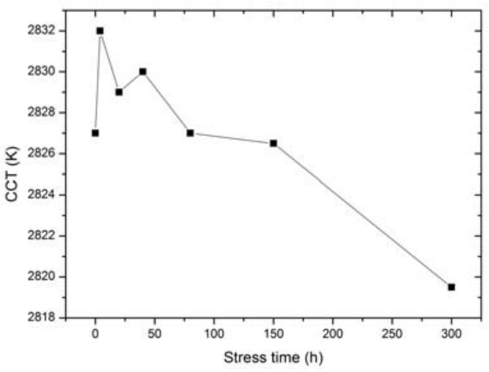

(c) CCT

Figura 6.64: The x,y coordinates and CCT measurements for the OSLON_170 white LEDs.

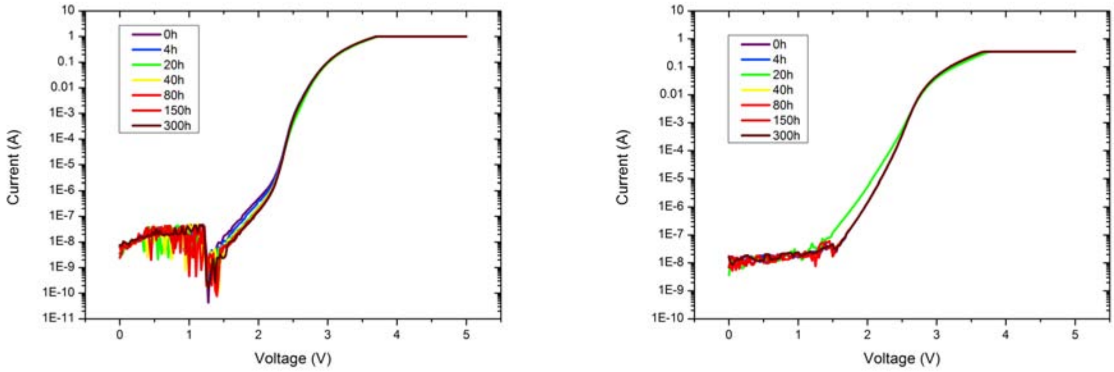

(a) OSLON_170_B1

(b) OSLON_170_G1

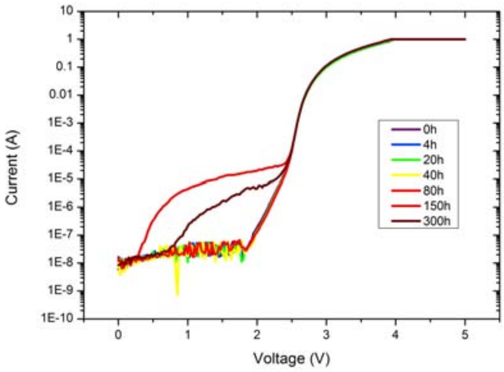

(c) OSLON_170_W1

Figura 6.65: I-V characteristics of the OSLON_170 devices.

6.4.3 REBEL LEDs

The OP trend for a current of 100mA and 350mA is reported in Figure 6.66. The red and blue devices show a slight OP decay. Since it is not visible any kind of darkening or deterioration of the package, degradation of optical characteristics can be attributed only to changes of electrical nature. However the results of the previous stress suggest that for the red LEDs this decay can be due to a degradation of the lens (although not visible).

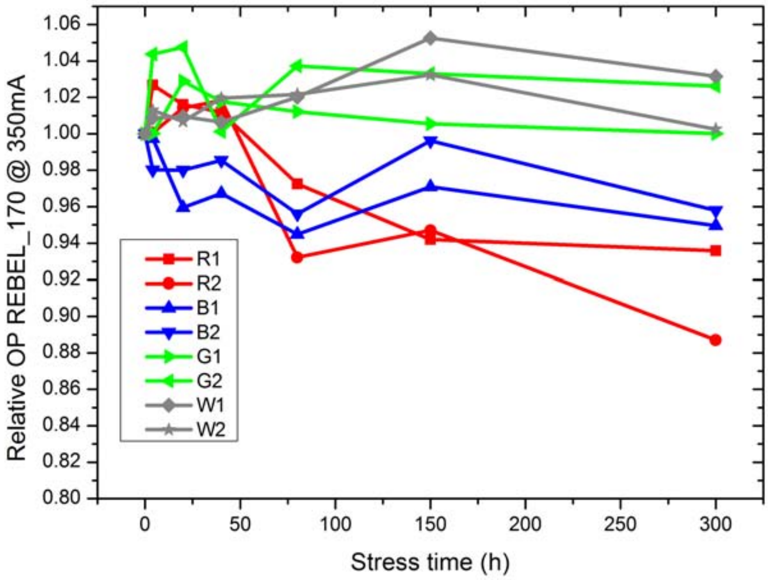

Figura 6.66: OP trend at 350mA of the REBEL_170 devices.

As concerns the I-V measuraments, the devices show an increase in series resistance, especially in the green and white devices.

In Figure 6.68 are reported the x,y coordinate and CCT measurements at 350mA. Even in this case, the colorimetric properties remain virtually constant.

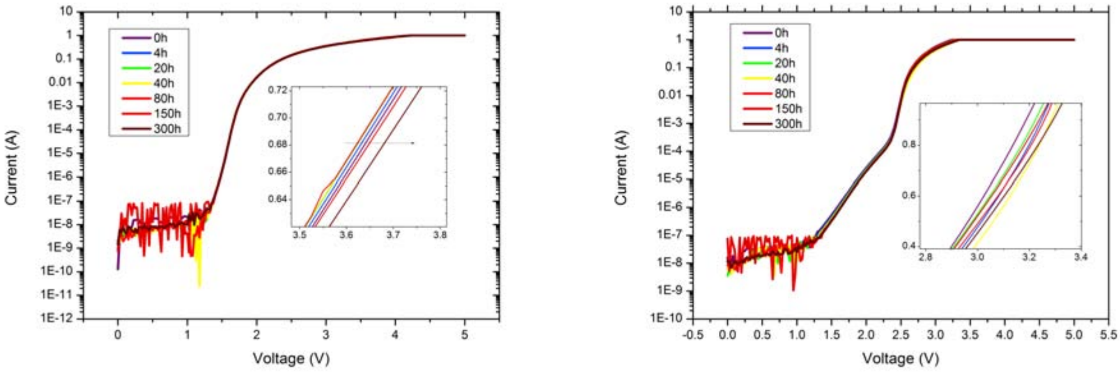

(a) REBEL_170_R1

(b) REBEL_170_B2

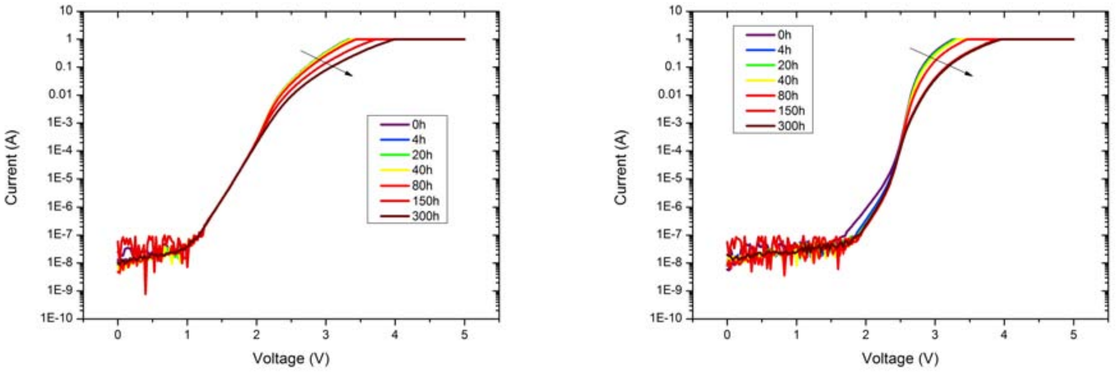

(c) REBEL_170_G2

(d) REBEL_125_700_W1

Figura 6.67: I-V characteristics of the REBEL_170 devices.

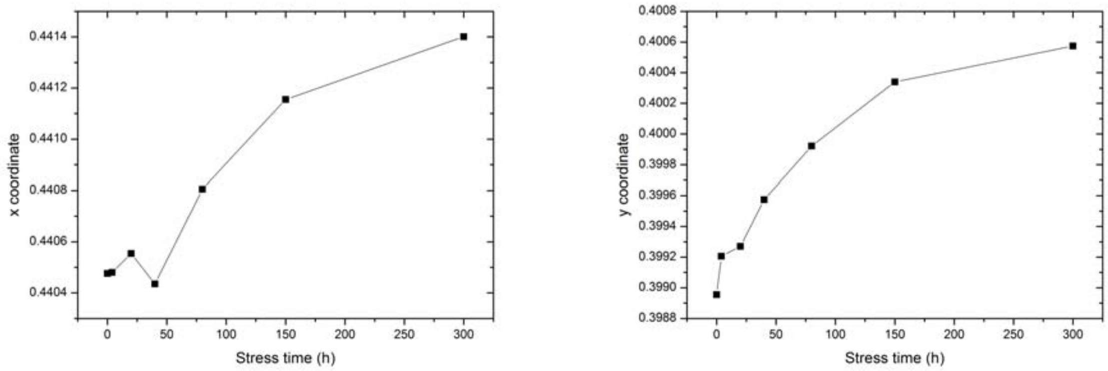

(a) x coordinate (b) y coordinate

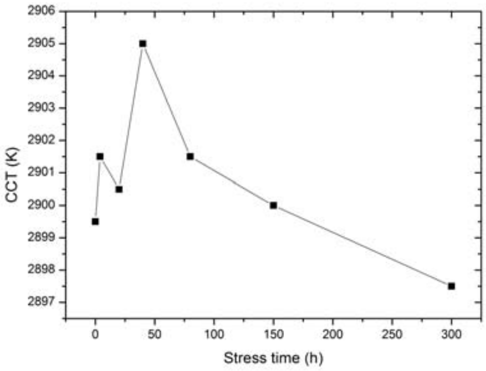

(c) CCT

Figura 6.68: The x,y coordinates and CCT measuraments for the REBEL_170 white LEDs.

6.4.4 Samsung, LG and SEOUL LEDs

Figure 6.69 shows the trend of the normalized optical power at 350mA after 300 hours of operation. The SEOUL P and the SEOUL M2 devices suffer of relevant OP decay.

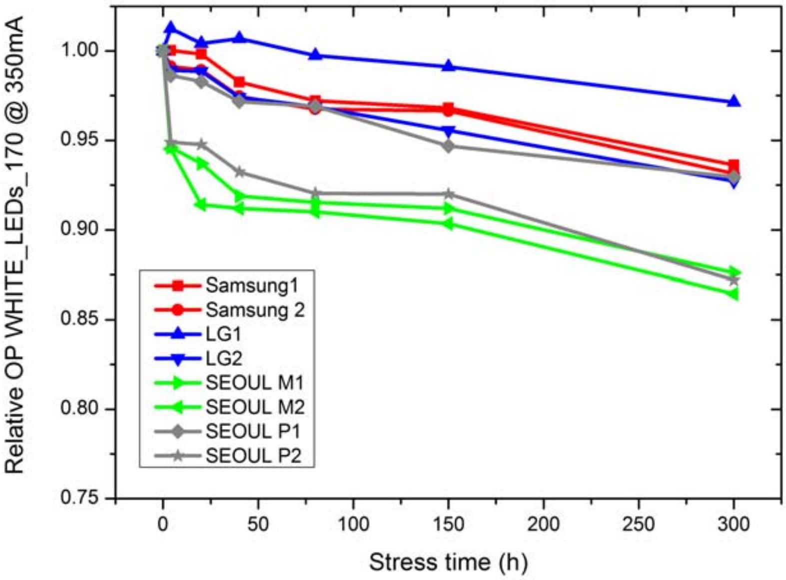

Figura 6.69: OP trend at 350mA of the WHITE_LEDs_170 devices.

Since it is note visible any kind of yellowing or deterioration of the package, degradation of optical characteristics can be attributed only to changes of electrical nature. Figure 6.70 shows the spectrum of these LEDs 350mA, which confirm the considerable OP decay in the SEOUL devices.

As concerns the I-V measurements, the LG devices an increase of the series resistance as showed in Figure 6.71 a), while the SEOUL and Samsung devices show characteristics with in which some variation of the current flow can be noticed: they may be due to the contamporaney presence of a parellel ans series resistance. The first tend to increase the current flow while the second to decrease it.

In Figures 6.72 to 6.75 are reported the x,y coordinates and CCT measurements. They are the average of the two LEDs values at 350mAThe variations are very limited for all the devices

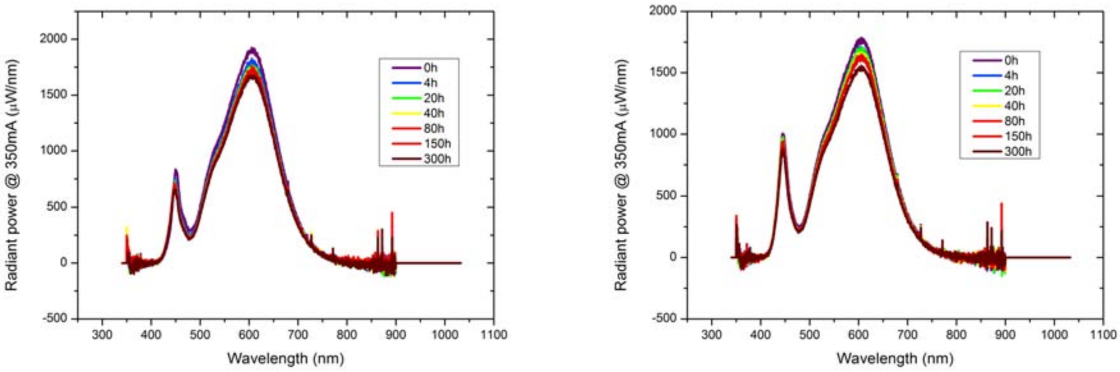

(a) WHITE_LEDs_170_SEOUL M2 (b) WHITE_LEDs_170_SEOUL P2

Figura 6.70: Spectrum of the WHITE_LEDs_170 devices.

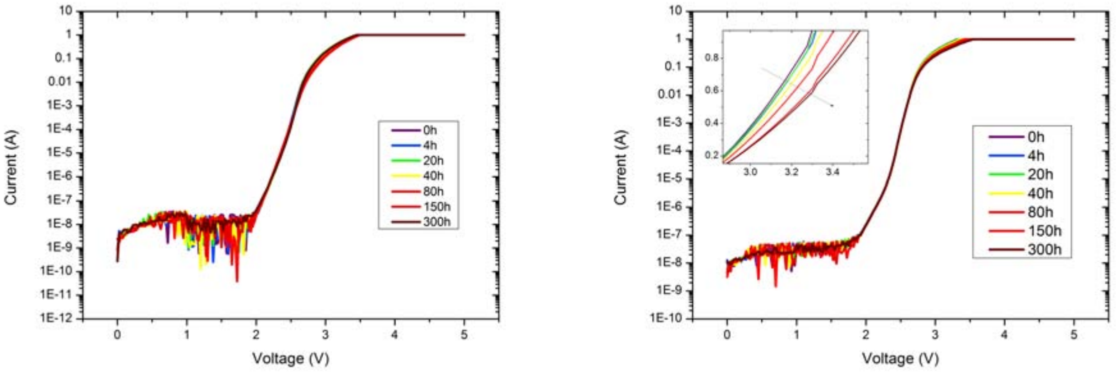

(a) WHITE_LEDs_170_Samsung1 (b) WHITE_LEDs_170_LG1

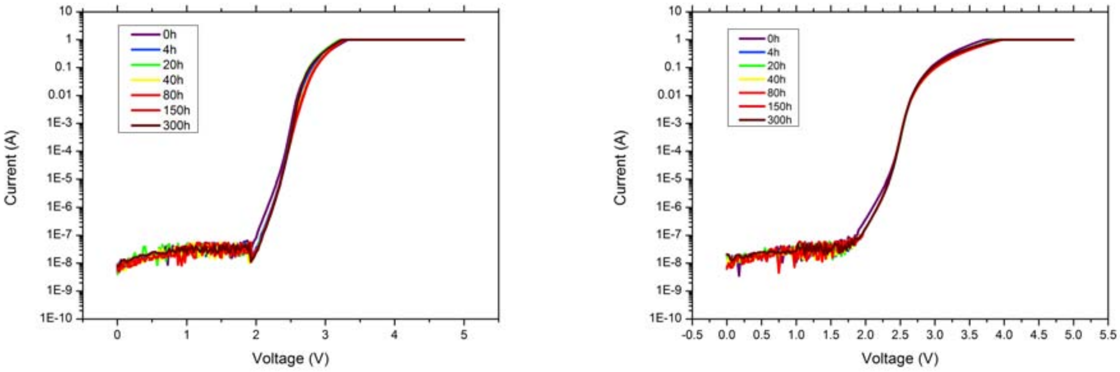

(c) WHITE_LEDs_170_SEOUL M1 (d) WHITE_LEDs_170_SEOUL P1

Figura 6.71: I-V characteristics of the WHITE_LEDs_170 devices.

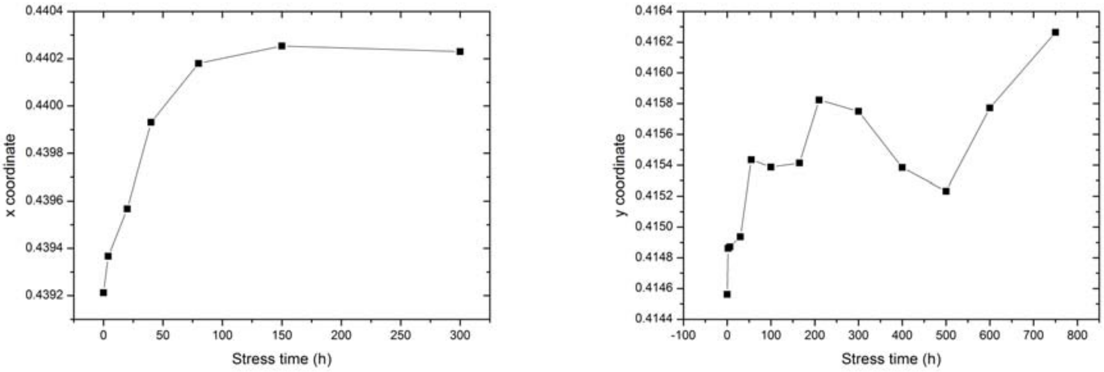

(a) x coordinate

(b) y coordinate

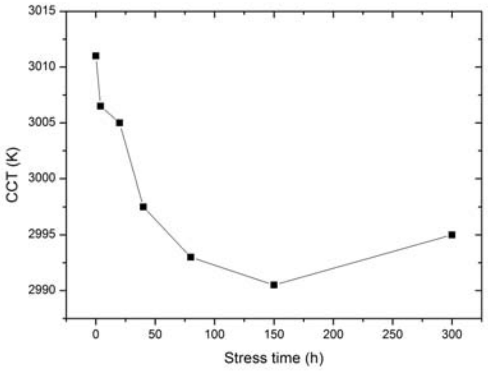

(c) CCT

Figura 6.72: The x,y coordinate and CCT measuraments for the Samsung LEDs.

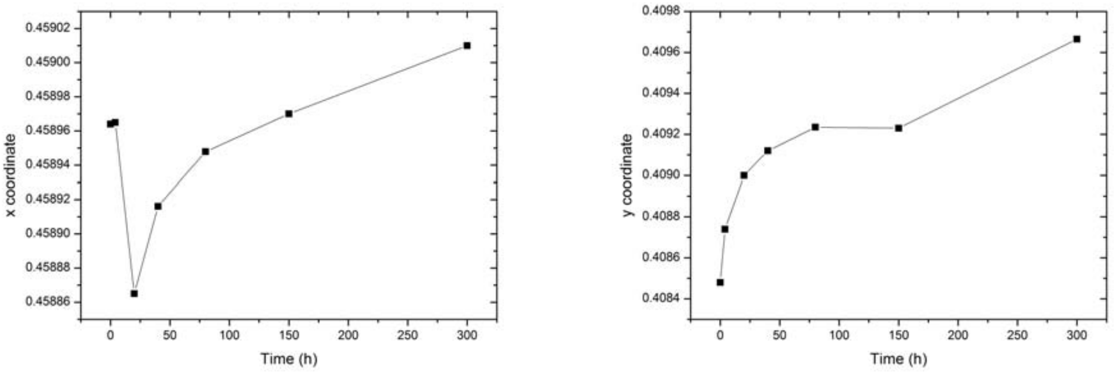

(a) x coordinate

(b) y coordinate

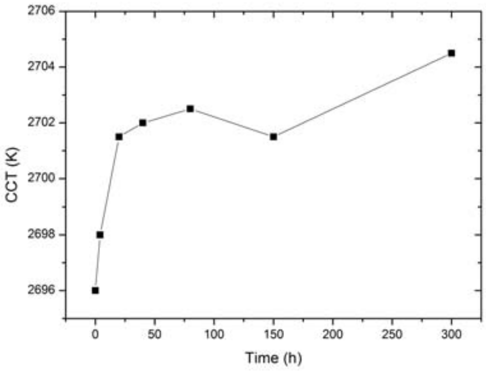

(c) CCT

Figura 6.73: The x,y coordinate and CCT measuraments for the LG LEDs.

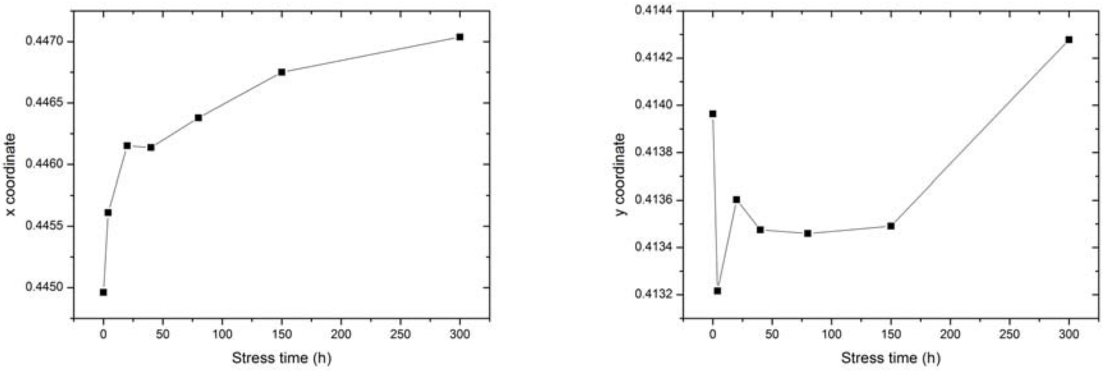

(a) x coordinate

(b) y coordinate

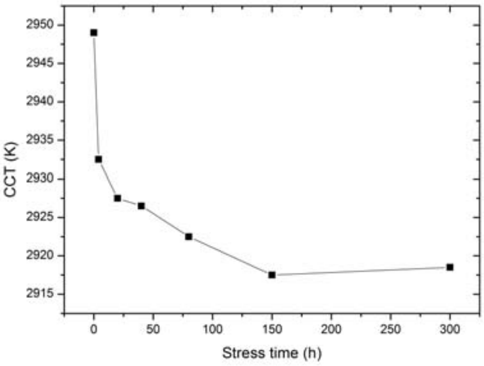

(c) CCT

Figura 6.74: The x,y coordinate and CCT measuraments for the SEOUL M LEDs.

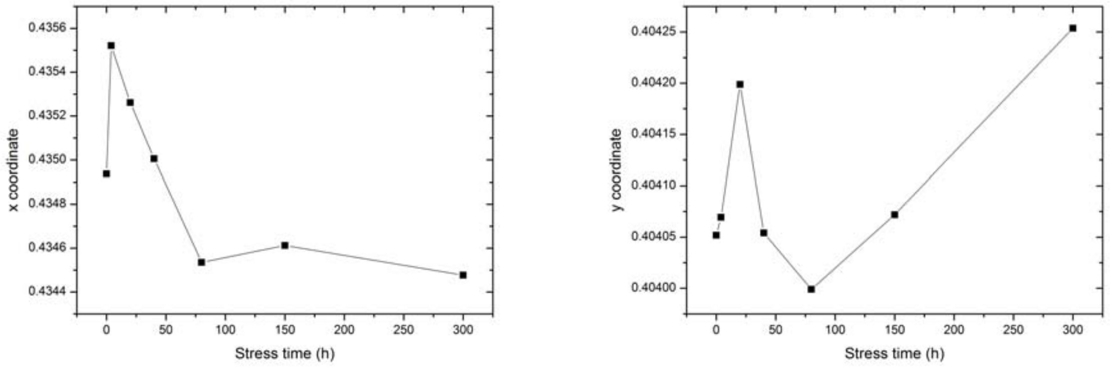

(a) x coordinate

(b) y coordinate

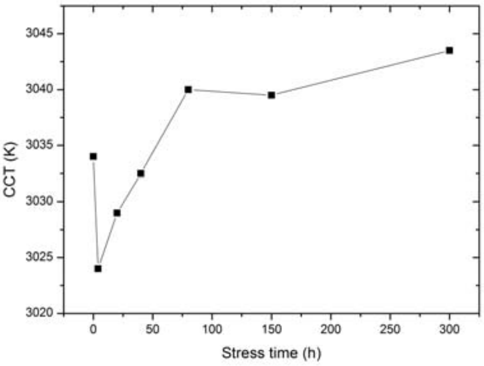

(c) CCT

Figura 6.75: The x,y coordinate and CCT measuraments for the SEOUL P LEDs.

6.4.5 Summary

In table 6.4 are presented the OP levels reached for every single LED stressed, together with the x,y percent variation and the initial and final CCT for the white LEDs.

These results highlight the fact that almost all the devices suffer of an OP decay during this stress. The CREE and OSLON devices are electrically very stable in this stress condition. Instead the REBEL, SEOUL and LG LEDs show an increase in the series resistance.

In this case, the generation of nonradiative center has not been noticed, thus it is probably triggered by the flow of current in the active region.

Only the CREE white devices seem to show a phosphor degradation.

LED name	OP(%)
XP-E_170_R1	-5.62
XP-E_170_R2	-7.59
XP-E_170_B1	-7.59
XP-E_170_B2	-8.59
XP-E_170_G1	-2.40
XP-E_170_G2	-2.88
OSLON_170_R1	-1.52
OSLON_170_R2	-5.66
OSLON_170_B1	-4.25
OSLON_170_B2	-6.33
OSLON_170_G1	-1.82
OSLON_170_G2	4.02
REBEL_170_R1	-6.41
REBEL_170_R2	-11.30
REBEL_125_700_B1	-5.04
REBEL_125_700_B2	-4.21
REBEL_170_G1	0.01
REBEL_170_G2	2.62

(a) Monochromatic LEDs.

LED name	OP(%)	x coord (%)	y coord (%)	CCT (K)
XP-E_170_W1	-13.49	-2.02	-0.69	2995-3128
XP-E_170_W2	-12.94	-1.75	-0.51	3030-3150
OSLON_170_W1	-4.87	0.35	0.43	2826-2816
OSLON_170_W2	-2.49	0.40	0.66	2828-2823
REBEL_170_W1	3.16	0.26	0.42	2850-2845
REBEL_170_W2	0.25	0.16	0.39	2949-2950
WHITE_LEDs_170_Samsung1	-6.38	0.23	0.05	3020-3005
WHITE_LEDs_170_Samsung2	-6.86	0.23	0.01	3002-2985
WHITE_LEDs_170_LG1	-2.86	0.03	0.23	2718-2723
WHITE_LEDs_170_LG2	-7.27	-0.02	0.35	2674-2686
WHITE_LEDs_170_SEOUL M1	-12.39	0.50	0.05	2985-2951
WHITE_LEDs_170_SEOUL M2	-13.55	0.44	0.10	2913-2886
WHITE_LEDs_170_SEOUL P1	-7.05	-0.23	0.03	3022-3040
WHITE_LEDs_170_SEOUL P2	-12.79	0.02	0.07	3046-3047

(b) White LEDs.

Tabella 6.4: Optical characteristics of the LEDs stressed at 170°C.

6.5 Comments to the results

6.5.1 XP-E LEDs

The monochromatic LEDs have demonstrated to be optically quite stable in all the stress condition. The highest decay in the OP has been detected during the pure thermal stress despite the only 300 hours of stress. This allow us to state that the mechanism that limit the optical reliability of these devices are activated by high temperatures. From the electrical point of view, the devices has showed an increase in the series resistance only in the current stress tests and more accentuated in the 125-1A stress. Therefore this increase may be triggered by the current flow in the active region that can induces a morphological degradation of the contact layers. During the 125-1000 stress the two green LEDs catastrophically crashed into a short circuit.

As concern the white LEDs, their principal optical weakness consists in degradation of phosphors activated by high temperatures. This is confirmed by a slight increase in the CCT of these devices toward cooler white point. From the electrical point of view, also this LEDs has showed an increas in the series reisistance during the stress current. Two white LEDs catastrophically crashed into a short circuit during the 125-700 stress. This may be due to the increase of the series resistance which leads to higher junction temperature that can cause a lattice fusion inside the active area of the chip.

6.5.2 OSLON LEDs

The I-V characteristics of the blue, green and white LEDs have pointed out the generation of nonradiative center during the current stress that cause a decrease in the OP especially in the blue and white devices. Since this phenomenon has not been noticed during the pure thermal stress we can state that this creation of nonradiative centers is triggered by the current flow in the active region.

The white LEDs showed a substantial decrease in the conversion efficiency of the phosphor during the 125-700 and 125-1000 stress tests, probably due to the high temperatures reached by the devices. However, during the 125-1000 stress the two white LEDs showed a catastrophic breaking of the lens, which confirm the high temperatures reached by the devices.

6.5.3 REBEL LEDs

These devices show an increase of the series resistance in all the stress conditions. This increase is more pronounced at high temperatures and may be due to a worsening of the ohmic contact. The I-V characteristics of the blue, green and white LEDs have pointed out the generation of nonradiative centers during the current stress that can cause a decrease in the OP of the devices. Since this phenomenon has not been noticed during the pure thermal stress we can state that this creation of nonradiative centers is triggered by the current flow in the active region.

The reds LEDs have showed a lens breaking during the 125-700 and 125-1000 stress test. This may be due to the high series resistance of the devices, that combined with the temperature of the oven can lead to very high junction temperatures. However also the white LEDs have showed lens cracking during these stresses. This can suggest that the material of the REBEL lenses are less resistant to high temperature levels compared to that of the other manufactures; furthermore, both thermal characterization and stress tests results confirm that the thermal management of the Rebel ceramic package are less optimized than that of devices from Osram and Cree

6.5.4 WHITE_LEDs

The samsung and LG devices have demonstrated to be optically quite stable while the SEOUL devices have showed strong OP decay in all stress condition. This allows us to state that the mechanism that limit the optical reliability of these devices are activated by high temperatures. The I-V characteristics of these LEDs have pointed out the generation of nonradiative centers during the current stress, which can affect the optical characteristics of the devices. Since this phenomenon has not been noticed during the pure thermal stress we can state that this creation of nonradiative centers is triggered by the current flow in the active region. The LG and SEOUL M devices has also showed an increase in the series resistance.

Conclusion

In this thesis work reliability characteristics of the reg, green and blue LEDs of three different manufacturers and of the white LEDs of six manufacturers have been analyzed. This devices are the state-of-art of the commercial LEDs. The importance of the reliability issue of these devices is considerable, considering the fact that in color-mixing applications it is very important to understand how the degradation kinetics changes in the various types of LEDs subjected to the same operating conditions, in order to provide important guidelines for the design of high performing LED light sources.

An initial characterization has carried out that the XP-E monochromatic LEDs present the best electrical and optical characteristics among the considered devices. As a matter of fact their efficiency is much higher compared to that of the OSLON and REBEL devices. As concerns the white LEDs, the Samsung devices have showed the highest values of luminous flux and efficiency, however very similar to those of XP-E, LG and SEOUL Z5M LEDs. The OSLON devices have showed the worst optical characteristics except for the red LEDs.

In order to understand the degradation mechanism these LEDs have been submitted to four different current/temperature stress conditions (three for the Samsung, LG ans SEOUL devices). Measurements performed have shown different degradation mechanisms and dynamics for the various LEDs studied, both form the electrical and optical poin of view.

XP-E color LEDs have demonstrated to be optically quite stable in all the stress conditions, while from the electrical point of view, they have showed an increase in the series resistance during high current stress conditions. Therfore the slight optical deterioration can be attribuited to the high temperatures reached by the devices, while the electrical to the current flow in active region, which can induces a morphological degradation of the contact layers. As concerns the white LEDs, their principal weakness consists in degradation of phosphors activated by high temperatures, confirmed by a slight increase in the CCT of these devices during the operation.

The Oslon devices have showed the generation of nonradiative recombination centers during the current stress tests, which can lead to a decrease in the OP of the devices. Their presence is put in evidence by the creation of a preferential path for the current flow that is pointed out in the I-V plots. Since this phenomenon has not been noticed during the pure thermal stress test it could be triggered by the current flow in the active region. The white LEDs have shown a substantial decrease in the conversion efficiency of the phosphos during the 125-700 and 125-1000 stress tests, probably due to the high temperatures reached by the devices.

The REBEL devices have showed an increase of the series resistance in all the stress conditions. This increase is more pronounced at high temperatures and may be due to a worsening of the ohmic contact. Like the OSLON devices, they have showed the creation of a parasitic path for the current flow, that may be due to the generation of nonradiative recombination centers represented by defects current-diffused in the active layer. The reds LEDs have showed a lens breaking during the 125-700 and 125-1000 stress test. This may be due to the high thermal resistance of the devices, that combined with the temperature of the oven can lead to very high junction temperatures. However also the white LEDs have showed lens cracking during these stresses. This can suggest that the material of the REBEL lenses are less resistant to high temperature levels compared to that of the other manufactures; furthermore, both thermal characterization and stress tests results confirm that the thermal management of the Rebel ceramic package are less optimized than that of devices from Osram and Cree.

The samsung and LG devices have demonstrated to be optically quite stable while the SEOUL devices have showed strong OP decay in all stress condition and considerable chromatic variation diring the current stress. Thus the mechanism that limit the optical reliability of these devices are activated by high temperatures and could be due to a degradation of transparency characteristics of encapsulating materials. The I-V characteristics of these LEDs have pointed out the generation of nonradiative centers during the current stress, which can affect the optical characteristics of the devices.

Since this phenomenon has not been noticed during the pure thermal stress, this creation of nonradiative centers is triggered by the current flow in the active region. The LG and SEOUL M devices has also showed an increase in the series resistance. that can be due to the high temperatures reached by the devices.

These aging tests showed that, in order to obtain a device totally reliable, we need a few more steps forward in the thermal design of the package, the choice of encapsulant materials and technologies (especially in the REBEL LEDs) and in improvements concern the electrical characteristics of the devices, with a review of the chip structure and the further reduction of lattice imperfections/ impurities that are considered the principal cause of the generation of nonradiative centers here observed in the OSLON, REBEL Samsung and SEOUL devices. A deeper investigation should be conducted as well on the structural changes of the chip during the ageing, concerning the variations of the dopant concentration and the eterostructure conformation.

Despite this, in contexts of non-extreme temperatures and currents, these devices display high strength characteristics and optical qualities that make them, strong candidates in color mixing applications. However the different degradation mechanisms in the various color LEDs, makes indispensable the use of photdiodes and control electronic circuits for the development of color-mixing based lamps to assure the chromatic performances of the device during operation.

Bibliography

[1] F. Schubert, *Light Emitting Diodes.* Cambridge University Press, 2009.

[2] R. R. Baniya, "Study of various metrics evaluating color quality of light sources," Thesis for the degree of Master of Science, AALTO University School of Electrical Engineering, 2012.

[3] I. L. Azevedo, M. G. Morgan, and F. Morgan, "The transition to solid-state lighting," *Proceedings of the IEEE*, vol. 97, no. 3, pp. 481–510, March 2009.

[4] M. H. Crawford, "Leds for solid-state lighting: Performance challenges and recent advances," *IEEE JOURNAL OF SELECTED TOPICS IN QUANTUM ELECTRONICS*, vol. 15, no. 4, pp. 1028–1040, July/August 2009.

[5] S. M. Sze and K. N. Kwok, *Physics of Semiconductor Devices.* Wiley Interscience, 2007.

[6] M. Meneghini, A. Tazzoli, G. Mura, G. Meneghesso, and E. Zanoni, "A review on the physical mechanisms that limit the reliability of gan-based leds," *IEEE TRANSACTIONS ON ELECTRON DEVICES*, vol. 57, no. 1, pp. 108–118, January 2010.

[7] M. Meneghini, L. Trevisanello, s. Podda, G. Meneghesso, and E. Zanoni, "Stability and performance evaluation of high-brightness light-emitting diodes under dc and pulsed bias conditions,," *Proc. SPIE*, vol. 6337, p. 633 70R, January 2006.

[8] "CREE XLamp XP-E LEDs," CREE, Datasheet, Available at http://www.cree.com/led-components-and-modules/products/xlamp/discrete-directional/~/media/Files/Cree/LED%20Components%20and%20Modules/XLamp/Data%20and%20Binning/XLampXPE.pdf.

[9] "CREE XLamp XP-E High-Efficiency White LEDs," CREE, Datasheet, Available at http://www.cree.com/led-components-and-modules/products/xlamp/discrete-directional/~/media/Files/Cree/LED%20Components%20and%20Modules/XLamp/Data%20and%20Binning/XLampXPEHEW.pdf.

[10] "Reliability of the OSLON SSL and OSLON Square Product Groups," OSRAM Opto Semiconductors, Application note, Available at http%3A%2F%2Fcatalog.osram-os.com%2Fcatalogue%2Fcatalogue.do%3Bjsessionid%3D3CCDD83058A002792748258519DFBB96%3Fact%3DdownloadFile%26favOid%3D0200000400025a6c000100b6&ei=s_3HUducAfCK4gT61YDgAw&usg=AFQjCNEkfElWVYT5D_b9f390v2WuJTIyDA&sig2=kep-ceBOx4h8QTYO4L2NlA.

[11] "OSLON OSRAM SSL 80 Warm White LEDs," OSRAM Opto Semiconductors, Datasheet, Available at http://catalog.osram-os.com/catalogue/catalogue.do?act=showBookmark&favOid=0000000700021b4500eb003a.

[12] "OSLON OSRAM SSL 80 Blue LEDs," OSRAM Opto Semiconductors, Datasheet, Available at http://www.osram.communicode.de/catalogue/catalogue.do?favOid=000000000001f31903c60023&act=showBookmark.

[13] "OSLON OSRAM SSL 80 Red LEDs," OSRAM Opto Semiconductors, Datasheet, Available at http://catalog.osram-os.com/catalogue/catalogue.do?act=showBookmark&favOid=0000000700021b4500eb003a.

[14] "OSLON OSRAM SX Grren LEDs," OSRAM Opto Semiconductors, Datasheet, Available at http://catalog.osram-os.com/catalogue/catalogue.do?favOid=000000020000e60d05820023&act=showBookmark.

[15] "LUXEON Rebel Illumination Portfolio," Philiphs Lumileds, Datasheet.

[16] "LUXEON Rebel Color Portfolio," Philiphs Lumileds, Datasheet.

[17] "Samsung LH351A-3535 Ceramic LED," Samsung, Datasheet.

[18] "LG 3535 3W Ceramic PKG," LG, Datasheet.

[19] “Specification SSC-SZ5-M series,” SEOUL SEMICONDUCTOR, Datasheet, Available at http://www.seoulsemicon.com/_upload/Goods_Spec/SZ5-M0-WW-C8(0).pdf.

[20] “Specification SSC-SZ5-P series,” SEOUL SEMICONDUCTOR, Datasheet, Available at http://www.seoulsemicon.com/_upload/Goods_Spec/SZ5-P0-WW-C8(0).pdf.

[21] “Series 2600a system sourcemeter instruments,” Keithley, Datasheet, Available at: http://www.farnell.com/datasheets/1506705.pdf.

[22] “Hp 3488a switch unit datasheets,” HP, Datasheet, Available at: http://www.testequipmentdepot.com/usedequipment/pdf/3488A.pdf.

[23] “A guide to integrating sphere theory and applications,” Labsphere Company, Tech. Rep., Available at: http://www.labsphere.com/uploads/technicalguides/aguidetointegratingsphereradiometryandphotometry.pdf.

[24] Y. Xi and M. E. F. Schubert, “Junction-temperature measurement in gan ultraviolet light-emitting diodes using diode forward voltage method,” *APPLIED PHYSICS LETTERS*, vol. 85, no. 12, pp. 2163–2166, September 2004.

[25] “Cree XLamp LEDs Chemical Compatibility,” CREE, Support document, June 2013, Available at http://www.cree.com/~/media/Files/Cree/LED%20Components%20and%20Modules/XLamp/XLamp%20Application%20Notes/XLamp_Chemical_Comp.pdf.